Universitat Autònoma de Barcelona

The one-armed ATLAS Forward Proton detector

Ivan López Paz

The one-armed ATLAS Forward Proton detector

Characterization, Installation, Commissioning and Performance

Ph. D. Dissertation
Cerdanyola (Barcelona), March 20, 2018

Ivan López Paz
Institut de Física d'Altes Energies
Universitat Autònoma de Barcelona

Thesis director
Sebastian Grinstein
ICREA / Institut de Física d'Altes Energies
Universitat Autònoma de Barcelona

Thesis director
Jörn Lange
Institut de Física d'Altes Energies

Universitat Autònoma de Barcelona

Institut de Física d'Altes Energies

The one-armed ATLAS Forward Proton detector

Characterization, Installation, Commissioning and Performance

Ivan López Paz

Abstract

The ATLAS experiment at the European Laboratory for Particle Physics (CERN), Geneva, has been taking data successfully since the Large Hadron Collider (LHC) accelerator started operations in 2010. Since then, it has been generating proton-proton collisions to study the frontiers of particle physics, at a centre of mass energy of 7-8 TeV first and, more recently, 13 TeV. However, the experiment is in constant evolution: detector ageing due to radiation damage, increasing collision rates and pile-up, and new scientific objectives often require upgrades of the ATLAS detectors. These ever-growing challenges motivate the continued research and development of new detector technologies.

To enhance the physics search of the experiment the ATLAS collaboration recently added a forward detector to identify intact protons that emerge from LHC collisions at very shallow angles. The ATLAS Forward Proton (AFP) detector enables the identification of diffractive processes and, ultimately, of central exclusive events, thus allowing, for example, the search of new heavy resonances in clean events. AFP consists of silicon trackers installed very close to the LHC proton beam and at $\sim$210 m from the interaction point (IP) at each side of ATLAS, in addition to Time-of-Flight detectors for pile-up removal. AFP needs the silicon tracker to fulfil challenging radiation hardness, spatial resolution and active area requirements. The novel 3D pixel sensor technology, first employed in the ATLAS Insertable B-Layer, was further developed and qualified for AFP.

The *one-armed AFP detector*, on which this thesis is focused, refers to the stage in which the AFP detector consisted only of silicon trackers in one side of ATLAS, installed at the beginning of 2016. The full installation was successfully finished one year later, when both silicon trackers and Time-of-Flight detectors were installed in both sides of ATLAS. This thesis describes the full process of technology characterization of the silicon tracker, production, installation, operation and particle physics data analysis of the one-armed AFP detector.

El detector de Protons Difractius d'un braç d'ATLAS

Caracterització, Instal·lació, Comissionat i Rendiment

Ivan López Paz

Resum

L'experiment ATLAS al Laboratori Europeu de Física de Partícules (CERN), Ginebra, ha obtingut dades amb èxit des que el Gran Col·lisionador d'Hadrons (LHC en anglès) començà a ser operatiu el 2010. Des de llavors, ha estat generant col·lisions de protó-protó per estudiar les fronteres de la física de partícules, a una energia al centre de masses de, primer 7-8 TeV i més recentment de 13 TeV. Tot i això, l'experiment es troba en evolució constant: la degradació dels detectors a causa de la radiació, l'increment de la freqüència de les col·lisions i nous objectius científics sovint requereixen millores als detectors d'ATLAS. Aquests nous reptes motiven la continuada recerca i el desenvolupament de noves tecnologies de detectors.

Per ampliar la recerca de física de partícules a l'experiment, la col·laboració d'ATLAS afegí recentment un detector "forward" per identificar protons emergits de col·lisions al LHC a angles petits. El detector de Protons Difractius d'ATLAS (o AFP, de l'anglès "ATLAS Forward Proton") capacita la identificació de processos difractius i esdeveniments centrals exclusius, permetent per exemple la cerca de noves ressonàncies pesades en esdeveniment nets. L'AFP consisteix en detectors de traces de silici instal·lats a poca distància del feix de protons del LHC i a $\sim$210 m del punt d'interacció a cada costat d'ATLAS, juntament amb detectors de temps de vol per reduir senyals de fons produïts per l'acumulació de col·lisions. Els detectors de silici han de demostrar la suficient resistència a la radiació, una bona resolució espacial i els requeriments d'àrea activa necessaris per AFP. La tecnologia de sensors de píxels 3D, primerament utilitzada en el detector IBL d'ATLAS, ha sigut desenvolupat i qualificat per AFP.

El *detector AFP d'un braç*, en el qual aquesta tesi està basada, es refereix a l'etapa en la qual el detector AFP consistia només de detectors de traces de silici en un dels costats d'ATLAS, que va ser instal·lat a principis de 2016. La instal·lació es va completar un any després, quan tant els detectors de traces com els de temps de vol es van instal·lar als dos costats d'ATLAS. Aquesta tesi descriu el procés complet de caracterització de la tecnologia del detector de traces de silici, producció, instal·lació i anàlisi de dades del detector AFP en la seva primera etapa.

Acknowledgements

In these few lines I would like to thank all the people that made this thesis possible. In case anybody feels excluded, please contact the author.

First of all, I am very grateful Sebastian Grinstein for giving me the opportunity to carry out my thesis in his group and for his supervision. Thanks also to Jörn Lange, who had the patience to supervise my work as well, and with whom I learned a lot during the last years.

I would like to thank my colleagues from the IFAE pixel group for their help and support throughout these years. Grazie Emanuele, Stefano, Chiara e Giulia, Danke Fabian, grazas David and thanks Vagelis. We may have spent long or short time together in the group, but I am grateful to all of you.

I want to thank everybody from the office, which made working life (and lunch time) more enjoyable, without forgetting about the people that left, in particular the current (and former) students Gerard, Raquel, Alfonso, Bruno and John.

People from CNM have been very helpful, and thus I would like to thank Giulio, Marta, Virginia, David and Sergi for their support.

An important part of this thesis would have not been possible without the people from the AFP community. Thanks to Michael Rijssenbeek for his help during my stay at CERN. Also, thanks to the Kris, Martin, Giulio, Elzbieta, Maciej, Rafal, Chris and Michal for their great job and help during the AFP installation in which I could learn a lot about different detector aspects I was not aware before, and thanks to Paul, Tom, Lada and Libor for the nice test-beams. I would also like to thank Mario Martínez and Rafal Staszewski (again) for their advise in the analysis of the AFP data.

Gracias a mis amigos, con los que he podido compartir grandes momentos, buenos viajes y mejorables barbacoas.

Por último, y no menos importante, quiero agradecer a mi familia. Sin su apoyo y ayuda no me habría sido posible llegar hasta aquí. Muchas gracias a mis padres Jerónimo y Pilar, y mis hermanos Cristina y Álex.

Contents

1. Physics Motivation: Diffractive Physics

The ATLAS Forward Proton (AFP) detector was designed to identify events with intact forward protons in the final state in proton-proton collisions at the LHC. In general, these events are associated with diffractive scattering. While the majority of the high energy proton-proton interactions at the LHC are described by perturbative Quantum Chromodynamics, diffractive processes are generally soft and effective theories are needed to obtain theoretical predictions. However, the ultimate target of the physics program of AFP is the study of Central Exclusive events. In these processes all the final state particles can, in principle, be measured by combining forward and central detectors. The central final state of such events can be any resonance, opening the window to potential discovery of new particles, while opening the possibility to measure the properties of known particles in a clean environment.

In this chapter, the physics motivation for the AFP experiment is presented.

1.1. The Standard Model

The Standard Model (SM) of particle physics is a theory that includes all known particles and describes their interactions. The SM encompasses the electromagnetic, weak and strong forces, but does not incorporate the gravitational force. It successfully predicts, with great accuracy, different properties of the weak and electromagnetic interactions. For instance, the fine structure constant (α), which indicates the strength of the electromagnetic force, was measured with an uncertainty of 0.23 parts per billion [1]. However, it is not a complete theory, since, as already mentioned, it does not include gravity, nor explains dark matter, the mass scale or dark energy. Therefore the limits of the SM still need to be explored.

The SM is a theory of interacting quantum fields. Excitations in these fields correspond to particles, and each field corresponds to a different type (flavour) of a particle. These particles can be classified in three groups: quarks, leptons and gauge bosons. Table 1.1 summarizes the standard model particles and their properties.

The gauge theory of electromagnetism, Quantum Electrodynamics (QED), describes the interaction of charged particles through a mediating gauge boson, the photon (γ). Similarly to QED, Quantum Chromodynamics (QCD) describe the strong interaction through its gauge bosons, the gluons. The QCD equivalent of the electric charge is a property called *colour*. Three strong charges exist, the label colour was applied to them since the combination of the three (red, blue and green) yields a total neutral charge. Quarks carry a single colour, while gluons carry a non-singlet combination of colour and anti-colour charges. Thus, unlike the photons, gluons can interact with each other. In addition, the weak force describes the interaction between fermions (quarks and leptons) thorough a mediating charged (W^+ and W^-) or neutral (Z^0) gauge boson.

1.1.1. Strong Interactions

Strong interactions are responsible for the presence of *hadrons*, particles formed by two (*mesons*, e.g. pions) or three (*baryons*, e.g. protons and neutrons) quarks. All hadrons have neutral colour charge, either by a group of a quark (colour) and an anti-quark (anti-

Table 1.1.: Summary of particles in the Standard Model. Data is taken from [1].

		Particle	Mass	Q			
Fermions	Quarks	up (u)	$2.2^{+0.6}_{-0.4}$ MeV	2/3 e	Weak	EM interaction	Strong
		down (d)	$4.7^{+0.5}_{-0.4}$ MeV	-1/3 e			
		charm (c)	1.28±0.03 GeV	2/3 e			
		strange (s)	96^{+8}_{-4} MeV	-1/3 e			
		top (t)	173.1±0.6 GeV	2/3 e			
		bottom (b)	$4.18^{+0.04}_{-0.03}$ GeV	-1/3 e			
	Leptons	electron (e)	510.9989461±0.0000031 keV	-1 e			
		muon (μ)	105.6583745±0.0000024 MeV	-1 e			
		tau (τ)	1776.86±0.12 MeV	-1 e			
		electron neutrino (ν_e)	<2 eV	0			
		muon neutrino (ν_μ)	<0.19 MeV	0			
		tau neutrino (ν_τ)	<18.2 MeV	0			
Gauge bosons		Z^0 boson	91.1876±0.0021 GeV	0			
		$W^\pm$ boson	80.385±0.015 GeV	±1 e			
		photon (γ)	0	0			
		8×gluon (g)	0	0			
		Higgs boson (H)	125.09±0.24 GeV	0			

colour) like for mesons or by a group of three quarks (of red, green and blue colour charges) like for baryons.

The strength of the chromodynamic interactions is set by the strong coupling constant (α_S). One feature of QCD is its *asymptotic freedom*, the fact that α_S gets weaker at shorter distances or high momenta (Q^2), while at low momenta or large distances the strong coupling constant strength increases, confining the quarks and gluons to colourless objects (hadrons). This is the origin of the concept of colour confinement. This effect, the dependance of α_S on Q^2, is named *running coupling constant*.

To contrast the SM predictions with measurements, high energy protons are collided at the Large Hadron Collider (LHC) [2] at CERN. The experiments at the LHC usually study collisions which result in the scattering of the proton constituents (partons), i.e. quarks and gluons. Since α_S becomes small at high energies, the hard scattering among partons can be calculated using perturbation techniques of quantum field theory. In perturbative QCD (pQCD), scattering cross sections are calculated at order-by-order basis, each containing the same in-going and out-going particles but larger number of interactions. As each strong interaction introduces an extra factor of α_S in the scattering amplitude for each order calculation, higher order contributions become negligible when the strong coupling is weak, which is the case in hard scattering processes between partons. However, colour confinement does not allow a direct experimental test of the parton level cross section. As the distance between the parton increases, the strong coupling potential grows and eventually generates new gluons and quarks (or anti-quarks) that immediately recombine into stable colourless particles (hadrons). This non-perturbative process is known as *hadronization* or *fragmentation*. Thus, the hard scattering of partons results in showers of collimated particles (jets).

The perturbation component of the hard scattering can be calculated analytically. Feynman diagrams can be used to represent the contribution of each order and facilitate the calculation. Some leading order and next-to-leading order diagrams are shown in Fig. 1.1.

In proton-proton collisions, the fraction of the proton momentum carried by each parton ($x = p_{parton}/p_{proton}$) is unknown. Since parton interactions inside the proton occur at low energies, pQCD is not applicable. Instead, parametrization of the *parton distribution func-*

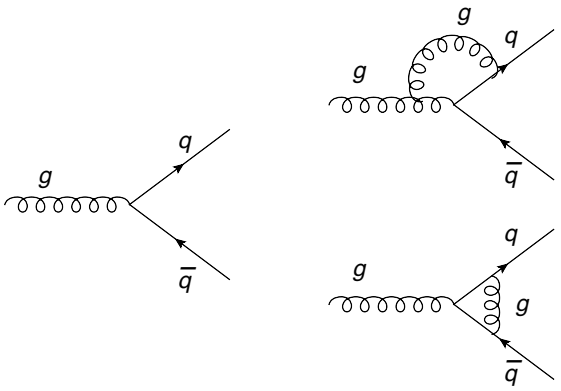

Figure 1.1.: Example of leading order (left) and next-to-leading order (right) Feynman diagrams for a process $g \to q\bar{q}$.

tions (PDF, $f_p(x, Q^2)$) are used. The PDFs are independent of the specific interaction and can be measured experimentally (for example, in deep inelastic scattering experiments). Using the DGLAP equation [3], the PDFs measured at a given scale can be used to evolve the distribution for the process of interest. Fig. 1.2 shows the proton PDFs obtained at scales $Q^2 = 10$ GeV^2 and 10^4 GeV^2 [4]. The cross section of a QCD mediated process can

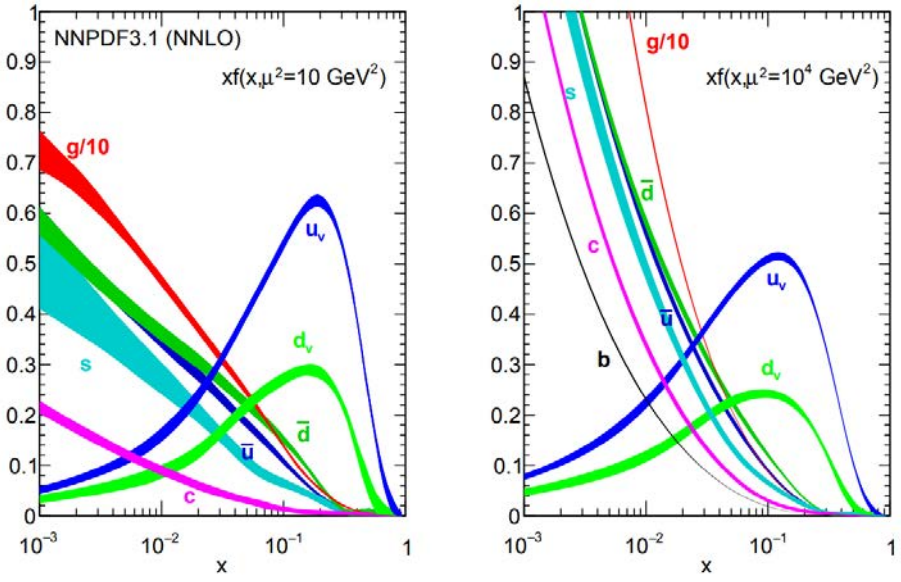

Figure 1.2.: Proton parton distribution functions (PDF) as a function of the proton momentum fraction carried by the parton (x) at scales $Q^2 = 10$ GeV^2 (left) and 10^4 GeV^2 (right). Taken from [4].

be calculated as a convolution of parton distribution functions and the cross section of the participating partons.

$$\mathrm{d}\sigma(pp \to X) = f_p(x_1, Q^2) f_p(x_2, Q^2) \mathrm{d}\sigma_{had}(x_1, x_2, Q^2), \tag{1.1}$$

where $f_p(x, Q^2)$ is the parton distribution function of the proton, $x_{1/2}$ are the momentum fraction that participates in the interaction in each of the protons and σ_{had} is the cross section of the process between the partons. To date, proton-proton cross sections measured

at colliders are in good agreement with the predictions performed with pQCD in high momentum transfer processes [1, 5, 6].

In events in which the partons in the protons participate in the hard scattering, the rest of the proton fragmentates as the total colour charge becomes non-neutral. The quarks and gluons originating from this fragmentation can interact with the ones originating from the other proton and emit radiation, generating further final state particles. All the interactions in the event other than the hard scattering constitute the *underlying event*.

1.2. Diffractive Physics

Diffractive processes are those in which no quantum numbers are exchanged between the interacting particles (charge, colour, ...). However, diffractive interactions typically involve small momentum transfer, and thus are not well described by perturbative QCD. In fact, QCD fails to explain the increase of the total hadron-hadron cross section with the centre-of-mass-energy [7]. Models have been proposed to obtain the main features of the diffractive production mechanism. In particular, the Regge theory has been rather successful in modelling the diffractive hadronic interactions in terms of exchanges of colourless Pomerons ($\mathbb{P}$), which are usually modelled as the exchange of two gluons [8].

Depending on the energy scale (e.g. transfer momentum) in which the diffractive interactions happen, they can be categorized as *soft* or *hard* diffraction:

- *Soft Diffraction:* the energy scale is lower than the hadron scale ($<$1 GeV). In such case, the interactions cannot be resolved by perturbative QCD.
- *Hard Diffraction:* due to asymptotic freedom, the running coupling becomes small enough at hadron energy scales ($>$1 GeV) to allow treating the interactions perturbatively.

1.2.1. Diffractive Event Signature

Diffractive processes in hadron collider experiments can be mostly identified by the following signatures:

- *Intact forward proton(s):* As no quantum numbers are exchanged, the proton(s) may not be fragmented in the final state. Usually, the energy lost by the intact proton in the interaction is low. Therefore the proton is scattered by a small angle with respect to the beam direction.
- *Large rapidity gaps:* A rapidity gap is defined as rapidity regions with no measured particles. The appearance of rapidity gaps in diffractive events is a consequence of the lack of colour exchange, which suppresses radiation between interacting particles.

However, in hadron colliders like the Tevatron and the LHC, the final state particles can interact with each other, which can translate in a suppression of rapidity gaps and intact protons. This effect must be accounted for in the cross section calculation (see *rapidity gap survival probability* discussion in Sec. 1.2.3). Furthermore, in environments with a high number of collisions per event (pile-up) the large rapidity gaps can be suppressed by pile-up event. Finally, large rapidity gaps can also be present in non-diffractive interactions as a statistical fluctuation of the final state particle geometry distribution.

Experimentally, technical difficulties exist to measure forward protons. Detectors in colliders do not have a 4π coverage, since some space is left for the beam-pipes. Thus, as intact protons in the final states of diffractive events are scattered at very low angles, they usually escape the instrumented region. In order to measure such protons, detectors need

to be placed very close to the beam and far away from the interaction point. Therefore, diffractive events can be studied with specialized detectors which are able to detect forward intact protons far from the collision where they originate, so-called *forward detectors*.

1.2.2. Soft Diffraction

Soft interactions can be divided in *elastic* and *inelastic*. In the former, the initial and final particles are identical. The cross section contribution of elastic events in pp collisions at the LHC (at a centre-of-mass energy of 8 TeV) is [9]

$$\sigma_{el}(pp \to pp) = 24.33 \pm 0.04(\text{stat.}) \pm 0.39(\text{syst.}) \text{ mb}, \tag{1.2}$$

which constitutes ∼25% of the total pp cross section (i.e. $pp \to$ anything).

Inelastic soft events, on the other hand, can be either diffractive or non-diffractive. In soft *single diffraction*, one of the two incoming particles gets dissociated, while the other remains intact, e.g. $pp \to pX$, where X is any state (see Fig. 1.3).

In *double diffraction*, however, both incoming particles are dissociated, although only vacuum quantum numbers are exchanged between them, e.g. $pp \to XY$, where X and Y are any state. Thus, this is an example of a diffractive process with no intact forward proton signature, but shows a central large rapidity gap separating the products of the dissociated protons (see previous section).

It is possible that each particle emits a Pomeron which dissociates to create an additional central state. This is called *central diffraction* or *double Pomeron exchange* (DPE). In DPE the incoming particles can stay intact in the final state or dissociate (one or both).

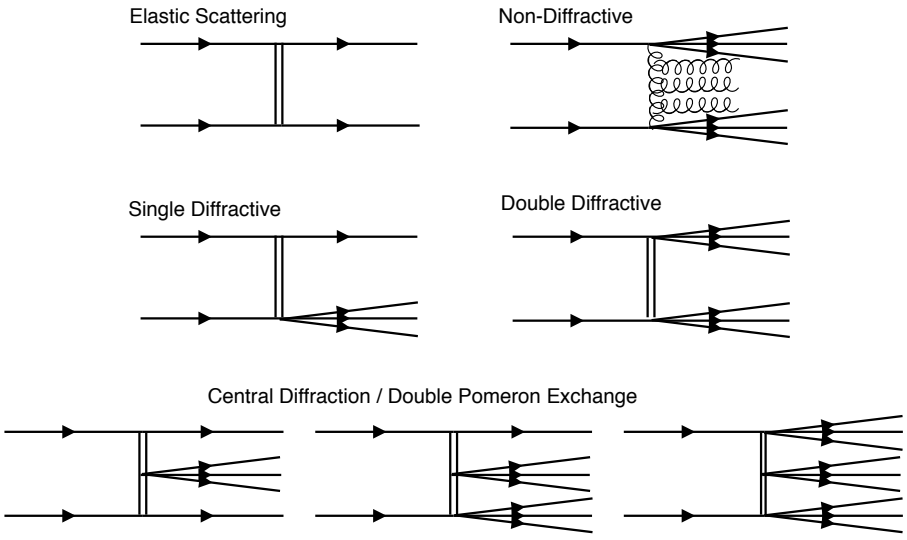

Figure 1.3.: Feynman diagrams of soft processes: Elastic scattering (top left), non-diffractive (top right), single diffractive (middle left), double diffractive (middle right) and central diffraction (bottom). The double lines represent momentum exchange with the vacuum quantum numbers (i.e. a pomeron or photon).

Regge Theory and the Pomeron

The Regge theory is a phenomenological approach that allows to explain the soft interaction processes in QCD which are not accessible via perturbative QCD calculations. It is based

on the continuation of the angular momentum to the complex plane. According to the Regge theory, the elastic strong interactions can be understood as an exchange of families of particles that fall into the same *trajectory*. These Regge trajectories are described in terms of $\alpha(t)$, the complex continuation of the angular momentum as a function of the transverse momentum, which coincides with the particle spin at values of t that matches the particle squared mass (see Fig. 1.4). Each trajectory corresponding to a family of particles is named after its lowest mass particle. Experimentally the trajectories are well described by a straight line, i.e.

$$\alpha(t) = \alpha(0) + \alpha' t. \tag{1.3}$$

Fig. 1.4 shows an example of Regge trajectories, which includes four degenerate families of particles (ρ, f, ω and a) in a plot of spin as a function of their squared mass fitted by a straight line ($\alpha(t) = 0.5 + 0.9t$).

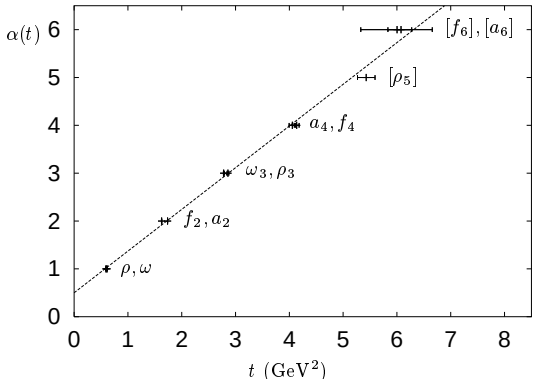

Figure 1.4.: Particle spins versus their squared masses. The straight line is $\alpha(t) = 0.5 + 0.9t$. Taken from [8].

One of the results from the Regge theory is that the total cross section at large centre of mass energies is proportional to a sum over the contributing trajectories as:

$$\sigma_{tot} \sim \sum_i s^{\alpha_i(0)-1}. \tag{1.4}$$

Since the trajectory intercept ($\alpha(0)$) is lower than 1 the total cross section would decrease as a function of $\sqrt{s}$. However, experimentally it has been observed otherwise (see proton-(anti-)proton cross section in Fig. 1.5): thus the Pomeron trajectory was introduced, with $\alpha_{\mathbb{P}}(0) = 1.08$ [7], which would be responsible for the total cross section increase with the centre-of-mass energy. Hence, it was found that hadronic total cross sections could be fitted with the sum of powers

$$\sigma_{tot} = Xs^{0.0808} + Ys^{-0.4525}, \tag{1.5}$$

where the first exponent corresponds to $\alpha_{\mathbb{P}}(0) - 1$ (Pomeron trajectory contribution) and the second to $\alpha_{\mathbb{R}}(0) - 1$ (Regge trajectory contribution) [7]. The Pomeron trajectory, however, does not correspond to any real resonance as opposed to the other trajectories.

1.2.3. Hard Diffraction

In non-diffractive hard interactions parton distribution functions are used to parametrize the proton structure. In hard diffraction a similar approach can be used with the diffractive

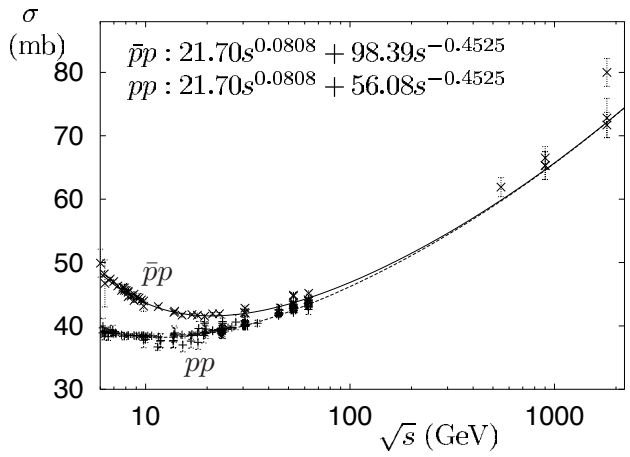

Figure 1.5.: Total proton-(anti-)proton cross section at different centre-of-mass energies. The full line corresponds to the fit for the $\bar{p}p$ data while the dashed line corresponds to the fit for the pp data. Taken from [8].

parton distribution function (dPDF), $f_d(x, Q^2, \xi, t)$ where ξ is the momentum fraction of the proton carried by the exchanged Pomeron. In hard diffractive processes the Pomeron is described as a colourless object with a partonic structure (gluons and quark singlets) with the quantum numbers of the vacuum. The Pomeron partons participate in the hard scattering. The diffractive parton distribution function can be factorised into a Pomeron flux ($f_{\mathbb{P}/p}(\xi, t)$ and a Pomeron partonic structure term ($\varphi_{\mathbb{P}}(x/\xi, Q^2)$), i.e.

$$f_d(x, Q^2, \xi, t) = f_{\mathbb{P}/p}(\xi, t)\varphi_{\mathbb{P}}(x/\xi, Q^2). \tag{1.6}$$

Fig. 1.6 shows the partonic density of quark singlet and gluons ($\varphi_{\mathbb{P}}$) at different energy scales, as measured by the H1 collaboration [10]. In Fig. 1.6 it can be seen how the Pomeron is predominantly gluonic.

In order to obtain the cross section of hadron-hadron hard diffractive events it is needed to introduce an extra factor, the *rapidity gap survival probability* (already mentioned in Sec. 1.2.1). It takes into account extra soft interactions between initial or final states which can suppress the rapidity gap and the intact proton in proton-proton collisions. This effect was observed when comparing diffractive deep inelastic scattering results from HERA (electron-proton) with Tevatron diffractive cross sections (proton-antiproton). It was found that the measured diffractive cross sections in HERA extrapolated to Tevatron energies ($\sqrt{s}$ = 1.8 TeV) were larger than the measured value by a factor ∼10 [12]. In processes where one of the participating protons emit a Pomeron which undergoes a hard interaction with the remaining one and yield only one intact proton (or a rapidity gap), named *single diffractive* (SD), the cross section is computed as:

$$\mathrm{d}\sigma = S^2 f_{\mathbb{P}/p}(\xi, t)\varphi_{\mathbb{P}}(x_1/\xi, Q^2) f_p(x_2, Q^2)\mathrm{d}\sigma_{had}(x_1, x_2, Q^2), \tag{1.7}$$

where S^2 is the rapidity gap survival probability and f_p denotes the non-diffractive proton PDF. Some examples of hard SD processes are shown in Fig. 1.7. Experimentally, the processes in the examples would be observed with an intact forward (diffractive) proton separated by a large rapidity gap with the rest of the activity, i.e. the Pomeron remnants, the hard scattering products and the proton remnants.

Another example of diffractive events are *central diffractive* processes (CD) or double Pomeron Exchange (DPE), where both protons emit a Pomeron and leave the collision

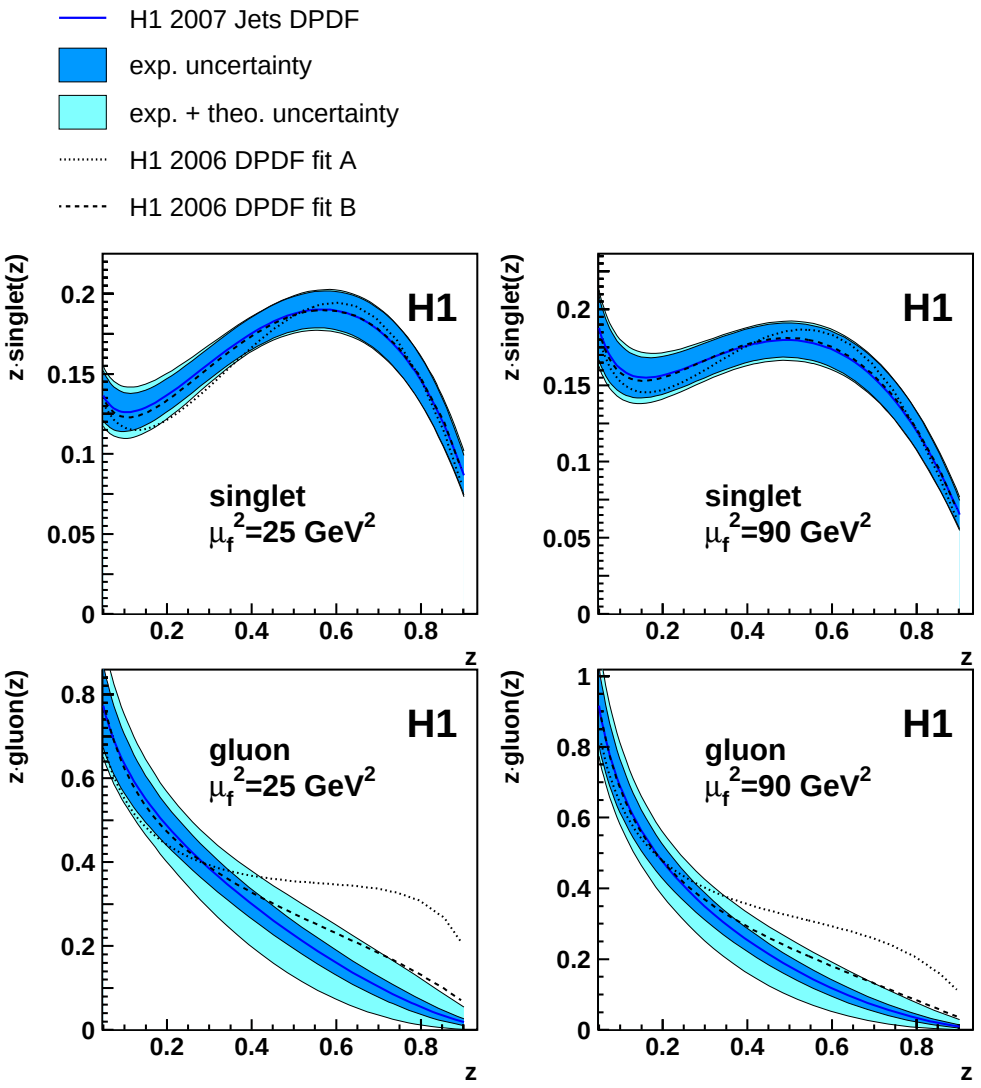

Figure 1.6.: The diffractive quark density (top) and the diffractive gluon density (bottom) for two values of the squared factorisation scale μ_f^2 =25 GeV^2 (left) and 90 GeV^2 (right), as a function of the fraction of the momentum carried by the Pomeron (z). The solid line indicates the H1 2007 Jets DPDF, surrounded by the experimental uncertainty (dark shaded band) and the experimental and theoretical uncertainties added in quadrature (light shaded band). The dotted and dashed lines show the parton densities corresponding to the H1 2006 fit A and fit B from [11].

intact. The cross section is calculated similarly to the hard SD events. Fig. 1.8 shows two Feynman diagrams of CD processes. The signatures of such events are two forward protons from each side of the interaction point, followed by large rapidity gaps in both sides, the Pomeron remnants and the central scattering products.

1.3. Central Exclusive Production

Central Exclusive Production (CEP) is a special type of diffractive events with two intact protons in the final state and where the whole energy of the colourless interaction is used to produce a central system. The lowest order process involves the exchange of two gluons. As opposed to other processes, no proton or Pomeron remnant that can escape the detector

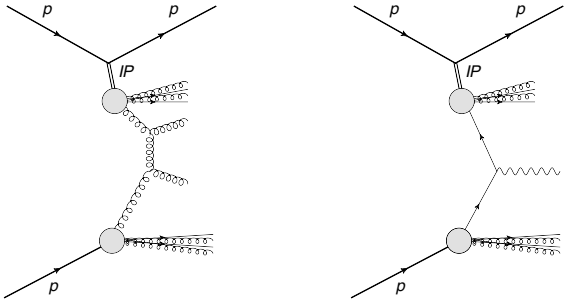

Figure 1.7.: Feynman diagrams of hard single diffractive processes with jets (left) and W/Z bosons in the final state. The double lines represent a Pomeron, and the blobs indicate the dissociation of an object with a partonic structure (proton or Pomeron).

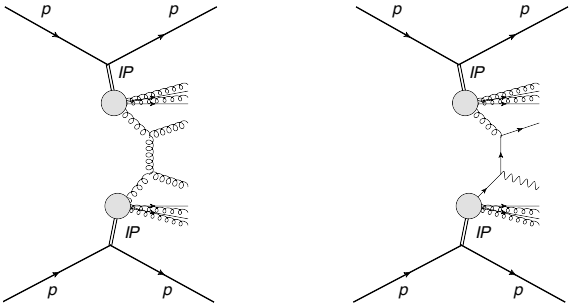

Figure 1.8.: Feynman diagrams of hard central diffractive processes with jets (left) and jet+photon in the final state. The double lines represent a Pomeron, and the blobs indicate the dissociation of an object with a partonic structure (Pomeron).

acceptance are produced. Hence, in such events all final state particles can be measured: the protons can be detected by the use of a forward detector while the rest are produced in the central region and contained within the central detector system. Its signature, with two forward protons and the centrally produced particles, is clean (without remnants from the same interaction that complicate the event reconstruction). The mass of the central object can be determined in two independent ways: using the outgoing protons and measuring the decays in the central system. Fig. 1.9 (top) shows two examples of CEP processes, with a Higgs boson and a dijet final states.

Similar to the CEP processes are the $\gamma\gamma$ production events. Although $\gamma\gamma$ production is not technically a diffractive process, since the exchanged photons do not have the quantum numbers of the vacuum, it can be measured in the same way as exclusive production. In $\gamma\gamma$ interactions, each of the protons emit a photon to interact with each other, which results again in two intact forward protons, see Fig. 1.9 (bottom). Such events are useful to study $\gamma\gamma$ processes in proton colliders given their clean signature (similar to that of CEP processes), which enables the possibility to explore photon anomalous couplings beyond the standard model.

1.4. Previous (Hard) Diffractive Physics Experiments

The first instance of hard diffraction was observed at the CERN SPS collider with the UA8 experiment [13], in collisions at $\sqrt{s} = 630$ GeV. These diffractive events contained jets and a forward proton with >90% the initial energy in the final state (i.e., $pp \to pX$, with X

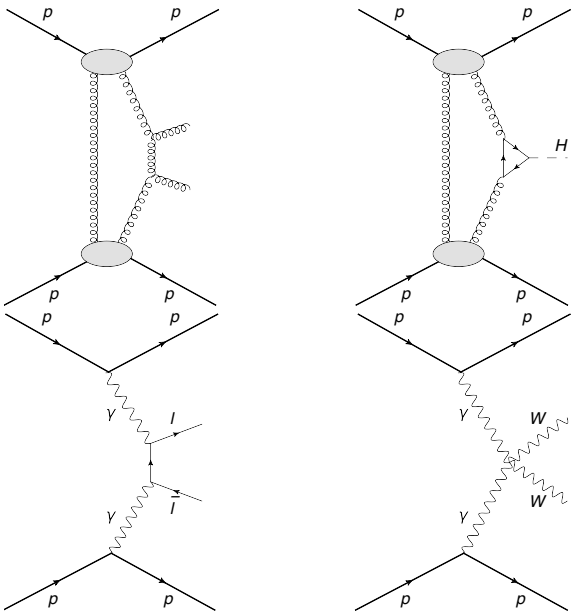

Figure 1.9.: Feynman diagrams of central exclusive production processes (top) with a dijets (left) and a Higgs boson (right) in the final state. Below are Feynamn diagrams of $\gamma\gamma$ productions with two leptons and intact protons (left), and two gauge bosons (W, Z or γ) and two protons in the final state (right).

being any final state with jets). While the hard scattering processes were observed in the UA2 calorimeter, the forward protons were measured using a Roman Pot spectrometer [14]. The Roman Pots consist in movable pots along the beam-pipe structure containing a detector, usually placed ∼100 m away from the interaction point, with the goal to approach this detector to the circulating beam. Using the knowledge of the accelerator magnetic system between the interaction point and the Roman Pot, and the trajectory of the proton measured with the detectors therein (wire chambers in UA8), it is possible to reconstruct the proton kinematics.

Hard diffraction was studied in the *ep* HERA accelerator as well, in diffractive deep inelastic events. At HERA, two co-existing experiments (H1 and ZEUS) contained a leading proton spectrometer. The Roman Pots in the H1 Forward Proton Spectrometer (FPS) [15] were equipped with multi-layer scintillating fibres, while ZEUS' Leading Proton Spectrometer (LPS) [16] consisted of a silicon micro-strip tracker. Within the HERA experiments, the partonic structure of the Pomeron was measured (see Fig. 1.6) as well as the dijet single diffractive cross section [10]. The cross section of the inclusive diffraction ($ep \to eXp$) was also measured [17].

At the Tevatron proton-antiproton collider, both CDF and D0 experiments were equipped with Roman Pot detectors, which allowed the study of hard diffraction in collisions with centre-of-mass energies up to 1.96 TeV. Although both experiments used Roman Pots, only D0 contained Roman Pots in both sides from the interaction point (i.e., the leading proton and antiproton sides), while CDF had Roman Pots to detect only the leading antiproton. The Roman Pot stations of both CDF and D0 contained scintillating fibres.

At the CDF experiment, dijet single diffraction was measured using the Roman Pot detectors [18]. The ratio of single diffractive over non-diffractive dijet events was observed to be lower than expected from HERA results by one order of magnitude, which is due to the probability of soft interactions between the initial or final states (gap survival probability), suppressing diffractive signatures [12, 19] (see Fig. 1.10 (top left)). The CDF experiment

also studied W boson production in single diffraction processes. It was able to reconstruct in an event-by-event basis the mass of the W boson using the reconstruction of the energy lost of the detected antiproton measured by the Roman Pot detector, and the calorimeter information in the central region of the CDF experiment [20] (see Fig. 1.10 (top right)).

Central Exclusive Production processes were also studied at Tevatron. The CDF collaboration observed exclusive production for the first time in hadron colliders and measured the cross section of the exclusive production of dijets [21]. This was accomplished by requiring an anti-proton tag in the Roman Pot spectrometer, a veto in the beam shower counters on the proton side and a dijet mass over total central mass measured in the calorimeter greater than 0.8 (i.e. $R_{jj} = M_{jj}/M_X > 0.8$) to reduce the processes with underlying events like the Double Pomeron Exchange. The D0 collaboration showed evidence of CEP dijet events at $M_{jj} > 100$ GeV [22]. Similar to the dijet production, the diphoton exclusive production cross section was measured at CDF [23] ,which constituted the first observation of such process in hadron-hadron colliders.

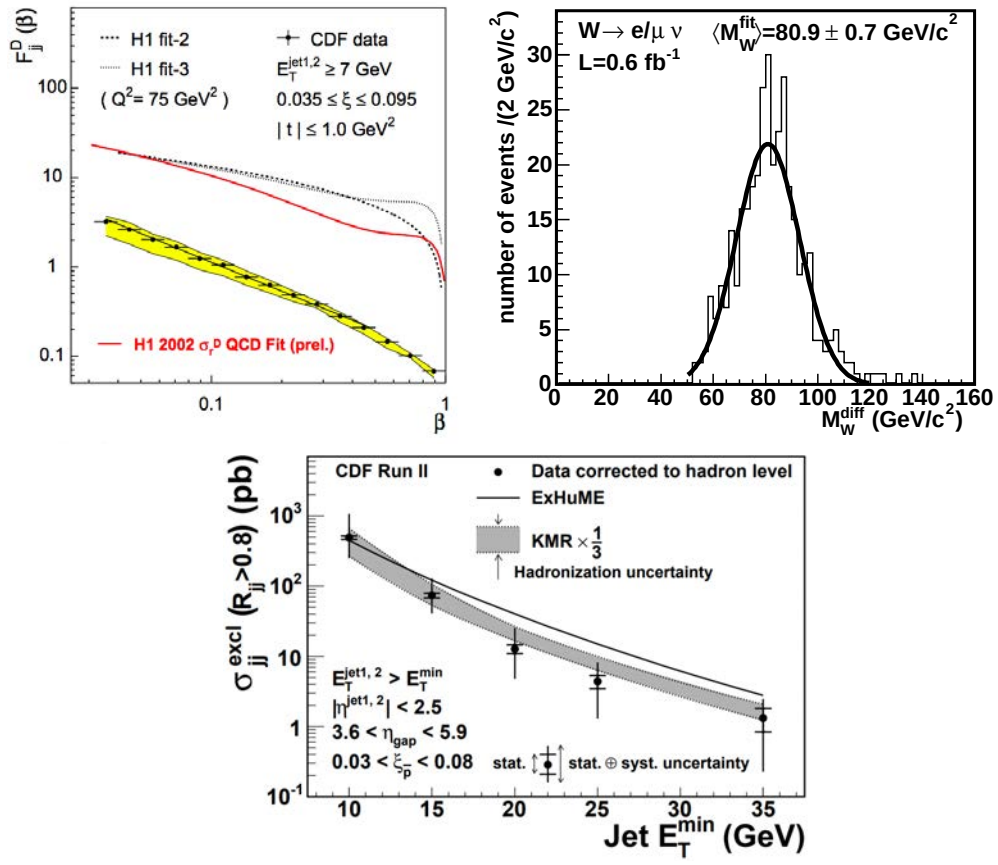

Figure 1.10.: Selection of Tevatron results on diffraction. Top left [12, 19]: the CDF diffractive structure function $f_d(x, Q^2, \xi, t)$ versus $\beta = x/\xi$ compared with predictions based on factorization and parton densities obtained by H1 from diffractive deep inelastic scattering at HERA. Top right [20]: W boson mass distribution obtained from forward proton tagged event by an event-by-event mass reconstruction of the leading mass kinematics. Bottom [21]: Exclusive dijet cross section measured by the CDF collaboration, as a function of the minimum jet transverse energy, compared with Monte Carlo and analytical leading order calculations.

ATLAS and CMS at the LHC proton-proton accelerator have Roman Pot detectors

hundreds of meters away from the interaction point. Until 2015, only ALFA (ATLAS) and TOTEM (CMS) detectors were present. However, the main goals of these detectors are the study of soft diffraction, elastic and total cross section determination. Still, hard diffraction studies could be performed by the ATLAS [24] and CMS [25] experiments without forward proton tagging, through the observation of large rapidity gaps and reconstructing the proton relative energy loss (ξ) using the calorimeter information. The cross section of the single diffractive dijet production was measured in both experiments, yielding a new rapidity gap survival probability measurement at $\sqrt{s} = 7$ TeV with big uncertainties (see Fig. 1.11 (left)). Moreover, the rapidity gap cross section was studied, although the results are not fully compatible with simulations [26] (see Fig. 1.11 (right)).

Exclusive central production processes have been studied in the ATLAS collaboration without forward proton tagging, leading to the measurement of the exclusive $\gamma\gamma \to \ell^+\ell^-$ ($\ell = e, \mu$) [27] and $\gamma\gamma \to W^+W^-$ [28] in proton-proton collisions. With no proton detection, exclusive events are selected by requiring isolated vertices in the inner detector with isolated tracks associated to the exclusive final states to suppress events with underlying events.

The following sections introduce the forward detector for hard diffraction installed in ATLAS in 2016 (AFP), which is expected to improve these results with proton tagging. In parallel, CMS installed tracking and timing detectors in the same year, complementing the TOTEM detector and forming the CMS-TOTEM Precision Proton Spectrometer (CT-PPS).

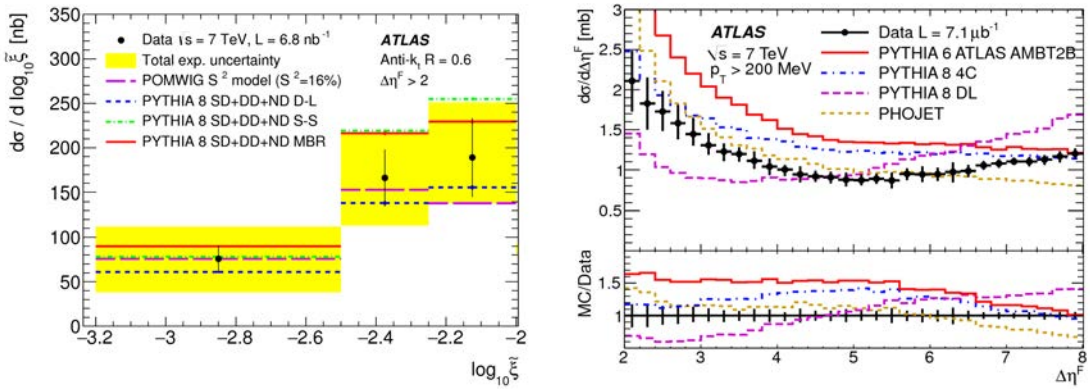

Figure 1.11.: Selection of ATLAS results on diffraction. Left [24]: The diffractive dijet differential cross section as a function of ξ for events with rapidity gaps $\Delta\eta^{\mathrm{F}} > 2$. The error bars on the data and the MC models indicate their respective statistical uncertainties, while the yellow bands show the total uncertainties on the data. The 'POMWIG S^2' model represents the MC data accounting for the rapidity gap survival probability $S^2 = 0.16$. Right [26]: Inelastic cross section differential in forward gap size $\Delta\eta^{\mathrm{F}}$ for particles with p_{T} >200 MeV and $\Delta\eta^{\mathrm{F}} > 2$. The error bars indicate the total uncertainties. Full lines show the predictions of several MC generators.

1.5. Physics Goals and Requirements For a Forward Detector for Hard Diffraction in ATLAS

In order to enhance the physics potential of ATLAS the collaboration decided to install a forward proton system capable of performing hard diffractive measurements, the ATLAS Forward Proton (AFP) detector. The ultimate goal of AFP is to identify CEP processes

and exploit these events to look for new physics. The research lines for the AFP detector include [29]:

- Aid the study of rapidity gap events in hadron colliders and shed some light into the discrepancies between HERA and Tevatron/LHC results of rapidity gap survival probabilities. Moreover, some disagreement exist between LHC data and simulation [26] in terms of rapidity gap distributions which could be studied with AFP.
- Study the Pomeron parton structure in hard interactions, since it was proven [30] that the ratio between γ+jet and dijet DPE (Fig. 1.8) differential cross sections is sensitive to the quark content in the Pomeron.
- Observation of possible new resonances in central exclusive production events. Historically, CEP processes were of interest for the discovery of the Higgs boson, as it can be produced in such events and the kinematic parameters of the exclusive process are determined by the kinematic parameters of the outgoing protons, although the Higgs boson was finally measured with other signatures [31, 32]. However, AFP could be useful to observe other unknown resonances with higher mass which couple to gluons or photons.
- Measure two-photon production of W, Z or γ pairs to study possible anomalous couplings, which would indicate the existence of new physics. With enough luminosity, AFP could improve the existing limits on such couplings [33].

The AFP detector will be able to observe diffractive events by identifying forward intact protons from proton-proton collisions in ATLAS. In order to have enough acceptance to measure low scattering angle particles it needs to be installed far from the interaction point, and very close (few millimetres) to the proton beam. At these distances radiation hardness is crucial.

Kinematic reconstruction can be performed by measuring the diffractive proton trajectory with the knowledge of the beam optics (the magnet system between the interaction point and the AFP detector). Thus at least two distant measurements of the proton position are needed for each side of ATLAS. The position measurement precision would be key to obtain a valuable proton kinematic reconstruction information.

To obtain enough events for some of the hard diffraction processes, AFP would need to participate in data taking conditions with several collisions per event. However, identifying which of the collisions is the source of the proton measured at AFP under these conditions is challenging. A possibility to palliate this problem is to introduce a Time-of-Flight system able to reconstruct with enough resolution the vertex position from which the diffractive proton originates.

This thesis covers the AFP pixel tracker technology qualification, the tracker module production, the detector installation and commissioning, and the very first performance studies.

2. Experiment Layout: The AFP Detector in the ATLAS Experiment

The CERN laboratory in Switzerland houses the largest circular hadron accelerator to date, the Large Hadron Collider (LHC). The LHC is able to accelerate protons to record energies to collide them in order to study the frontiers of the standard model of particle physics. One of the experiments in which the proton-proton collisions take place is the ATLAS experiment, which is composed of several detector systems with the goal of measuring the products of such events.

The AFP detector is one of the sub-systems forming the ATLAS experiment. It is installed at ∼200 m from the ATLAS interaction point and is able to detect diffractive protons at few millimetres away from the LHC proton beam.

In this chapter the ATLAS experiment in the LHC accelerator is described, and the AFP detector as it was configured in 2016 is presented as one of its subsystems.

2.1. The Large Hadron Collider

The Large Hadron Collider (LHC) [2] is a circular proton accelerator with 27 km circumference located at CERN (Geneva, Switzerland). The LHC is the last component of a large accelerator complex that is able to accelerate protons to energies up to 7 TeV along each of its two beam-pipes, adding up to a maximum design center of mass energy ($\sqrt{s}$) of 14 TeV. So far LHC Run 1 period (2011-2012) produced collisions with a $\sqrt{s}$ of 7 and 8 TeV, and only at the start of Run 2 period (2015 - present) the operational centre of mass energy was increased to 13 TeV.

A schema of the CERN accelerator complex is shown in Fig. 2.1. The acceleration chain is as follows: protons are obtained from hydrogen ionization, which then are accelerated to an energy of 50 MeV at the LINAC2 linear accelerator, before reaching the CERN Proton Synchrotron Booster (PS Booster). There, the protons reach an energy of 1.4 GeV to be injected to the PS accelerator, where the protons are accelerated to 25 GeV. Next, at the CERN SPS (Super Proton Synchrotron) the protons reach 450 GeV before being injected into the LHC machine.

In the LHC the protons travel along the beam-pipes in bunches of $\sim 10^{11}$, with a bunch-to-bunch spacing of 25 ns at a revolution frequency of 11 kHz. The bunches are then collided in each of the four experimental interaction points (IP) in the LHC: ATLAS [35], CMS [36], ALICE [37] and LHCb [38].

Both ATLAS (A Toroidal LHC AparatuS) and CMS (Compact Muon Spectrometer) are multipurpose experiments for high luminosities. The ALICE (A Large Ion Collider Experiment) experiment was designed for heavy-ion physics and the LHCb (LHC-beauty) experiment aims to study b-quark physics.

The rate of events generated at the LHC depends on the *instantaneous luminosity* delivered by the machine and the total ($pp \to X$) cross section (σ_{tot}), namely

$$R_{tot} = \mathcal{L}\sigma_{tot}. \tag{2.1}$$

The luminosity ($\mathcal{L}$) depends on the beam parameters:

$$\mathcal{L} = \frac{N_b^2 n_b f_{ref} \gamma}{4\pi\varepsilon_N \beta^*} F \tag{2.2}$$

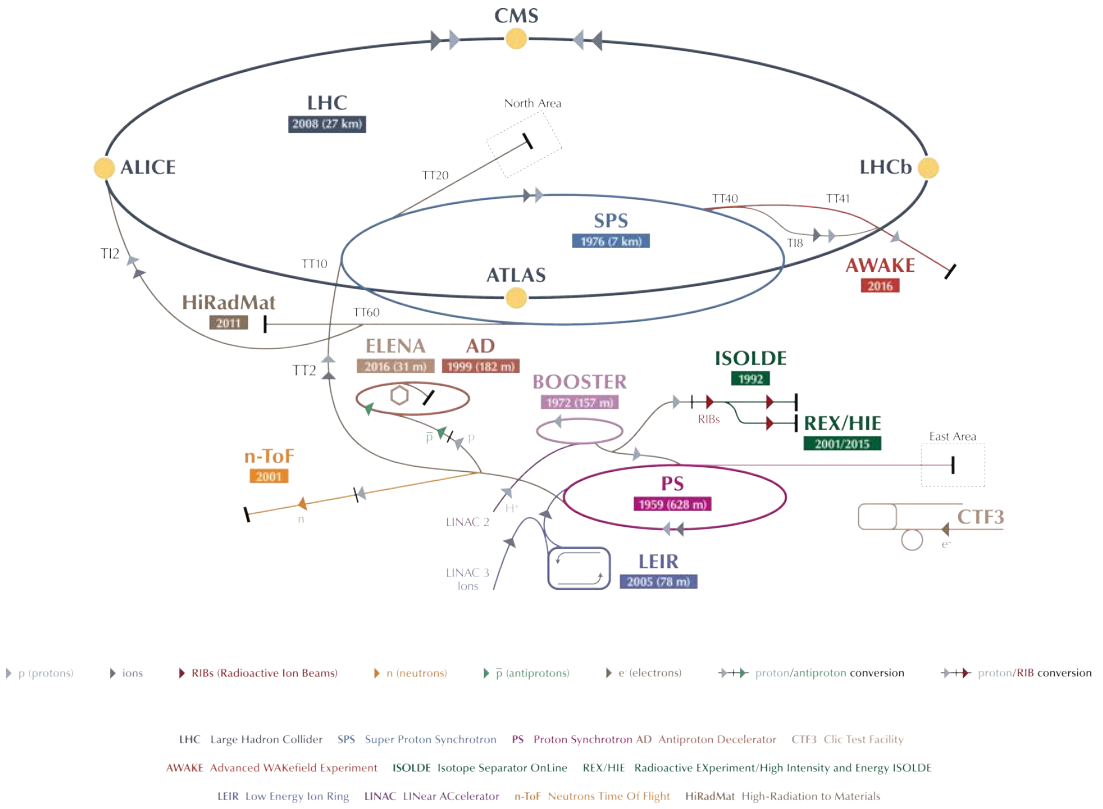

Figure 2.1.: The CERN accelerator complex. Taken from [34].

where N_b is the number of particles per bunch, n_b the number of bunches per beam, f_{rev} the revolution frequency, γ the Lorentz relativistic factor, ε_N the normalized beam emittance [1], β^* is the betatron function at the interaction point [2] ($\beta^* = 0.4$ m in 2016) and F is the geometrical correction which takes into account the crossing angle of the bunches. The *integrated luminosity* L provides information about the total collected number of events:

$$L = \int \mathcal{L} \mathrm{d}t = \frac{n_{ev}}{\sigma_{tot}}. \tag{2.3}$$

During the year 2016 the instantaneous luminosity was $\sim 10^{34}$ cm^{-2}s^{-1}. That year the LHC delivered a total integrated luminosity to ATLAS of 38.5 fb^{-1} out of which 35.6 fb^{-1} was recorded by the experiment (see Fig. 2.2).

Given the high proton density of protons per bunch and the high intensities, it is possible to record interactions from more than one interaction in the same event. The extra interactions are referred as *pile-up*. The probability of having a certain number (μ) of interactions per bunch-crossing follows a Poisson distribution. The average number of interactions, $\langle\mu\rangle$, which quantifies the pile-up activity, is given by the ratio between the rate of generated events and the bunch crossing rate, i.e.

$$\langle\mu\rangle = \frac{\mathcal{L}\sigma_{tot}}{n_b f_{rev}}. \tag{2.4}$$

[1] The beam emittance is a measurement of the spread of the beam particles in position and momentum. A small emittance is preferred for small distance confinement and uniform transverse momentum.

[2] The betatron function at a given point (here the IP) is a measure of the distance from the given point to the position at which the beam is twice as wide. Smaller values at the IP are preferred for larger luminosities.

The average pile-up in ATLAS during the 2016 (2015) period of LHC Run 2 was 24.9 (13.7) (see Fig. 2.2). Note however, that the LHC parameters during data taking period relevant to this thesis were non-standard, in which the pile-up was reduced to $\langle\mu\rangle$ ∼0.03 and $\langle\mu\rangle$ ∼0.3 (see Sec. 4.3.4).

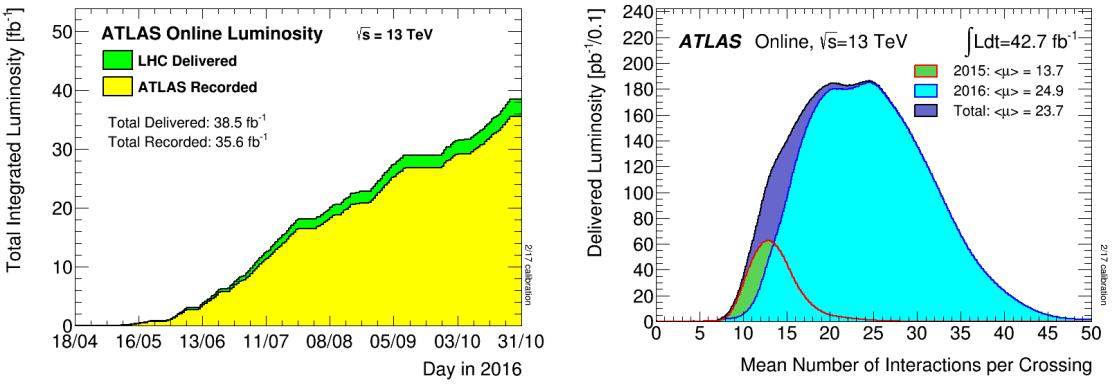

Figure 2.2.: Cumulative integrated luminosity delivered by the LHC and recorded by ATLAS during 2016 (left) and pile-up distribution in ATLAS during stable beams in 2015 and 2016 (right). Taken from [39].

2.2. The ATLAS Experiment

The ATLAS experiment is placed in one of the proton-proton interaction points of the LHC (Point 1). The full size of the detector is about 42 m in length and 25 m in height. It hosts many sub-detectors (see Fig. 2.3) with the goal of reconstructing the particles arising from the proton collisions: the inner detector (Sec. 2.2.1), the electromagnetic and hadronic calorimeters (Sec. 2.2.2) and the muon spectrometer detectors (Sec. 2.2.3). Magnetic systems with fields of up to 4 T are used to aid particle momentum identification. In addition, further away from the interaction point, ATLAS features forward detectors (Sec. 2.2.5) for the study of events with final-state particles leaving the interaction point in shallow angles, for e.g. luminosity measurements and elastic and diffractive physics.

The inner ATLAS detector system (tracker) is used to determine the paths (tracks) of charged particles that are produced in the LHC collisions. Their momenta can be determined due to the 2 T solenoid that surrounds the tracker. Energetic electrons and photons are absorbed by the electromagnetic calorimeter where their energy is measured, while mesons and baryons interact mostly in the hadronic calorimeter, where they generate a particle shower whose energy is measured. Muons are passing the calorimeters and are identified in the muon spectrometers where their properties are determined. Neutrinos and hypothetical other weakly interacting particles cannot be observed in the experiment due to their low cross section. However, their presence and their properties can be inferred from energy and momentum conservation (so called "missing transverse energy/momentum").

2.2.1. Inner Detector

The Inner Detector (ID) is the inner-most detector system of ATLAS. It is able to measure the positions of the charged particles generated in the proton-proton collision. This information is used to reconstruct their tracks, from which the point of the original collision (primary vertex) or a late decay (secondary vertex) can be measured and the momentum

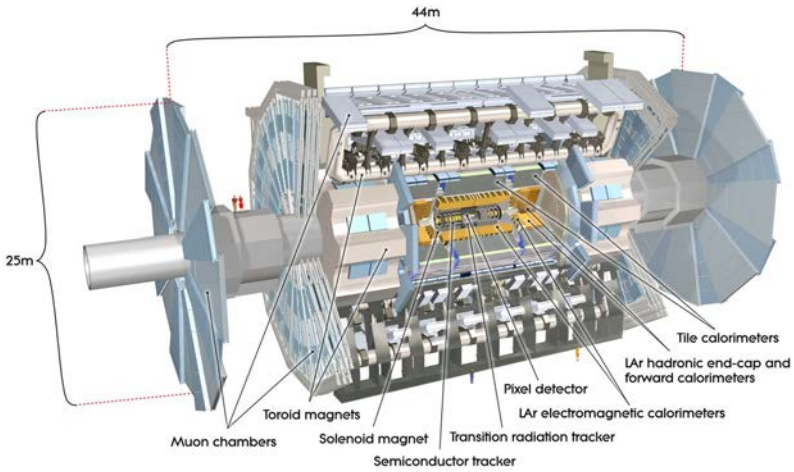

Figure 2.3.: The ATLAS detector. Taken from [40].

of those particles can be determined, which is possible with the magnetic field generated by the ATLAS barrel solenoid (see Sec 2.2.4).

The ID consists of three sub-detectors, from inner-most to outer-most (see Fig. 2.4): the *Pixel Detector* [41] which includes the recently installed Insertable B-Layer (IBL) [42], the *SemiConductor Tracker* (SCT) [43, 44] and the *Transient Radiation Tracker* (TRT) [45, 46]. The overall coverage of the Inner Detector is $|\eta| < 2.5$.

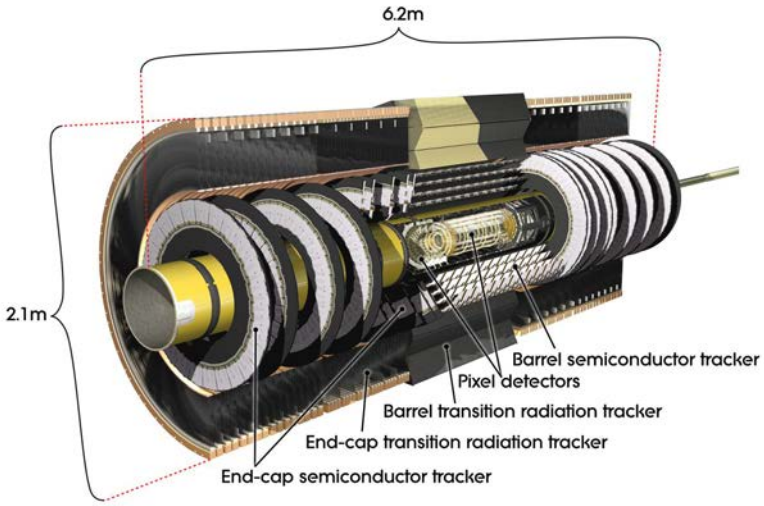

Figure 2.4.: The ATLAS Inner Detector sub-systems. Taken from [47].

Pixel detector

A total of four barrel layers of pixelated silicon sensors compose the Pixel Detector [41], in addition to six end-caps (discs perpendicular to the beam axis), three end-caps at each side. The barrel layers are placed at a radius of 3.2, 5.1, 8.9 and 12.3 cm with a length in z of $|z|$ <332 mm for the inner layer and $|z|$ <400 mm for the rest. The end-caps are installed at $|z|$ =495, 580 and 650 mm with a radial extension of 88.8 mm< R < 149.6 mm, which makes the Pixel detector, including the end-caps, 1.4 m long along the beam axis, covering a pseudo-rapidity range of $|\eta| < 2.5$. The sensors in the three outer layers and

the end-caps are standard n-in-n planar sensors with a pixel size of 50×400 μm^2.

The inner-most layer, the Insertable B-Layer [42] was installed in 2015 at a distance of ∼3.2 cm from the beam-pipe centre. Its purpose is to improve the impact parameter resolution, which is a critical parameter for the identification of relatively long-lived particles ($c\tau$ ∼400 - 500 μm) like b hadrons (b-tagging) as well as to guarantee the redundancy of the pixel system during its ageing. As opposed to the other layers, it combines two different silicon sensor technologies: n-in-n planar (central 75% of the barrel) and n-in-p 3D (25% of barrel, at the ends) technologies. The IBL sensors have a pixel size of 50×250 μm^2. In total, the Pixel Detector consists of a total of more than 80 million pixels.

The Pixel Detector is the subsystem closest to the LHC proton-proton collisions. As a consequence, it is also the most exposed to radiation damage. Fig. 2.5 shows the fluence[3] per fb^{-1} in the Inner detector region. The IBL layer was designed for 550 fb^{-1} [42], the estimated luminosity accumulated before the replacement of the Inner Detector for the high luminosity period in 2025. Thus the estimated fluence the end of its life time is ∼3×10^{15} n_{eq}/cm^2 (5×10^{15} n_{eq}/cm^2 with a safety factor).

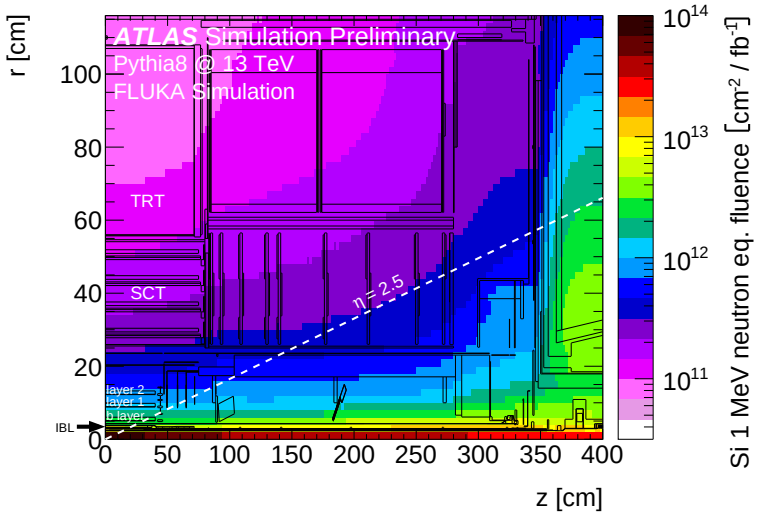

Figure 2.5.: 1 MeV neutron equivalent fluence per fb^{-1} of integrated luminosity in the ATLAS inner detector. The minimum-bias proton-proton events are simulated at 13 TeV centre-of-mass energy and a predicted inelastic cross section of 78.4 mb. Particle tracking and interactions with material are simulated with the FLUKA 2011 code using the Run 2 geometry description of the ATLAS detector. Taken from [48].

SemiConductor Tracker (SCT)

The SCT [43, 44] is composed by four barrel layers and nine end-caps per side of microstrip p-in-n silicon sensors. The barrel layers are installed at radii of 30.0, 37.3, 44.7, and 52.0 cm and cover a length of $|z| < 74.5$ cm. Each layer contains modules of two silicon strip sensors with a small stereo angle of 40 mrad to provide 2D information. Nine end-caps are distributed along the beam axis, in a range of $|z|$ =85–272 cm, with an outer radius of 56 cm and an different inner radii, from 27 to 44 cm, so that the SCT has an instrumented coverage in pseudo-rapidity of $|\eta| < 2.5$. The strips in the barrel modules have a 80 μm pitch, while the pitch of the end-cap module strips ranges from 56.9 to 90.4 μm.

[3]The fluence is a measurement of the radiation damage. It is measured in units of "1 MeV neutron equivalent" per unit surface, i.e. the amount of 1 MeV neutrons needed to reproduce the same radiation damage effects. See Sec 3.1.3 for more information.

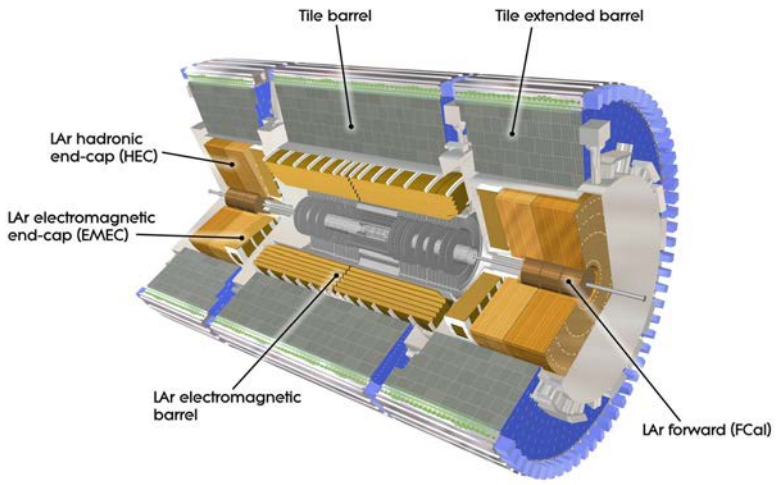

Figure 2.6.: The ATLAS Calorimeter sub-systems. Taken from [49].

Transient Radiation Tracker (TRT)

The TRT [45, 46] consists of 4 mm diameter straw-tube detectors filled with an ionizing gas mixture. The walls of the tubes are under a ∼1500 V potential with respect to the 31 μm diameter gold-plated tungsten wire in the center, which allow to measure positions with a 130 μm resolution per straw. The TRT barrel is composed of 52544 straws of 1.44 m length along the beam direction covering 56< R <107 cm. The end-caps, on the other hand, are made of 122,880 straws each, which are distributed along the beam axis with a coverage of 85< $|z|$ <271 cm and 64< R <100 cm.

2.2.2. Calorimeters

The purpose of the ATLAS calorimeters is to measure the energy of the charged and neutral particles from the collisions in the range from the GeV scale to the TeV scale.

In general, calorimeters in particle physics are made of a material in which the traversing particles deposit their energy, generating a signal depending on the deposited energy. In homogeneous calorimeters the entire detector volume is sensitive to the particles and contributes to the signal formation. In sampling calorimeters, as used in ATLAS, the fractions of particle absorption and signal generation are carried out by different alternating layers. This approach allows to design a more compact detector. The data is later corrected to account for the fraction of the signal that is not detected.

The ATLAS calorimeter system has a total coverage in pseudo-rapidity of $|\eta| < 4.9$ and surrounds the Inner Detector. It consists of three sub-detectors (see Fig. 2.6): the Electromagnetic, the Hadronic, and the Forward calorimeters. The Forward calorimeter, which also contains electromagnetic and hadronic sections, cover the the pseudo-rapidity range of $3.1 < |\eta| < 4.9$. Together the calorimeter system covers $|\eta| < 4.9$ and usually is used to measure jets in the range of 20 GeV$\lesssim p_{\mathrm{T}} \lesssim$1 TeV.

Electromagnetic CALorimeter (ECAL)

The electromagnetic (EM) calorimeter absorbs electrons and photons in the range from 50 MeV to 3 TeV to measure their energies and directions. It also participates in the reconstruction of hadronic jets. The EM calorimeter consists of accordion-shaped layers of lead absorber planes and liquid Argon (LAr) [50] in a pseudo-rapidity range of $|\eta| < 3.2$,

divided in a barrel ($|\eta| < 1.457$) and two end-caps ($1.375 < |\eta| < 2.5$ and $2.5 < |\eta| < 3.2$). Particles passing through the LAr calorimeter ionize the argon, and the generated charge is collected by copper layers placed in the middle of the LAr sections, acting as readout electrodes.

The ECAL barrel is divided in 3 layers: The inner layer is $4.3X_0$ thick[4], and segmented in readout strips of $\Delta\eta \times \Delta\phi = 0.0031 \times 0.098$. The middle layer's readout is segmented in units of $\Delta\eta \times \Delta\phi = 0.0025 \times 0.0245$ and is $16X_0$ thick. The third one is read out with a $\Delta\eta \times \Delta\phi$ granularity of 0.05×0.0245 and is $2X_0$ thick. The end-caps, on the other hand, consist in 2 layers (3 in the $1.5 < |\eta| < 2.5$ region) with an η-dependent granularity.

Hadronic CALorimeter (HCAL)

The hadronic calorimeter measures the energy of the particles that escape the electromagnetic calorimeter, usually jets originating from quark and gluon hadronisation. The HCAL absorbs all the remaining particles from the collision, except for the muons, which are detected in the muon spectrometer, and the neutrinos, which are not detected by the detector. The HCAL is divided into the central region, the tile calorimeter (TileCal), and the hadronic end-cap calorimeter (HEC).

The TileCal's [51] absorber medium is made of steel and its active region of scintillator tiles. Traversing particles generate photons in the scintillator material, which are collected by photomultipliers (PMTs), which, in turn, generate electrons to form the output signal. The TileCal covers a total pseudo-rapidity range of $|\eta| < 1.7$ with a central barrel section of $|\eta| < 1.0$ and an extended barrel section covering $0.8 < |\eta| < 1.7$, both of them with three layers in total. The inner (outer) radius of all barrels is 2.28 m (4.25 m), segmented in depth in three layers of 1.5, 4.1 and 1.8 interaction lengths (λ)[5] thick for the barrel and 1.5, 2.6 and 3.3λ for the extended barrel. Each of the barrels is segmented in 64 modules in ϕ of $\Delta\phi \sim 0.1$. The readout has a $\Delta\eta \times \Delta\phi$ granularity of 0.1×0.1 in the two inner layers and a granularity of $\Delta\eta \times \Delta\phi = 0.2 \times 0.1$ in the outermost barrel layer.

The HEC on the other hand uses copper as absorption material and LAr as active medium. It covers a pseudo-rapidity of $1.5 < |\eta| < 3.2$ in the form of two wheels on each side with a varying granularity depending on η, from $\Delta\eta \times \Delta\phi = 0.1 \times 0.1$ to a granularity of 0.2×0.2 in $\Delta\eta \times \Delta\phi$ in the higher pseudo-rapidity region. In addition, the HEC overlaps with the ECAL and the FCAL in η.

Forward CALorimeter (FCAL)

Consisting of one electromagnetic and two hadronic calorimeters, the forward calorimeter is placed at a $3.1 < |\eta| < 4.9$ range to maximize the calorimetry acceptance around the interaction point, with a granularity of $\Delta\eta \times \Delta\phi = 0.2 \times 0.2$. All layers utilize LAr as a detection medium, with a copper structure. The inner (electromagnetic) layer uses copper as an absorber while the outer (hadronic) layers utilize tungsten.

2.2.3. Muon Spectrometer

Beyond the hadronic calorimeters the only particles that are not yet detected are the neutrinos (which are not detectable in ATLAS, but inferred) and the muons, which are measured in the muon spectrometer. The ATLAS Muon Spectrometer [52] consists of four sub-detectors (see Fig. 2.7): the Monitored Drift-Tube (MDT) Chambers [53], the Cathode Strip Chambers (CSC) [54], the Resistive Plate Chambers (RPC) and the Thin

[4]The radiation length (X_0) is defined as the thickness over which a high energy electron reduces its energy by a factor of $1/e$.

[5]The nuclear interaction length (λ) is defined as the thickness over which high energy hadrons need to pass through to reduce their number by a factor of $1/e$

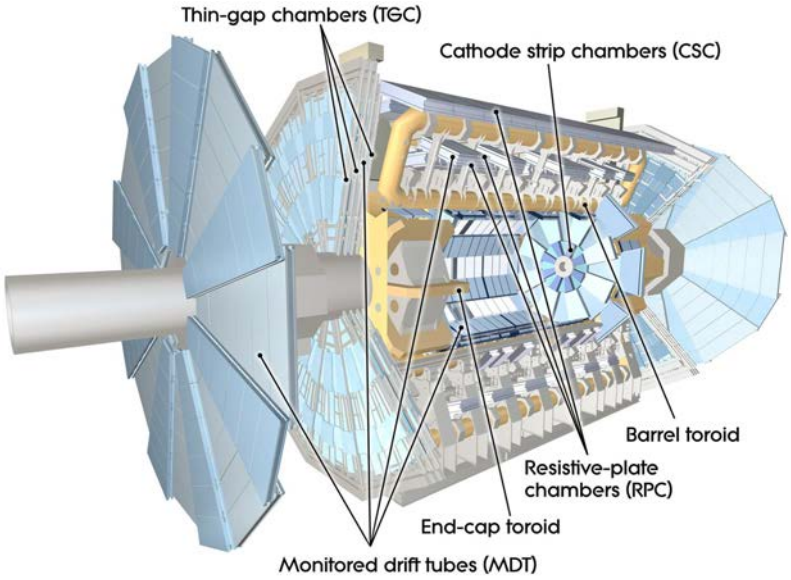

Figure 2.7.: The ATLAS Muon sub-systems. Taken from [55].

Gas Chambers (TGC). Together, these systems cover a range of $|\eta| < 2.7$ and are able to measure muon tracks with good momentum resolution in the range of 10 GeV$\lesssim p_{\mathrm{T}} \lesssim$1 TeV.

Monitored Drift-Tube (MDT) Chambers

The MDT subsystem [53] consists of drift chambers that provide precision tracking information from the muons that reach the Muon Spectrometer. It is used to resolve the muon momentum by determining the curvature of the track in the magnetic field produced by the toroid magnets (see Sec 2.2.4). Each drift tube is made of an Aluminium 400 μm thick tube of 3 cm diameter filled with a mixture of Ar-CO_2 under 3 bar pressure. The length of the drift tube varies from 0.9 to 6.2 m, and is grouped in multi-layers of three to four layers of tube.

Each of the 1,150 chambers consists of two multi-layers (adding up to 354000 tubes), to achieve a position resolution of $\sim$40 μm and 35 μm for 6 and 8 layer chambers. The chambers are distributed to cover a pseudo-rapidity range of $|\eta| < 2.7$, although the innermost layer covers $|\eta| < 2.0$.

During the winter shut-down of 2016/2017, new MDT tubes with half the previous diameter (i.e. 1.5 cm) were installed to improve the muon momentum reconstruction [56].

Cathode Strip Chambers (CSC)

With the goal to assist the measurement of the muon momentum in the forward region by precision tracking measurement, the CSC [54] covers the pseudo-rapidity range of $2.0 < |\eta| < 2.7$ with multi-wire proportional chambers with segmented cathodes that reach a position resolution of 60 μm. It is formed by 32 four-layered Cathode Strip Chambers filled with a Ar-CO_2 mixture, 16 on each end-cap. Each layer is segmented by 250 and 420 wires (these two chamber versions are used alternately and partially overlapping).

Resistive Plate Chambers (RPC)

Together with the Thin Gas Chambers, the Resistive Plate Chambers are used for muon triggering, while also providing a position measurement along the MDT tubes in the non-

bending plane [57]. The RPC system consists of parallel plates of a very high resistive material separated by a gas (detector) volume, which is ionized by the traversing muons.

The sub-detector covers a total range in pseudo-rapidity of $|\eta| < 1.05$ with RPCs. They consist of 2 mm thick bakelite electrode plates spaced by 2 mm, coated with graphite painting. A high voltage potential of about 9.6 kV is applied between the two coated surfaces, which makes the RPC work in avalanche mode. The 2 mm gap is filled with a gas mixture of $C_2H_2F_4$, C_4H_{10} and SF_6.

Thin Gap Chambers (TGC)

The Thin Gap Chambers (TGC) [52] are multi-wire proportional chambers, which cover the forward region of the ATLAS detector for muon triggering in the range $1.05 < |\eta| < 2.4$, although their tracking capabilities extend up to $1.05 < |\eta| < 2.7$. The 50 μm diameter anode wires inside the chambers are arranged in a pitch of 1.8 mm, and a distance of 1.4 mm with respect to the cathodes. Each chamber provides a spatial resolution of about 1 mm and a time resolution of 5 ns.

2.2.4. Magnet System

The ATLAS Magnet system [58] consists of a solenoid magnet that surrounds the inner detector and three toroid magnets (one barrel and two end-cap toroids) in the muon system in order to bend the muon trajectory and provide a momentum measurement. The inner solenoid has a magnetic field of 2 T, while the toroidal magnets provide a magnetic field that of up to 4 T.

2.2.5. Forward Detectors

In addition to the previously described sub-detectors, ATLAS houses forward detector subsystems in order to extend the physics reach of the experiment and to carry out luminosity measurements. The following detectors in order of distance from the ATLAS interaction point, fall in this category: LUCID, ZDC, AFP and ALFA.

LUminosity measurement Using Cherenkov Integrating Detector (LUCID)

The LUCID [59] detector was designed to provide a precise measurement of the luminosity of the ATLAS collisions. It consists of two modules (one at each side of ATLAS) around the beam-pipe at 17 m from the interaction point. Each module consists of 20 PMTs of 15 mm diameter during Run I. The PMTs are grouped in 5 sets of detectors with different features. Due to the increase of pile-up with respect to Run I the diameter of the PMTs were reduced to 10 mm in Run II to avoid saturation.

Zero-Degree Calorimeter (ZDC)

The Zero Degree Calorimeter [60] consists of two tungsten/quartz sampling calorimeters (one at each side of ATLAS) located at 140 m away from the interaction point between the two LHC proton beam-pipes. It detects spectator neutrons in heavy ion collisions with a coverage of $|\eta| > 8.3$ in order to measure the impact parameter of the collision.

ATLAS Forward Proton (AFP)

Located at $\sim$210 m from the ATLAS IP, the AFP detector is intended to detect and reconstruct the kinematic parameters of protons leaving intact the ATLAS detector. To achieve this, the final design consists of four horizontal Roman Pot stations (two at each side of ATLAS) able to move tracker and Time-of-Flight detectors as close as $\sim$3 mm from

the LHC proton beams. Since this thesis is focused on the AFP tracker, the detector is fully described in Sec. 2.3.

Absolute Luminosity For ATLAS (ALFA)

Further away from the interaction point than the AFP detector, at 240 m, the ALFA detector [61] is installed. It consists of four stations (two at each side of the ATLAS IP), each containing two vertical Roman Pots equipped with multi-layer scintillating fibres as tracking detectors.

It is designed to determine the proton-proton total cross-section and the LHC luminosity by the detection of protons interacting elastically in the IP. The elastic cross-section is related to the total cross-section (σ_{tot}) by the optical theorem:

$$\sigma_{tot} = 4\pi \mathrm{Im}[f_{el}(t=0)]. \tag{2.5}$$

where $f_{el}(t=0)$ is the elastic scattering amplitude evaluated for a zero four-momentum transfer (t, see Sec A), i.e. the forward direction. The Roman Pots move the detectors few millimetres (depending on the beam optics) close to the proton beam so that it is able to measure very low t protons, which are scattered at very low angles from the ATLAS central detector. The tracking and beam optics information are combined to reconstruct the transfer momentum from the detected protons.

The geometry of ALFA was optimised to have acceptance for elastic events ($\xi = 0$) in dedicated beam optics conditions, as opposed to the AFP design which focuses on hard diffraction. In order to be able to measure protons from elastic scattering events, the β^* needs to be increased, which in turn reduces the luminosity (see Eq. 2.2). So far, the ALFA collaboration has been able to perform the measurements of the proton-proton cross-section at 7 [62] and 8 TeV [9] center-of-mass energy.

2.2.6. Minimum Bias Trigger Scintillator (MBTS)

The analysis presented in Chapter 5 of this thesis utilizes information from the Minimum Bias Trigger Scintillator (MBTS) [63] which is not classified in any of the previous detector categories.

The Minimum Bias Trigger Scintillators consist of 2 cm polystyrene scintillator disks positioned at each end of the detector in front of the liquid-argon end-cap calorimeter cryostats, at $z = \pm 3.56$ m, in order to trigger on maximally inclusive events. They are segmented into two rings in pseudo-rapidity and eight (four) sectors in azimuth in the inner (outer) ring and cover the range $2.08 < |\eta| < 3.86$. The inner ring has an acceptance at $2.76 < |\eta| < 3.86$ (or 15 cm$< R <$45 cm) while the outer ring covers the pseudo-rapidity region of $2.08 < |\eta| < 2.76$ (or 45 cm$< R <$90 cm).

2.2.7. ATLAS Trigger and Data Acquisition

The rate in which two groups of bunches of protons from each circular beam cross each other is ∼30 MHz.[6] The data size per event is ∼1 MB, which would not be feasible to store at such rate. In order to solve this, the events are filtered by a two-level trigger system: the hardware-based Level-1 (L1) trigger, and the High-Level Trigger (HLT) which is processor and software-based. Fig. 2.8 shows the structure of the ATLAS TDAQ system.

During data taking, ATLAS sub-systems (e.g., MBTS, Muon detectors, ...) send trigger signals to a Central Trigger Processor (CTP) which issues a trigger across all the readouts of the ATLAS sub-systems (ReadOut Drivers, ROD). This is called *Level-1 (L1) Accept*

[6] The LHC clock is 40 MHz, but the accelerator is not completely filled with protons, so in some of the clock cycles of 25 ns no protons are crossed.

and is part of the Level 1 trigger stage. By L1 trigger selection, the ∼30 MHz potential events are reduced to ∼100 kHz.

After the Level-1 trigger is issued, the event data of each sub-detector is collected by a collection of ReadOut Systems (ROS) as *event fragments*. A second trigger filter based on event data and Region of Interests, the HLT, reducing the final data storage rate to ∼1 kHz at the Tier-0 computer.

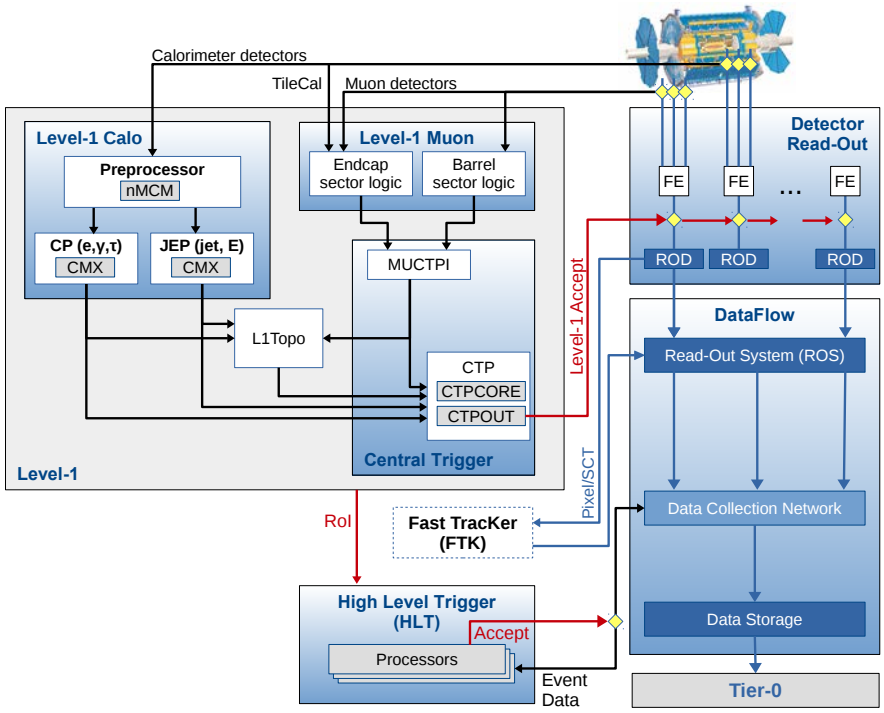

Figure 2.8.: The ATLAS TDAQ system, divided in two stage trigger levels: the level-1 trigger, which is issued to the detector read-out systems to trigger event data taking, and High Level Trigger (HLT), which is based on event data triggers the event storage into the Tier-0. Taken from [64].

2.3. The AFP Detector

The ATLAS Forward Proton (AFP) detector [29] is a forward detector of the ATLAS experiment. It has been designed to identify protons that emerge intact from the ATLAS interaction point at very low angles. Such processes are usually associated to diffractive scattering. A representation of the AFP detector and its working principle is shown in Fig. 2.9.

The following sections describe the final AFP detector as it is in 2017, however, as already mentioned, the detector was installed in two stages, the first one starting in 2016 with the one-arm AFP (also known as AFP0+2), which is the main topic of this thesis and is described in Sec. 2.3.7.

2.3.1. Detector Principle

In many LHC proton-proton collisions, one or two of the protons escape the ATLAS detector "intact" inside the LHC beam-pipe. Due to the LHC dipoles and quadrupole magnets along the beam line, the trajectory of the outgoing protons is modified according to their momentum and energy. Each proton that falls in the AFP acceptance is detected by the silicon tracking modules which are located in four "stations", two stations at each side of the interaction point, at 205 m and 217 m from the centre of the ATLAS detector. With these two measurements, and with the knowledge of the beam optics, it is possible to reconstruct the kinematic parameters of the proton, namely its transverse momentum and the energy it lost in the collision.

In environments with several collisions per event, the AFP tracker does not provide enough information to identify the interaction point of the proton. To determine the position of the interaction vertex in events with high pile-up, the AFP detector includes a Time-of-Flight (ToF) system in the two far stations. Using the ToF timing information, the position of the interaction point can be estimated.

The detector packages are enclosed inside Roman Pots, each Roman Pot being part of a station that is integrated into the LHC beam-pipe structure. The purpose of such structure is to move the detectors to a position within a few millimetres (∼3 mm) away from the LHC beam in order to observe intact protons with low scattering angle, a signature of diffraction (see Sec. 1.5).

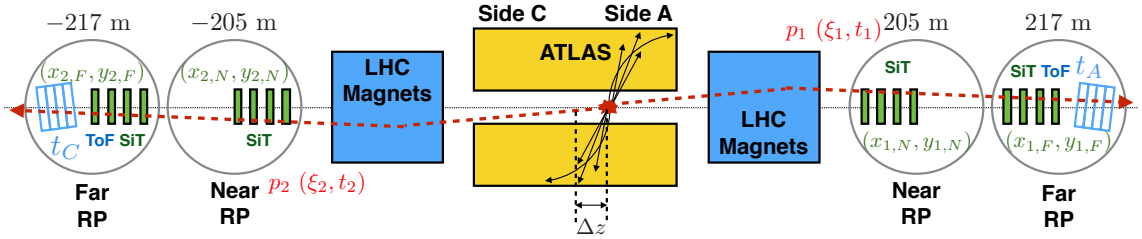

Figure 2.9.: Drawing showing the AFP detector principle for a central diffractive event, where two protons leave ATLAS and are detected in the AFP Roman Pots. The protons (p_1 and p_2) have their trajectory modified by the LHC magnets as a function of their kinematic parameters (ξ and t). Once they arrive at the Roman Pot stations (at ±210 m from the ATLAS IP), their position is measured by the tracker detectors, which allow to reconstruct their trajectory and thus their energy and momentum. Their Time-of-Flight is measured by the ToF system to identify the original vertex of the protons (Δz). Note that the drawing is not to scale.

2.3.2. Roman Pot station

Roman Pots are the main mechanical support for the AFP detector packages, and are responsible for the movement of the detectors towards the proton beam and away from it, to a safe "garage" position (∼4 cm from the beam). A total of four Roman Pot stations, copies of the TOTEM [65] detector horizontal Roman Pots, are used in the AFP detector.

Fig. 2.10 shows a drawing of the design of a Roman Pot station, which replaces a section of the LHC beam pipe. The detectors are installed on a flange, covered by an aluminium cylindrical pot, which separates the secondary vacuum inside the station from the primary vacuum inside the LHC beam pipe (see Fig. 2.10 right). The floor of the pot is thinned

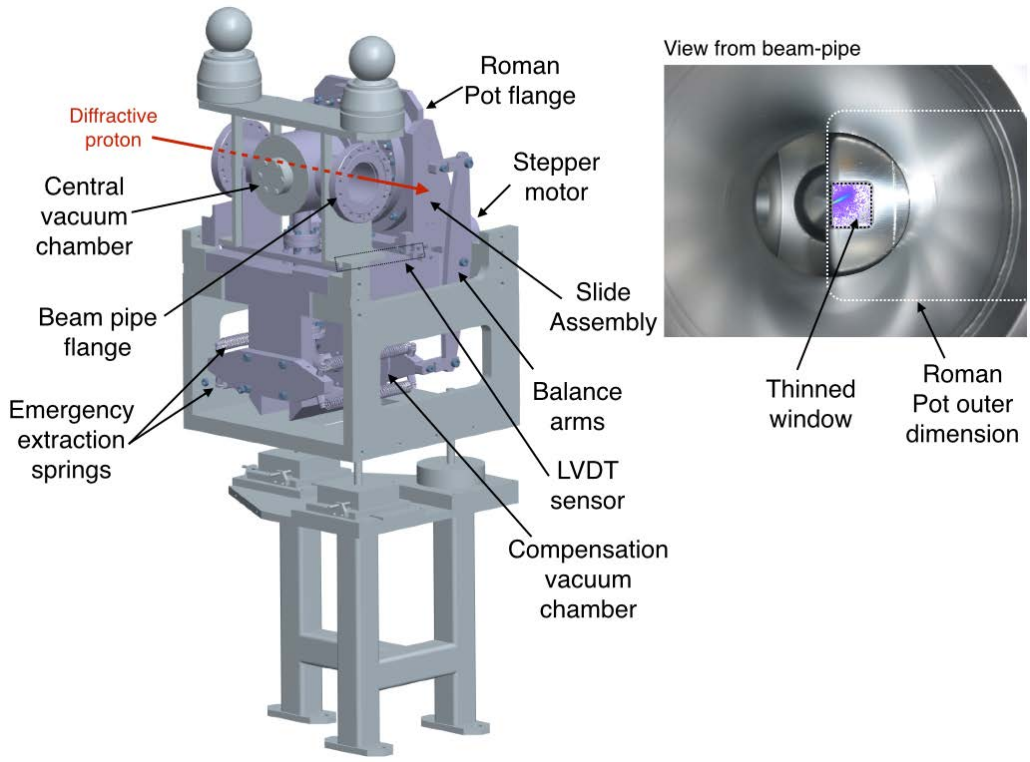

Figure 2.10.: A 3D model of the Roman Pot station assembly (left) and a picture of the Roman Pot as viewed from the beam-pipe inserted in beam position (right).

down from 2 mm elsewhere 300 μm on the side of the wall facing the beam and the area facing the sensors. The side wall of the pot coinciding with the tracker active area is thinned down to minimize the distance between the content of the pot and the beam and reducing the material budget at the detector's acceptance. A stepper motor moves the pot and its movement is monitored by the motor itself, an LVDT (Linear Variable Differential Transformer) sensor and a resolver. The vacuum system is compensated by a system of bellows placed below the Roman Pot and connected via balance arms to the pot. The balance arms also connect the pot to the emergency extraction springs, which move the pot outside the beam pipe (i.e. to garage position) in case the motor fails.

2.3.3. Silicon Tracker

Each Roman Pot station houses a set of 4 silicon sensor planes. The AFP Silicon Tracker (SiT) has a total of 8 planes per side, see Fig. 2.11. As the trajectory of the diffractive proton depends on its momentum and energy due to the LHC dipole and quadrupole magnets, it is possible to determine its kinematics by reconstructing the proton trajectory from one station to the other. In particular, the (x, y) coordinates are obtained for each station using the silicon tracker from which the proton relative energy loss ($\xi = 1 - E_p/E_{beam}$) and momentum transfer (t) are reconstructed. The reconstruction depends on the optics and precise sensor positioning knowledge. The silicon tracker planes are able to provide trigger signals, but these signals span over several bunch crossings, limiting the readout rate. Thus the triggers from SiT are only useful for low luminosity conditions.

The tracker devices are based on silicon hybrid detectors: the sensitive part (sensor) is coupled to a read-out chip (front-end), as will be described in Sec. 3.3. Ch. 3 describes the detectors of choice for the AFP detector, 3D pixel sensors coupled to the FE-I4 front-end

chip, and presents the result of their characterization in test-beam studies.

The read-out chip in the SiT planes are connected to a high density cable (flex) which is then connected to a feed-through vacuum tight cable to the outside of the Roman Pot flange. This cable carries the data input/output, the commands, the global LHC clock and the trigger signals to the data acquisition system and trigger logic electronics. Each sensor is mounted on an aluminium-carbon fibre (Al-Cf) composite carrier card which serves as a mechanical support and thermal conductor (the Al-Cf composite was chosen over only aluminium because of its better thermal conductivity). The carrier card is mounted on an aluminium heat exchanger with a 14° angle tilt, which takes pressured cold air from a supply outside the Roman Pot and distributes it inside where the heat from the carrier cards is absorbed by the air flow and removed from the Roman Pot. The heat exchanger and Roman Pot are thermally insulated from each other. The silicon tracker structure, including the heat exchanger, are fixed to the Roman Pot flange, which are separated by a stack of thin shims (100 and 20 μm thick) in order to adjust the height of the tracker before installation.

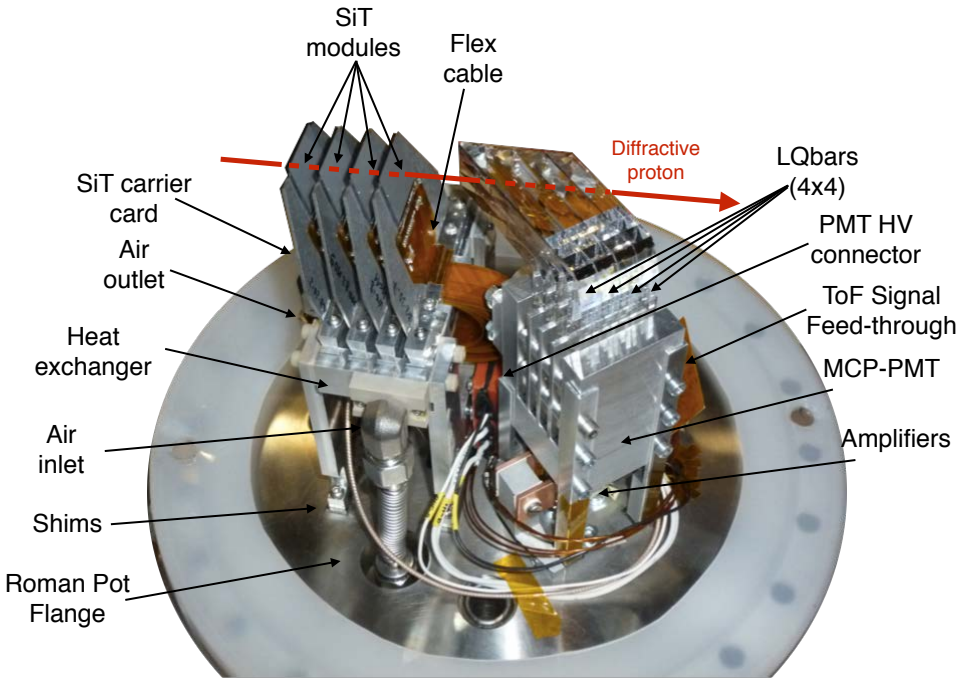

Figure 2.11.: Picture of the detector packages (left:Silicon Tracker, right:Time-of-Flight) mounted on a flange before their installation into an AFP Roman Pot at 217 m from the ATLAS interaction point (Far station).

2.3.4. Time-of-Flight Detector

The goal of the ToF detector is to determine the primary vertex of the two protons by measuring the time of arrival:

$$\Delta z = \frac{c}{2}(t_A - t_C) \tag{2.6}$$

where $t_{A/C}$ is the measured time by the ToF detectors in the A/C side Roman Pots (see Fig. 2.9), which can be then compared with the vertex measurement in the Inner Detector.

Therefore, the resolution of this measurement is

$$\delta z = \frac{c}{\sqrt{2}}\delta t, \tag{2.7}$$

where δt is the time resolution of the ToF detector (here assuming that time resolution is the same in both sides). AFP was designed to operate with an average pile-up of $\langle\mu\rangle \geq 50$, the pile-up foreseen for LHC Run 2 (2015-2018). In order to distinguish pile-up events in such a collision-dense condition, a time resolution of about 10 ps is needed, which translates into a vertex resolution of 2.1 mm [29].

The Time-of-Flight detector design consists of 16 L-shaped quartz bars (LQbars) installed in each of the far Roman Pot stations on either side, grouped in 4 trains of 4 bars each (see Fig. 2.12). The radiator width varies from train to train in order to have better granularity in the low diffraction mass region (i.e. closer to the proton beam): 2 mm, 4 mm, 5 mm and 5.5 mm. The LQbars are at the Cherenkov angle (48°) with respect to the proton direction, so that the radiated photons are emitted directly along the bar direction, which is transported by total reflection towards the end of the bars, where it is detected by a Micro-Channel Plate Photo-Multiplier (MCP-PMT) [29]. The signals from the MCP-PMT channels are amplified and discriminated with a Constant-Fraction Discriminator (CFD), which allows signal discrimination with no time-walk contribution (i.e. signals arriving late due to their low amplitude). The output signals from the CFD are

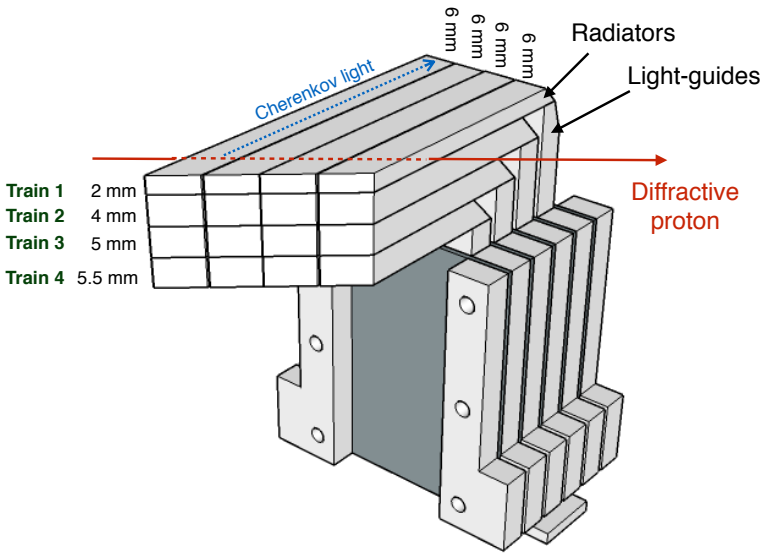

Figure 2.12.: 3D model of the Time-of-Flight system. The ToF detector is divided in 4 Cherenkov radiator trains with 4 L-shaped Quartz bars (LQbars) each. The radiators are installed at the Cherenkov angle with respect to the incoming diffractive protons.

distributed into two High-Precision Time-to-Digital Converters (HPTDC) [66], measuring the time of arrival synchronized with the global LHC clock in ∼25 ps bins. Their FPGAs are programmed so that the digital output format of the HPTDC coincides with the one of the FE-I4 chip of the silicon tracker modules. The output data is then sent to the Local Trigger Board, then to the opto-board and finally to the data acquisition system by optical cables (see Sec. 2.3.5). A reference clock is used to synchronize the local ToF detector clocks of each side.

As opposed to the SiT trigger signals from the FE-I4 chip, the ToF system is capable to generate short signals ($\mathcal{O}(1$ ns) [67]) that can also be used for triggering, which would

reduce the trigger dead-time with respect to SiT. This feature has been integrated in 2017 as trigger source for high pile-up conditions.

2.3.5. AFP Trigger and Data Acquisition (TDAQ)

Detector read-out and triggering is performed by the Trigger and Data Acquisition (TDAQ) system. A schematic showing the connectivity of the AFP TDAQ components is shown in Fig. 2.13.

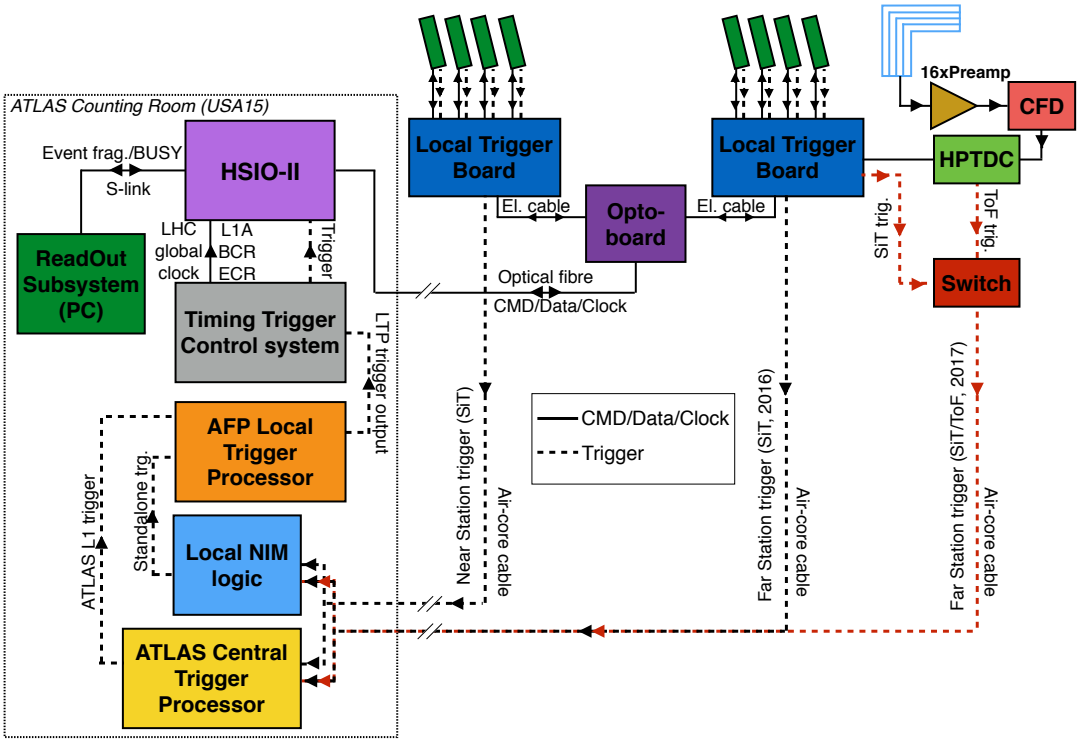

Figure 2.13.: Drawing showing the connectivity of the AFP TDAQ system. The trigger and readout system in 2016 consisted in SiT detectors only (no ToF was installed) and the trigger signal produced in the far station by the SiT followed a similar path as the near station. The red dashed line indicates the new trigger path for the Far stations, implemented in 2017, in which the trigger signal from the SiT is sent to the HPTDC which allows to select between SiT and ToF trigger signals.

Local Trigger Board

The Local Trigger Board (LTB) [68] was designed to serve as an interface between the detector systems and the opto-board, pass-through high and low voltages to the silicon trackers and to generate SiT-based trigger signals for each station (AFP has a total of 4 LTB, one per station). It is installed in the back (external side) of the Roman Pot flange and is connected to the SiT inside the pot via flexible feed-through cables. For the tracker-based trigger signal formation, the LTB includes a HitBus chip [69]. Trigger signals from a maximum of three silicon tracker planes are sent to the HitBus chip, which outputs a signal from any of the possible trigger logics. These logics include: single channel signal pass-through, logical OR/AND of the three inputs and a majority vote logic (i.e. two-out-of-three trigger signal). A jumper bank makes it possible to select which three of

the four planes per station participate in the trigger logic. The HitBus chip output is a CMOS signal, which is too low to reach the end of the ∼300 m air-core cable that connects the LTB to the ATLAS L1 trigger system. Thus before sending the signal to the ATLAS counting room it is converted into NIM standard via a NIM driver included in the LTB.

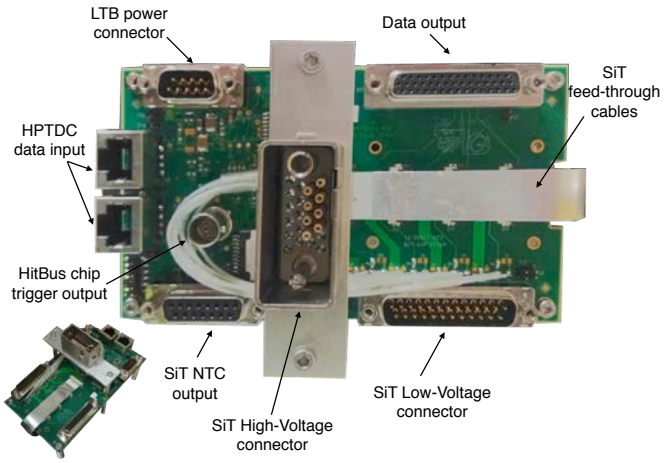

Figure 2.14.: Picture of a Local Trigger Board (LTB). The HitBus chip that generates the output trigger signal and the NIM driver (see text) are not visible in the figure.

Central and Local Trigger Processors

Once in the counting room, the signal is split: a copy of the trigger signal arrives to the ATLAS Central Trigger Processor (CTP) [70], responsible of issuing the Level-1 trigger to the ATLAS sub-systems, while the second copy is sent to a local NIM logic, which produces trigger signals based on the LTB outputs allowing AFP to trigger itself during standalone running (i.e. ATLAS not producing triggers).

The output of both paths are connected to the AFP Local Trigger Processor (LTP), which selects the trigger source, either from the ATLAS CTP if AFP is participating in combined data taking, or from the local NIM logic otherwise, usually for commissioning runs. The selected trigger signal is sent to the Timing, Trigger and Control (TTC) system [70, 71] (see following sections).

Opto-board

Data and clock transmission over long distances (∼300 m from the Roman Pot AFP stations up to the read-out system in the ATLAS counting room) needs to be done via optical fibres. Therefore, electrical signals from the detector packages (SiT and ToF) need to be converted to light for optical fibre communication. This is done by the opto-board [72] (see Fig. 2.15), which was initially designed for the ATLAS IBL. A total of two opto-boards, one per side, installed in a distribution panel placed between two stations (i.e. ∼6 m from either station) are connected to the LTB in each station by an electrical cable bundle. The optical I/O side of the opto-board is connected to the HSIO (see next section) in the counting room by optical fibre.

Figure 2.15.: Picture of an IBL/AFP opto-board, connected to the electrical signals from the detectors (left) to convert them to optical signals and send them to the DAQ system via optical fibres (right). Taken from [73]

Data Acquisition System (HSIO-II)

The main component on the data acquisition system in AFP [74, 75] is the HSIO-II (High Speed Input Output) [75] board, shown in Fig. 2.16. Developed at SLAC[7], the HSIO-II is one of the main read-out systems for the FE-I4 detectors (see Sec. 3.4). Two HSIO-II (one per side) in the counting room near the ATLAS experiment receive data from, and send commands and clock signals to the SiT and ToF detectors via optical fibres. Moreover, the HSIO is used to calibrate the silicon tracker modules.

During data taking, the HSIO-II receives the trigger commands (either from the standalone local NIM logic or from the ATLAS CTP) and the LHC clock from the TTC system, which are processed by the board's firmware. The board also processes the Bunch Counter Reset (BCR) and the Event Counter Reset (ECR) commands. In addition, a TTC board is able to generate random triggers, useful for read-out functionality tests.

Data from the HSIO-II is sent to the ATLAS ReadOut System (ROS), which is the interface between the detector specific DAQ and the central ATLAS DAQ. The ROS gets event fragments (event information from a specific ATLAS DAQ subsystem) from the HSIO-II, into a buffer, in such a way that events can be buffered in case the ROS is overloaded. If too many events enter the buffer, the ROS can generate a BUSY signal.

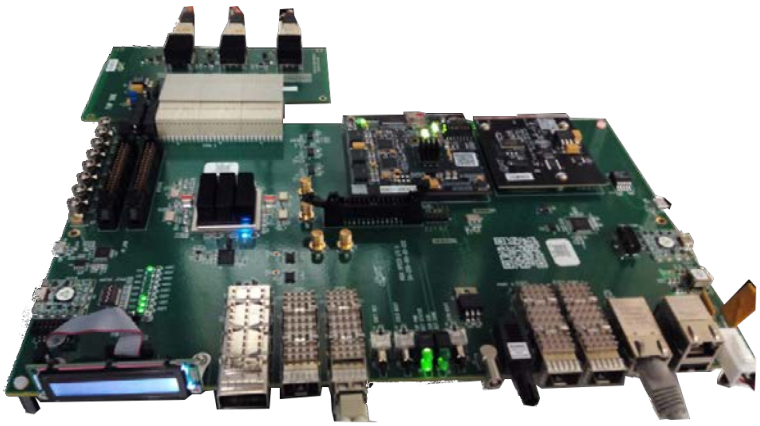

Figure 2.16.: Picture of an HSIO-II board equipped with an optical fibre adapter card.

[7]Stanford Linear Accelerator Collider, California, U.S.A.

2.3.6. Detector Control System (DCS)

The Detector Control System (DCS) is in charge of supplying the correct operational voltages, currents, and pressures to the components of the detectors. The DCS also controls the Roman Pot station movement, as well as monitors the behaviour of all the systems (e.g. power consumption and temperature). Moreover, in order to ensure the detector's integrity, limits and safety procedures are set for the diverse operational parameters of the detectors (e.g. compliance limits for leakage currents).

The hardware controlled by DCS include: Roman Pot movement system and secondary vacuum, cooling of the detectors, distribution of low and high voltage, temperature monitoring of the different systems, monitoring of the temperature and voltages of the DAQ modules and hardware interlock systems switching off the required voltages in case of temperature exceeding limits in the detectors or infrastructure.

Part of the DCS system is installed in the ATLAS counting room, where the control servers for the cooling, movement and power supplies sit, while the distribution panel is placed between two stations (see Fig. 2.17) in the LHC tunnel.

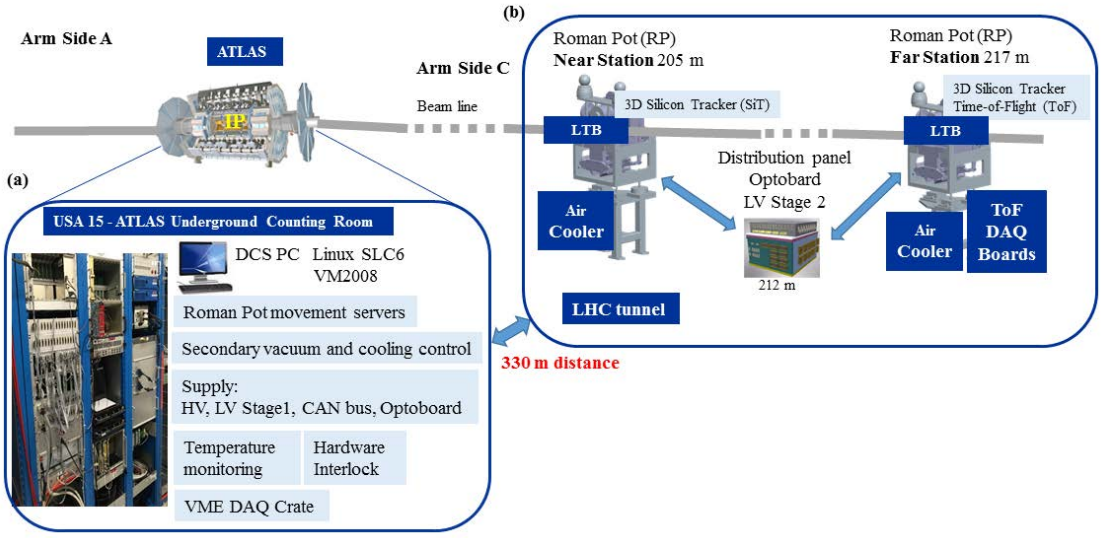

Figure 2.17.: Placement of the AFP detector and the infrastructure in the ATLAS Underground Counting Room USA15 (a) and in the LHC tunnel (b). Taken from [76].

2.3.7. One-Arm AFP (AFP0+2) Detector

The installation of the AFP detector started in 2016, with the installation of two Roman Pot stations in one side of ATLAS (the C-side). This detector configuration is known as the one-arm AFP detector or AFP0+2. The decision to install a single-sided proton detector as opposed to an AFP1+1 solution was taken since two Roman Pot stations in one side still allow for proton kinematic reconstruction for single diffraction analysis at very low pile-up (information from the two stations are needed for the reconstruction). Only silicon trackers were installed in the Roman Pots on the one-arm AFP detector, since pile-up removal with the ToF system is only possible with time measurements from both AFP sides.

The TDAQ system for the one-arm AFP is equivalent to the final detector, although only one HSIO-II board, one opto-board and two Local Trigger Boards (one per station) are needed. Trigger signal generation was performed from SiT signal output in both stations.

This was changed in the 2017 final stage installation.

3. Technology Characterization: Silicon 3D Pixel Detectors for the AFP Detector

Silicon 3D pixel sensors are a state-of-the-art technology that was only recently introduced to high energy physics collider experiments with the ATLAS IBL detector (see Sec. 2.2.1). Its pixel topology, in which the electrodes penetrate the silicon bulk as columns perpendicular to the surface, makes the technology more radiation hard than the traditional planar technology counterpart. On the other hand, 3D sensors are more difficult to fabricate than planar sensors. However, in an environment as demanding as AFP in terms of radiation and given the small number of required sensors, 3D pixel sensors become a clear candidate as a technology for the tracker package of the detector.

Nonetheless, the suitability of the technology for its use in AFP had to be determined. Tests were performed in so called test-beam facilities, before and after irradiation, to reproduce the environment of the real experiment.

In this chapter, a general introduction to silicon detectors will be presented. The 3D technology will be described in detail. The characterization and qualification of the pixel module prototypes in test-beams will be presented. These results enabled the AFP detector to be approved for installation.

3.1. Introduction

The use of silicon detectors for tracking is nowadays standard in high energy physics experiments due to their radiation hardness, compactness, cost per channel and rate capability. Moreover, R&D on silicon appliciations in high radiation environments is still evolving to push the limits of the material to meet more demanding requirements. In this section the working principle and properties of silicon detectors will be presented. In particular, the 3D technology will be introduced in the framework of high energy physics experiments.

3.1.1. Semiconductor physics

The last energy level with the lowest energy in which there can be electrons in an atom is called the valence energy level and is responsible of the covalent bonds between atoms. Higher energy levels are inside the conduction energy band, in which the electrons can move freely across the material lattice. The difference between these two energy levels constitutes the energy band gap, a region in which no electrons are allowed. The width of the energy band gap is material dependent and can be used to clasify materials as conductors, semiconductors and insulators.

In conductor materials the valence and the conduction band overlap, while in insulators the energy band gap is higher than $\sim$3 eV; materials with energy gaps in the range of 0 eV$\lesssim E_g \lesssim$3 eV are considered semiconductors, in which a non-negligible amount of electrons can reach the conduction band at room temperature.

Charge Carrier Concentration

In intrinsic semiconductors like silicon, when an electron in the valence band is excited to the conduction band, it leaves a hole which acts as a particle with positive charge moving freely in the valence band, as the electrons will move to cover the empty space left by the excited electron. Therefore holes, together with electrons, contribute to the total charge carrier concentration.

The electron concentration moving freely in the conduction band can be calculated as

$$n = \int_{E_C}^{\infty} g(E) f(E) \mathrm{d}E, \tag{3.1}$$

with $f(E)$ being the Fermi-Dirac distribution, $g(E)$ the density of states, and the integral is over all energies from the minimum conduction band energy level (E_C) to infinity. A similar expression is valid for the concentration of free holes in the valence energy band p, integrating from 0 to the maximum valence energy level (E_V). The density of states can be obtained by assuming the electrons are in a box potential (i.e. infinity potential in the boundaries and zero potential otherwise), which leads to

$$g(E) = 4\pi \left(\frac{m_n}{h^2}\right)^{2/3} \sqrt{E - E_C}, \tag{3.2}$$

where m_n is the effective mass of the electron ($m_n = 1.08 m_e$ with m_e being the rest electron mass). The Fermi-Dirac distribution reads

$$f(E) = \frac{1}{1 + e^{(E-E_F)/(k_B T)}}, \tag{3.3}$$

where k_B is the Boltzmann constant, T the temperature and E_F is the Fermi energy, usually at the center of the band gap, i.e.

$$E_F \sim \frac{E_C - E_V}{2}. \tag{3.4}$$

Integrating Eq. 3.1, the free electron and hole concentrations are obtained:

$$n = 2 \left(\frac{2\pi m_n k_B T}{h^2}\right)^{3/2} e^{-(E_C - E_F)/(k_B T)} = N_C e^{-(E_C - E_F)/(k_B T)} \tag{3.5}$$

$$p = 2 \left(\frac{2\pi m_p k_B T}{h^2}\right)^{3/2} e^{-(E_F - E_V)/(k_B T)} = N_V e^{-(E_F - E_V)/(k_B T)}. \tag{3.6}$$

N_C and N_V are called the effective density of states. The product of the expressions for electrons and holes

$$np = n_i^2 = N_C N_V e^{-E_g/k_B T} \tag{3.7}$$

leads to the intrinsic charge carrier concentration n_i, assuming $n = p = n_i$ for intrinsic semiconductors. E_g is the energy band gap, i.e. the difference between the lowest level of the conduction band and the highest energy level of the valence band ($E_C - E_V$). In silicon, the energy band gap is E_g =1.12 eV, therefore the intrinsic charge carrier concentration at 300 K is $n_i = 1.45 \times 10^{10}$ cm^{-3}.

PN-junction

In an intrinsic semiconductor like silicon the number of free charge carriers is too large to allow particle detection. For this reason pn-junctions are used. To this end, impurities are introduced which increase either the concentration of electrons (n-type) or holes (p-type). The process of introducing impurities in a semiconductor is known as doping. In the case of silicon, the elements used as impurities for doping are the following:

- *N-type*: From *group IV* in the periodic table as phosphorus, which has one electron extra in the valence level and therefore provides an extra electron in the conduction band. In such cases the impurities are called *donors*.
- *P-type*: From *group III* in the periodic table such as boron, with one electron less in the valence layer and thus traps electrons from the valence band introducing an extra hole. These impurities are then named *acceptors*.

Acceptors and donors introduce a shallow energy level above the valence band and below the conduction band, respectively. These impurities allow the creation of *pn-junctions* (see Fig. 3.1).

A pn-junction consist of an interface between a p-doped and an n-doped semiconductor region. The electrons from the n-type region and the holes from the p-type region diffuse towards the opposite region where they recombine with the majority carriers of the respective regions. This creates a volume close to the junction with a negligible amount of free charge carriers, namely a *depletion zone*. In addition, as the depletion zone is electrically charged by the donors and acceptors, an electric field near the junction that counteracts the diffusion is present, which is characterized by a *built-in voltage* V_{bi}.

The distance along which the depletion zone extends in a pn-junction is, in a one-dimensional approximation

$$d = \sqrt{\frac{2\epsilon}{e}\frac{N_A + N_D}{N_A N_D} V_{bi}} \underset{N_{A/D} \gg N_{D/A}}{\approx} \sqrt{\frac{2\epsilon}{eN_{D/A}} V_{bi}}, \tag{3.8}$$

where it has been assumed that in the pn-junction the concentration of either acceptor or donor dominates over the other one, which is normally the case. In order to allow particle detection, the depleted region of the pn-junction has to be increased.

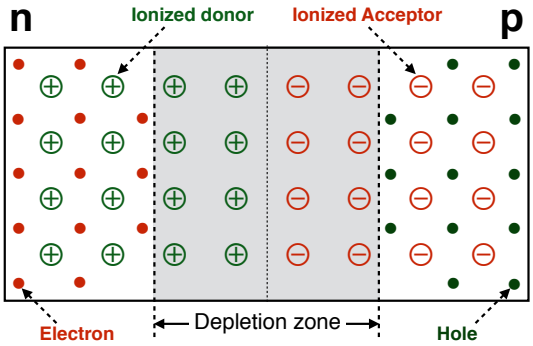

Figure 3.1.: Sketch of a pn-junction: the n-doped (left) and the p-doped (right) region of the semiconductor are in contact, which causes the recombination of the free charge carriers creating a volume with negligible amount of charge carriers, the depletion zone.

Reverse Bias

The depletion distance can be further increased by applying an external reverse *bias voltage* V_{bias}, i.e. apply a positive potential to the n-type region with respect to the p-type region. Then, Eq. 3.8 extends to

$$d \approx \sqrt{\frac{2\epsilon}{eN_{D/A}}(V_{bi} + V_{bias})}. \tag{3.9}$$

The voltage at which the full volume is depleted is named *depletion voltage* V_{depl}, which is the minimum desired operational voltage in silicon sensors.

Free charge carriers generated inside the depleted volume of a pn-junction contribute to the so-called *leakage current*. The leakage current is proportional to the depleted volume. Therefore, in the ideal case, the current increases with $\sqrt{V_{bias}}$ (see Eq. 3.9) until the the depletion voltage is reached. Afterwards, the leakage current stays in a plateau until it reaches the electrical *breakdown*, where the charge carriers reach enough energy to create further electron-hole pairs, causing the current to rapidly increase.

Leakage current is a critical factor during sensor operation which can complicate the measurement of signal due to the introduction of noise. The temperature dependence of the leakage current follows the relation

$$I_{leak} \propto T^2 \exp\left(\frac{-E_g}{2k_B T}\right). \tag{3.10}$$

Hence, at 0°C the leakage current is ∼6 times smaller than at room temperature (25°C), which makes important to operate silicon detectors at low temperatures when their current is large, e.g. due to radiation damage (see Sec. 3.1.3). Moreover, this expression is useful in order to scale different leakage current measurements to the same temperature. However, it assumes that all the current comes from bulk contribution and surface currents are neglected, an approximation that in some cases is not valid.

3.1.2. Silicon Detectors

Silicon detectors consist of a reverse biased pn-junction, where particles crossing the silicon bulk create electron-hole pairs by ionization. The charge carriers are collected by heavily doped p- and n-type regions (usually noted as p^+ and n^+, respectively), which play the role of electrodes.

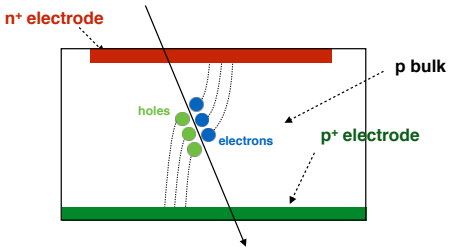

Figure 3.2.: Sketch of a n-on-p pad diode.

Detectors consisting in a single pn-junction (i.e. with no segmentation) are called *pad diodes* (see Fig. 3.2). Pad diode detectors are usually used for prototyping, as their construction is simpler, or for applications where high granularity is not a requirement. When the electrode is divided in parallel strips along one direction the sensor is called a *strip* detector. The electrodes then are connected to the readout electronics at the end of the sensor. Strip sensors can only measure tracks in one dimension, so two strip sensors would be needed to measure in two dimensions. However this can lead to ambiguity, where more than one possible track points in space are possible for a single set of measurements when detecting more than one particle. *Pixel* detectors on the other hand solve the ambiguity problem of the strip detector: the electrodes in the sensor are segmented in a two dimensional pattern, so every pixel provides two dimensional coordinates of the hit position (as long as the pixel size in both directions is small enough), with a granularity of typically $\mathcal{O}(100\ \mu\text{m})$. This allows pixel detectors to be able to cope with high particle densities. In

order to connect all the pixels independently to the read-out electronics, the electrodes are connected to a read-out chip via *bump-bonding*, which consists in coupling each sensitive pixel to a read-out channel through solder bumps.

In the following sections, the generation and collection of charge carriers is described, as well as some common concepts in silicon detectors.

Charge Generation

In order for high energy quanta ($E \gg E_g$) to excite an electron from the valence band to the conduction band in silicon, 3.6 eV are needed, which is three times higher than the energy band gap (E_g =1.12 eV). The difference is due to the generation of phonons which are dissipated as thermal energy. The number of electron-hole pairs generated by a traversing particle is, thus, the fraction between the total energy deposited and 3.6 eV.

Interaction of Charged Particles with Silicon

Charged particles impinging into a material lose energy by interacting with the electrons of the atoms forming the material continuously losing energy along their path through matter. For a range in momentum of $0.1 \lesssim \beta\gamma \lesssim 1000$ the mean energy loss per unit length (stopping power) can be described by the Bethe-Bloch equation [1]:

$$-\left\langle \frac{\mathrm{d}E}{\mathrm{d}x} \right\rangle = Kz^2 \frac{Z}{A}\frac{1}{\beta^2}\left(\frac{1}{2}\ln\frac{2m_e c^2\beta^2\gamma^2 T_{max}}{I^2} - \beta^2 - \frac{\delta(\beta\gamma)}{2}\right) \tag{3.11}$$

where $K = 4\pi N_A r_e^2 m_e c^2$, A is the atomic mass of the absorber, Z is its atomic number, I is the mean excitation energy of the medium, T_{max} is the maximum single-collision energy transfer, $\beta = v/c$, $\gamma = 1/\sqrt{1-\beta^2}$ is the Lorentz factor and $\delta(\beta\gamma)$ is a correction factor for high energy ionization [77]. At higher momenta radiative effects become important, which are not covered by the Bethe-Bloch equation. Fig. 3.3 shows the Bethe-Bloch formula represented for muons, pions and protons in silicon. A minimum in the distribution can be observed, which hardly increases for several orders of magnitudes of momentum: particles at this minima are named minimum ionizing particles (m.i.p.). A m.i.p. in silicon has an average stopping power of $\left\langle \frac{\mathrm{d}E}{\mathrm{d}x} \right\rangle = 1.66$ MeVcm^2/g (or 107 e/h pairs per μm). Due to the slow increase in energy loss ratio, most relativistic particles detected in ATLAS have a stopping power similar to a m.i.p., and thus, in practical cases, can be considered as such.

Impinging electrons (and positrons) can be easily deflected by the electric fields of the atoms which makes *bremsstrahlung* the main energy loss mechanism already at low energies (e.g. at ∼100 MeV in silicon). Electrons of ∼2 MeV energy from β radioactive sources (^{90}Sr, see 3.5.4) are often used for laboratory energy collection determination, since at such energies the electrons are m.i.p.s in silicon (1.6 MeVcm^2/g).

The energy loss probability distribution follows, in good approximation, a Landau distribution [79]. This distribution features long tails which experimentally affect the calculation of the mean energy loss. Therefore it is common to quote the most probable value (MPV). The MPV of the Landau distribution from a particle can be obtained by the following expression [1]:

$$\Delta_p = \xi\left(\ln\frac{2m_e c^2\beta^2\gamma^2}{I} + \ln\frac{\xi}{I} + 0.200 - \beta^2 - \delta(\beta\gamma)\right), \tag{3.12}$$

with $\xi = (K/2)Z/A(x/\beta^2)$ MeV for a detector with a thickness x in units of [g cm^{-2}]. Thus, the most probable energy loss over thickness Δ_p/x varies as a function of the thickness of the material as $a\ln x + b$. The energy deposition distribution for 500 MeV pions at different silicon thickness can be seen in Fig. 3.4. For instance, in 230 μm thick silicon, the most probable energy loss for a m.i.p. is $\Delta_p/x = 1.06$ MeV cm^2/g (or 69 e/h pairs per μm).

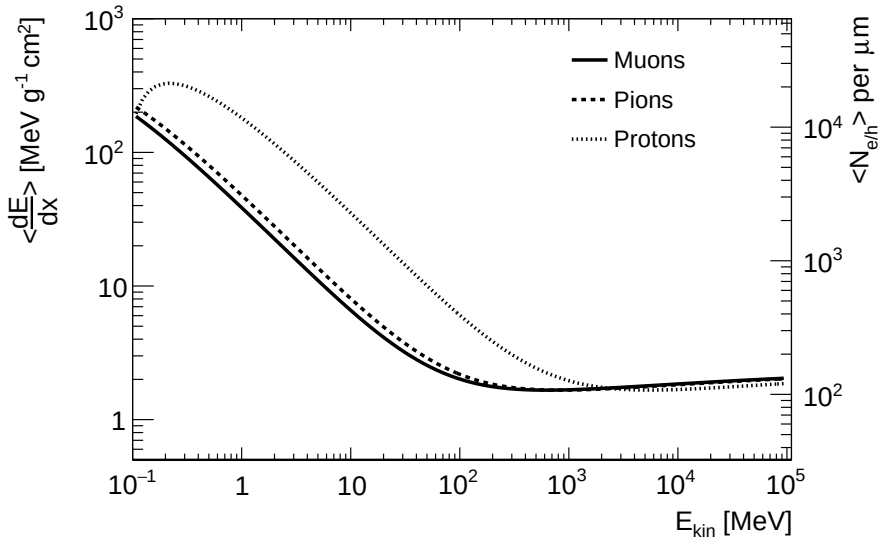

Figure 3.3.: Average stopping power of muons, protons and pions in silicon and average number of electron/hole pairs per micrometre as a function of kinetic energy. Adapted from [78].

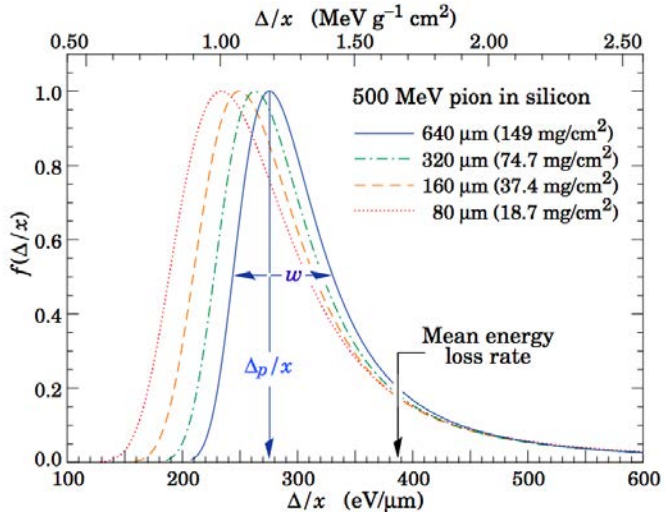

Figure 3.4.: Energy deposition distribution for 500 MeV pions at different silicon thickness normalized to the most probable value of each distribution. Taken from [1].

Interaction of Electromagnetic Radiation with Silicon

The absorption probability of photons interacting with matter increases exponentially as a function of depth, and the cross section depends on the photon energy (which determine the absorption mechanism) and the material. Photons can interact with matter via three processes:

- *photoelectric effect*: in which a photon is absorbed by an atom completely and frees an electron with a kinetic energy equal to the photon initial energy minus an ionization energy. As the cross section of the photoelectric effect is strongly dependent on Z ($\sigma_{pe} \propto Z^n$, with n ranging from 4 to 5 [80]), high-Z materials are preferred for photon absorption. It is the dominating process at low photon energies in silicon. Below

~100 keV, the absorption probability by photoelectric effect falls several orders of magnitude.

- *Compton scattering*: at higher energies the photons are scattered with the electrons in the material, resulting in a lower energy photon and a recoil the electron.

- *pair production*: photons with an energy higher than twice the electron mass (i.e. 1.022 MeV) can create e^+/e^- pairs which, in turn, can emit further photons by bremsstrahlung.

For instance, in some laboratory measurements a ^{241}Am radioactive source is used to test charge collection in silicon devices (see 3.5.4). One of the products of its decay are photons of 59.5 keV (~16500 e/h pairs), which in silicon can be either absorbed via photoelectric effect or Compton scattering. On the other hand high energy photons from *pp* collisions, like the ones measured for the observation of the Higgs boson by an excess of events in the di-photon mass distribution at 125 GeV of the order of several GeV, have a very low probability of being detected in a 230 μm thick silicon (see Fig. 3.5).

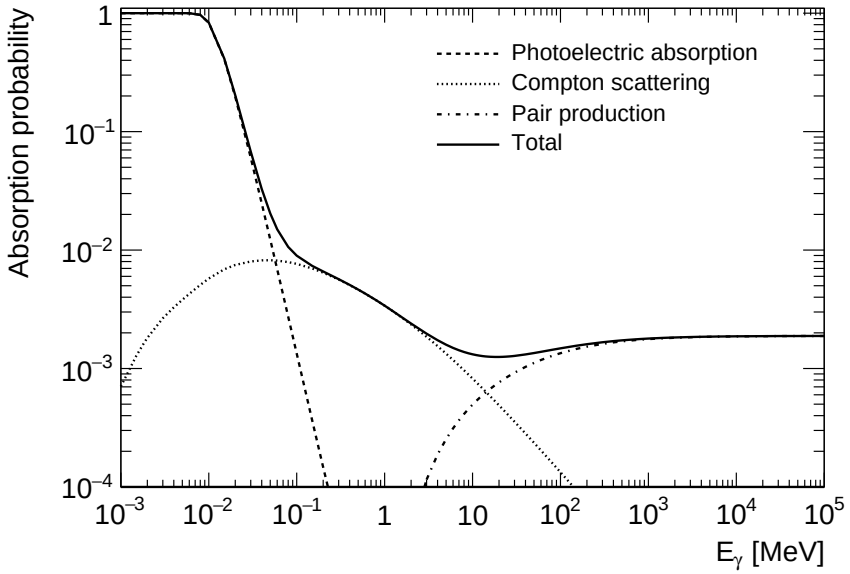

Figure 3.5.: Photon absorption probability in 230 μm thick silicon as a function of the photon energy and the contribution of each aborption mechanism. Adapted from [78], data from [81].

Charge Collection

The particles impinging the silicon, as stated in previous sections, generate a number of free charge carriers proportional to the particle's deposited energy. These charges generated in the silicon bulk are under the influence of the depletion electric field and drift towards the electrodes with a drift velocity v_{drift}, which is given by

$$v_{drift,e/h}(E) = \mu_{e/h} E, \tag{3.13}$$

where subscript e/h indicates the type of charge, i.e. electrons or holes, E is the absolute value of the electric field and μ is the mobility of the charge in the medium.

The charge drift causes an induced current (i) in a read-out electrode, given by the Shockley-Ramo theorem [82, 83]:

$$i(t) = q\,\mathbf{v_{drift}} \cdot \mathbf{E_w}, \tag{3.14}$$

where q is the moving charge, $\mathbf{v_{drift}}$ is its drift velocity and $\mathbf{E_w}$ is the *weighting field* of the read-out electrode, which is obtained by applying a unit potential (ϕ_w) in the read-out electrode and a zero potential to all the others and by solving the Laplace equation $\nabla^2\phi_w = 0$.

The integral over time of the induced current results in the collected charge, $Q = \int_{t_1}^{t_2} i(t)\mathrm{d}t = e\Delta\phi_w$. When all charge carriers reach the electrodes, the collected charge is equal to the number of generated electron/hole pairs (full charge collection). after irradiation (see Sec. 3.1.3) part of the charge carriers might be trapped during the collection time.

3.1.3. Radiation Damage in Silicon Detectors

In high energy physics experiments, it is critical to understand the effects of radiation in the detectors, as it can reduce their performance until they are not longer capable to detect particles. While silicon detectors can sustain high levels of radiation damage, it still affects the sensor behaviour. Radiation damage effects are classified in bulk and surface effects.

Surface effects of radiation damage are focused in the interface between the silicon and the dielectric that protects the bulk (SiO_2) (see Sec. 3.1.4) or in the oxide itself. Bulk effects, on the other hand, are originated from defects in the silicon bulk. Since the latter is the main contribution of sensor performance degradiation, the following discussion will focus on the radiation damage by bulk defects.

Radiation Damage Mechanism

The origin of bulk damage is the interaction of particles with the atoms forming the silicon crystal by displacing them from their lattice position. This causes imperfections that can cause a change in the energy levels. As a consequence, given enough radiation damage, the electrical behaviour of the bulk can deteriorate.

The average minimum energy needed to displace a silicon atom is ∼25 eV. The displacement of an atom from its position in the crystal lattice results in a vacancy and a knock on Si atom, the *primary knock on atom* (PKA), which can either move to an interstitial position in the crystal (causing point-like defects) or, if the PKA energy is high enough, it can cause further damage to the lattice by knocking on further Si atoms. At the end of their path, knock on atoms with enough recoil energy lose most of their energy in localised positions (cluster defects). The radiation damage introduced by the impinging particle depends on its energy, mass and charge. An electron would need more than 255 keV, energy at which the maximum recoil energy can reach the displacement energy threshold of 25 keV while a proton or a neutron, due to their higher mass (and hence higher recoil energy in the silicon atom) would need just ∼190 eV to produce a PKA. Fig. 3.6 shows a summary of the bulk radiation damage effects in the bulk. Its main effects (discussed below) are: higher leakage current, a change in the effective doping concentration that changes the voltages required to deplete the bulk, and a reduction of the charge collection efficiency due to trapping.

The NIEL Scaling Hypothesis

In order to parametrize and compare radiation damage effects caused by different types of particles and energies, the bulk radiation damage is expressed in terms of Non-Ionizing

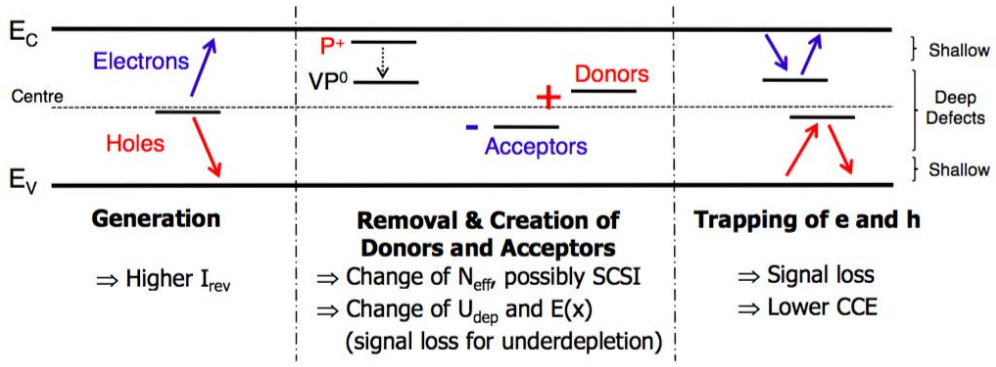

Figure 3.6.: Summary of macroscopic effects of defect energy levels in the forbidden band gap: the generation of deep defects (left) can cause higher leakage currents (here I_{rev}), a change of the effective trapping concentration (middle) can cause a change in the depletion voltage (here U_{dep}) and electric field in some cases leading to a Space Charge Sign Inversion (SCSI), and deep defects can cause the trapping of the charge carriers (right) causing lower Charge Collection Efficiency (CCE). Taken from [84].

Energy Loss (NIEL) damage. The particle fluence Φ_{part} (number of particles per unit area) is typically scaled to the equivalent fluence of reference particles (1 MeV neutrons) with the same NIEL. The correction factor κ (named hardness factor) is obtained by weighting the physical fluence with an energy dependent damage cross section $D(E)$ (see Fig. 3.7) and normalized to the integrated fluence and the damage cross section of the reference particles (i.e. $D(E_n = 1\text{ MeV}) = 95\text{ MeV mb}$):

$$\kappa = \frac{\int_{E_{min}}^{E_{max}} D(E_{part})\Phi_{part}(E)\mathrm{d}E}{D(E_n = 1\text{ MeV}) \int_{E_{min}}^{E_{max}} \Phi_{part}(E)\mathrm{d}E}, \tag{3.15}$$

so the equivalent fluence is

$$\Phi_{eq} = \kappa\Phi_{part} = \kappa \int_{E_{min}}^{E_{max}} \Phi_{part}(E)\mathrm{d}E. \tag{3.16}$$

In particular, for a monochromatic 23 MeV proton beam irradiation (as available in the KIT irradiation facility), the correction factor is $\kappa = 2.6$, while for 23 GeV protons (as offered by the CERN PS irradiation facility), $\kappa = 0.6$, which shows that radiation damage is smaller for higher energy protons. Some samples in this thesis were irradiated with reactor neutrons at JSI Ljubljana, which offers a non-monochromatic neutron irradiation with a total hardness factor of $\kappa \simeq 0.9$.

Impact on Sensor Performance

One consequence of radiation induced impurities is the appearance of energy levels with high capture probability, *increasing the trapping* of charge carriers, lowering the charge collection efficiency and therefore decreasing hit efficiency (see Fig. 3.6 right).

Another effect of bulk radiation damage is the *variation of the effective doping concentration*, i.e. the difference between donors and acceptors ($N_{eff} = N_D - N_A$): some energy levels introduced in the forbidden energy band gap by radiation damage act as acceptors (see Fig. 3.6 centre) which, after heavy enough irradiation can change the dominant doping type in the bulk in n-doped silicon, known as *type inversion* or *Space Charge Sign Inversion (SCSI)*. Since the sensors used in this thesis are made from p-doped silicon they don't

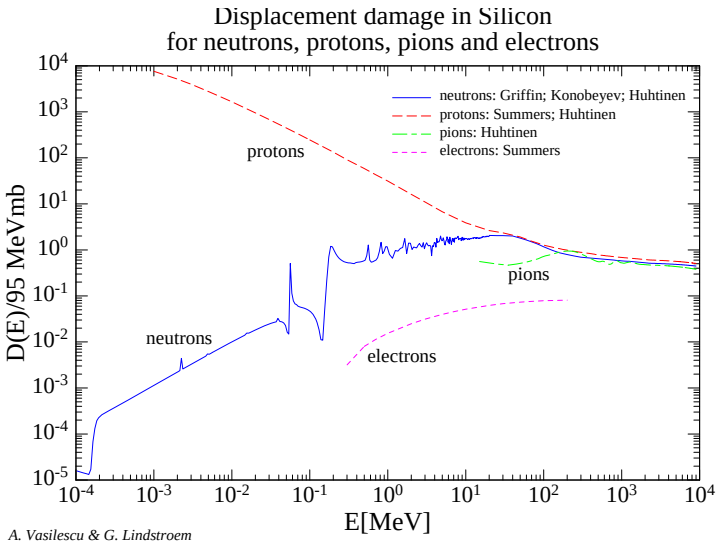

Figure 3.7.: Displacement damage cross section as a function of particle energy for electrons, pions, protons and neutrons. Taken from [85].

suffer from type inversion. However, the effective doping concentration variation in the bulk affects the depletion voltage in either silicon type, as $V_{depl} \propto |N_{eff}|$ (see Eq. 3.8). So, the depletion voltage, for p-type silicon, increases as a function of irradiation, requiring a higher operational voltage to reach full efficiency.

With radiation damage, *leakage current increases*, since new deep energy levels appear between the conduction and valence bands (see Fig. 3.6 left) due to crystal defects. This increment in current is proportional to the fluence and a current-related damage rate α [86]:

$$\Delta I_{leak} = \alpha \Phi V, \tag{3.17}$$

where V refers to the Si bulk volume. Leakage current caused by radiation damage anneals after irradiation at a rate dependent on time and temperature. This effect is contained in the α parameter, and its evolution is presented in Fig. 3.8. Short-term annealing is usually performed for detector irradiation studies. This reduces part of the effective doping concentration, obtained from the irradiation. It also lowers the leakage current and reduces the possible different initial annealing of the sample that depends on details of the irradiation, transport and storage. However, too long periods (few weeks at room temperature) of annealing can cause the depletion voltage to increase and thus degrade the sensor performance. This is known as *reverse annealing*.

3.1.4. 3D Silicon Detectors

3D silicon detectors were first introduced in 1997 by Kenney, Parker et al [87, 88]. The novelty of this type of detectors comes from the fact that the electrodes are shaped like columns that penetrate the sensor bulk, as opposed to the traditional planar detectors where the electrodes are implanted in the surface of the silicon (see Fig. 3.9). This is achieved by high aspect ratio etching techniques, which allows the manufacture of thin and deep columns into the silicon (see below). Due to the column electrode structure, the inter-electrode distance and sensor thickness are decoupled. Therefore, the 3D technology offers short inter-electrode distances whithout sacrificing charge collection, which translates into lower depletion voltages and thus lower power dissipation. Moreover, shorter drift

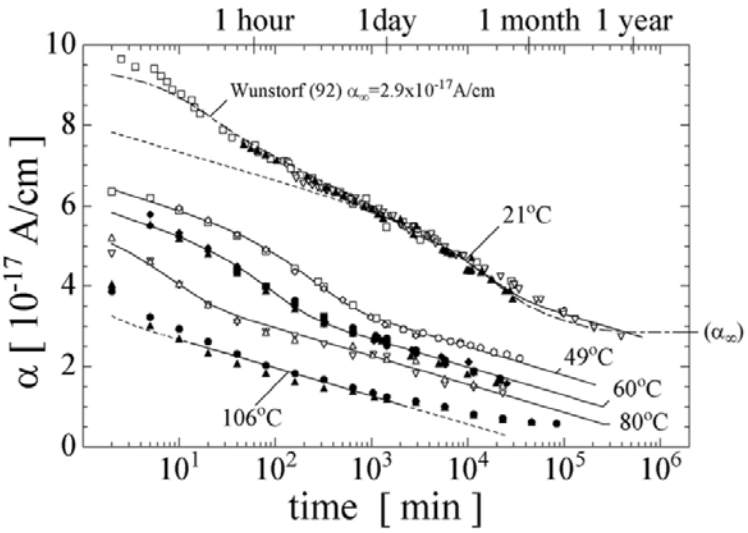

Figure 3.8.: Current-related damage parameter α evolution with time for different annealing temperatures. Taken from [86].

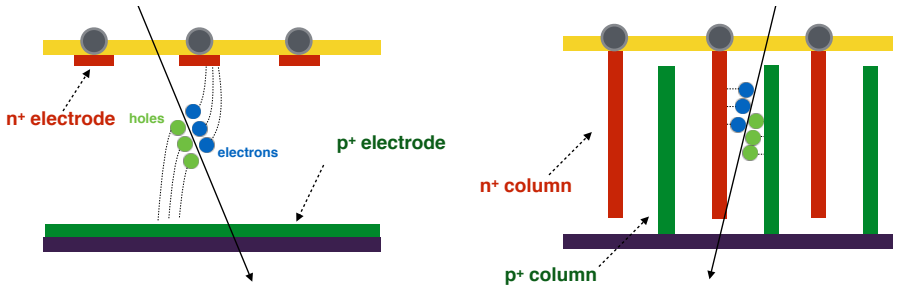

Figure 3.9.: Comparison between a planar (left) and a 3D (right) sensor design.

distances reduce the probability of the charge carriers being trapped by radiation-induced defects, making the 3D technology intrinsically radiation hard.

However, the 3D technology has also some disadvantages: the production yield is lower than its planar counterpart and requires more production steps which, as a consequence increases the cost with respect to traditional planar sensors.

Fabrication

In this section, an example of a fabrication process of a 3D pixel sensor is described (see Fig. 3.10).

A polished p-doped silicon wafer is first covered by a thin layer of SiO_2 by *wet oxidation*: water vapour at very high temperature (∼1000 °C) is used to grow an oxide layer. A photo-resist is deposited over the silicon dioxide and illuminated with UV light through a mask leaving open the regions where the p-stop[1] will be implanted with boron ions.

Columns of high aspect ratio are etched in the silicon via a *Deep Reactive Ionization Etching (DRIE)* process, one of such process being the Bosch method. It consists of a series of alternating steps of plasma etching with fluorine ions from SF_6 and a deposition of a

[1]High dose p^+-implantation surrounding the electrodes to isolate them, preventing unwanted currents between neighbouring electrodes.

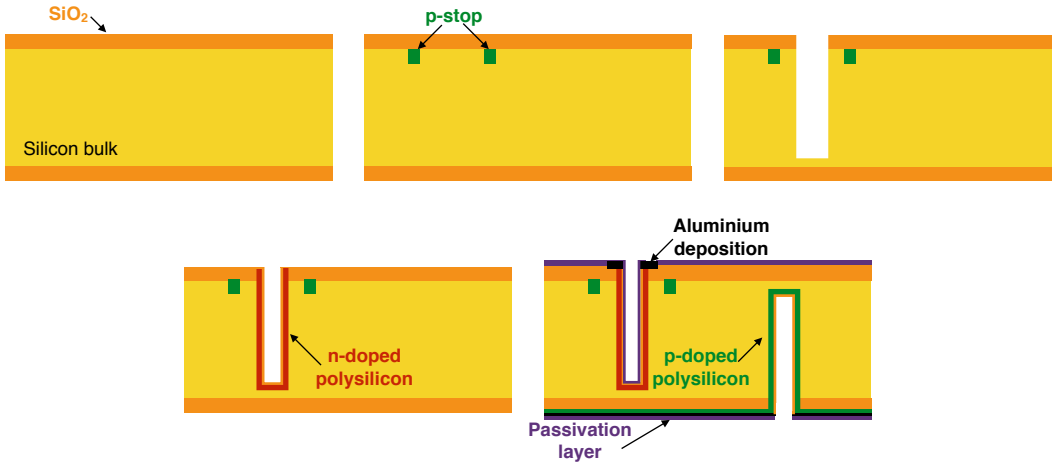

Figure 3.10.: Sketch of the fabrication process of a double-sided 3D pixel sensor.

passivation layer with C_4F_8. The passivation layer protects the side-walls of the column from being further etched by the plasma, with the wafer oxide and photo-resist layers acting as protection mask. Fig. 3.11 shows a sketch of the column etching process.

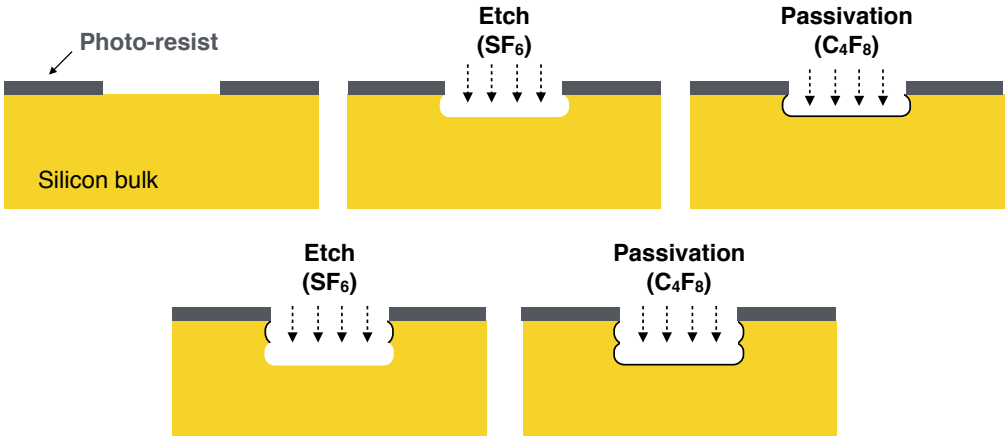

Figure 3.11.: Sketch of the DRIE process with the Bosch method, showing a plasma etching step followed by the deposition of a passivation layer step. Adapted from [89].

After etching of the columns has finished, the holes are partially filled with polysilicon and doped with phosphorus ions to create the n^+-columns. A SiO_2 layer is grown afterwards in order to protect the n-doped region. The p^+-column is fabricated similarly to the n^+-column, although this time the doping ions are boron atoms. In a double-sided process these are etched from the back side of the wafer. Later, the columns are covered with aluminium to facilitate the electrical contact and the full wafer surface is passivated (see Fig. 3.17).

3.1.5. Present and Future of 3D Detectors in HEP

The use of 3D pixel detectors for high energy physics is recent (see Table 3.1). At the time of writing this thesis, this type of sensors has been installed in the ATLAS Insertable B-Layer (IBL) in 2014 [42, 90], in the AFP detector in 2016 [29, 91] and in the CMS-TOTEM

Precision Proton Spectrometer (CT-PPS) in 2017 [92, 93]. In addition, 3D sensors are being considered for the inner-most layer(s) of the upgraded ATLAS and CMS Pixel detectors for the High Luminosity LHC period. Table 3.1 shows a summary of the experiments in High Energy Physics using (or planning to use) 3D pixel technology, with the radiation hardness requirement and sensor geometry: thickness, pixel pitch, number of read-out electrodes per pixel (1E/2E) and inter-electrode distance.

Table 3.1.: Summary of experiments in High Energy Physics using (or planning to use) 3D pixel technology. The installation date refers to the year in which the experiment was equipped with 3D sensors (CT-PPS was installed in 2016 with strip sensors, which only in 2017 were replaced with 3D detectors).

	IBL	AFP	CT-PPS	HL-LHC Tracker
Fluence [10^{15} n_{eq}/cm^2]	5	3 non-unif.	1 non-unif.	26–30[a]
Installation	2014	2016/2017	2017	2025
Pixel size [μm^2]	50×250	50×250	150×100	50×50/25×100
Active sensor thickness	230	230	230	100-150
Pixel configuration	2E	2E	2E	1E/2E
Electrode distance [μm]	67	67	60	35/52/28
Read-out chip	FE-I4B	FE-I4B	PSI46dig	Successor of RD53

[a]Scaled to 4000 fb^{-1} luminosity: ATLAS foresees a one replacement scenario, in which the inner layers are replaced after 2000 fb^{-1} [94], while CMS designed its Phase 2 inner tracker for a total luminosity of 3000 fb^{-1} [95]. The largest fluence is expected in the innermost layer of CMS inner tracker, designed closer to the interaction point (28 mm in CMS and 39 mm in ATLAS).

IBL: First Use of 3D Silicon Detectors

In order to improve its detector performance and gain redundancy for eventual problems in the Pixel system, ATLAS installed a new inner layer in May 2014. It was designed to cope with a fluence of 5×10^{15} n_{eq}/cm^2 (with a safety factor of about 1.6) at the end of its life time corresponding to the end of LHC Phase-I (∼2023), before the whole ATLAS inner detector is to be replaced [42]. Two silicon sensor technologies co-exist in IBL: the planar pixel sensors (75% of the area) in the centre part, and the 3D pixel sensors (25% of the area) at the ends of the barrel. In total, it consists of 14 staves, each one containing a total of 20 modules, 12 double chips[2] planar modules and 8 single chip 3D detectors. Every pixel chip (FE-I4, see Sec. 3.3.1) contains 26,880 pixels which totals to 12 million pixels only on this layer. The full IBL layer has a radius of ∼3.2 cm and covers a range of $|z| < 33.2$ cm.

As stated before, the purpose of IBL is the improvement of the spatial resolution of the ATLAS track reconstruction and compensate the possible deterioration of the rest of the ATLAS pixel detector. The addition of IBL improves the track impact parameter resolution (d_0). Therefore it is possible to more accurately distinguish relatively long lived particles like b-mesons by measuring secondary vertices (b-tagging) with the aid of IBL.

The performance of the 3D prototype for IBL has been extensively studied in test-beams [96] and proven to meet the high tracking efficiency requirement after irradiation (>97%).

[2]Planar sensors are coupled to two front-end chips.

AFP and CT-PPS

Radiation hardness is a key requirement for the forward detectors like the ATLAS Forward Proton detector [29] and its CMS counter-part, the CMS TOTEM Precision Proton Spectrometer (CT-PPS) [92]. In particular, for these detectors it is needed to cope with non-uniform irradiation as the expected fluence ranges from $\sim 1-3\times10^{15}$ n_{eq}/cm^2 to orders of magnitude lower in few millimetres. Being in such harsh environments makes the 3D detectors a suitable candidate technology for their tracking detectors. The AFP detector uses a slightly modified IBL-generation sensors as tracking detectors in the Roman Pots on both sides of ATLAS (see Sec. 2.3), while CT-PPS needed to develop a new pixel geometry that could couple to the PSI46dig [97] chip, the front-end used for the upgrade of the CMS pixel detector at the beginning of 2017.

AFP Roman Pots are equipped with 3D pixel detectors since February of 2016, when two Roman Pot stations were installed in one side of ATLAS (see Sec. 4.2). The full installation was finalized in 2017, which includes the Time-of-Flight detectors. In parallel, silicon strip detectors were installed in CT-PPS Roman Pots during the Year End Technical Stop (YETS) of 2015-2016, which were replaced by 3D pixel sensors during the Extended YETS of 2016-2017 [93].

Inner Tracker (ITk) Upgrade for the HL-LHC

The current inner detectors in the ATLAS and CMS experiments will receive a fluence of few 10^{15} n_{eq}/cm^2 on the inner layers before the start of the High Luminosity LHC (HL-LHC) program in 2025. The HL-LHC program foresees an increase in the luminosity and therefore an increase of the radiation hardness requirements: the layers closest to the interaction point are expected to need to withstand a fluence of 1.3×10^{16} n_{eq}/cm^2, assuming a replacement scenario[3], with a safety factor of 1.5. For this reason, the whole inner detectors of ATLAS and CMS will be replaced by a new trackers [94, 95].

The 3D technology is a candidate for the innermost layer of the Inner Tracker (ITk) in ATLAS and the corresponding CMS tracker upgrade for Phase 2. By increasing the granularity (two options are being considered, 50×50 and 25×100 μm^2, see Fig. 3.12) and reducing the inter-electrode distance with respect to the AFP/IBL generation 3D pixel detectors (see Table 3.1), the sensors become more radiation hard, as the trapping probability and the depletion voltage are both reduced. However, the active sensor thickness will be reduced down to 100-150 μm, which decreases the total charge collection. A new read-out chip with a lower achievable threshold and compatible with the smaller pixel size is being developed (currently named RD53 chip) [98].

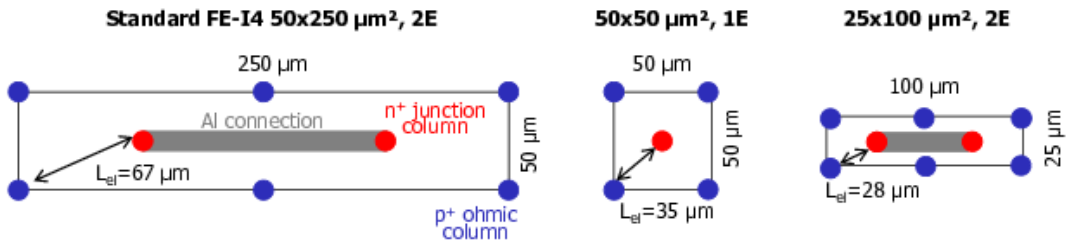

Figure 3.12.: Geometry of a 3D pixel cell for a standard IBL/AFP FE-I4 pixel with 50×250 μm^2, 2E configuration (left), and for a 50×50 μm^2, 1E, (centre) and a 25×100 μm^2, 2E, (right) pixel. Taken from [99].

[3]The ASIC is at the moment not specified to be radiation hard enough to operate for a full HL-LHC period of 4000 fb^{-1}, hence the replacement of the innermost layer was proposed at 2000 fb^{-1}.

Even though at the time of writing this work a chip with the small-pitch geometry (50×50 μm) is not available, ITk geometry 3D sensors have been produced compatible with the IBL/AFP generation FE-I4 read-out chip[4]. IBL/AFP generation detectors and small pitch sensors coupled with the FE-I4 chip have been irradiated up to the expected fluence in ITk. First test-beam results [100, 99, 101] indicate that, while IBL/AFP generation detectors show good radiation hardness at ITk fluences, small-pitch detectors require lower bias voltage to reach full efficiency than the older generation detectors (Fig. 3.13), and they are therefore more radiation hard: they need ∼110 V to reach high hit reconstruction efficiency at fluences of 1.4×10^{16} n_{eq}/cm^2, using a threshold of 1500 electrons. This requirement is lower (100 V) with a lower threshold (1000 electrons), which shows that the efficiency will benefit from the lower achievable threshold of the future ITk chip.

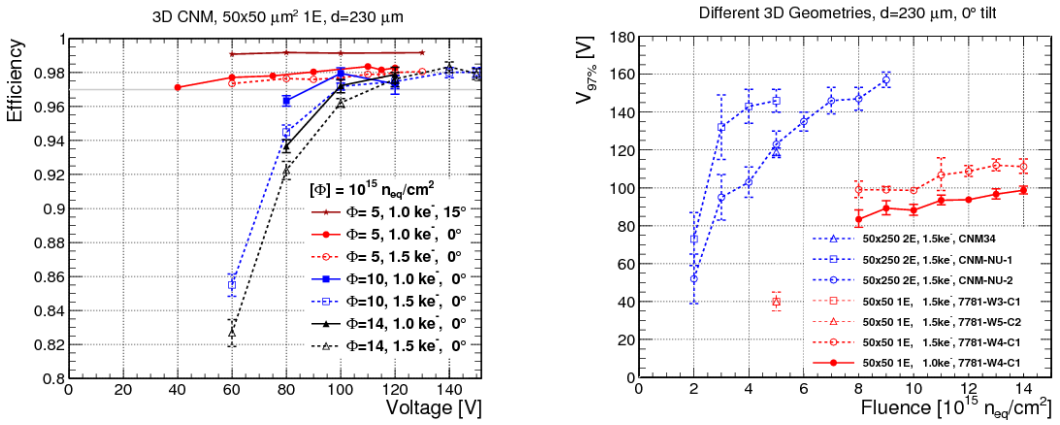

Figure 3.13.: Efficiency as a function of voltage for different fluences, thresholds and tilts of a 50×50 μm^2 pixel size sensors (left) and the bias voltage to reach 97% efficiency (right) for different fluences for the IBL generation (50×250 μm^2, 2E) and the small-pitch pixel generation (50×50 μm^2, 1E). Taken from [101].

3.2. Tracker Requirements for AFP

It has been shown that 3D pixel sensor modules are able to sustain IBL uniform fluences [96]. However, AFP expected beam profile is highly non-uniform and thus requires to sustain non-homogeneous fluences, reaching an expected fluence after 100 fb^{-1} of ∼3×10^{15} n_{eq}/cm^2 in the hot-spot and several order of magnitude lower few millimetres away (see Fig. 3.14). This is a consequence of the beam optics: the trajectory of the protons leaving the interaction point are bent by the LHC magnets between ATLAS and the AFP tracker as a function of the proton transverse momentum and energy. In the standard LHC optics configuration this effect translates into a hot-spot in a diagonal band. Therefore, the sensors need to be operable after a highly non-uniform radiation.

As already mentioned, uniformly distributed fluences up to ∼5×10^{15} n_{eq}/cm^2 in 3D silicon FE-I4 pixel detectors were studied in the effort to characterize the technology for its use in IBL [96]. However, the non-uniform beam profile expected in AFP introduces new challenges: as the sensor gets further irradiated, the depletion voltage (and so the voltage needed for full efficiency) increases. Due to the non-uniform irradiation a scenario is possible in which the full efficiency voltage in the most irradiated region is larger than the breakdown voltage in the lowest irradiated region. In such a case applying a high bias

[4]Small-pitch sensors coupled to a 50×250 μm^2 compatible chip implies a large inactive area of 80%.

voltage would cause a too high leakage current leading to noise and, in some cases, prevent the device to be operated, while an intermediate voltage would reduce the charge collection efficiency in the irradiated region and therefore the hit efficiency of the sensor.

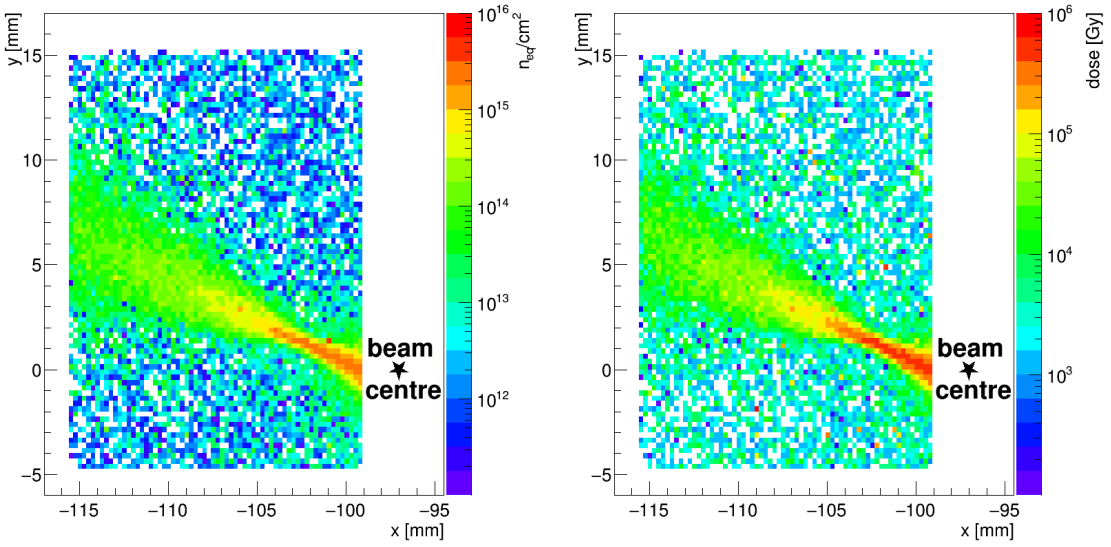

Figure 3.14.: Expected fluence (left) and total ionizing does in the AFP silicon tracker detectors after 100 fb^{-1} total luminosity at data taking position. Taken from [29].

A second issue to address is the inactive area of the sensor facing the beam. In order to be able to move the active area of the detectors as close as possible from the LHC proton beam to gain acceptance, the active pixels of the sensors need to be installed close to the floor of the Roman Pots (see Sec. 2.3.2) and hence, close to the LHC proton beam. However, the IBL sensors have a ∼1.5 mm distance of non-instrumented region which extends along the edge (see Sec. 3.3.2) which faces the beam (and the Roman Pot floor).

Although the original plan was to utilize 3D sensors without inactive edges, the production of such sensors were not yet fully studied and due to time constraints it was not possible to carry out a well tested production with this change in design. Therefore, slim-edging of IBL sensors was pursued as an alternative, and a compromise between small inactive area and the risk of early breakdown due to an edge too close to the active region [102] was decided to be <200 μm. Hence, for AFP the edges in the IBL sensors needed to be slim-edged down to <200 μm without losing efficiency in the last pixel row, where the highest diffraction mass acceptance is expected.

Finally, according to simulations, an important source of resolution loss in the reconstruction of the proton kinematics (i.e. proton energy loss and transverse momentum) is the detector position resolution. Fig. 3.15 shows the proton transverse momentum and energy resolution from simulations, where the benchmark full tracker pointing resolution is 10 μm in the short pixel direction and 30 μm in the long pixel direction. The detector resolution constitutes a major contribution to the total proton transverse momentum and energy reconstruction uncertainties with up to $\delta\xi$ ∼10 GeV and δp_{T} ∼0.07 GeV.

Thus, in order to ensure a good physics performance from the AFP detector (see Sec. 1.5), the silicon tracker has to meet the following requirements:

1. A hit efficiency of ≥97% before and after non-uniform irradiation, consistent with the IBL target efficiencies.

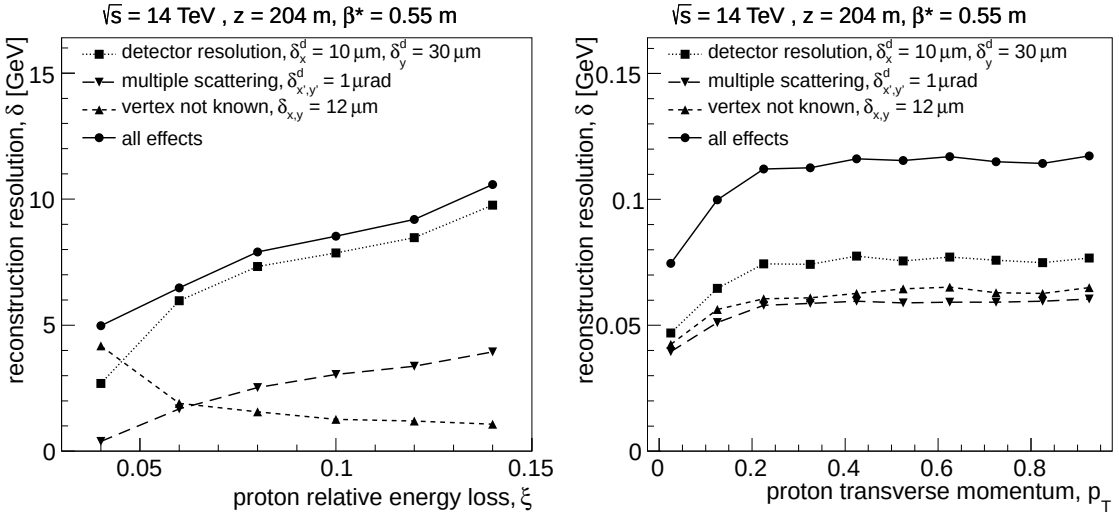

Figure 3.15.: The resolution of the reconstructed proton relative energy loss (left) and transverse momentum (right). The experimental effects taken into account are: the AFP detector spatial resolution, the lack of information about the vertex coordinates, and multiple scattering. Taken from [29].

2. An inactive region of $<$200 μm.

3. A pointing position resolution of $\sim$10$\times$30 μm^2 per station (four planes).

3.3. Prototype AFP Pixel Module for Qualification

The AFP pixel module is the building block of the AFP silicon tracker. Each module consists in a *3D pixel sensor* coupled to an *FE-I4 read-out chip* via bump-bonding, mounted on an aluminium-carbon fibre composite holder with a flexible printed circuit, to which the chip is wire-bonded. The performance of the pixel module depends on the sensor (Sec. 3.3.2) and the read-out electronics (Sec. 3.3.1).

3.3.1. The FE-I4 Read-Out Chip

The FE-I4 readout chip [103] was designed to sustain the high radiation doses that were foreseen for the sensors in the IBL detector until the end of LHC Run 3 ($\sim$2023). It is qualified to work up to a total ionising dose of 250 Mrad.

The chip has a total of 26,880 channels distributed in an array of 336$\times$80 pixels, and was designed to be bump-bonded to sensors with pixels of 50$\times$250 μm^2. In each channel a charge sensitive amplifier is followed by a discriminator. The chip uses a 40 MHz clock, compatible with the LHC collision frequency.

The electrons collected from the pixel sensor electrodes enter the readout chip through the metal bump (see Fig. 3.16). The signal is processed by a pre-amplifier where a digital-to-analog converter (DAC) controls the fall time of the pre-amplifier output (FDAC). In this way, the time during which the signal is above the discriminator threshold (Time-over-Threshold or ToT), measured in the digital electronics in units of clock cycles (25 ns), can be calibrated. Since the ToT is closely related to the charge collected, its measurement can be used to estimate the energy lost by the incident particle. A leakage current compensation circuit is used to filter the DC current coming from the silicon leakage current. Afterwards, the amplified signal arrives at a discriminator with an adjustable threshold, which can be

calibrated by another DAC (TDAC). The output of the discriminator is split. One part is processed by the digital part of the read-out chain after being split, the other copy of the signal is combined with the discriminator output of the other pixels in a logical OR, the so-called HitOR (i.e. the resulting signal indicates if at least one pixel is hit).

Near the metal bump there is a charge injection mechanism used for calibration purposes: it injects an adjustable amount of charge at the beginning of the analog electronics to simulate a hit. By using an adjustable voltage V_{cal} and a set of capacitors (C_{inj1} and C_{inj2}) a test pulse of charge $V_{cal} \times C_{inj}$ can be injected at the pre-amplifier input. The injection total capacitance has a typical value of $\sim$ 6.1 fF, while the V_{cal} is $\sim$1.5 mV/DAC.

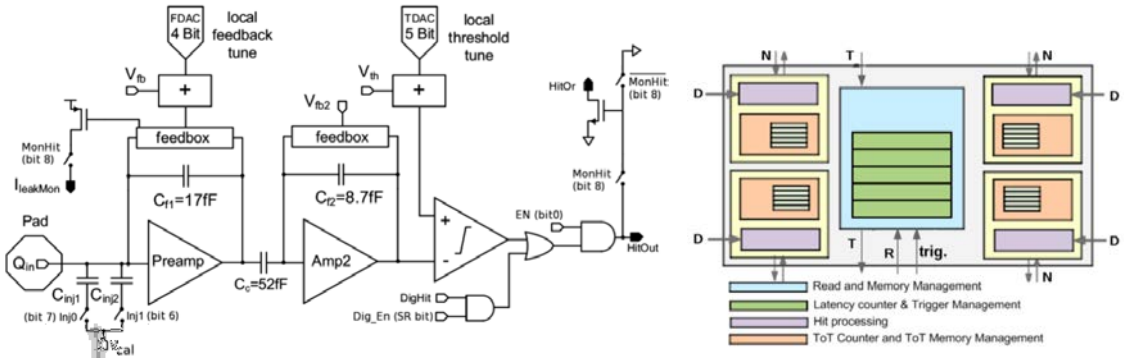

Figure 3.16.: Analog circuit of the FE-I4 chip (left) and the Pixel Digital Region (right). The selected connections shown are: trigger input, analog discriminator inputs (D), neighbour logic inputs and outputs (N), read token in and out (T), and read signal input (R). Taken from [96].

Each Pixel Digital Region (PDR) groups a total of 4 pixel read-outs (see Fig. 3.16): there are 168 PDR in each of the 40 Digital Double Columns (DDC), which are connected together via the End of Column Logic (EOCL). Still the hit processing and ToT counting is done for each separate pixel, the last starting to count once the analog discriminator fires. A digital threshold is applied during this process, which can be modified with a register (HitDiscConfig), the options being: a digital threshold of 1 ToT (the analog discriminator fires) up to 3 ToT (the output of the analog discriminator has to be at least 3 bunch crossings long). At least one of the four pixels forming the PDR need to pass the digital threshold for the hit information of the four pixels to be sent out, including the data of pixels in that same PDR that passed the analog but not the digital threshold (encoded as "small hits"). The event information is then sent to the EOCL which stores the data into a buffer and generates the BCID.

3.3.2. The IBL/AFP Generation 3D Pixel Sensor

IBL/AFP 3D pixel sensors have a granularity of 50×250 μm^2, and as the FE-I4 chip, 336×80 pixels. Each pixel is composed of two shorted n^+-columns connected to the readout bump (2E pixel configuration), surrounded by six p^+-columns which define the boundaries of the pixel. The thickness of the high resistivity ($\rho = 10 - 30$ kΩ cm) silicon bulk is 230 μm (see Fig. 3.12). This pixel geometry yields a capacitance of 169 fF [104].

During the IBL production, two different designs were fabricated by two different vendors, CNM[5] and FBK[6]. While both designs feature the column-like electrodes characteristic

[5]Centre Nacional de Microelectrònica, Barcelona
[6]Fondazione Bruno Kessler, Trento

of the 3D technology, the electrodes fully traverse the silicon bulk in the case of the FBK sensors, while the columns in the CNM design are 210 μm, i.e. the end of the columns are at 20 μm from the opposite side of the silicon bulk. Figure 3.17 shows a cross section of both 3D solutions.

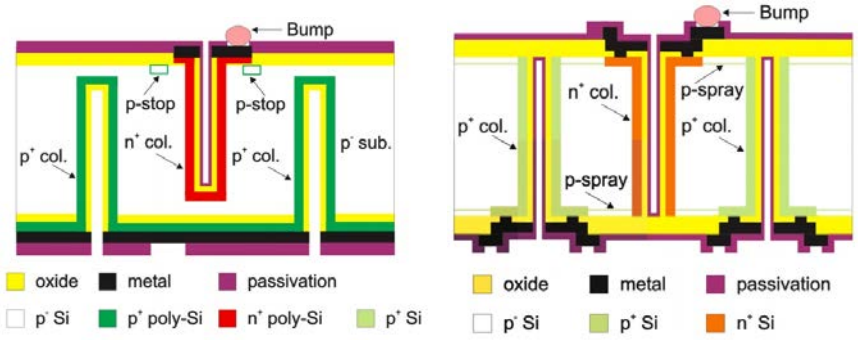

Figure 3.17.: Cross section of the IBL CNM (left) and FBK (right) designs.

The columns are isolated with *p-stop* in the CNM sensors, while the FBK pixels use a *p-spray* for inter-pixel isolation. The p-stop consists in an implantation of a high-dose p^+-implant surrounding the base of the n^+-columns, while the p-spray isolation introduces a larger uniform p^+-implant with a dose small enough that an overlap with the n^+-column doesn't lead to breakdown.

The silicon in both designs span beyond the instrumented region by 200 μm in the long pixel direction and up to ~1.5 mm along the short pixel direction in order to allow for a bias connection from the pixel side (*bias tab*), as mentioned before in Sec. 3.2. Although this is only necessary for single-sided processes, also FBK and CNM implemented this in their double-sided IBL process in favour of a common sensor design among all potential IBL vendors. In order to isolate the active region from possible defects in the sensor edge, CNM and FBK use different solutions (see Fig. 3.18). In FBK 3D sensors the non-instrumented area has a so-called p-fence, i.e. an array of p^+-columns. CNM sensors have in addition a grounded guard-ring consisting of n^+-columns surrounding the instrumented region and shorted together, so electrons generated beyond it are collected by the guard-ring instead of the last active pixel. AFP requires a small non-instrumented edge in the side where the IBL sensors have a dead space due to the aforementioned bias tab of ~1.5 mm. Hence, for AFP sensors, the bias tab is diced away, achieving a slim edge of <200 μm from the last active pixel.

Table 3.2 shows a summary of the major differences between the sensors from the two vendors. Both designs were originally studied in test-beams in order to characterize them in the context of the requirements for the IBL detector. It was found that both 3D FE-I4 detector designs are able to sustain a uniform fluence of up to 5×10^{15} n_{eq}/cm^2 and provide a >97% efficiency with a much lower operational voltage than their planar counterparts [96]. As opposed to IBL, the AFP tracker needs to sustain a very non-uniform radiation damage distribution with a peak fluence of ~3×10^{15} n_{eq}/cm^2. As a consequence, the suitability of 3D FE-I4 pixel detectors as silicon tracker detectors for the AFP project was studied in several test-beams as well (see following sections).

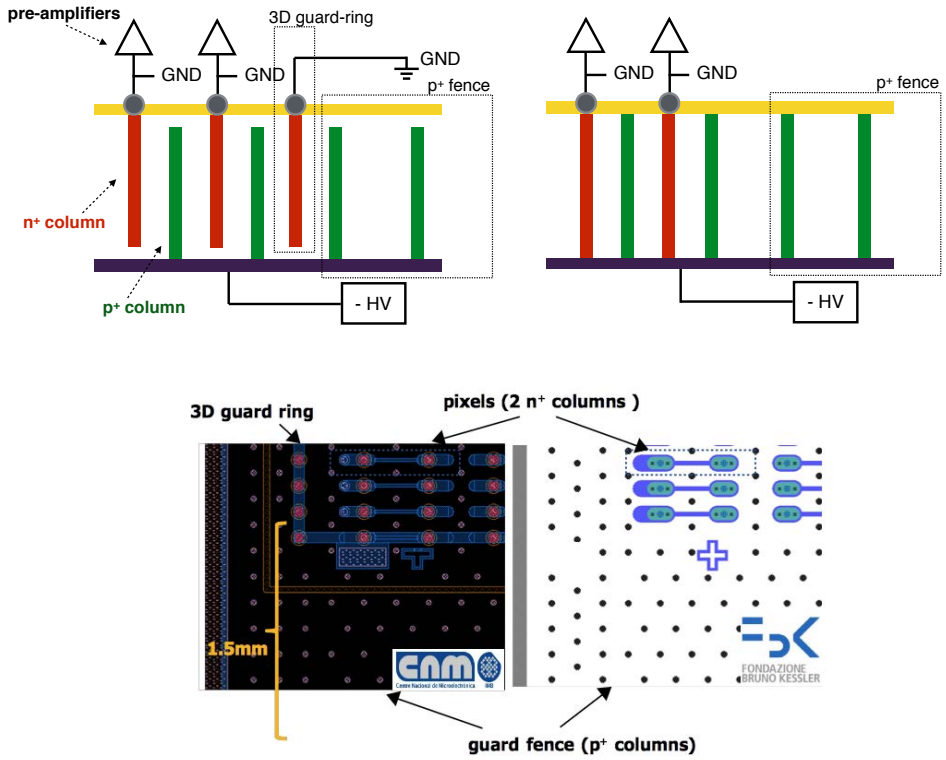

Figure 3.18.: Schematics of the pixel structure around the end of the instrumented area of the IBL CNM (left) and FBK (right) designs. The top figures show the cross section of both designs and how they are biased, while the bottom figures show the pixel geometry.

Table 3.2.: Differences in designs for the IBL/AFP generation of 3D pixel sensors.

Vendor	Columns	Inter-pixel isolation	Edge
FBK	Fully pass-through	p-Spray	p-fence
CNM	Not fully pass-through	p-Stop	p-fence + guard-ring

3.4. FE-I4 Read-out Data Acquisition Systems

Several read out systems have been developed for the FE-I3[7] and FE-I4 ASICs. However, the results shown in this thesis were obtained with the two most commonly used: the USBPix [105] and the RCE [106, 107], which are briefly described below.

3.4.1. USBPix

The USBPix [105] read-out system is a portable DAQ system which consists of a Multi-IO board with a USB micro-controller, an FPGA and 2 MB of on-board (SRAM) memory, see Fig. 3.19. It provides a TTL connection, used for triggering in some applications (beam tests). Communication with a computer is done via a USB connection, with a dedicated software named STControl [105].

The Multi-IO board has to be connected to an adapter card which provides communication lines and voltage regulation for the chip. Two adapter cards exist for the readout

[7]Previous version of the FE-I4 chip, used for the ATLAS Pixel Detector before IBL.

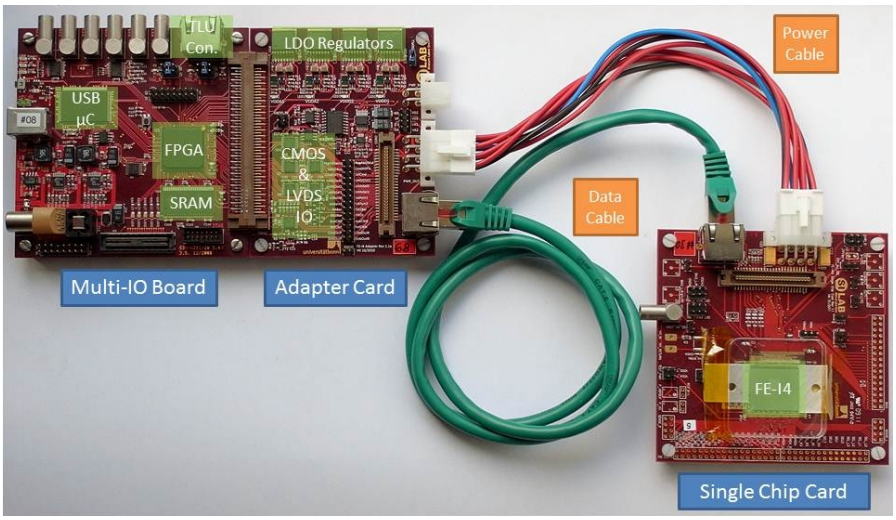

Figure 3.19.: Picture of the USBPix DAQ system, where a Multi-IO board is connected to a single chip adapter card to connect an FE-I4 device mounted in a PCB (single chip card). [105]

of FE-I4 devices: a single chip adapter card and a Burn-In Card (BIC). The single chip adapter card can connect the Multi-IO board to one FE-I4 chip with a flat ribbon cable for both data and power lines or an ethernet cable for data and a separate power cable (Molex). On the other hand, the BIC adapter is used for multiple chip testing, as it allows connection with four FE-I4 recursively or at the same time (only ethernet connection is possible).

3.4.2. RCE

The RCE (Reconfigurable Cluster Element) read-out system [106, 107] is a DAQ hardware for ATLAS pixel modules. The RCE supports FE-I3 and FE-I4 ASICs, AFP hitbus and HPTDC (see Sec. 2.3.5). Two versions of RCE systems are available for ATLAS pixel module read-out: the RCE/HSIO and the HSIO-II. The first one connects an RCE board in an Advanced Telecommunication Computing Architecture (ATCA) crate to an High Speed Input/Output (HSIO) module via an optical fibre which handles the data stream and triggers of the pixel modules. The HSIO-II, on the other hand, does not require an ATCA crate, since the HSIO-II module itself houses an RCE. In both versions, the HSIO module has the possibility of connecting adapter boards for FE-I4 pixel modules read-out via ethernet, usually for laboratory and test-beam module testing, or optical fibre, used as read-out option for the AFP detector (see Fig. 2.16).

3.5. Module Calibration and Operation

The calibration procedure and operation of FE-I4 devices can be performed similarly with either read-out system (see Sec. 3.4). The following sections describe the tuning and measurements that are usually done to test the FE-I4 modules.

3.5.1. Analog/Digital scan

Analog and Digital scans are usually performed initially to verify the front-end functionality and the system connectivity. The Analog scan consists in injecting a signal a certain

amount of times with a charge well above the threshold. If the chip works well, the recorded hits should equal the number of signals injected. The same principle applies for the Digital scan, but in this case the signals are injected after the analog discriminator to test the digital electronics of each pixel.

Examples of successful Analog and Digital scans are shown in Fig. 3.20, where a total of 200 signals are injected to the analog (left) and digital (right) circuits of each pixel. Here, all the injected signals were successfully read-out, showing the well-functioning of all the pixel circuits.

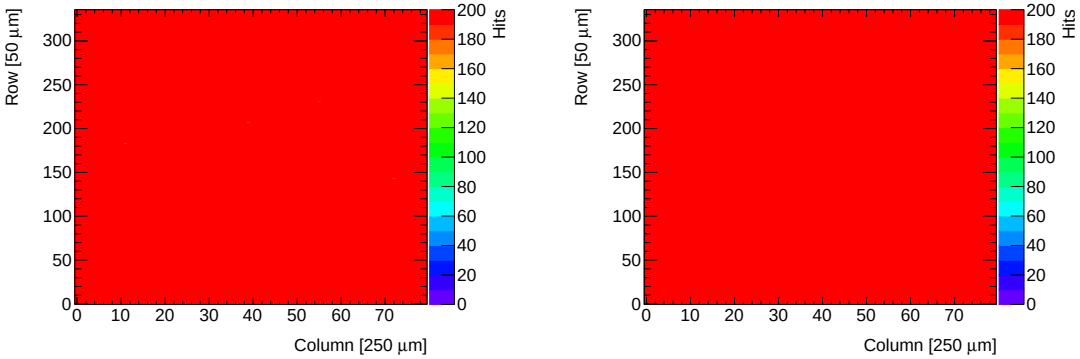

Figure 3.20.: Results from Analog (left) and Digital (right) scans. A total of 200 signals were injected to the analog/digital circuits for each pixel.

3.5.2. Threshold and Noise

During operation, a uniform threshold distribution is required over all the pixels of the device. A too high threshold can lead to a reduction of the hit efficiency, while a too low threshold introduces noise. For this reason the threshold level can be adjusted globally (at the chip level) and independently in each pixel.

In order to measure the threshold of each pixel, a pulse of known charge is injected at the input of the pre-amplifier a controlled amount of times using the charge injection mechanism (see Sec. 3.3.1). The number of times the pulse is observed at the end of the read-out chain is measured before increasing the charge of the injected signal in several steps and repeating the procedure. For a perfect discriminator, the number of observed pulses as a function of injected charge should follow a step function, rising at the threshold value. However, noise makes the signal fluctuate. Therefore, the expected response function is a convolution of a step function and a Gaussian distribution, known as an S-curve. Thus, the hit probability follows a distribution

$$p(Q) = \frac{1}{2}\mathrm{Erfc}\left(\frac{Q_{thr} - Q}{\sqrt{2}\sigma_{noise}}\right), \tag{3.18}$$

where $\mathrm{Erfc}(x)$ is defined as

$$\mathrm{Erfc}(x) = \frac{2}{\sqrt{\pi}}\int_x^\infty e^{-t^2}\mathrm{d}t. \tag{3.19}$$

The threshold is then the 50% point of the S-curve (Q_{thr}) and the noise is the width (σ_{noise}) of the convoluted Gaussian (see Fig. 3.21, bottom).

Two chip registers are used to modify the global threshold of all the pixels of the chip: `Vthin_Coarse` and `Vthin_Fine`. The tuning of these registers so that the average threshold

over the pixels is closest to the target threshold is the first step for threshold calibration. Once the global registers are set, the calibration is done for each individual pixel by modifying its `TDAC` register to achieve the target threshold. Algorithms to automatize for both global and local threshold calibrations are implemented for all DAQ systems (see Sec. 3.4).

After the threshold calibration, the distribution of threshold values for all the pixels is measured, as well as the noise distribution. Typical target thresholds range from 1500 to 3000 e^-. After calibration, the width of the threshold distribution is not larger than 100 e^- and the noise has a typical value of $\sim$150 e^- before irradiation (see Fig. 3.21).

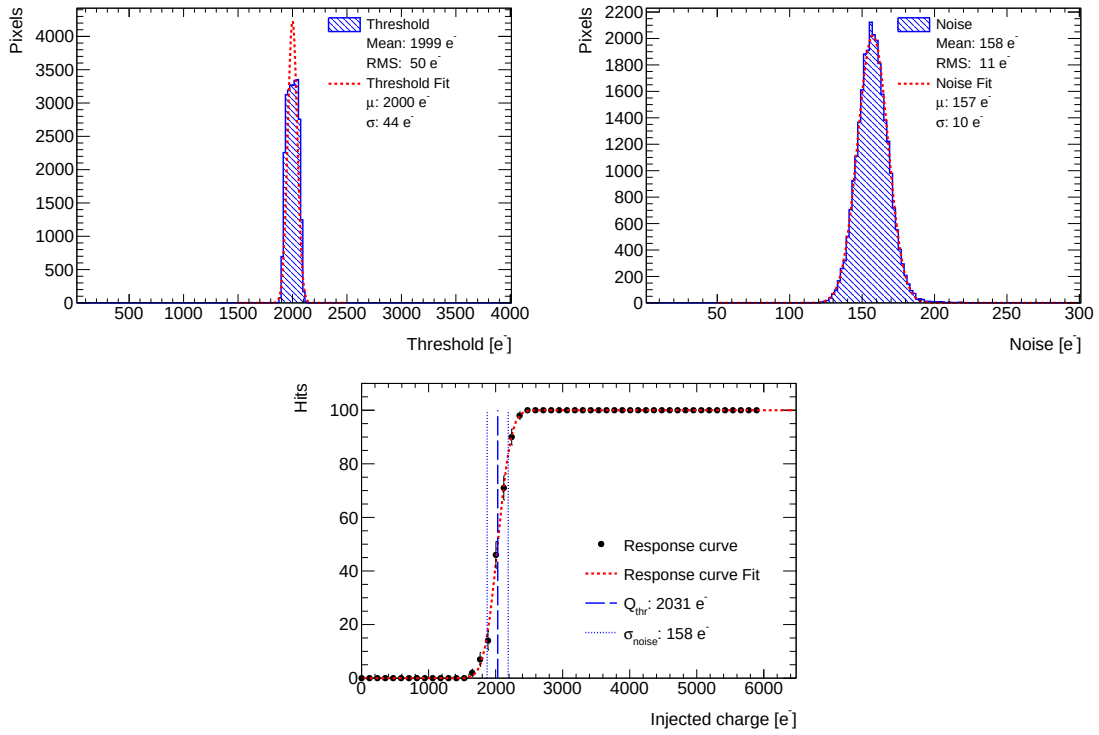

Figure 3.21.: Results from a threshold scan after calibration to a target threshold of 2000 e^-: the threshold (top left), noise (top right) distributions of all the pixels and an example of the response curve for one of the pixels (bottom) for an non-irradiated sample. Threshold and noise distributions are fitted with a Gaussian distribution, while the response curve is fitted with the S-curve from Eq. 3.18.

3.5.3. Time-over-Threshold (ToT)

The Time-over-Threshold (ToT) corresponds to the number of clock cycles (bunch crossings, 25 ns) that the signal is above threshold and is recorded with 4-bits. This is a function of the deposited charge. As with the threshold, the ToT response is calibrated for each pixel in order to obtain a uniform behaviour.

The ToT response is measured by injecting a known reference charge with the charge injection mechanism and measuring the ToT output of the chip. Reference charges for ToT calibration are typically 16000 or 20000 e^-, which approximately correspond to the expected Most Probable Value (MPV) and average charge deposited in a 230 μm thick silicon detector by a minimum ionizing particle.

A global register is used to perform a first global calibration of the average ToT response over all the pixels, the `PrmpVbpf` register. This register controls the global feedback current

of the pre-amplifier by adjusting the signal falling time. The fine tuning is done at per-pixel-level, by modifying the FDAC register for each channel. The calibration is performed by measuring the ToT response for the target charge while varying the register values over its full range to obtain the desired tuning. All DAQ systems have an automatized ToT calibration algorithm.

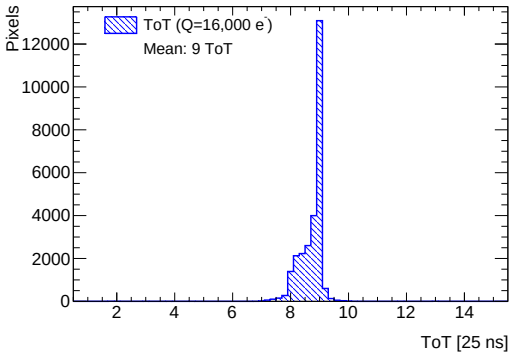

Figure 3.22.: Results from a ToT scan after calibration, using an injected charge of 16000 electrons.

The ToT depends on the threshold calibration and vice-versa, therefore threshold and ToT calibration are performed iteratively to obtain the optimum settings for both parameters.

3.5.4. Tests with Radioactive Sources

A basic test of the pixel detector is to verify that the charge collection mechanism works. This can be done with radioactive sources, in what is called *source scan*. A radioactive source is placed on top of the sensor so that the radiated particles can be detected by the device. Source scans can be used to detect bump-bonding problems in the detectors, as pixels with disconnected bumps do not show any response as shown in Fig. 3.23.

During a source scan the readout of the chip is initiated by a trigger signal, which can be either provided externally by e.g. a scintillator or by the self-trigger mode featured in the front-end, which takes advantage of the hitOr signal from the FE-I4 (the logical sum of all the output signals along the device, see Sec. 3.3.1) using it as a trigger signal.

The usual sources used for these measurements are, for example, ^{90}Sr and ^{241}Am:

- ^{90}Sr has a half-life of 29.1 years and decays to

$$^{90}\mathrm{Sr} \rightarrow {}^{90}\mathrm{Y} + e^- + \bar{\nu}_e \tag{3.20}$$
$$^{90}\mathrm{Y} \rightarrow {}^{90}\mathrm{Zr} + e^- + \bar{\nu}_e. \tag{3.21}$$

  The half-life of the second reaction is 68 hours, the ^{90}Zr isotope is stable. The electron from the first β decay is usually stopped before reaching the detector as its maximum energy is 0.546 MeV while the second electron (E_{max}=2.280 MeV) traverses the silicon. As a charged particle source, the expected charge (ToT) distribution is a Landau distribution convoluted with a Gaussian distribution (Landau⊗Gaus): the Landau distribution describes the energy loss of the impinging charged particle, while the Gaussian distribution accounts for detector fluctuations and noise [79], which widens the distribution. An example of a ToT distribution from a source scan using a ^{90}Sr source is shown in Fig. 3.24, with a fitted Landau⊗Gaus distribution. Two most probable values (MPV) quoted in the legend: the one corresponding to

the convoluted Landau distribution (MPV_{Landau}) and the one corresponding to the whole distribution (MPV_{Distr}). The expected most probable deposited energy by an electron of such energy in 230 μm silicon is 1.06 MeVcm^2/g which corresponds to a charge collection of 16000 e$^-$. In Fig. 3.24, this charge corresponds to about 8 ToT, since the device was calibrated to a response of 10 ToT for a charge collection of 20000 e$^-$. However, since the electrons from the ^{90}Sr don't arrive in perpendicular incidence to the silicon sensor, most of the charge generated inside the bulk is split between more than one pixel (*charge sharing*), which reduces the expected amount of charge collected per pixel. This can be corrected by summing the charge collection of the neighbouring hit pixels (cluster).

- ^{241}Am has a half-life of 432.6 years and decays to

$$^{241}\mathrm{Am} \rightarrow {}^{237}\mathrm{Np}^* + \alpha \tag{3.22}$$

$$^{237}\mathrm{Np}^* \rightarrow {}^{237}\mathrm{Np} + \gamma. \tag{3.23}$$

The energy of the photon in the gamma decay can be 59.5 keV (35.9%), 26.3 keV (2.4%) and 13.9 keV (42.0%) (other decays have negligible probability). The expected peak in charge from the highest energy photon is ~16000 e^-, while the other decay products have either too low energy or too low rate to observe a peak with the 4-bit ToT resolution of the FE-I4. An example of the ^{241}Am spectra measured with an FE-I4 in ToT is shown in Fig. 3.24. The highest peak, corresponding to the 59.5 keV photons, is fitted with a Gaussian distribution.

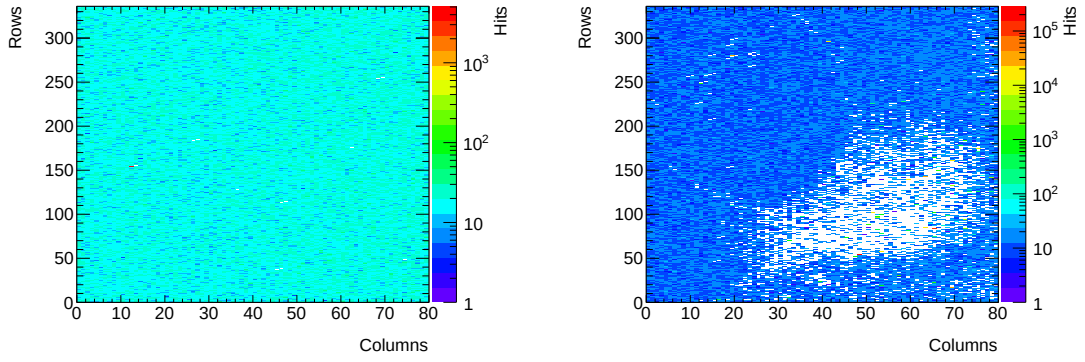

Figure 3.23.: Example of source scan hit maps for a module with good quality bump-bonding (left) and a module with a large area of disconnected bumps (right).

3.5.5. ToT to Charge Calibration

The ToT is not exactly linear with the charge collected, but can be parametrized with a 2nd degree polynomial function. For this reason, a ToT-to-charge calibration procedure is implemented: pulses of different charges are injected via the charge injection mechanism covering the full range of possible charges. As the amount of charge injected is known, the ToT is then correlated with the charge injected which allows for a first calibration which removes the non-linear behaviour (see Fig. 3.25). For a precise calibration, a second calibration with radioactive gamma sources (e.g. ^{241}Am, see Sec. 3.5.4) can be done by measuring the detector response under such source. Since the peak of the photon spectra for the radioactive source and the expected amount of electron-hole pairs generated by that energy are known it is possible to calibrate the charge collection by comparing the detector response with the expected one.

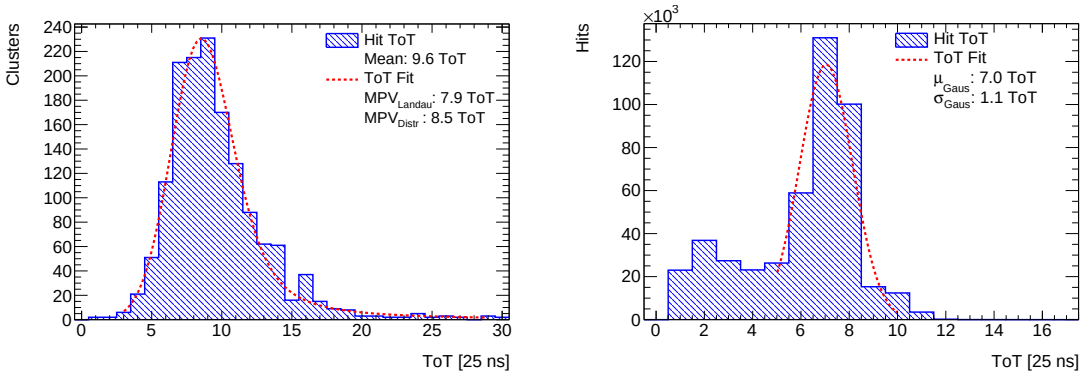

Figure 3.24.: Example of source scan ToT distributions performed with ^{90}Sr (left) and ^{241}Am (right) as radioactive sources. Both measurements were done with a calibration of a 10 ToT response for a charge injection of 20000 e^-. Notice that to recover the expected charge collection, reduced by charge sharing, the sum of ToT from neighbouring hit pixels (cluster) is plotted.

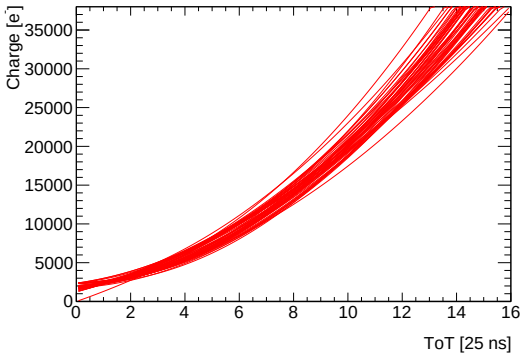

Figure 3.25.: ToT response as a function of the charge injected for 50 selected pixels in an FE-I4 device for a calibration of calibration of a 10 ToT response for a charge injection of 20000 e^-.

3.6. Test-Beam Characterization

This section is dedicated to test-beam studies performed in order to demonstrate the capability of the slim-edged 3D pixel FE-I4 devices from the IBL sensor generation to cope with the requirements for their use in the AFP detector, as listed in Sec. 3.2.

3.6.1. Test-Beam Facilities and Set-up

Test-beam facilities are widely used across different instrumentation fields, e.g. calorimetry, timing, tracking, etc. In these facilities, particle beams are used to study various performance aspects of the detector.

Facilities

In order to study the detectors that compose AFP, their performance was studied in several test-beam campaigns. The following results are based on test-beams from two main facilities:

- **DESY** (Deutsches Elektronen Synchrotron) at Hamburg, Germany, provides electrons of adjustable energy of ∼1-6 GeV. At these electron energies care has to be taken to minimise multiple scattering effects.
- **CERN SPS** (CERN Super Proton Synchrotron) provides 120 GeV (charged) pion beams, which makes it easier to perform measurements that require precise position resolutions and for setups with large material budgets.

Set-up(s)

Regardless of the test-beam facility, the general set-up is similar: the devices under test are placed in a beam telescope, which is used to reconstruct the track of particles passing through in order to interpolate the position of the particle into the devices under test and thus determine properties like efficiency and resolutions.

The beam telescopes used in most of the test-beams are the copies of the EUDET [108] telescope. It consists of a total of six MIMOSA26 [109] tracker planes and a set of scintillators that generate the trigger signal for the whole telescope. The active region of the scintillators cover the area of the MIMOSA detectors and are connected as an input to a Trigger Logic Unit (TLU) [108]. The TLU is used to distribute the trigger signals across the read-out systems in the set-up and is controlled through a National Instruments (NI) crate. Another possibility is to use the HitOr signal of an FE-I4 as a trigger signal, giving the possibility of a region-of-interest trigger as pixels contributing to the HitOr signal can be masked out. However, this option is not commonly used in the results shown in this thesis.

The MIMOSA detectors are monolithic CMOS pixel sensors, with a size of 13.7×21.5 mm^2, divided into 576×1152 pixels of 18.5 μm pitch, allowing, in some cases, a pointing position resolution of $\sim$3 μm [108]. The read-out time for each MIMOSA device is performed by a rolling shutter, taking 16 cycles of 80 MHz per row (columns are read out in parallel) resulting in an integration time of 115.2 μs. Data from the MIMOSA devices are sent to the NI crate, which operates and acquires data for the sensors.

The devices under test, in this case FE-I4 devices, are installed in the middle of the telescope and connected to their respective DAQ systems, usually USBPix or RCE (see Sec. 3.4).

The data acquisition is configured and controlled by a computer which runs the EUDAQ [110] software, a generic data acquisition system software to which all the hardware (TLU, MIMOSAs and FE-I4 readout systems) are integrated. From EUDAQ data taking can be started and stopped. The output format is compatible with the reconstruction software EUTelescope [111].

In some test-beams a different set-up is used: a custom made FE-I4-based telescope. In this case the track reconstruction is done with FE-I4 modules. The HitOr signal from the telescope planes can be used as an input to the RCE for the trigger signal by using a dedicated electronic board to apply a trigger logic. Since the DUTs are usually FE-I4 devices too, only one read-out system is needed, the RCE, which makes the set-up significantly simpler and portable. The RCE CosmicGui software has the option to take data from all the devices in an event-by-event basis as in the case of the EUDET telescopes, which allows for track reconstruction. The data output format is a ROOT [112] file, which is compatible with a second beam telescope reconstruction software framework called Judith [113].

3.6.2. Test-Beam Track Reconstruction

From the position measurements obtained by the detectors forming the telescope, the track of the particle is reconstructed with the goal of interpolating the position of the detected

particle to the devices under test, which are compared with the data obtained from the latter in the same event. These tracks serve as reference measurements for e.g. efficiency and position resolution determination.

As stated previously, the track reconstruction can be performed with two different software packages: EUTelescope compatible with the EUDET telescopes output format, and Judith for data obtained by FE-I4 telescopes. The complexity and data formats differ between the two solutions, however, the reconstruction steps are similar.

The first step in track reconstruction consists of noisy pixel masking based on the average of the pixel occupancies. Afterwards hit clustering in all the planes is performed. The clustering algorithm simply consists in grouping hits at a certain distance from each other, then for each cluster a *cluster centre* is defined. The cluster centre in Judith is usually calculated by a centre-of-gravity average using the charge information as weights, while in EUtelescope the geometrical average is taken.

The next step is the alignment, which is done in two stages, the coarse and the fine alignments. In Judith, the *coarse alignment* is cluster-based (i.e. no track reconstruction is performed). The differences in cluster positions between consecutive planes are calculated. From these distributions the offset between each pair of planes is determined. The position of each plane is then corrected with these offsets. Similarly, in EUtelescope the position correlations between planes are used to obtain a first estimation of the misalignment.

The *fine alignment* stage, on the other hand, performs a track reconstruction based on the clusters of all the planes except the plane to be aligned. In Judith, these tracks are interpolated to the plane that is being aligned and the position difference between the tracks and the clusters are measured to obtain the residuals. The offset from zero of the residual distribution is a measurement of the misalignment that needs to be corrected. Rotations can be determined up to some extent by measuring correlations between track position and residuals from different axis. This process is repeated for all the planes recursively, as misalignment in the reference planes affect the accuracy of track reconstruction. When the telescope planes are aligned, the devices under test undergo an alignment process similar to that for the reference devices using tracks reconstructed by the later ones to measure residuals in the DUTs. EUtelescope, on the other hand, uses the *Millepede II* package [114] which performs a least squares fit using the output of a track reconstruction via a *Kalman filter* [115]. It performs the alignment of all the planes, including the DUTs.

Once all planes are aligned the final tracks are reconstructed using only the telescope planes. Track reconstruction in Judith is performed by a straight line fit (also during the alignment step), which for test-beams with low multiple scattering (as at CERN SPS) is accurate enough. Kalman filter is utilized by EUtelescope in the last track reconstruction, which accounts for multiple scattering. The output is a collection of hits, clusters and tracks associated to each event and their position in a common reference system for all the tracking planes.

After track reconstruction, the analysis can be performed in either Judith or the TBMon framework [116], where efficiencies and position resolutions can be obtained (see next sections).

3.6.3. Test-Beam Campaigns

Table 3.3 compiles all the test-beam campaigns of AFP-related test-beams until 2016. A summary of the results obtained in the test-beams up to May 2016 will be presented in the following sections.

Table 3.3.: List of AFP-related test-beam campaigns up to 2016. Only results from data obtained in test-beams up to May 2016 are presented in this thesis, as later test-beams were focused on Time-of-Flight detector studies only.

Test-beam	Facility	Measurement
August 2012	CERN	Non-uniform irradiation efficiencies
October 2012	CERN	FE-I3 slim-edge (not successful)
June 2013	DESY	Slim-edge efficiency
July 2013	DESY	Non-uniform irradiation efficiencies, FBK with Al mask
January 2014	DESY	Non-uniform irradiation efficiencies, CNM with Al mask
October 2014	CERN	Non-uniform irradiation efficiencies different settings and slim-edge efficiency extension
November 2014	CERN	Integration test-beam (tracking, Time-of-Flight, read-out)
September 2015	CERN	Integration test-beam (tracking, Time-of-Flight, read-out)
April-May 2016	CERN	AFP tracker studies

3.6.4. Hit Reconstruction Efficiency (after Non-Uniform Irradiation)

To study the effect of the non-uniform radiation damage on the FE-I4 3D pixel modules, devices were irradiated with a non-uniform beam profile up to fluences $\sim 4\times10^{15}$ n_{eq}/cm^2. The performance of those devices are measured then in test-beams.

Hit Reconstruction Efficiency

The hit efficiency is defined as the fraction of impinging particles that are detected by the device.

The efficiency is determined as follows. Tracks are reconstructed using the telescope planes and are interpolated into the device under test (see Sec. 3.6.2). For each event, the neighbouring hits read by the DUT are grouped in clusters and for each of these, a centre is calculated. This cluster centre represents the DUT estimation of the track position, and by default is calculated by charge weighted averaging the hit positions inside the cluster. The position of the track interpolated into the device under test is compared to the position of all the cluster centres in the DUT. If there is a cluster centre around a track position inside a *matching window* (typically 150×400 μm^2 along the short and long pixel direction respectively) the track is associated to a DUT cluster. The efficiency is the number of tracks associated to a cluster in the DUT divided by the total number of tracks that are extrapolated inside the DUT..

Efficiency in Non-Irradiated Devices

Non-irradiated 3D pixel devices were tested in a test-beam at CERN SPS using a custom made FE-I4 telescope [117]. The devices in this study, CNM and FBK FE-I4 detectors, were left-overs from the IBL module production, and thus they were not of the best quality. The hit efficiency was measured at perpendicular incidence and at 14° angle along the short pixel direction. The 14° angle inclination was used for the final AFP design. The threshold was set to 2000 e^- and a calibration of 10 ToT response at 20,000 ke^- charge collected was selected. Results are shown in Fig. 3.26.

The devices reach, at very low voltages, an efficiency plateau of 97–98%, reasonable for IBL-spare quality devices. The CNM device, at perpendicular incidence, reaches an efficiency plateau at 4 V while for the FBK one only $\lesssim$1 V is needed. The difference is due to the non-passing-through 3D columns in the CNM device, which needs a slightly higher voltage to reach full lateral depletion. With a 14° tilt, both devices show a >99.9%

efficiency already at 1 V. This is a well-known effect of 3D devices, which at perpendicular incidence show localised inefficiency regions due to the presence of the inactive electrode columns and some low field regions in between, which can be palliated by introducing a tilt. These results are compatible with the ones obtained in the IBL pre-production test-beam studies [96].

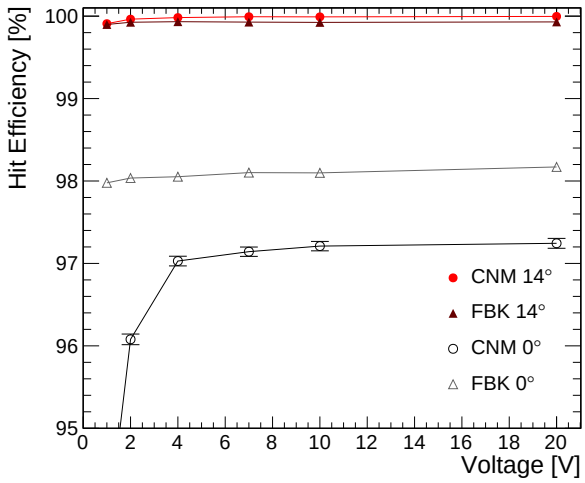

Figure 3.26.: Hit efficiency as a function of bias voltage for non-irradiated CNM and FBK 3D FE-I4 devices, at perpendicular incidence (0°) and with a 14° angle along the short pixel direction (50 μm).

Irradiation Campaigns

Irradiation campaigns were carried out in two different facilities at different degrees of non-uniformities:

- At CERN-PS, with a 23 GeV proton beam focussed with 12×12 mm^2 FWHM with maximum fluences of 4.0 and 9.4×10^{15} n$_{eq}$/cm^2. The distribution of the fluence over the sensor irradiated up to 4.0×10^{15} n$_{eq}$/cm^2 is shown in Fig. 3.27(top-left). The spread is relatively large compared with the expected beam profile in the AFP detector.

  Device CNM-83 showed a low breakdown voltage before irradiation and still was irradiated at a very large peak fluence (9.4 10^{15} n$_{eq}$/cm^2), hence it was not possible to operate the device at high enough bias voltages to overcome radiation damage. Moreover, the fluence in this device is much higher than for the other planes and the one expected for AFP. Therefore, results obtained with CNM-83 are not presented hereafter.

- At KIT[8], with 23 MeV protons. In this case, to achieve the non-uniformity the devices were irradiated covered with a 5 mm thick aluminium mask with a hole so that the particles could reach the sensors only through the hole, either a 3 mm diameter circular hole or a slit with 4 mm width and 12 mm length over the sensor (see Fig. 3.27(top-centre and top-right)). The irradiation fluences ranged from 1.8 to 3.6×10^{15} n$_{eq}$/cm^2.

[8]Karlsruhe Institute of Technology, Germany

Table 3.4 shows a list of the devices under test which were irradiated non-uniformly during these campaigns.

Table 3.4.: List of irradiated devices under test for the non-uniform irradiation study test-beam campaigns.

Device Name	Irrad. Facility	Non-uniform irradiation method	Fluence peak [10^{15} n_{eq}/cm^2]
CNM-57	CERN-PS	Focused beam (12×12 mm^2 FWHM)	4.0 (max)
CNM-83	CERN-PS	Focused beam (12×12 mm^2 FWHM)	9.4 (max)
FBK-12-02-08	KIT	Aluminium mask with circular hole	1.8
CNM-S5-R7	KIT	Aluminium mask with slit	3.3
CNM-S3-R5	KIT	Aluminium mask with slit	3.6

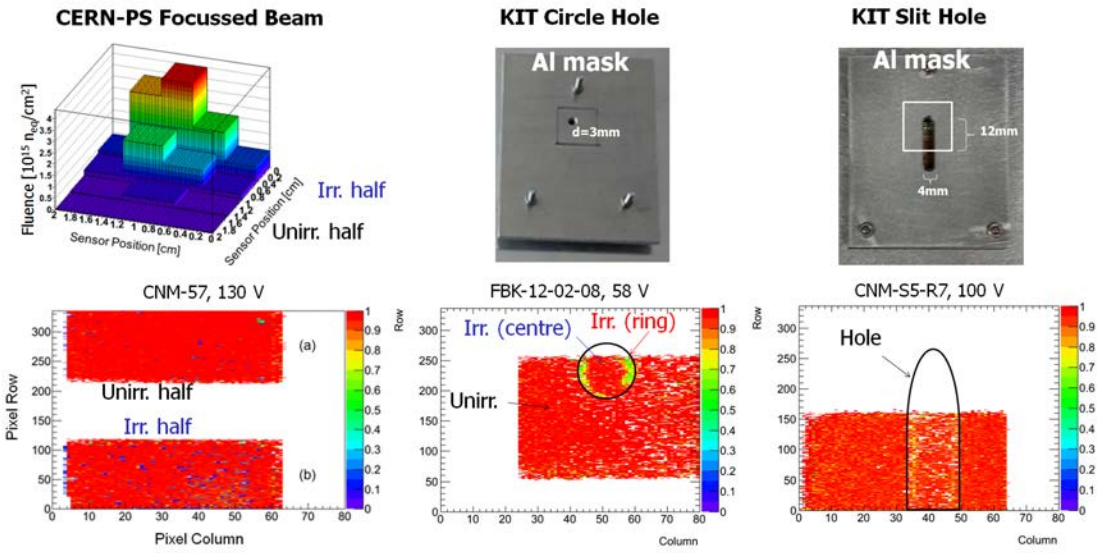

Figure 3.27.: Hit efficiency map measured after non-uniform irradiation at CERN PS with a focused beam (fluence profile shown above) and at KIT with an aluminium shield with a hole.

Efficiency in (non-uniformly) Irradiated Devices

Efficiency maps for the different irradiation campaign configurations are shown in Fig. 3.27 (bottom). Note that since the telescope planes and trigger scintillators are about 2×1 cm^2, the surface of the full detectors could not be covered in a single configuration, hence the white spaces in the efficiency maps correspond to the regions not covered by the telescope. The efficiency map from the CERN-PS irradiated device includes two sets of measurements.

Three different regions can be observed in the devices irradiated with the aluminium mask at KIT: The non-irradiated region covered by the mask (Unirr.) which shows a very high efficiency, the centre of the hole that was irradiated at the target fluence (Irr. centre) with a similarly high efficiency, and a region coinciding with the boundaries of the mask hole (Irr. ring) with a lower efficiency.

The efficiency over these regions as a function of the bias voltage are shown in Fig. 3.28. It shows how a high efficiency is recovered in the centre of the irradiated regions with

sufficiently high bias voltage. Note that the devices under test are leftovers from the IBL sensor production so the breakdown voltages after irradiation are not optimal, and thus the efficiency measurements for different voltages stop at relatively low voltages for such level of irradiation in 3D FE-I4 devices. This is the case for device CNM-S5-R7, which reached 96% in the irradiated region at a highest measured voltage of 90 V. The devices FBK-12-02-08 (with a lower nominal fluence) and CNM-57 (measured at higher voltages) showed an efficiency of at least 97% in that region.

The device CNM-S3-R5 in Fig. 3.28 shows a lower efficiency than expected from other measurements, even in the non-irradiated region. It was found that the reason of this degradation of efficiency is the non-optimal parameters of data taking with this device: the ToT was not calibrated, featuring a broad distribution with a peak at ∼8 ToT at a charge collection of 20,000 electrons, compared to the 10 ToT for the same reference charge in the other devices. The low and broad ToT distribution, combined with the removal of events with only low ToT (<2) hits due to the HitDiscConfig=2 (see Sec. 3.3.1)register in the chip set in this device reduced the total hit reconstruction efficiency of CNM-S3-R5. This effect is more important in the irradiated regions, where charge collection is naturally reduced by radiation damage.

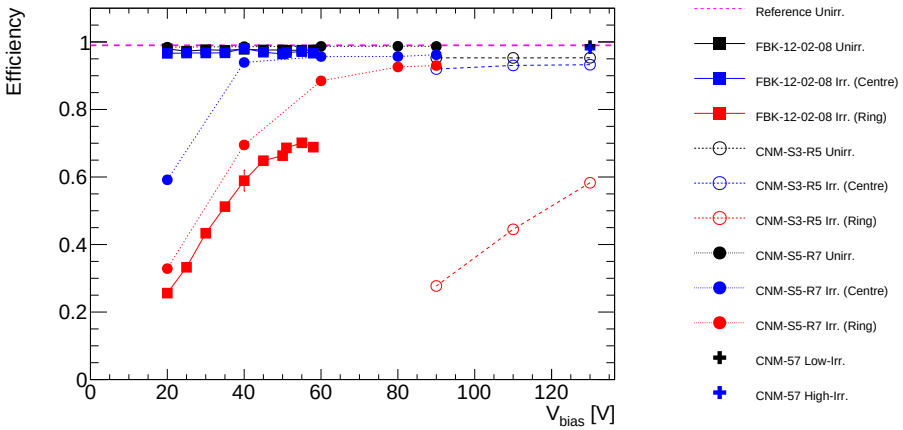

Figure 3.28.: Hit efficiency as a function of bias voltage for different DUTs after non-uniform irradiation for different regions (non-irradiated, irradiated centre and irradiated ring). Note that device CNM-S3-R5 was measured with non-optimal parameters (see text). The hit efficiency of a reference non-irradiated sensor is also shown as a dashed line.

The position resolution of the CERN beam tests (which relies on high energy pions and the high resolution EUDET telescope) is enough to be able to resolve the structure inside a single pixel. It is interesting to see the evolution of such efficiency over the three irradiation regions from the devices irradiated with the Al mask. This can be seen in Fig. 3.29, where the efficiency in 5×2 pixels around the transition between the non-irradiated (Fig. 3.29 left), "irradiated ring" (Fig. 3.29 centre) and "irradiated centre" (Fig. 3.29 right) region is shown with sub-pixel resolution, for two voltages (40 and 80 V). The left-most region of these plots show the usual behaviour of a non-irradiated CNM 3D device, i.e. high efficiency in most of the pixel region with a drop in efficiency around the columns where the active volume (between the end of the column and the end of the silicon bulk) is smaller. One can notice that, in the irradiated regions, the lowest efficiency is localised at the position furthest away from the n^+- and p^+-columns: there, the sensor exhibits the minimum electric field and charge carriers generated at these distances from the electrodes have a larger probability of being trapped. This effect is enhanced in the transition between

the non-irradiated region and the "irradiated centre" region. Inside the "irradiated centre" region most of the efficiency is recovered for the highest voltage.

The low efficiency region could be caused by a larger radiation damage from low energy scattered protons at the edge of the Al slit holes, a real sensor effect from the abrupt transition between the irradiated and non-irradiated region or an effect of the readout chip. Nevertheless, the gradient in the fluence distribution expected for AFP is much smaller than in the irradiated devices studied here. Therefore, this effect is not expected to be observed in the real operation of the AFP detector.

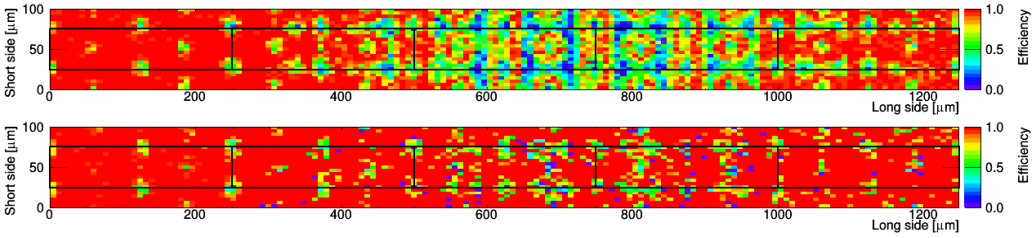

Figure 3.29.: Efficiency in 5×2 pixels around the transition region between non-irradiated, irradiated ring and irradiated centre on a device irradiated at KIT with 5 mm thick aluminium shield with a slit hole (CNM-S5-R7). The bias voltage was 40 V (top) and 80 V (bottom) with lower statistics. Superimposed in black lines are the central pixel limits (for clarity).

Conclusions

The radiation hardness of 3D sensors under non-uniform irradiation was studied in several test-beam campaigns, with irradiations up to fluences expected for the standard luminosity AFP scenario. Irradiation campaigns were carried out at CERN-PS with a focused beam and at Karlsruhe with an Al mask with a hole to achieve a fluence gradient. High hit efficiencies at perpendicular beam incidence were observed (for favourable chip-parameter settings), of at least 97% in both irradiated and non-irradiated areas of the sensor. Note that the efficiency for CNM-S5-R7 of 96% was measured at a relatively low bias voltages for such level of irradiation due to the low breakdown voltage of the device (IBL-spare quality class). Good quality devices with higher breakdown voltages would achieve efficiencies of >97%, fulfilling the requirements for the AFP tracker (see Sec. 3.2). A small region of lower efficiency was observed around the area under the Al shield hole used in the irradiation at Karlsruhe. However, the gradient in the fluence distribution will not be as abrupt as the one obtained with the Al mask at KIT. Furthermore, this effect might be due to an issue that is unrelated to the pixel detector (namely scattering of particles at the Al edges).

3.6.5. Slim-Edge Efficiency Test-Beam Studies

Another goal of these test-beam studies is to characterize the behaviour of the edges of the 3D FE-I4 devices after slim-edging. Since the IBL devices were diced to achieve a slim-edge for AFP at the side closest to the beam, it is critical to verify that the efficiency in this region is not degraded after the procedure and to know the exact extension of the active region.

Devices Under Test

The list of all the devices under test measured in the slim-edge test-beam campaigns are shown in Table 3.5. Devices with both CNM and FBK design were measured, as well

as slim-edged and non-slim-edged sensors. The dead area was reduced using a standard diamond saw in the opposite side of the wire-bonds, which is the region of interest for AFP, although both sides (wire-bond/opposite to wire-bond sides) were measured for some of the devices. Moreover, edge efficiencies of irradiated FBK devices were measured, which were irradiated at two different fluences (2 and 5×10^{15} n_{eq}/cm^2) and annealed for 120 min at 60°C. Table 3.5 also shows the maximum measured voltage, often limited by the breakdown voltage of the sensor.

Table 3.5.: Efficiency extension, sensitivity beyond the last instrumented pixel and remaining insensitive edge of the devices under test. All values refer to the maximum measured voltage.

		Sample	Edge side	Irradiation [n_{eq}/cm^2]	Max. voltage	Edge exten. after cut	Sensitivity extension	Remaining inactive edge
Slim-edged	AFP prototypes	FBK-S1-R9	Non-wb	0	20 V	91 μm	77 μm	14 μm
			Wb	0	20 V	-	107 μm	-
		FBK-S2-R10	Non-wb	0	30 V	87 μm	75 μm	12 μm
			Wb	0	30 V	-	117 μm	-
		CNM-S3-R5	Non-wb	0	30 V	215 μm	1 μm	214 μm
		CNM-S5-R7	Non-wb	0	30 V	150 μm	7 μm	143 μm
Not	slim-edged	FBK-9	Wb	2×10^{15}	100 V	-	59 μm	-
		FBK-11	Wb	5×10^{15}	200 V	-	90 μm	-
		FBK13	Non-wb	0	30 V	-	107 μm	-
			Wb	0	30 V	-	119 μm	-

Results

The projection of the efficiency around the last instrumented pixel for two slim-edged devices under test are shown in Fig. 3.30, for a CNM (top) and an FBK (bottom) sensor. Both modules were not irradiated and biased at 30 V (CNM) and 20 V (FBK). The physical cutting edge of the sensor is indicated as a red vertical line. An S-curve is fitted around the drop of the efficiency curve beyond the last pixel: the *sensitivity extension* is defined as the distance from the end of the edge pixel and the 50% point of the S-curve. Note that the smearing of the curve is caused by the telescope resolution, ∼12-15 μm, as this data was taken at DESY with a set-up that was not optimized to reduce multiple scattering effects.

It can be seen how in both cases the detectors are fully efficient up to the last pixel row, and the efficiency is even extended by 77 μm beyond in the FBK case. This difference in behaviour is a consequence of the difference in design between the two sensors (see Sec. 3.3.2): the 3D guard-ring present in the CNM design prevents the collection of charges beyond the instrumented area, while such constraint does not exist in the FBK sensors (no guard-ring), where also charge deposited in the extended depleted area beyond the last pixel row is collected.

A voltage dependence of the sensitive region was observed in the FBK sensors, as shown in Fig. 3.31 meaning that the charge collecting region after the last instrumented pixel grows with increasing voltage. At large enough voltages (∼20 V), the sensitivity extension reaches a plateau in the non-irradiated devices. Measurements of the uniformly irradiated and non-slim-edged devices (also in Fig. 3.31) show that the sensitivity extension is still present but reduced due to radiation-induced changes in the depletion zone and trapping of the charge carriers, especially at low voltages.

The edge efficiency was also measured at the edge opposite to the slim-edged side, as well as in detectors that were not slim-edged (FBK-13): it has been observed that the sensitivity extension grows significantly larger than at the slim-edged side. This effect might be caused

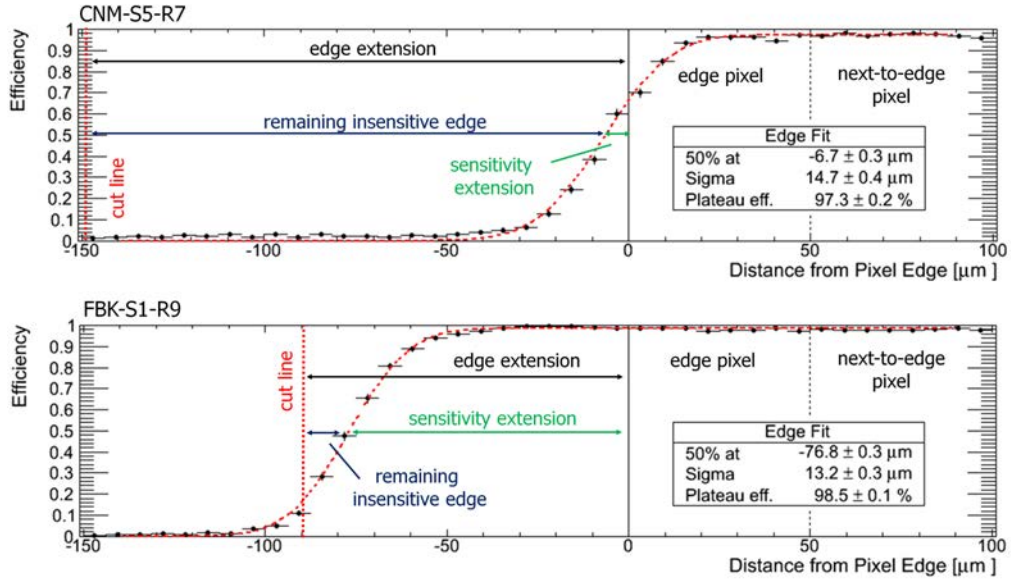

Figure 3.30.: Efficiency around the last pixel row for an un-irradiated and slim-edged CNM sensor at 30 V (top) and FBK sensor at 20 V (bottom) measured at DESY. The smearing of the curve is caused by the telescope resolution (∼12-15 μm)

by cut-induced defects at the slim-edged side. For a better understanding, simulations are needed in the future to complement the measurements.

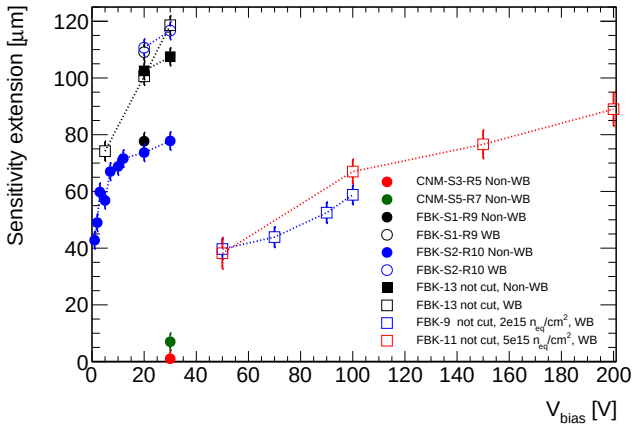

Figure 3.31.: Sensitivity extension beyond the last pixel as a function of voltage. Sensors FBK-9, 11 and 13 were not slim-edged. Circle and square markers correspond to measurements in slim-edged and not slim-edged devices respectively. Empty markers are measurements in the wire-bond side of the sensor and full markers are measurements on the opposite side from the wire-bond pads (i.e. the AFP edge).

Conclusions

Table 3.5 shows a summary with the results obtained from the edge efficiency studies (for the maximum measured voltages). In conclusion, the sensitivity extension in CNM devices is prevented by the presence of a guard-ring which translates in a well defined active region

termination, while the FBK design is able to collect charge from 60-90 μm from the last pixel row even after irradiation. In particular, it was possible to obtain slim edges of inactive regions of 12-14 μm after edge dicing in FBK devices. On the other hand, the extension of the sensitive region can affect the position resolution in the last pixel row, which is the most crucial region in AFP. CNM design fulfils the slim edge requirements of AFP, with an inactive area of 143-214 μm (see Sec. 3.2).

3.6.6. Position Resolution

The AFP tracker detectors are required to have a position resolution of $\sim$10$\times$30 μm^2 per station (i.e. four planes), which is crucial for the reconstruction of ξ with good resolution. The FE-I4 devices feature pixels with size 50$\times$250 μm^2 which implies a digital resolution of 14$\times$72 μm^2, i.e. $pitch/\sqrt{12}$ in the case of only one-hit clusters. In cases where two neighbouring pixels register a hit, it is possible to interpolate the position of the particle between them improving the resolution, especially if charge (or ToT) information is available and allows for a weighted average. In order to benefit from the improvement in position resolution by pixel interpolation, the design foresees that the planes are at a 14° angle to increase the number of events with 2-pixel clusters along the short pixel direction.

The two considered scenarios are sketched in Fig. 3.32, which shows a cross section of an FE-I4 at perpendicular incidence and tilted by 14°.

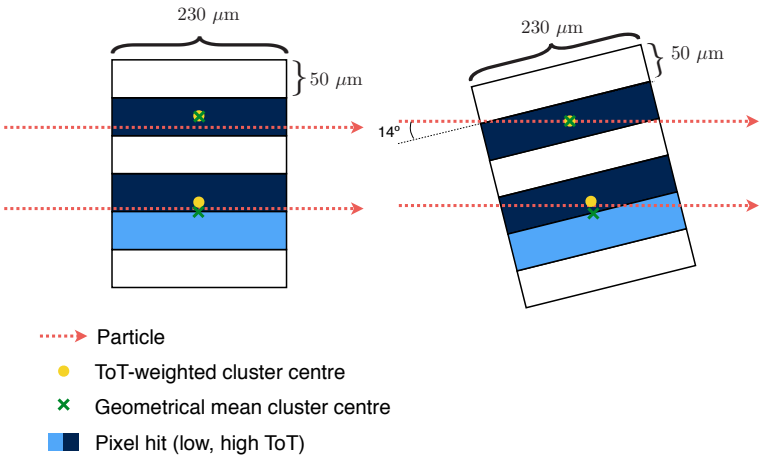

Figure 3.32.: Cross section sketch of the particle detection of an FE-I4 at perpendicular beam incidence (left) and tilted by 14°. The cluster centre measured by the geometrical mean and the ToT-weighted algorithm are indicated. Charge sharing at 0° occurs only when the particle traverses a pixel very close to the neighbouring pixel, while at 14°, the charge sharing scenario is enhanced by geometry, increasing the accuracy of single-plane track position estimation.

Position resolution at 0°

This study was performed with the ACONITE telescope which is similar to the EUDET [108] telescope (see Sec. 3.6.1). In scenarios where multiple scattering is low, as at CERN SPS, the telescope provides 4$\pm$1 μm pointing resolution with the set-up geometry with which the data was taken [108, 118].

Fig. 3.33 shows the one-dimensional cluster size distribution of a CNM 3D FE-I4 device placed perpendicular with respect to the CERN SPS 120 GeV pion beam. The distributions along both directions sharply peak at 1 pixel, which is to be expected due to the geometry of the set-up. The fraction of clusters with a size of two pixels in the short (long) pixel direction is 18.5% (2.2%). This difference is explained by sharing among neighbouring pixels charge produced near the boundaries of one pixel, also called *charge sharing*. Since the long pixel direction is 5 times longer than the short one, charge sharing is much more unlikely to happen between neighbouring pixels along that direction. Clusters with larger sizes represent 1.8% and 0.1% of the detected particles along the short and long pixel direction respectively. The source of clusters longer than two is likely to be delta-electrons in the case of perpendicular beam incidence.

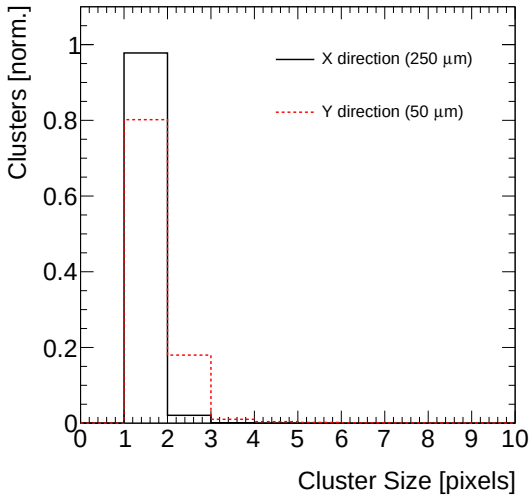

Figure 3.33.: Cluster size distribution of a CNM device from data taken during a test-beam at CERN SPS, with the plane placed at 0° (i.e. perpendicular to the beam). The red distribution shows the cluster size distribution along the long (250 μm) pixel direction while the blue histogram shows the same for the short (50 μm) pixel direction. The area of both distributions are normalized to unity.

The residual distributions of this device are shown in Fig. 3.34. The residual is defined as the distance between the track position interpolated to the DUT and the matched cluster-centre measured by the DUT. The width of the residual distributions ($RMS_{track-DUT}$, the root mean squared of the residual distribution) are a measurement of the plane resolution, entangled with the telescope pointing resolution, which in this set-up is $\sigma_{track} = 4 \pm 1$ μm.

Several algorithms to obtain the cluster-centre position were investigated. Fig. 3.34 (top) uses the *geometrical mean* of the hit positions inside the cluster while Fig. 3.34 (bottom) uses a *ToT-weighting* algorithm, which consists in a weighted average of the hit positions forming the cluster, using the charge information obtained by the 4-bit Time-over-Threshold featured in the FE-I4 chip as weights.

One-hit cluster residuals show a uniform distribution compatible with the digital resolution, although the observed resolutions are smaller than $pitch/\sqrt{12}$. This is a consequence of charge sharing: when tracks reach positions near the boundaries of the pixel, it is more likely to have charge sharing which effectively reduces the pixel area in which one-hit clusters can occur, and is not affected by the used clustering algorithm. The one-hit residual distribution along the long pixel direction shows a deep in the central region, which is caused by a slightly lower efficiency in the centre of the pixel, coinciding with the central

p-columns which delimit the pixel.

Clusters with two hits, on the other hand, show a narrower distribution in the short pixel direction. In a normal incidence configuration the charge sharing region is close to the neighbouring pixels. The geometrical mean algorithm, in two-hit clusters will determine the centre exactly between the two neighbouring pixels, which is a good approximation (see Fig. 3.32). This is especially true in the case of two-hit clusters along the long pixel direction, which is the reason of the sharp peak observed in its residual distribution. ToT-weighted clustering algorithm in such cases performs a pixel interpolation between the neighbouring pixels, which yields results comparable to the geometrical mean in the short pixel direction, although the moderate ToT 4-bit resolution and the Landau charge deposition fluctuations could affect the position resolution. Larger clusters than two-hit pixels are usually produced by δ-electrons in the 0° configuration (a fraction of two-hit clusters in the long pixel direction are also produced by knock-on electrons), which introduces large tails in the residual distributions.

Position resolution at 14°

In order to maximize the position resolution and benefit from the charge information available in the FE-I4, a configuration with a 14° angle along the short pixel direction with respect to normal beam incidence was investigated, with the objective of increasing the events with two-hit clusters.

These position resolution studies were performed with a FE-I4 telescope. It consisted of five 3D FE-I4 modules out of which, for the following results, four planes were used for track reconstruction and the central plane was used as DUT. All planes were placed at 14° with respect to perpendicular incidence along the short pixel direction.

Since the four telescope planes and the DUT were 3D FE-I4 planes, the measurement of the telescope pointing resolution (σ_{track}) is entangled with the DUT single-plane resolution (σ_{SP}). Nevertheless, one can assume that all five planes have the same characteristics and performance and since multiple scattering with 120 GeV pions has negligible impact in the total 4-plane telescope resolution, it is safe to estimate the pointing resolution as $\sigma_{track} = \frac{\sigma_{SP}}{\sqrt{N}}$, where $N = 4$ is the number of planes used for track reconstruction.

One-dimensional cluster size distributions for the device under test are shown in Fig. 3.35 at 14° and 0°. Results at normal incidence are compatible with the ones obtained in the previous studies. In the tilted configuration, the cluster size distribution along the short pixel direction is now peaked at 2 as expected from the geometry of the set-up.

As the pointing resolution of the telescope in this set-up along the long pixel direction was poor, and the geometry on that axis is equivalent to the normal incidence studies described in the previous section, position resolutions in the long pixel direction were not studied.

The residual distributions in the short pixel direction of the DUT using the ToT-weighted algorithm are shown in Fig. 3.36 (left). In this case, for cluster sizes $\leq$2 it is possible to fit a Gaussian distribution, the width of which is quoted in the figure ($\sigma_{track-DUT}$). As opposed to the results obtained in the previous studies (0°), the residual widths for cluster sizes $\leq$2 along the short pixel direction are lower than 10 μm. One-hit clusters are mainly produced by tracks traversing a region near the middle of the pixel, and thus, as the track position is estimated at the centre of the pixel for single-hit events, the prediction is accurate and produces a good position resolution (see Fig. 3.32).

In this case, the most probable cluster size is 2 (~80% of the events). The ToT-weighted clustering algorithm, thanks to its inter-pixel interpolation, greatly improves the position resolution over the normal incidence configuration, since now the range covered by two-hit clusters is greater, which allows to reach residual widths of 6–7 μm. On the other hand,

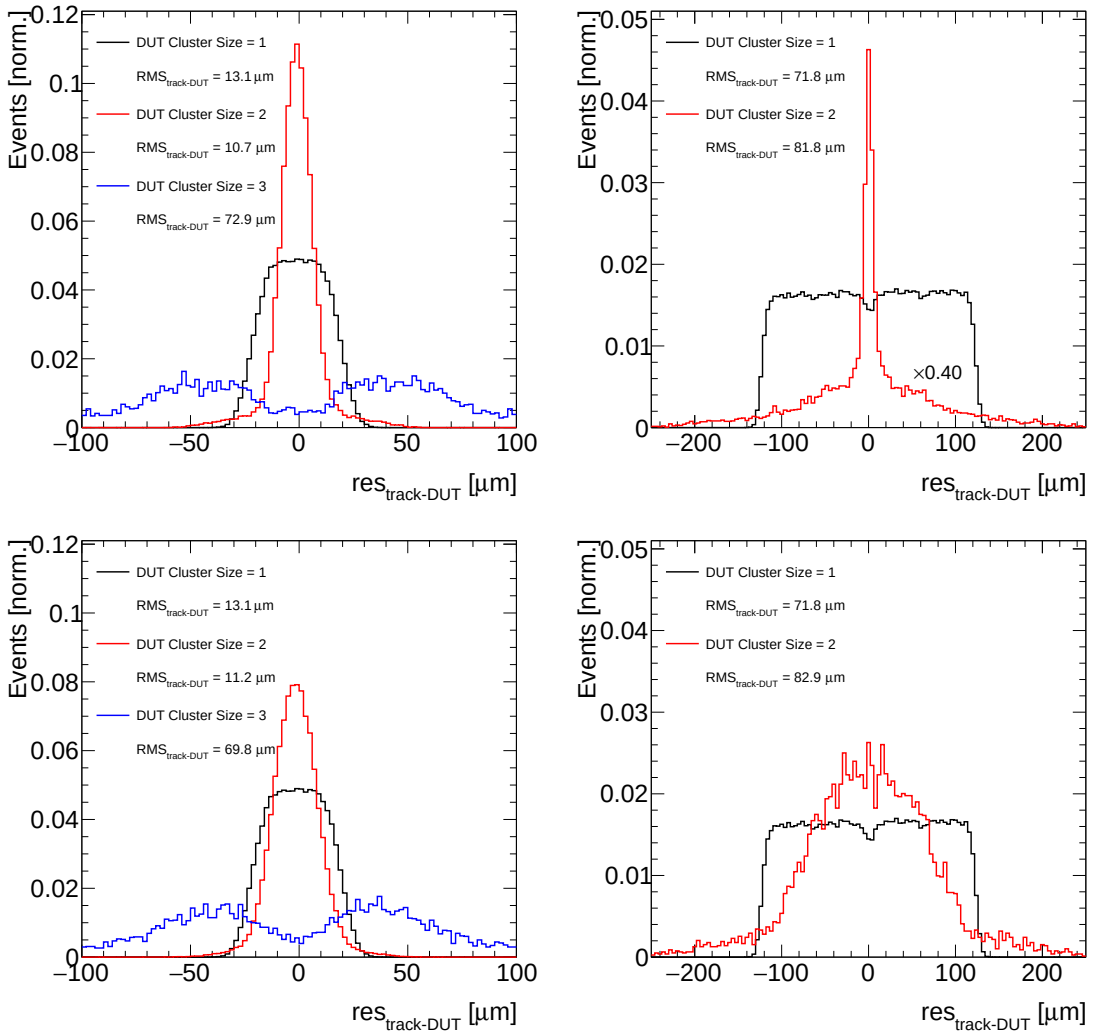

Figure 3.34.: Residual distribution of a CNM device along the short (left) and long (right) pixel direction and different cluster sizes from data taken during a test-beam at CERN SPS, with the plane placed at 0° (i.e. perpendicular to the beam). Geometrical mean (top) and ToT-weighting (bottom) algorithms were used to determine the cluster-centre positions. The area of all distributions are normalized to unity. The histogram corresponding to the geometrical mean residual for cluster size 2 events along the long pixel direction (top-left) is scaled by 0.40.

the geometrical mean algorithm, as it always assumes the particle position in between the two pixels, does not benefit from increasing the frequency of two-hit cluster events.

For larger clusters, as they are produced by knock-on electrons the resolution is degraded. However, given that the frequency of >2-hit clusters is so low, it can be considered to reject such events from a track reconstruction without losing much efficiency.

Fig. 3.36 (right), shows the residual distribution for all clusters and for cluster sizes $\leq$2. From these distributions one can determine a single-plane resolution, which can be obtained by quadratically subtracting the telescope pointing resolution to the width of the residual distributions:

$$\sigma_{SP} = \sqrt{\sigma^2_{track-DUT} - \sigma^2_{track}}. \tag{3.24}$$

where $\sigma_{track-DUT}$ is the width obtained from a Gaussian fit and σ_{track} is the telescope

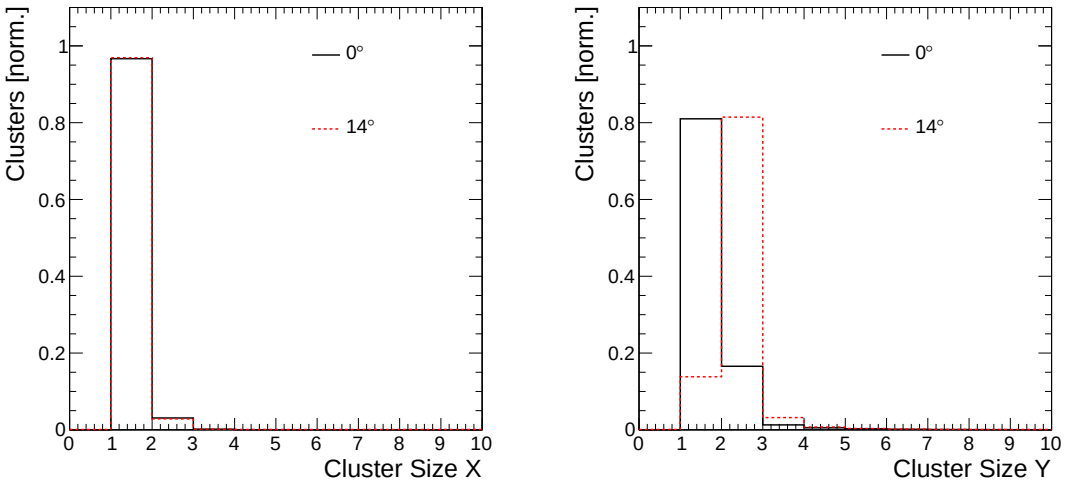

Figure 3.35.: Cluster size distribution of a CNM device from data taken during a test-beam at CERN SPS, with the plane placed at 0° (i.e. perpendicular to the beam) and 14°. The left distribution shows the cluster size distribution along the long (X, 250 μm) pixel direction while the right histogram shows the same for the short (Y, 50 μm) pixel direction. The area of all distributions are normalized to unity.

pointing resolution.

From the distributions in Fig. 3.36 (right), the width of the distribution for cluster sizes $\leq$2 is found to be $\sigma_{track-DUT} = 6.5 \pm 0.6$ μm which translates to a single-plane resolution (assuming the resolution of the four-plane system to be half of the single plane) of $\sigma_{SP} = 5.8 \pm 0.5$ μm and $\sigma_{track} = 2.9 \pm 0.5$ μm.

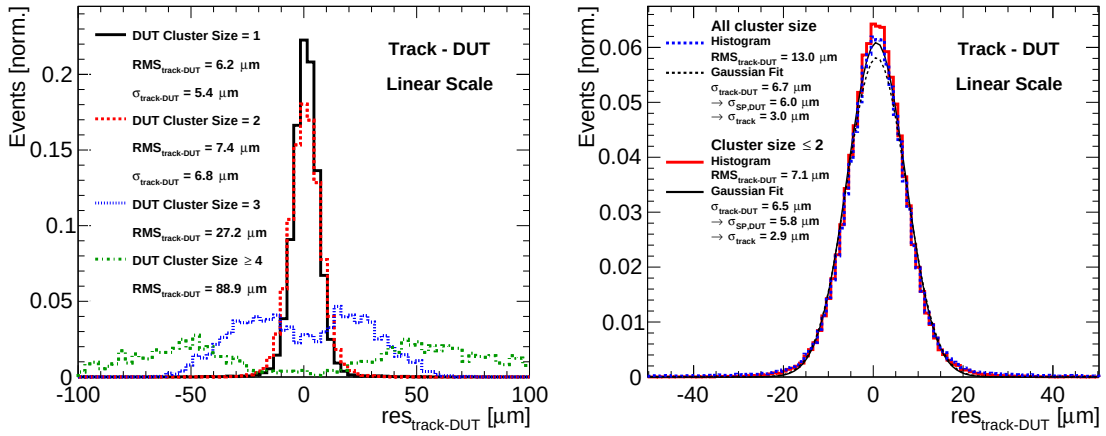

Figure 3.36.: Residual distribution of a CNM device along the short pixel direction and different cluster sizes (left) and for all cluster sizes (right) from data taken during a test-beam at CERN SPS, with the plane placed at 14° (i.e. perpendicular to the beam). The area of all distributions are normalized to unity.

Conclusions

The position resolution was studied for 3D FE-I4 devices. In the short pixel direction, a single plane position resolution of 6 μm in a 14° angle with respect to the normal

incidence was obtained. This result, half of the one expected from the digital resolution, is a consequence of the maximization of charge sharing events and the use of centre-of-gravity cluster centre calculation using the FE-I4 ToT hit information. In a four plane tracker, the expected pointing resolution is therefore 3 μm (i.e. $1/\sqrt{N_{planes}}$), which surpasses the requirements set for the AFP detector (see Sec. 3.2).

The long pixel direction, on the other hand, shows a single plane resolution compatible with $pitch/\sqrt{12}$, 72 μm, regardless of the clustering algorithm. However, the full four-plane tracker pointing resolution in this direction can be improved, over the single plane resolution, by staggering all the planes by 1/4 the pixel pitch, which in the ideal case, improves the resolution up to 1/4 of the binary resolution, i.e. 18 μm.

3.7. Tracker Characterization Conclusions

The 3D technology has proven to reach the performance requirements for the AFP detector. These results show that the AFP modules, as described in Sec. 3.3 are radiation hard enough to sustain the harsh environment expected during AFP operation. Moreover, the FE-I4 CNM 3D detectors have shown an excellent position resolution and the possibility to slim-edge those devices without a significant effect in their performance. Although the FBK 3D sensors also fulfilled AFP requirements in terms of radiation hardness, slim-edges and position resolution, the vendor was not available to produce modules for the AFP installation and thus only CNM devices were installed.

3.8. Tracker and Time-of-Flight Read-Out Integration

Although the Time-of-Flight system is not the main focus of this thesis, the availability of the timing system in some test-beam campaigns allowed the study of the ToF sub-system performance within the full AFP detector set-up, i.e. in combination with the silicon tracker. The goal of such test-beams was to study the principle of operation of the combined AFP tracker and timing (ToF) systems.

The common read-out based on the RCE (see Sec. 3.4.2) was exercised, while combined measurements were carried out. For this, the set-up consisted in a ToF prototype detector, a set of three quartz bars coupled to silicon photo-multipliers (SiPM) by STMicroelectronics for timing reference and five FE-I4 3D silicon modules, four upstream and one just behind the ToF detector. Fig. 3.37 shows the set-up of the integration test-beam performed at the CERN SPS facility, with pions with an energy of 120 GeV.

The ToF prototype (see Fig. 3.37 and Fig. 3.38) consisted in up to eight L-shaped Quartz bars (LQbars), two of each grouped in a *train* [9], at the Cherenkov angle with respect to the pion beam. The radiator bars in this prototype were 3 mm thick (y-coordinate) in Train 1 and 5 mm in the other trains, and 6 mm wide along the beam direction (z-coordinate). The bars were optically isolated from train to train by a Mylar foil, which reflects all light leaving the radiator towards the neighbouring trains. The light-guides of the LQbars were placed in an aluminium structure for mechanical support, in which the bars from different trains are separated by a spacer. A mini-Planacon Micro-Channel Plate Photo-Multiplier (MCP-PMT) by Photonis was in contact with the light-guide end of the LQbars (without the use of optical grease), which detects the Cherenkov light from the quartz bars. The MCP-PMT channels were connected to pre-amplifiers.

The quartz bars and the SiPM used for timing reference were placed in movable stages: the active area of the detectors was 3×3 mm^2, not sufficient to cover the full ToF prototype,

[9] Note that this configuration contains half of the foreseen number of ToF channels in the final detector.

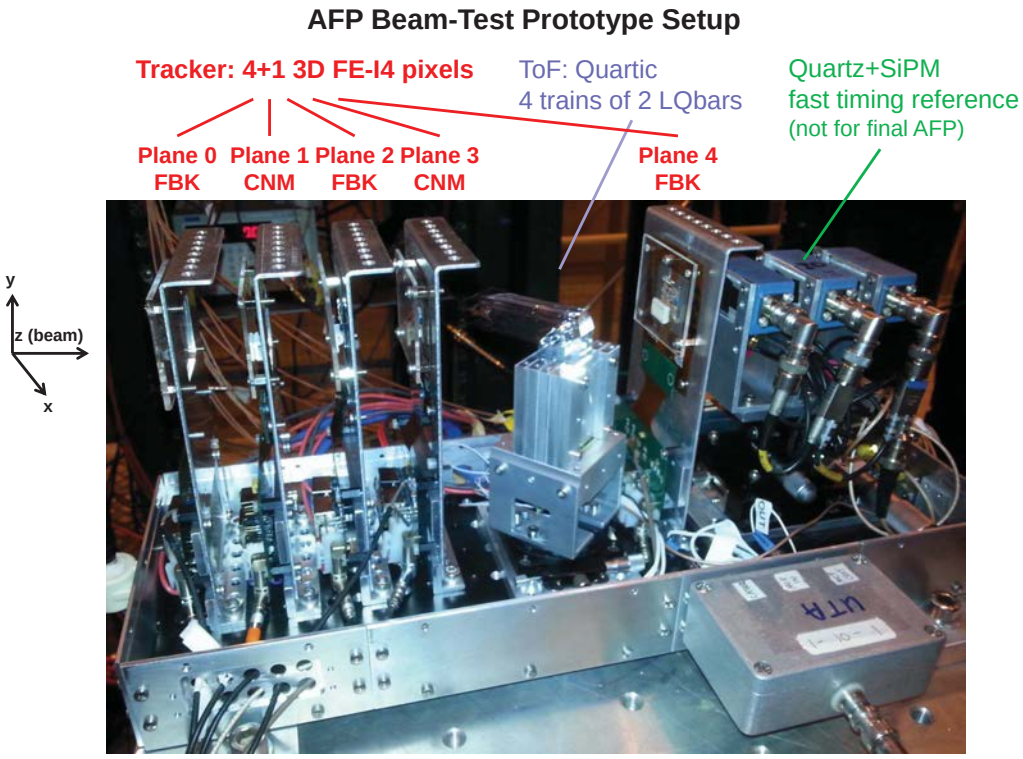

Figure 3.37.: Set-up for the tracker and Time-of-Flight integration test-beam.

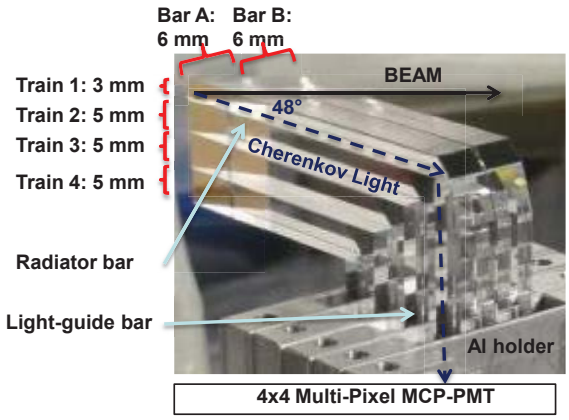

Figure 3.38.: The LQbar ToF prototype detector with four trains of two LQbars each (half of the final number of LQbars per train).

hence time resolution studies were performed for the two trains (1 and 2) with which there was an acceptance overlap.

The outputs of the SiPM and the pre-amplifiers were sent to a constant fraction discriminator (CFD) and from there to a High Precision Time to Digital Converter (HPTDC) [66]. The firmware of the HPTDC was configured to send output data with the same format as an FE-I4 chip via a single ethernet cable, which was connected to the HSIO/RCE readout.

The silicon tracker planes, were connected to the HSIO/RCE, as shown in Fig. 3.39(left). The HitOr signal of three modules were routed into a trigger logic custom-made PCB, which produced a TTL-compatible trigger signal from the coincidence of the three modules HitOr

output and was provided as trigger to the RCE system.

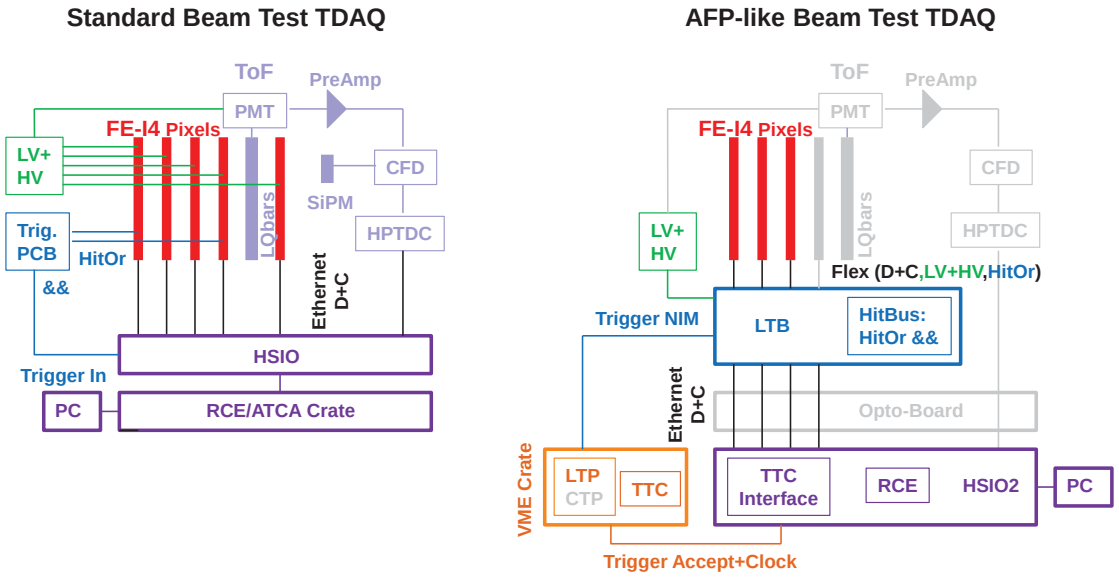

Figure 3.39.: Set-up for the tracker and Time-of-Flight integration test-beam (left) and for integration with the ATLAS TDAQ system (right). In grey are shown the components that were not connected for the ATLAS TDAQ integration tests.

In dedicated tests, the set-up was modified to be more similar to the final installed system configuration. The goal of these tests was to determine the compatibility of the RCE readout with the ATLAS TDAQ hardware. In Fig. 3.39(right) a sketch of the set-up is shown: three FE-I4 modules were connected to a Local Trigger Board (LTB) prototype that provides low and high voltage to each device and served as a pass-through for the data and commands from and to the RCE HSIO-II board via ethernet cables. The LTB also included a HitBus chip which allowed for a configurable trigger logic from the HitOr of the connected modules, and the output trigger signal was converted to NIM standard and sent to the Local Trigger Processor (LTP) in a VMEbus crate, which is a standardized module compatible with the ATLAS Central Trigger Processor system. The LTP created a trigger-accept signal which was sent to the TTC (Timing, Trigger and Control) interface module in the same VMEbus crate and from there to the RCE HSIO-II board via an optical fibre, together with the clock signal which was generated in the TTC module.

In addition to the readout tests, in some occasions the timing detectors (ToF prototype and SiPM reference) outputs were recorded with an oscilloscope in order to study their intrinsic time resolutions without contributions from the HPDC electronics.

Track reconstruction from data taken with the RCE was performed using the Judith reconstruction framework. Analysis of the data from the ToF prototype detector taken with RCE, however, was done by a custom-made ROOT-based software after the track reconstruction.

3.8.1. Spatial Tracker and ToF Hit Correlation

In order to verify the integration of the two sub-detectors, the spatial correlation between tracker and timing system hit information is measured. For this, after track reconstruction, the position of each track is correlated to the ToF channels which sent information to the RCE in the same event. The result is observed in Fig. 3.40: the correlation in the y-coordinate shows the position of each of the trains, which indicates that data from tracking

and timing detectors are synchronized event-by-event. Some outliers are observed which increase as a function of the MCP-PMT voltage due to the presence of crosstalk between different channels of the ToF detector, which was studied and will be shown in the following sections. Correlations in the x-coordinate show the coverage of the LQbars in the silicon tracker acceptance. The difference in multiplicity between the bars in train 1 and 4 with respect to the bars 2 and 3 is a consequence of the geometry of the set-up: train 1 is 3 mm wide in the y-coordinate, as opposed to the other trains which have a height of 5 mm; and Train 4, although being broader than Train 1, has an acceptance overlap with the the silicon tracker of only ∼2 mm. Moreover, the 120 GeV pion Gaussian beam was centred to the middle of the tracker devices, so lower number of tracks are expected in the first and the last trains due to the beam shape.

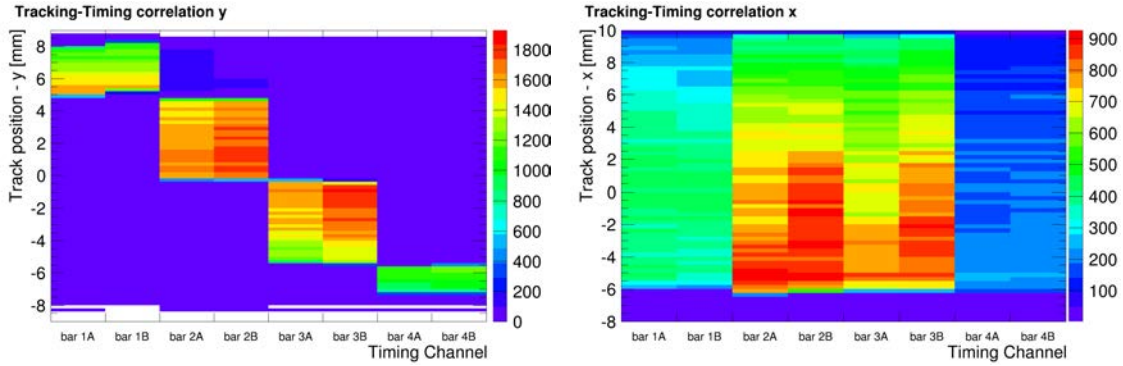

Figure 3.40.: Correlation between timing channel and reconstructed track position along y (left) and x (right) at $V_{MCP-PMT}$ =1,800 V.

3.8.2. LQbar Alignment

Taking advantage of the clear correlations observed between ToF and tracker detectors, the positions of the LQbars with respect to the tracker reference system can be obtained.

Events are selected with only one good quality reconstructed track and exactly 2 LQbars hit in the event to remove crosstalk contribution (notice that in this test-beam set-up a train consisted of 2 bars). Then, for each of the selected events, when a bar registers a hit the coordinates of the track are filled in a histogram. The result, as can be seen in the example for one of the bars in Fig. 3.41, is the beam distribution with the range positions of the specific bar. The edges of the distribution are fitted with an S-curve and three regions are defined:

- *Bar region*: delimited with the 50% points of the fitted S-curves.
- *ROI region*: delimited with the 50% points of the fitted S-curves minus 2σ of the convoluted Gaussian distribution.
- *Out-of ROI region*: delimited with the 50% points of the fitted S-curves plus 2σ.

These regions are used later for the computation of efficiency, crosstalk and noise of the LQbars. Results from the lowest possible MCP-PMT voltage were taken as a reference for alignment (1,800 V), as higher voltages introduce larger crosstalk levels.

3.8.3. LQbar Efficiency

The following quality track selection criteria is done for the measurements of efficiency, crosstalk and noise:

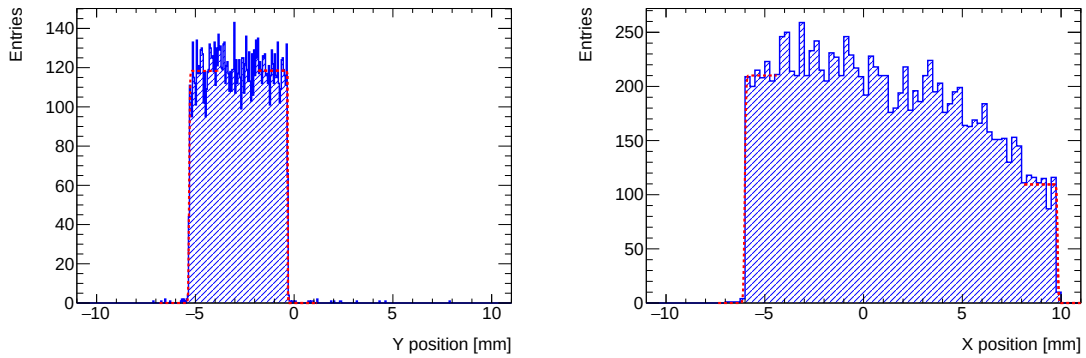

Figure 3.41.: Reconstructed track position distribution along y (left) and x (right) for events with only one track and a registered time from Bar 3A, used for alignment. The red dashed line corresponds to a S-curve fit. The MCP-PMT was operated at $V_{MCP-PMT}$ =1,800 V.

- *One track events*: Only one train should be hit in the event.
- *One cluster in tracker planes 4 and 5* (i.e. upstream and downstream the LQbars): Remove contribution of secondary particles from bars.
- *Good tracks* (χ^2/ndof<2): well fitted tracks.

With those cuts, the efficiency of a bar is calculated as the fraction of the events with a track that passes through that bar and triggers a hit in that bar over the total number of events with a track that pass through the bar of interest. This efficiency is defined for tracks inside the "bar region" defined in the previous section.

The efficiency distribution for two MCP-PMT bias voltages, $V_{MCP-PMT}$ =1800 and 1900 V, for all the "A" bars in the trains (i.e. the upstream bars) and fixed CFD threshold of 100 mV is shown in Fig. 3.42. It is possible to observe how the efficiency is on average greater in the ends of the bars (at $x \sim -6$ mm). This effect was observed during the design simulations, in which the light yield is reduced up to a factor of 2 farther away from the cut edge of the radiator bar, as the Cherenkov light cone generated by the traversing particle is not fully detected [67]. The efficiency distribution becomes more uniform at 1900 V, since the full bar reaches almost full efficiency. Fig. 3.42 also shows the efficiency as a function of the MCP-PMT operational voltage. It can be observed how the efficiency improves as a function of $V_{MCP-PMT}$ for all the bars: at 1,800 V the efficiencies range from 83% to 97%, while at 1,900 V the efficiencies of all the bars are around 99%. In particular, the "B" bars (downstream bars) show always higher efficiencies than the upstream bars in the trains, possibly caused by light crosstalk from the "A" bars.

3.8.4. LQbar Crosstalk

Crosstalk between bars from different trains is calculated for each bar as the fraction of events in which the bar registers a hit when a track passes through a neighbouring (or next-to-neighbouring) train over the total number of events in which the track passes through that neighbouring train. Thus, to determine if an LQbar hit comes from train-to-train crosstalk, the track in the event is required to be contained in the "Out of ROI region" of a bar sending a hit but inside the "Bar region" of a bar in a different train.

Fig. 3.43 shows crosstalk maps (top) for the bar 4A for two $V_{MCP-PMT}$ voltages and fixed CFD threshold of 100 mV, and the average crosstalk for each bar as a function

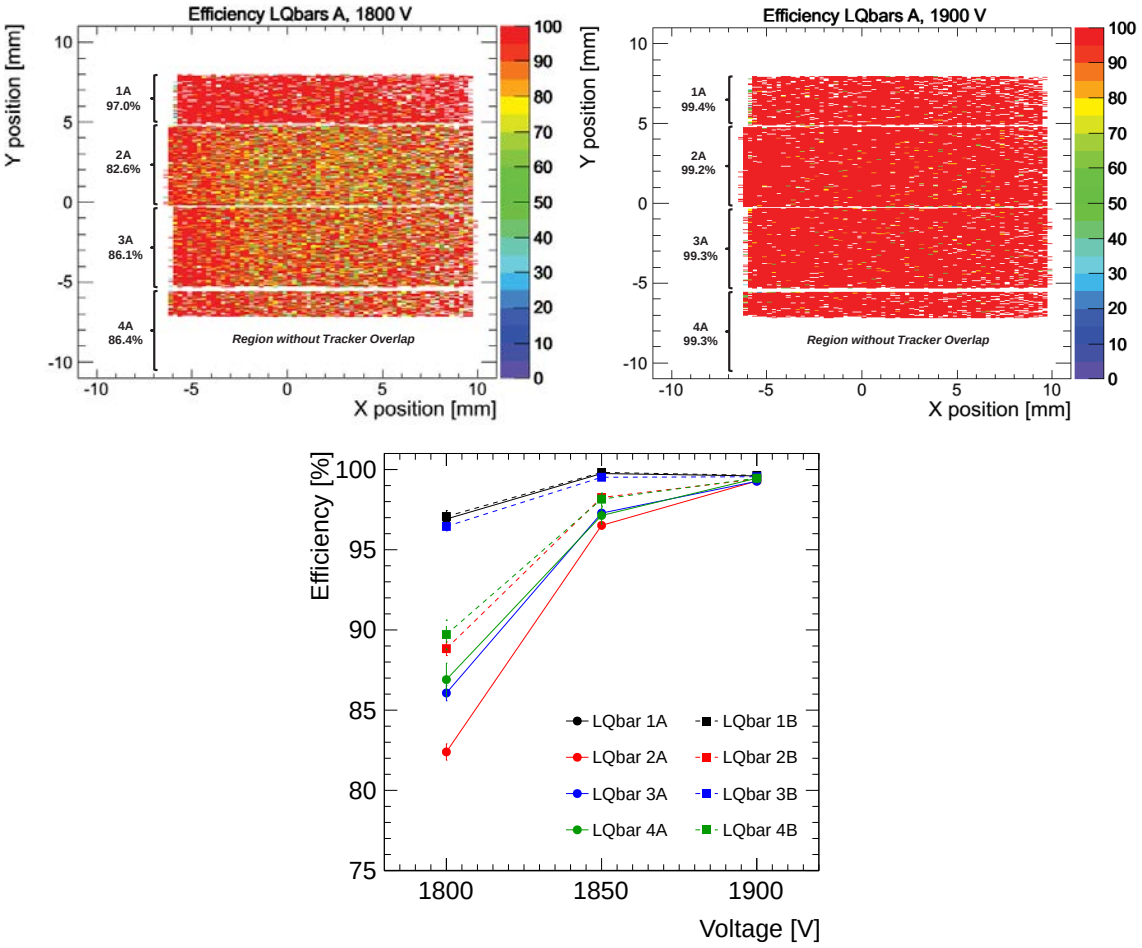

Figure 3.42.: Efficiency map of the upstream bars in all the trains for an MCP-PMT voltage of $V_{MCP-PMT}$ =1,800 V (top left) and $V_{MCP-PMT}$ =1,900 V (top right), and the total bar efficiency as a function of $V_{MCP-PMT}$ (bottom).

of operational voltage (bottom) for the first (left) and the second (right) neighbouring train. It shows how the crosstalk increases with the $V_{MCP-PMT}$ voltage varies from bar to bar for the highest measured voltage: 66-92% (8-47%) for the neighbouring (next-to-neighbouring) train. As with the efficiency, crosstalk is higher near the end of the bars, at $x = -6$ mm. During data taking, the radiators of the LQbars were optically isolated from train to train by intermediate Mylar foils, and by aluminium at the light-guides which serve as mechanical support for the bars. Hence, the crosstalk originates from the MCP-PMT level, possibly an optical leakage at the photo-cathode window and/or the lateral spread of photo-electrons in the MCP-PMT. A higher CFD threshold could reduce the crosstalk levels, as the crosstalk signal amplitude from neighbouring LQbar trains are significantly smaller than direct hit signals.

3.8.5. LQbar Noise Rate

The noise rate is measured as the mean signal firing rates of the LQbars in events in which the track missed all LQbars (i.e. $x < -7$ mm). Table 3.6 shows the noise rates for all the bars at different MCP-PMT voltages and a fixed CFD threshold of 100 mV. As with the crosstalk, the noise rates have a wide range across the bars, from 0 to 63 kHz at the highest measured voltage, and increasing with $V_{MCP-PMT}$. This corresponds to noise occupancies

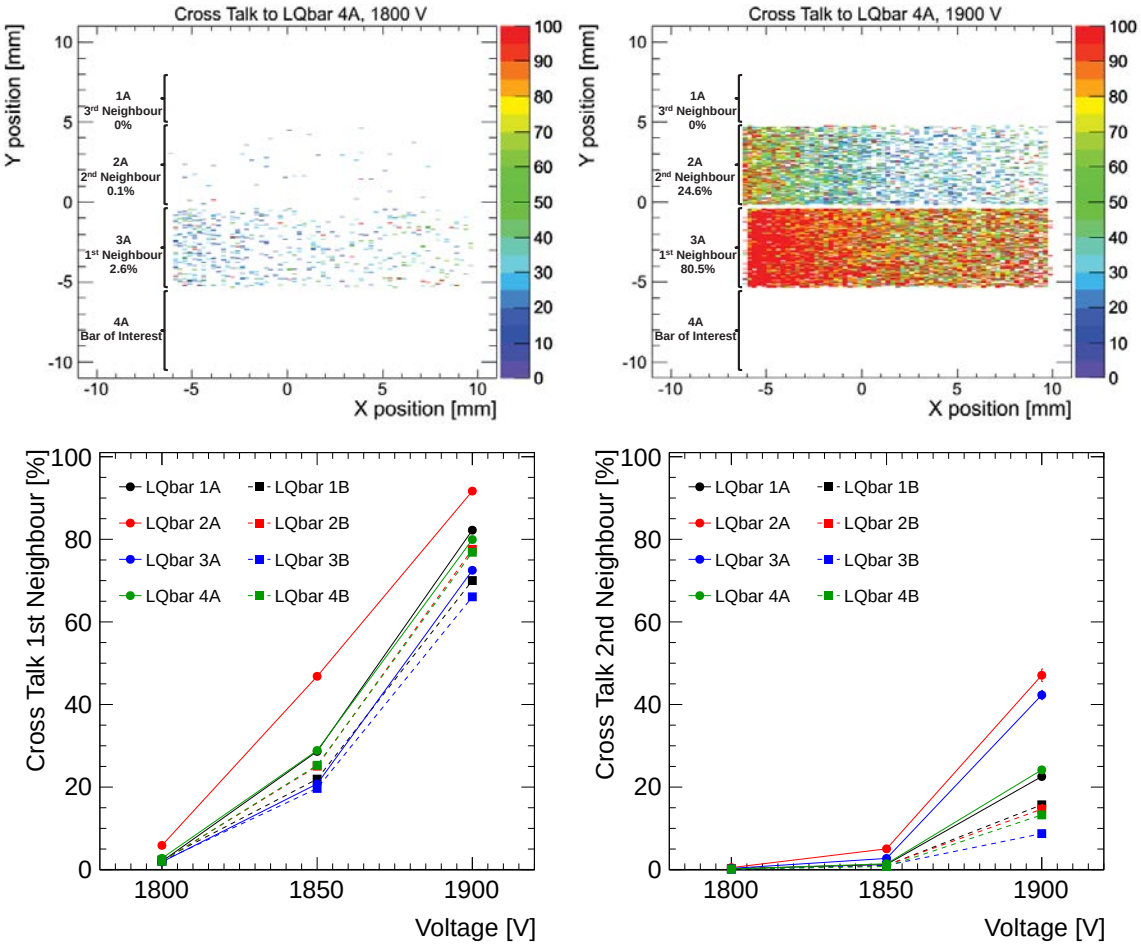

Figure 3.43.: Crosstalk maps (top) of the bar 4A for an MCP-PMT voltage of $V_{MCP-PMT}$ =1,800 V (left) and $V_{MCP-PMT}$ =1,900 V (right), and the total bar crosstalk (bottom) with the neighbouring (left) and next-to-neighbouring (right) trains as a function of $V_{MCP-PMT}$.

in the order of 10^{-4} to 10^{-3} for a 25 ns window.

3.8.6. Time Resolution with HPTDC

As mentioned above, the SiPM detectors used for timing reference did not overlap with the full AFP ToF prototype, and therefore only bars from two of the trains were studied in this test-beam. The HPTDC digitized the timing information from the CFD output of both LQbars and SiPMs, and encoded the time information in an FE-I4-like format. For each event this information is sent to the RCE system and saved together with the tracking information. Only two of the three available SiPMs (SiPM 1 and SiPM2) were used for measurements with the HPTDC.

Firstly, the time resolution was studied for the reference devices by calculating the time difference between the two SiPM. The histogram of the time difference distribution is shown in Fig. 3.44(left). The distribution shows an approximately Gaussian distribution with a total width of σ_{fit} = 25.1 ps, which includes the contribution of both SiPMs and their respective HPTDC channel. This result is consistent in all the data sets taken in the test-beam within less than 1 ps. Assuming that the SiPMs behave similarly and there is no correlation between the two devices, the single SiPM+HPTDC resolution is $\sigma_{fit}/\sqrt{2}$,

Table 3.6.: Noise rate per bar (in kHz) for different $V_{MCP-PMT}$ voltages.

	Noise rate [kHz]							
$V_{MCP-PMT}$	1A	1B	2A	2B	3A	3B	4A	4B
1800 V	0	3	45	7	10	16	29	28
1850 V	0	14	57	19	22	22	35	35
1900 V	0	19	63	29	47	49	46	47

resulting in $\sigma_{SiPM+HPTDC} = 17.7$ ps. The resolution of the SiPMs without HPTDC contribution was also measured with an oscilloscope to be $\sigma_{SiPM} = 11.0$ ps [117, 119], which gives the contribution from the HPTDC (by subtracting quadratically, assuming no correlations) as $\sigma_{HPTDC} = 13.9$ ps.

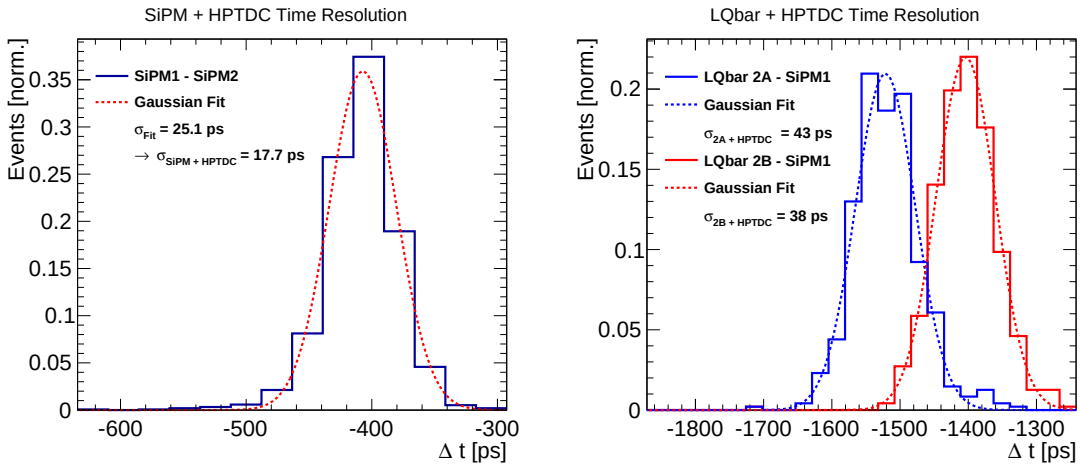

Figure 3.44.: Time difference distribution between SiPMs (left) and between bars in train 2 and SiPM 2 (right) with $V_{MCP-PMT}$ =1,900 V.

The LQbar time resolution is measured similarly. A Gaussian function is fitted to the LQbar-SiPM time difference distribution. Fig. 3.44(right) shows the time difference distribution of LQbars from train 2 with $V_{MCP-PMT}$ =1,900 V and SiPM 2 (measurements with SiPM 1 are consistent within a few ps). The spread of the distribution corresponds to the time resolution of the LQbar, which is convoluted with the time resolution of the SiPM. Hence, to obtain the single bar resolution, the 17.7 ps SiPM resolution obtained earlier is quadratically subtracted from the LQbar-SiPM fit result. Single bar resolutions for all measured voltages are listed in Table 3.7. It shows that the time resolution improves with higher $V_{MCP-PMT}$, reaching up to 38 ps resolution for a single bar at the highest measured voltage, including HPTDC contributions. Statistical and fit uncertainties are estimated to be 2 ps and a typically 6 ps systematic uncertainties is introduced to account for the reference SiPM differences and run-to-run variations.

The time resolution of the average time measured by the bars from the same train is also calculated and shown in Table 3.7. In this way, time resolutions of 35-37±6 ps are reached at the highest $V_{MCP-PMT}$ voltage. If the measurements were completely independent and all channels had the same performance, the average of all the N measurements should scale as $1/\sqrt{N}$ with respect to the single bar resolution. However, the observed improvement is less than the expected (here $1/\sqrt{2}$), which indicates the existence of correlations between bars of the same train possibly by optical leakage at the photo-cathode window and/or the lateral spread of photo-electrons in the MCP-PMT, in the same way as crosstalk.

Table 3.7.: Single bar resolutions measured for different $V_{MCP-PMT}$ voltages.

	Time resolution $\sigma_{LQbar+HPTDC}$ [ps]			
$V_{MCP-PMT}$	1750 V	1800 V	1850 V	1900 V
Bar 1A	78 ± 5	61 ± 6	52 ± 6	46 ± 5
Bar 1B	85 ± 6	60 ± 6	47 ± 6	41 ± 6
Average Train 1	67 ± 7	54 ± 12	44 ± 6	37 ± 6
Bar 2A	94 ± 5	80 ± 10	50 ± 6	43 ± 7
Bar 2B	94 ± 8	64 ± 5	45 ± 6	38 ± 6
Average Train 2	77 ± 7	63 ± 7	41 ± 6	35 ± 6

3.8.7. Conclusions

The integration of the AFP Time-of-Flight detector prototype in the silicon tracker read-out system was proven a success, showing that both detector systems with a common DAQ could be used for the final installation of AFP. In particular, event-by-event correlation between ToF and SiT were observed which allowed for performance studies in the ToF prototype with the use of track information. These studies showed that it is possible to reach 99% hit efficiency in the ToF system at high enough MCP-PMT voltage (1,900 V), at the expenses of increasing crosstalk and noise. However, operational parameters were not optimized for performance, e.g. a higher CFD threshold could have reduced crosstalk and noise.

The time resolution with two bars per train was measured to be 35-37±6 ps for the maximum voltage, which is compatible with the low-luminosity requirement of 30 ps resolution. With a four bars per train configuration, and the optimization of operation parameters it is expected to reach the 10-20 ps resolution needed for high-luminosity data taking conditions.

4. Production, Installation and Operation: One-Armed AFP Detector

After the successful qualification of the 3D silicon sensor technology, the module production was started. The module production included not only the fabrication process but also the quality assurance. After production, the detector was installed and commissioned. The first stage installation of the AFP detector was finished in February 2016, when two Roman Pots where installed at one side of ATLAS and equipped with silicon tracker detectors only (one-armed AFP). The full installation which includes the installation of two more Roman Pots at the other side of ATLAS and of the Time-of-Flight detectors was carried out in 2017.

This chapter describes the module production, installation and finally the operation of the one-armed AFP detector.

4.1. Pixel Module Production

In the previous chapter, the performance of the AFP tracker prototypes have been studied. It was decided that the AFP modules would consist of the same sensor and chip than the prototypes: 3D silicon pixel sensors coupled to the FE-I4 read-out chip (see Sec. 3.3.2).

The pixel module production was performed in the following step order:

1. *Sensor production:* consists of the fabrication of the sensitive part of the module performed at CNM.

2. *Bare assembly:* the coupling of the silicon sensor (bump-bonding) to the read-out chip electronics (FE-I4) (see Fig. 4.1, left).

3. *Module assembly:* the assembly of the bare assembly produced in the previous step on a mechanical carrier card and connected to a flexible printed circuit that allows the connectivity of the chip with the read-out system. The result of this step is the pixel *module* (see Fig. 4.1, right).

4. *Quality Assurance (QA):* the testing of the module performance. The QA is performed in two stages:
   a) At production site (IFAE) where the initial tests are performed before sending the modules to the installation site.
   b) At installation site (CERN) where the final quality of the modules is checked, accounting for possible malfunctions due to breakage during transport, and scored to decide their installation.

In the next sections, these production steps are described in detail.

4.1.1. Sensor productions

The first CNM sensor production (run 6682) for AFP was finished in July 2014. The production started with 13 4-inch wafers with the same fabrication mask as IBL, each one including 8 FE-I4-compatible 3D sensors. However, 8 of the 13 wafers were broken in the

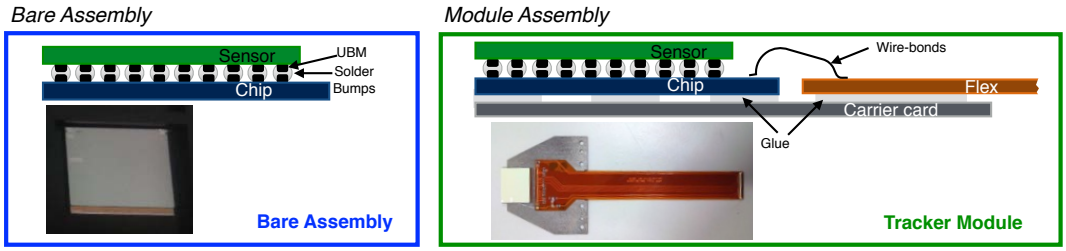

Figure 4.1.: Schematic and pictures of a bare assembly (left) and a tracker module (right). The production step which couples the read-out chip to the silicon sensor is referred as "bump-bonding", while the production of the tracker module by installing the bare assembly on a carrier card and wire-bonding to the flex connector is named "Module assembly process".

process. The cause was investigated by CNM and found to be due to damage in the edge of the wafers introduced during the DRIE process (see Sec. 3.1.4). The remaining wafers were sent to IZM[1] (Germany) to be processed for under bump metalization (UBM), which consists of the addition of a metalic layer on the sensor (and chip) connection pads to facilitate the coupling via solder bumps (see Sec. 4.1.2). The sensors are later returned to CNM to be diced. The diced sensors were slim-edged with a standard diamond saw down to ∼180 μm from the last active pixel on the side facing the LHC proton beam. The slim-edge width was measured under an optical microscope as shown in Fig. 4.2. Little variation in the cut distance in the whole production was obtained, with an RMS of 6 μm.

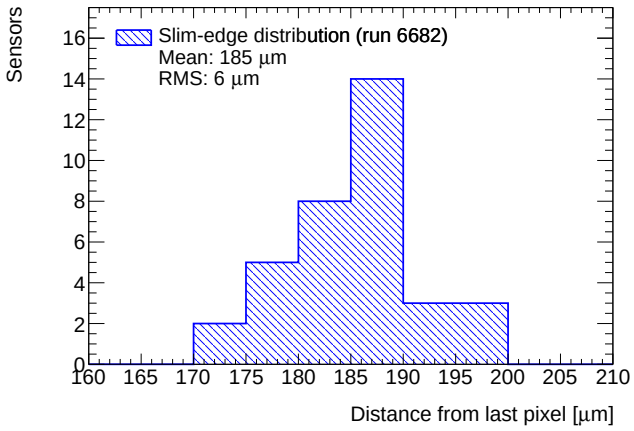

Figure 4.2.: Slim edge distance from the last active pixel as measured under an X-ray microscope for all the sensors produced in CNM sensor production run 6682.

The electrical characterization of the diced sensors was carried out at room temperature by means of a probe station: the n-side of the pixels were contacted through the under bump metalization with the probe station's grounded chuck while the p-side was contacted with a probe needle on the back of the sensor. This method of measuring IV-curves has been proven to not be fully reliable [120] since the contact of all the UBM pads with the chuck is not guaranteed, as it can depend on placement and needle and vacuum pressure. However, the IBL/AFP CNM design is not equipped with any other structure that allows to probe all

[1]Fraunhofer-Institute für Zuverlässigkeit und Mikrointegration

pixels. Given the low bias voltage requirements of the 3D sensors for maximum efficiency (see Sec. [121]), the sensors were classified in quality groups as follows: *red* sensors (lowest quality) reach a leakage current of 10 μA below 10 V, *yellow* sensors (medium quality) reach 10 μA between 10 and 20 V, and *green* sensors (best quality) reach that leakage current above 20 V. The breakdown voltages measured at sensor level through the UBM is shown in Fig. 4.3. In total 9 green and 5 yellow sensors were obtained from this production which implies a (good quality) sensor yield of 23%.

One of the proposed reasons for such a large fraction of sensors with low breakdown voltages was that the p-stop between n^+-implantations was larger than the design one, which could lead to high electric fields.To palliate this effect, 11 sensors of the lowest quality (red sensors) were irradiated with neutrons at the TRIGA reactor in JSI Ljubljana to fluences of 10^{12}–10^{14} n_{eq}/cm^2 in two irradiation campaigns. With this irradiation the electric field around the p-stop would decrease by reducing the p-stop, which could modify the electrical behaviour and increase the breakdown voltages. These fluences are low compared to the sensor specifications, maximally ∼3% of the expected radiation damage at the end of the AFP life time at standard luminosity, so the effect in the life span of the sensor is negligible, although the operational voltage would need to be slightly higher. A list of the sensors used for these tests is presented in Table 4.1. The IV-curves were measured after irradiation at 20, 0 and -25 °C (in Table 4.1 the 0 °C is used as reference). In the second campaign the curves were measured after one week annealing at room temperature. As a result, 6 out of 11 sensors improved their electrical behaviour[2]. Two of them were assembled, one of them in time for installation (AFP-B01-M04).

Table 4.1.: Summary of breakdown voltage evolution in the irradiation campaigns. Measurements at 0°C after irradiation are taken as a reference. Sensors are labelled as W##-S#, where the first number corresponds to the wafer number in the production and the second to the sensor number inside that wafer. All sensors were taken from the first sensor production (run 6682).

Sensor	Irrad $[n_{eq}/cm^2]$	$V_{bd}^{bef/after}$ [V]	Anneal.	Improved	Comments
W05-S1	10^{13}	7/21	No	Yes	Assembled: AFP-B01-M16
W11-S2	10^{14}	5/0	No	No	
W11-S3	10^{13}	5/16	No	Yes	
	$+10^{14}$	5/105	Yes	Yes	
W11-S5	10^{14}	3/13	Yes	Yes	
W11-S6	10^{12}	5/9	No	Yes	
	$+10^{14}$	9/41	Yes	Yes	
W11-S8	10^{14}	4/0	Yes	No	
W12-S1	10^{14}	6/6	Yes	Yes[a]	[a]: at −25°C, V_{bd} =37 V
W12-S4	10^{14}	4/4	Yes	No[b]	[b]: before anneal. at -25°C, V_{bd} =20 V
W12-S6	10^{14}	6/0	No	No	
W12-S7	10^{14}	5/7	Yes	Yes[c]	[c]: at −25°C, V_{bd} =21 V
W13-S1	10^{14}	5/165	Yes	Yes	Assembled and installed: AFP-B01-M04

Due to the low production yield, a second production of 3D sensors for AFP was requested to CNM (run 7945). The second production finished by March 2016. As opposed to the previous production, only two out of 12 wafers were lost in the fabrication process. In

[2]This thesis includes newer results from the ones presented in reference [91].

the new batch the fabrication process was improved: the edges of the wafers were protected during the DRIE step and the process parameters were optimized to reduce damage in the sidewall of the etched columns. Moreover, a temporary metallization was introduced in the process, which allowed a more reliable I-V measurement at wafer level. This structure was removed by chemical etching after electrical characterization. The results of these measurements are presented in Fig. 4.3, which shows a dramatic improvement over the first production in terms of breakdown voltage (the average breakdown voltage was 89 V) and sensor yield: 68 out of 80 sensors were qualified as green quality (see also Table 4.3). The fabrication of these sensors was finished after the first stage installation of the AFP detector and thus they were later used for the full AFP installation in 2017.

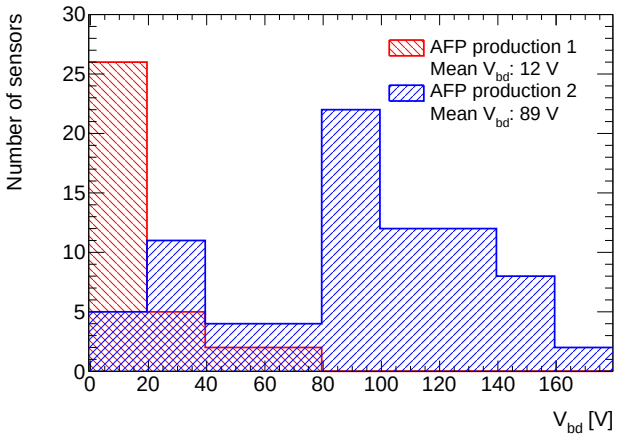

Figure 4.3.: Comparison of breakdown voltages between the two AFP 3D sensor productions measured on a probe station: the measurements of the first production were performed at sensor level through the UBM while for the second production, a temporary metal layer was included in the process from which the sensors were probed before dicing.

Table 4.2.: Wafer and sensor production yield for the AFP productions.

Production run	Wafer yield	Good wafers	Sensor yield	Good sensors
AFP 1 (6682)	38%	5	23%	9
AFP 2 (7945)	83%	10	85%	75

4.1.2. Bare Assembly

Sensor and read-out chip are coupled channel-by-channel by 25 μm diameter SnAg solder bumps, this process is known as *bump-bonding*. It requires that a metalic layer, usually Cr and Cu (or Ni), is deposited on the Al contact pads of both sensor and chip since solder bumps do not attach well to the Al. This process is called Under Bump Metallization (UBM), which is performed at IZM after the sensor fabrication as mentioned in the previous section. Bump-bonding was performed at IFAE. During the bonding cycle the 700 μm thick FE-I4 chips (with SnAg solder bumps) and the sensors were aligned, heated to 260 °C for a short period (about a minute) and pressed together lightly. To finish with the hybridization process, the assemblies were processed in a fluxless formic acid reflow oven.

Once the bump-bonding has finished, the bare assemblies were inspected using an X-ray machine to identify possible defects in the bump-bonding, like large areas of disconnected bumps. Out of the 24 sensors from the 6682 production run (first AFP sensor production) that underwent the hybridization process only one device showed an area of disconnected pixels. Afterwards, the IV-characteristics are measured again in order to determine if the bare assembly should undergo the next step in the production chain, the module assembly (see Sec. 4.1.3). Moreover, it is the first production step (see Sec. 4.1) which allows to determine the electrical behaviour quality by biasing the full sensor through the bump-bonds, not possible at sensor-level as explained in Sec. 4.1.1. The measurement is done with a probe station, with one needle probing the back side of the sensor and the other connected to the high voltage ground wire-bond pad in the chip. The results of the measurements are shown in Fig. 4.4. The sensors are characterized by the quality of their IV as follows: *red* sensors reach a leakage current of 100 μA below 10 V, *yellow* sensors reach 100 μA between 10 and 20 V, and *green* sensors reach that leakage current above. Sensors with green and yellow (due to the low yield of the production) quality are selected for assembly, except for the first two modules of the production, which were chosen from the worst quality (red) for mechanical testing and assembly training. After installation (in 2016 modules up to AFP-B1-M11 were produced in time for installation, see Sec. 4.1.3), further modules were produced as back-up devices, in some cases from red-quality bare assemblies. For one bare assembly (AFP-B1-M03, see Fig. 4.4), an unstable behaviour was observed: a breakdown voltage of 78 V was initially measured, however, a second I-V measurement on the same sensor showed a reduced V_{BD} down to 10 V. This effect was observed again in later stages of the production in the same device.

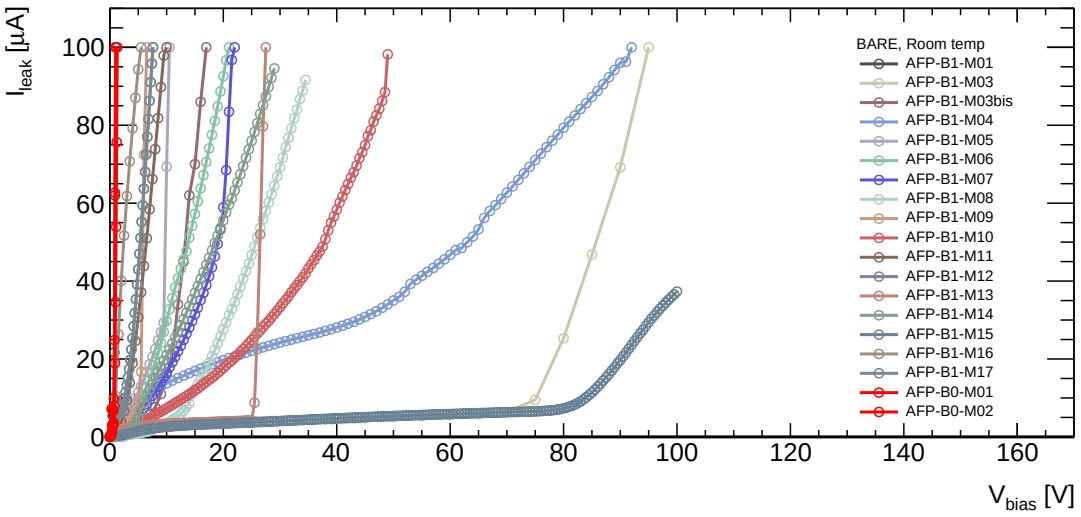

Figure 4.4.: IV-curves for all flip-chipped sensors assembled in pixel modules from the first AFP production. The measurements were performed at room temperature with a probe station, with one needle probing the back side of the sensor and the other connected to the high voltage ground wire-bond pad in the chip.

4.1.3. Module Assembly

Once the sensor and the read-out chip are coupled, i.e. the bare assembly is produced and tested, the module assembly is performed inside a clean room at IFAE. Fig. 4.5 shows pictures of the module assembly steps.

An aluminium-carbon fibre composite carrier card is first cleaned with isopropanol to remove the residues from the card production. Radiation-hard Araldite 2011 epoxy glue is placed on the carrier card in the area where the bare assembly will be glued. Since the cure time at room temperature of the glue is 6 hours, in addition a double-sided Tesa tape is glued in the center in order to immediately attach the bare assembly to the carrier card and prevent it from being moved during the curing of the glue. The bare assembly is then placed aligned to the alignment marks present in the carrier card with a pick-and-place machine. A Kapton flex cable is glued a few millimetres below the glued bare assembly with the same process.

After the glue has dried out, flex cable and read-out chip pads are wire-bonded together with a wire-bonding machine. In addition, several long (∼2 cm) wire-bonds are connected from the flex to the back of the sensor in an opening of the back passivation for the high voltage bias contact. This is due to the passivation design that was not modified from the IBL design. When the wire-bonding is finished, the wire-bonds are inspected to look for possible shorts or detached wires, which are repaired if found.

The FE-I4 features a 4-wire-bond pattern which regulates a stable 2 μA reference current in the read-out chip, named `IrefTune`. The recommended pattern of floating and connected wires varies from chip to chip. By default all the wires are connected and, in the case in which a wire-bond needs to be removed, the wire-bond is pulled with increasing force until it is broken which serves to determine the quality of the wire-bonding. In such cases, it was measured that 8–11 g were needed to break the bonds, which is safe for the wire-bonds.

After the assembly of the module has finished, it is labelled as AFP-B#-M##, where the first number corresponds to the batch number and the second to the module number of the batch. Batch 0 was used for pre-production with a prototype PCB carrier card while Batch 1 was used for the production for the AFP installation in 2016. The module is then ready to undergo quality assurance.

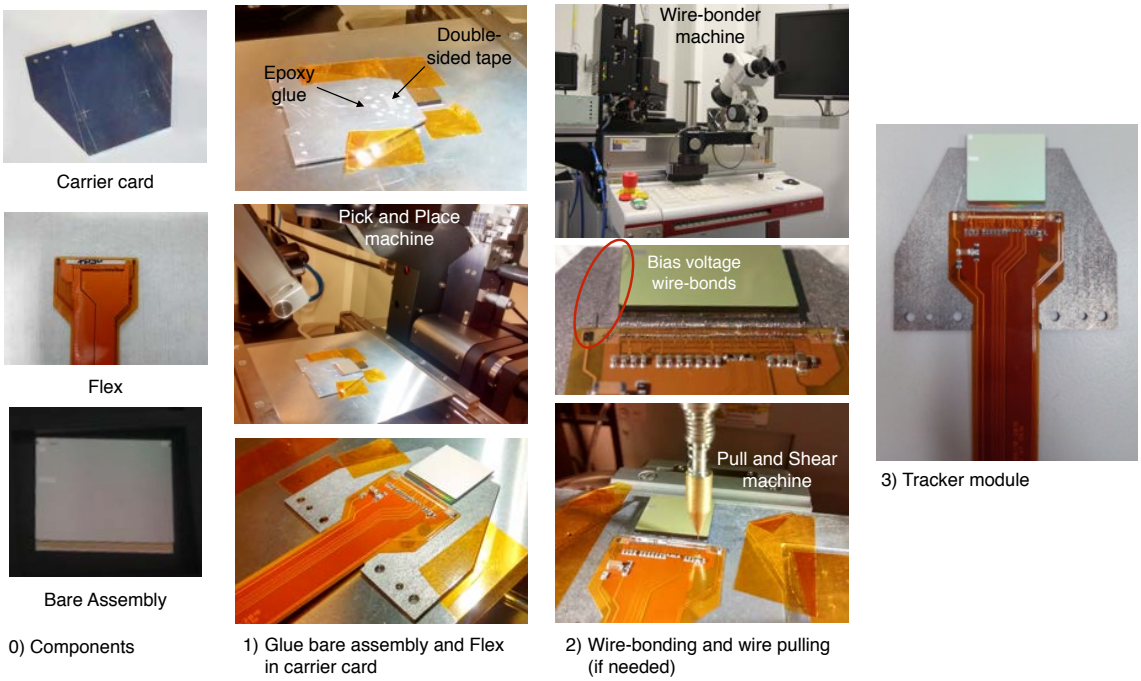

Figure 4.5.: Pictures showing the different steps in the assembly stage: 0) the components of a module, 1) the glueing of the bare assembly and the flex onto the carrier card, 2) the wire-bonding and wire pulling (if needed), and 4) the final tracker module.

Table 4.3.: Module production yields from both sensor productions. Note that only 11 modules were produced by the time of detector installation in 2016.

Production step	Sensor production	Total	Good	Yield
Bump-bonding	AFP 1 (6682)	22	21	95%
	AFP 2 (7945)	31	30	97%
Assembly	AFP 1 (6682)	17	17	100%
	AFP 2 (7945)	29	29	100%
Quality assurance	AFP 1 (6682)	17	14	82%
	AFP 2 (7945)	27	26	96%

4.1.4. Quality Assurance

After assembly, the modules undergo quality assurance tests, first at the production site (IFAE) and then at CERN. These tests are performed in order to ensure that the modules with the best performance are selected for installation. Table 4.4 shows the list of all the modules assembled from the first sensor production, which underwent quality assurance, although only 11 were assembled on time for the one-arm AFP installation.

Table 4.4.: List of all the modules assembled from the first sensor production (run 6682). The sensor quality at wafer level, disconnected pixels and noise level as measured at IFAE and at CERN are shown for each module. The horizontal line separates the modules that were assembled on time for the AFP first stage installation from the later ones.

Module (AFP-B01-)	Irrad [n_{eq}/cm^2]	Sensor quality	Discon. pixels	Chip comm.	Noise [e^-] (at IFAE)	Noise [e^-] (at CERN)	Installed in station
M01	No	red	No	Y/N[a]	320±37	–	No
M02	No	red	–	No	–	–	No
M03	No	yellow	No	Yes	202±18	166±11	Far
M04	10^{14}	red/green[b]	No	Yes	163±11	172±13	Far
M05	No	yellow	No	Yes	162±11	168±13	Near
M06	No	yellow	No	Yes	160±10	166±11	Near
M07	No	green	15%	Yes	154±13	175±15	No
M08	No	green	No	Yes	160±11	171±14	Near
M09	No	yellow	–	No	–	–	No
M10	No	green	No	Yes	156±11	165±12	Far
M11	No	green	No	Yes	166±11	171±15	Far
M12	No	green	No	Yes	169±11		No
M13	No	green	No	Yes	171±11		No
M14	No	green	No	Yes	165±11		No
M15	No	green	No	Yes	175±11		No
M16	10^{12}	red/green[b]	No	Yes	175±12		No
M17	No	green	No	Yes	262±20		No

[a] Chip was responsive only before transportation to CERN.
[b] Improved after pre-irradiation.

Alignment

The heat exchanger, i.e. the structure where the modules are installed on inside the Roman Pot (see Fig. 2.11), has been designed so that in the long pixel direction there is an offset of 65 μm from plane to plane in order to improve the station pointing position resolution along that direction. In addition, in order to install the silicon tracker planes very close to the Roman Pot floor (see Sec. 2.3.2) the position along the short pixel direction needs to

be known precisely. Therefore, reasonable alignment of the sensors on the holder is needed to be able to place the tracker module in the Roman Pot.

The assembled module is inspected under an X-ray scanner and the mis-alignment of the bare assembly with respect to the alignment mark is measured. Due to the thickness of the FE-I4 chip (700 μm), it is not possible to focus with an optical microscope both the chip and the alignment marks on the carrier card for a precise measurement, hence the X-ray scanner is used instead.

In particular, the following distances are measured:

- x: the distance between the alignment mark and the chip edge in the long pixel direction.
- y_1: the distance between the alignment mark and the chip edge in the short pixel direction.
- y_2: the distance between the chip edge and the first wire-bond pad. Note that the chip edge distance may vary from chip to chip by few micrometers, however the sensor is always at the same position with respect to the pad, since the sensor is bump-bonded to the chip which needs to be placed with precision for all pixels to be coupled, and the distance from the bump pads and the wire-bond pads are fixed by design.

Fig. 4.6 pictures the aforementioned distances. Together with the slim-edge distance ($y_{slimedge}$) measured previously, the total misalignments in both directions are calculated: the deviation from the centre of the alignment marks

$$x_{total} = \frac{x_{left} - x_{right}}{2}, \tag{4.1}$$

and the displacement with respect to the reference position in the short pixel direction:

$$y_{total} = (y_{1,ref} - y_1) + (y_{2,ref} - y_2) + (y_{slimeedge,ref} - y_{slimedge}), \tag{4.2}$$

where $y_{1,ref} = 0$ μm (chip edge aligned to mark) , $y_{2,ref} = 40$ μm (design chip cutting edge) and $y_{slimeedge,ref} = 180$ μm (target slim edge width). Both x_{total} and y_{total} quantify the precision of the placement which is needed for the installation in the Roman Pot and (most importantly for y_{total}) determine how close the active region of the sensors can be placed to the floor of the Roman Pot.

In addition, the rotation along the 2 cm of the sensor long pixel direction is measured as $y_{total,left} - y_{total,right}$, where the subscript $left/right$ denote the left or right y_{total} measurement.

Electrical Characterization

The quality assurance tests start with a measurement of the IV-curve. In this way, the quality of the sensor is verified after mounting and the connectivity of the high voltage wires is tested, which are the most fragile of the wire-bonds.

The IV-curves for the modules assembled during the first production are shown in Fig. 4.8. The measurements were performed with and without supplying voltage to the chip, since the FE-I4 power consumption increases the temperature and varies the IV behaviour. However, since no large differences on the breackdown voltage were observed under the two conditions, the IV-curves with the chip powered off are taken as reference. Two modules needed to be operated with a controlled temperature, the irradiated modules from the previous irradiation campaigns, so the modules were placed inside a climate

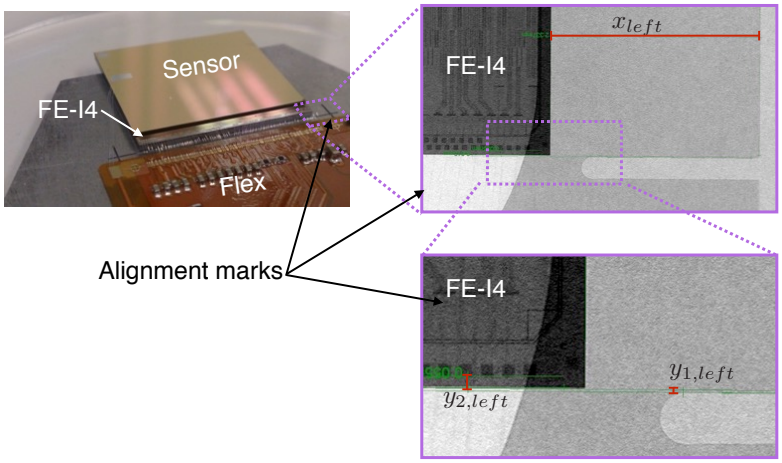

Figure 4.6.: X-ray picture of an assembly module showing the positions measured for the alignment determination.

chamber at +20 °C, while for the rest of the modules the measurement was done at room temperature.

The quality of the modules based on their electrical behaviour is determined again based on the assembly-level IV-curves. The criteria is the same as the one used at bare assembly-level: red modules reach a leakage current of 100 μA below 10 V, yellow modules reach it between 10 and 20 V and green ones reach that current beyond 20 V.Table 4.5 shows a summary of all the modules measured and their quality based on this criteria, for every module production step.

Voltage Regulator Calibration

The voltage regulators are then calibrated: the FE-I4 chip is supplied with 2 V, which are internally regulated in two different levels, the analog (VDDA) and the digital (VDDD) voltages. The working points of these voltages are 1.40 V (VDDA) and 1.20 V (VDDD), and the goal of the regulator calibration is to set the correct voltages. It is performed by measuring the regulator output by probing with a multimeter on the flex, while modifying two 8-bit chip registers, `VrefAnTune` (analog regulator) and `VrefDigTune` (digital regulator), covering the full range. Fig. 4.9 shows the dependence of the voltage regulator outputs on the respective chip registers. Afterwards, the values of the registers corresponding to the target voltages are set in the chip configuration file, and the calibration results are stored for future reference.

Once the voltage regulators are calibrated, the communication with the ASIC is tested and the calibration of the chip operational parameters is done.

Chip Read-out and Tuning

The read-out capability of the FE-I4 in the module assemblies is critical to pass the quality assurance. In order to test the chip read-out, the USBpix DAQ system was used (see Sec.3.4).

Analog and digital scans are performed, which are a first connectivity test for any module: the goal is to determine whether it is possible to read-out signals from the injection in either the analog or digital circuit of the chip. In total, 15 out of 17 modules produced

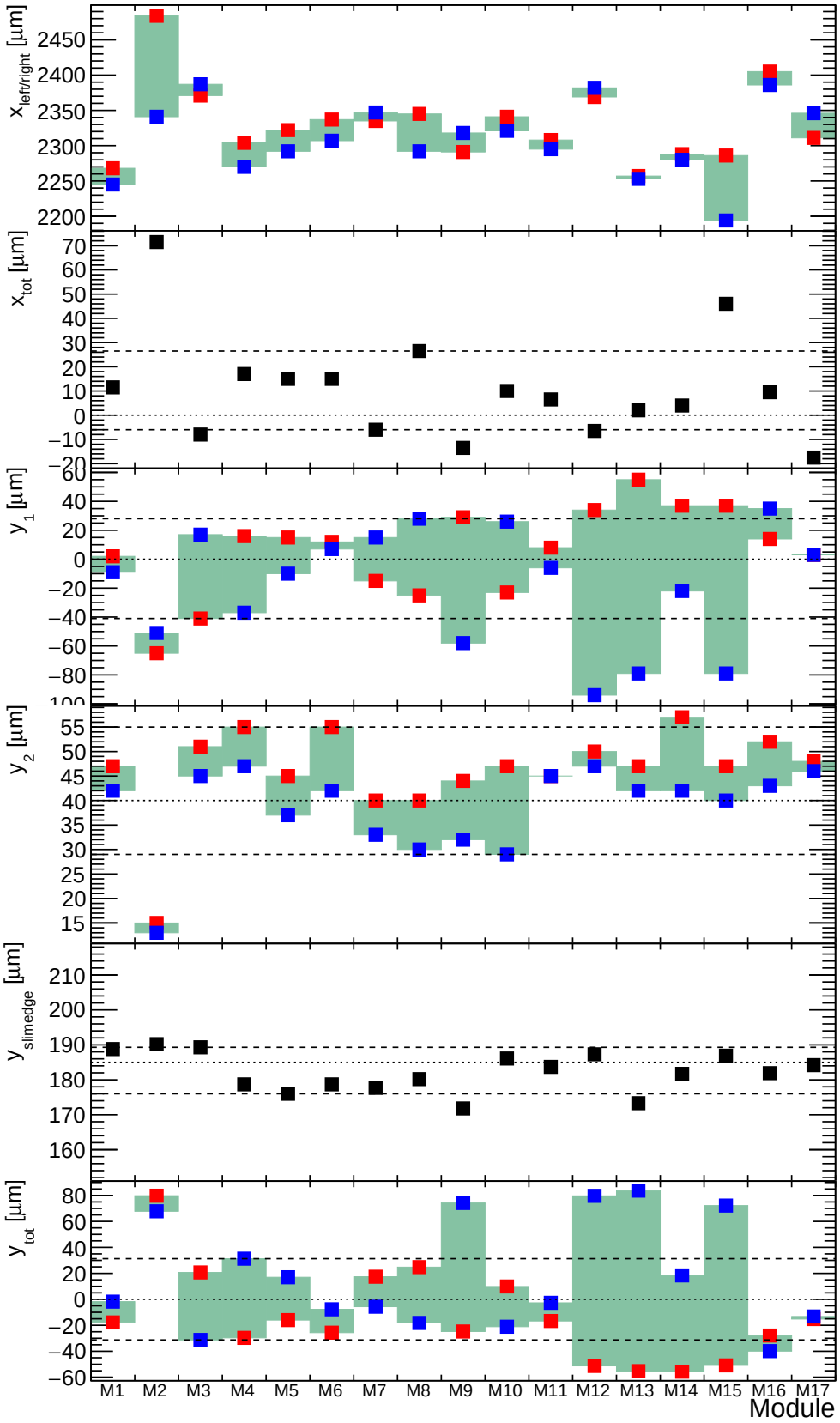

Figure 4.7.: Summary of distances measured for the modules produced from the first sensor production for AFP: red (blue) markers show the "left" ("right") measurements, and the green bands show the range between left and right. The distances are defined in the text. Dotted lines represent the reference distances while the dashed lines show the distance range of the modules that were installed in the tunnel.

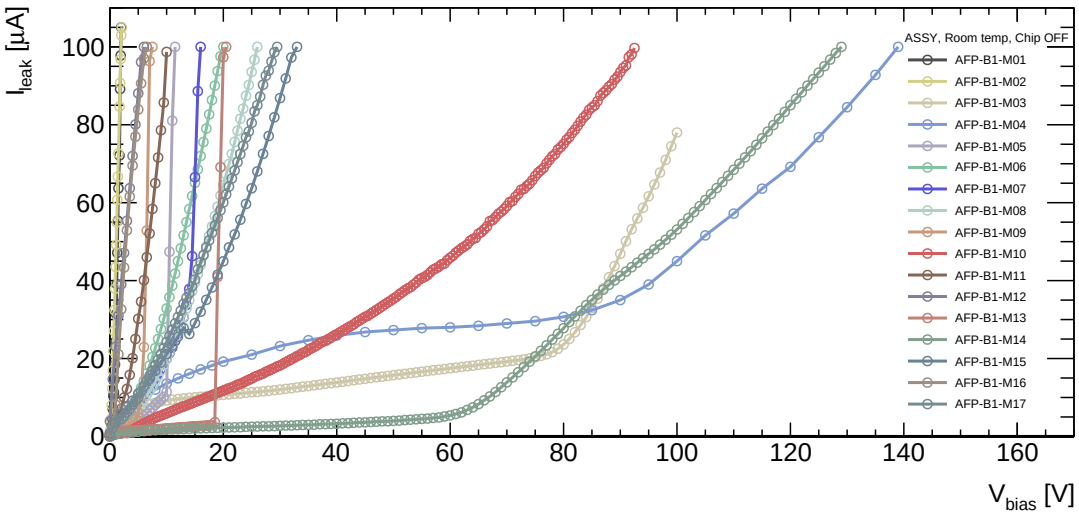

Figure 4.8.: IV-curves for all modules assembled from the first AFP production. The measurements were performed at room temperature with the chip powered off except for modules M04 and M16, which were measured at +20 °C inside a climate chamber.

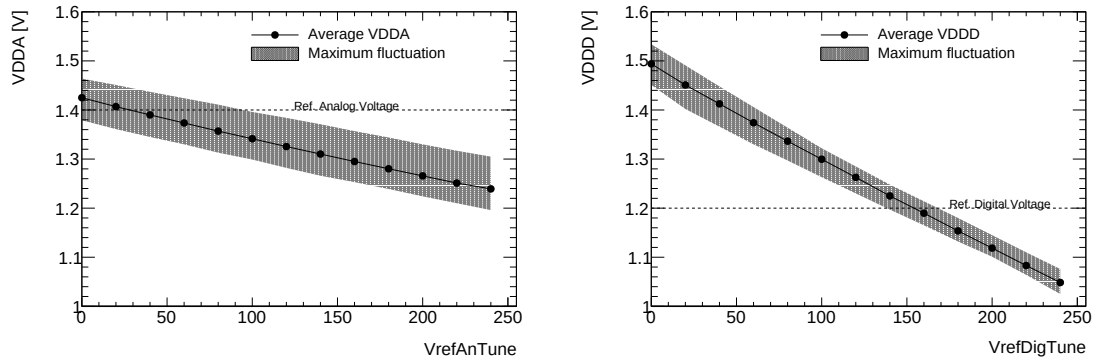

Figure 4.9.: Average analog (left) and digital (right) regulator voltage output as a function of the `VrefAnTune` and `VrefDigTune` chip register values, respectively. The band shows the maximum and minimum measurement deviations from the average. The horizontal dashed line represents the target voltage output for each of the regulators.

from the first sensor production showed communication with the read-out system before transportation to CERN (see Table 4.4).

The next test consists in determining the possibility of calibrating the module to the desired operational parameters, that is a threshold of 2000 electrons and a time-over-threshold response of 10 clock cycles (each cycle or Bunch Crossing lasts 25 ns) for a collected charge of 20000 electrons. Threshold and ToT are calibrated iteratively as they depend on each other. If the resulting calibration is not compatible with the target parameters, the module does not qualify for possible installation. All tested modules fulfil the tuning requirement. In addition, during the threshold measurement at the end of the calibration, the noise level is determined.

Normally, the noise values in these devices range around 150 to 170 e^-. The resulting noise for all the assembled modules tested at production site are shown in Table 4.4. Only two modules showed a particularly high noise: AFP-B01-M01 was produced with

Table 4.5.: Module quality based on voltage at which the leakage current reaches 100 μA for all modules at each module production step. The modules after the horitzontal line (after AFP-B1-M11) were produced after the first stage AFP installation in 2016.

Module	Bare		Assembly		CERN	
(AFP-B1-)	V(100 μA)	Quality	V(100 μA)	Quality	V(100 μA)	Quality
M01	0	Red	2	Red	2	Red
M02	0	Red	2	Red	2	Red
M03	95/17	G/Y[a]	>100	Green	114/35	Green
M04	88	Green	140	Green	150	Green
M05	10	Yellow	11	Yellow	11	Yellow
M06	20	Yellow	20	Yellow	21	Green
M07	22	Green	16	Yellow	16	Yellow
M08	35	Green	25	Green	26	Green
M09	6	Red	7	Red	–	–
M10	49	Green	93	Green	95	Green
M11	10	Yellow	10	Yellow	10	Yellow
M12	7	Red	6	Red	–	–
M13	27	Green	21	Green	–	–
M14	30	Green	129	Green	–	–
M15	>100	Green	33	Green	–	–
M16	6	Red	7	Red	–	–
M17	8	Red	30	Green	–	–

[a]Not stable IV measurement

a low quality sensor while AFP-B01-M17, on the other hand, was bump-bonded with a floating guard-ring (i.e., the bumps connecting which connect the guard-ring to ground were removed before bump-bonding for testing) which may have caused the increase in noise. At this stage, noise was not a critical aspect as these tests were not performed with the final DAQ, the RCE/HSIO-II, with which the calibration is repeated at CERN.

Bump-Bonding Connectivity

Up to this point, only the chip has been tested with the DAQ system. In order to verify the connection between sensor and chip, in addition of the aforementioned X-ray scan, a source scan is performed.

At the IFAE laboratory, a ^{90}Sr source is available for this purpose. The radioactive β source is placed on top of the module, while data taking is started in the USBpix system. After enough data has been collected, pixels that yield no hits and are not masked out from the read-out are considered disconnected from the chip. Only in one module a large number of disconnected pixels was observed (AFP-B01-M07).

Final Tests at CERN

The modules tested at IFAE are packaged and sent to CERN. At arrival, visual inspection under the microscope is performed, looking for possible damage during transportation.

The IV-curves of the modules are measured again at room temperature with the chip powered on and off, since the power consumption of the FE-I4 produces extra heat which may vary the IV-curve. The results are shown in Fig. 4.10. Noteworthy is the measurement of one module (AFP-B1-M03): after reaching the current limit of 100 μA during the first IV measurement (labeled as "AFP-B1-M03" in Fig. 4.10), its IV-curve changed (labeled

as "AFP-B1-M03bis" in the same figure), dramatically reducing the breakdown voltage. This behaviour was previously observed at bare assembly level on the same sensor, hence demostrating an unstable behaviour.

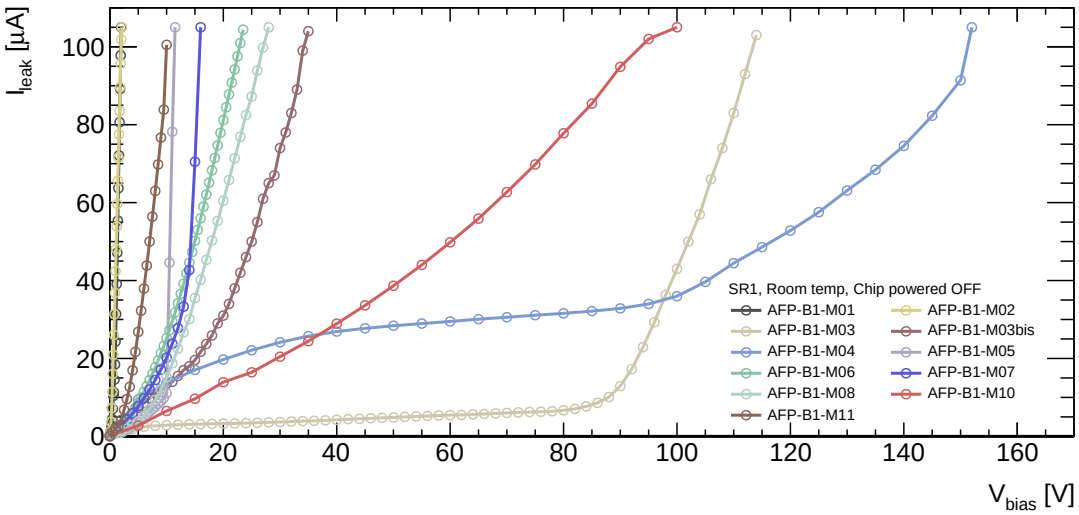

Figure 4.10.: IV-curves for all modules assembled from the first AFP production measured in the SR1 building at CERN. The measurements were performed at room temperature with the chip powered off.

The modules were tested and calibrated in the SR1 building at CERN. A test stand with an RCE/HSIO-II readout system (see Sec. 3.4.2) was used for chip read-out and tuning. The tuning was done (as at production site) at 2000 e^- threshold and a ToT response of 10 clock cycles for a reference charge of 20000 e^-. In addition to ensuring no read-out issues after transport, since HSIO-II is the DAQ system for the AFP detector, this step serves as a read-out test of the modules with the final DAQ for the modules. A total of three sensors failed the communication tests, one more than found at production site (see Fig. 4.4): AFP-B01-M01 module showed a very large current consumption, which ended up burning the power wire-bond. It was not possible to recover communication after reworking the wire-bonding. However, it was never planned anyway to utilize that module for installation. The modules with which the read-out was possible were correctly tuned. It is interesting to note that the noise levels observed with the RCE set-up at CERN are consistently higher by $\sim$10 e^-, as can be seen in Fig. 4.4, although this difference is almost negligible.

After the calibration, a scan with a radioactive ^{241}Am source is performed. This source scan has two goals: first, determine, and cross-check with the production site measurement, the connectivity of the bump-bonds; and second, serve as a calibration for the charge correction factor of the charge collection measurements (see Sec. 3.5.4). Only one sensor showed a large fraction (15%) of disconnected bumps (AFP-B01-M07), consistent with previous measurements.

Penalty Scoring

In order to quantify the quality of the modules before installation a penalty score system was introduced. A score of 10 is given for small deviations from each of the requirements, 100 for severe deviations and 1000 for unacceptable values. The parameters are the following:

- Alignment in X: How the FE-I4 and sensor is centred on the carrier card.
- Alignment in Y and rotation: A good placement allows to install the modules closer to the floor of the Roman Pots and thus closer to the LHC proton beam.
- Breakdown voltage: A high breakdown voltage assures to apply enough voltage after non-uniform irradiation.
- Leakage current: A low leakage current allows to operate the module with reduced noise.
- Module responsive to readout: Being able to read-out the module is a mandatory requirement.
- Tuning of device: In order to ensure a uniform calibration in the whole AFP detector, the modules should be able to be tuned (threshold and ToT) to the target values uniformly over all the pixels (i.e. threshold and ToT distributions should have a small width) with a moderate noise.
- Number of inactive pixels: It includes inactive pixels from bump-bonding connectivity problems and masked hot pixels (i.e. pixels that are masked because they are firing at too high rate). All modules should be able to detect a scattered proton for better track reconstruction and trigger efficiency.

Table 4.6 shows the scoring criteria. Note that, due to the overall low breakdown voltage in this production and a total module replacement being planned at the end of the first year, some of the quality criteria are relaxed, in particular the breakdown and leakage current requirements (also due to the high hit efficiency measured at low voltages in test-beams). The resulting scores after applying the penalty criteria for the AFP modules considered for installation are shown in Table 4.7. As a result, a total of 7 modules were found acceptable for installation after the quality assurance out of the 11 modules produced. Further devices were produced from the same sensor production after AFP detector installation in 2016.

Table 4.6.: Penalty scoring criteria used for the AFP module quality assurance. Higher scores are applied for values bigger than the reference values, except for V_{bd} where higher values are preferred.

Criteria	Penalty Score				Comparison Mode
	1000	100	10	0	
Align X [μm]	100	25	10	0	Absolute
Align Y [μm]	100	80	75	0	Absolute
Tilt [μm/2 cm]	250	50	20	0	Absolute
V_{bd} [V]	0	0.5	10	20	Absolute
I(10 V) [μA]	100	50	20	0	Absolute
R/O communication	No	–	–	Yes	Absolute
Threshold [e^-]	1000	500	50	0	Deviation from 2000 e^-
Threshold σ [e^-]	1000	150	100	0	Absolute
Noise [e^-]	300	200	180	0	Absolute
ToT	4	2	0.5	0	Deviation from 10ToT at 20 ke^-
ToT σ	4	2	0.5	0	Absolute
NoHit Pixels	1000	500	200	0	Absolute

Table 4.7.: Total penalty score of each module, as well as X and Y alignment, as well as tilt, breakdown voltage, leakage current, readout, threshold including noise, ToT tuning and number of not-responding pixels scores for the modules that were considered for the installation in AFP.

Module (AFP-B01-)	Station (Channel)	**Total Score**	x_{tot} [μm]	Score	y_{tot} [μm]	Score	y_{tilt} [$\mu m/2cm$]	Score	V_{bd} [V]	Score	$I(10\ V)$ [μA]	Score	R/O comm.	Score
M01		**4010**	11.5	10	-17.8	0				1000		0	No	1000
M02		**4100**	71.5	100	67.8	0				1000		0	No	1000
M03	F (2)	**110**	-6	0	-31.3	0	52	100	15	10	20	0	Yes	0
M04	F (3)	**120**	17	10	-29.7	0	60	100	95	0	17	0	Yes	0
M05	N (2)	**230**	15	10	-16.0	0	33	10	9	100	52	100	Yes	0
M06	N (1)	**130**	15	10	-25.7	0	18	0	1	100	41	10	Yes	0
M07		**1030**	-6	0	-5.7	0	23	10	15	10	20	10	Yes	0
M08	N (3)	**260**	26.5	100	-18.2	0	43	10	5	100	25	10	Yes	0
M09		**4110**	-13.5	10	-24.8	0	98	100		1000		0	No	1000
M10	F (1)	**10**	10	0	-21.1	0	31	10	50	0	15	0	Yes	0
M11	F (4)	**210**	7	0	-16.7	0	14	0	2	100	100	100	Yes	0

Module	Thr [e]	Score	Thr σ [e]	Score	Noise [e]	Score	ToT	Score	ToT σ	Score	NoHit Pixel	Score
M01		1000		0		0		1000		0		0
M02		1000		0		0		1000		0		0
M03	2022	0	63	0	167	0	9.97	0	0.23	0	17	0
M04	1993	0	70	0	171	0	9.99	0	0.1	0	268	10
M05	1986	0	70	0	168	0	9.98	0	0.1	0	238	10
M06	1991	0	66	0	167	0	9.98	0	0.16	0	219	10
M07	1992	0	92	0	175	0	9.98	0	0.26	0	15000	1000
M08	2211	10	102	10	171	0	10	0	0.16	0	294	10
M09		1000		0		0		1000		0		0
M10	1989	0	70	0	165	0	9.99	0	0.09	0	18	0
M11	2060	10	79	0	171	0	9.96	0	0.14	0	171	0

4.2. Installation

A total of two Roman Pot stations were installed during the winter LHC technical stop of 2015-2016, at 205 and 217 m from the ATLAS interaction point, in the C-side. The stations were populated with silicon tracker modules during the same technical stop.

The remaining 2 Roman Pot stations were installed in the A-side of ATLAS the next year end technical stop, completing the installation of the AFP detector which also includes the Time-of-Flight system.

4.2.1. Detector Installation

After quality assurance, seven modules were selected for installation. The devices were installed in Roman Pot flanges which were inserted in Roman Pot stations in the LHC tunnel. The installation was finished the 24th of February 2016 with 3 modules installed in the Near Roman Pot station and 4 modules in the Far Roman Pot Station.

Table 4.8.: Summary of installed modules in AFP in 2016.

Station/plane	Module	V_{op} [V]	Observations
Near station plane 0	AFP-B1-M06	10	–
Near station plane 1	AFP-B1-M05	5	–
Near station plane 2	AFP-B1-M08	10	–
Near station plane 3	–	–	Not installed in 2016
Far station plane 0	AFP-B1-M10	0	Short in High Voltage line
Far station plane 1	AFP-B1-M03	10	–
Far station plane 2	AFP-B1-M04	30	Irradiated (10^{14} n_{eq}/cm^2)
Far station plane 3	AFP-B1-M11	5	–

A summary of the installed devices is shown in Tab. 4.8. As the plane number grows, the module is farther away from the ATLAS interaction point. The position of the modules were chosen based on their quality score in view of a possible exchange of the worst quality modules at the middle of the year, so the worst quality modules were installed in positions of easier mechanical access (higher plane numbers). However, modules were not replaced in 2016, but during the second stage installation when all the remaining components of the AFP detector (ToF system, Roman Pots in side A, etc.) were installed.

After installation, a high voltage short-circuit was observed in one of the planes which was determined to be from the inside of the Roman Pot. Due to time constraints, it was not possible to open the station to fix the problem, therefore for the rest of the year this module (AFP-B1-M10) had to be operated without bias voltage. However, from test-beam results it is known that IBL/AFP generation 3D devices can be operated with very low or no high voltage with high efficiency before irradiation. However, in order to avoid potential trigger efficiency loss, the trigger board was configured so that the plane with the high voltage short did not participate in the trigger logic.

The IV-curves were measured after cooling to -5 °C with the FE-I4 chip powered on and configured, i.e. under running conditions. The results are shown in Fig. 4.11. Based on these measurements, the nominal operational voltage was chosen to be 10 V as a compromise between high bias voltage and low leakage current, unless the breakdown voltage was lower: in such cases the voltage was set to 5 V, i.e. a voltage in which full efficiency was obtained in previous studies (see Fig. 3.26). Since one of the planes was previously irradiated to a fluence of 10^{14} n_{eq}/cm^2, in order to ensure full efficiency the voltage was increased to 30 V for that plane.

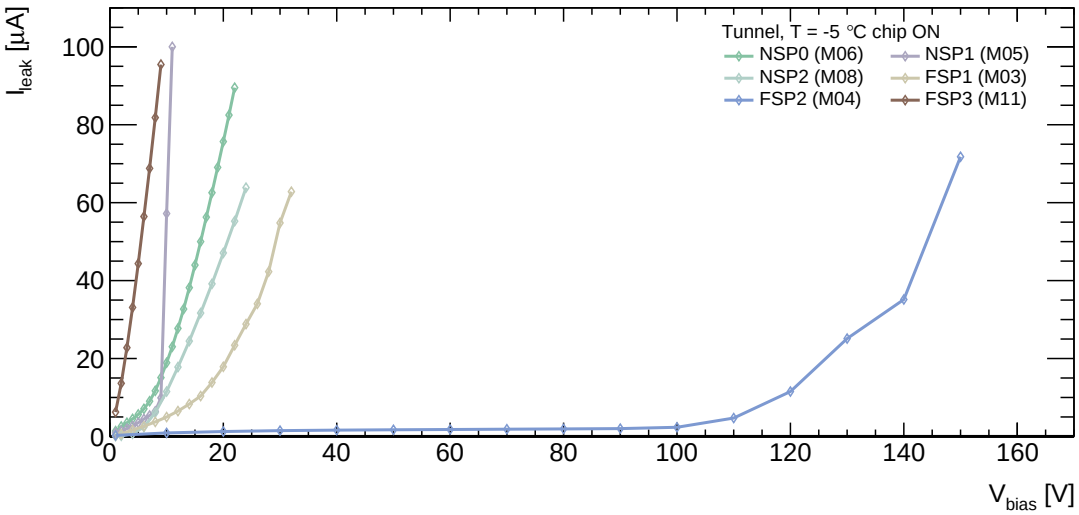

Figure 4.11.: IV-curves for all modules installed in the LHC tunnel in 2016 after installation. The measurements were done after cooling the modules to -5 °C via heat exchanger cooling with the FE-I4 chips powered on.

4.2.2. Trigger and Data Acquisition Integration

Data Acquisition

In normal operation, the ATLAS data taking is started before collisions start to wait for events to collect. To do so, all the sub-systems that will participate in data taking are enabled. In the process of starting data taking, all sub-systems undergo the same sequence (from initializing each sub-detector read-out system to start accepting triggers and recording data) even though the read-out systems of each sub-detector are different (hardware- and software-wise), which are integrated in the ATLAS TDAQ software. In addition, the input of trigger signals from the ATLAS sub-systems are enabled and prescaled as needed.

For physics data taking, the AFP readout system needs to be integrated to the ATLAS DAQ system in order to synchronize the AFP data with the data obtained from the rest of the ATLAS experiment sub-systems.

The software which controls the data taking in the RCE side was written based on the existing test-beam data taking software CosmicGui. This package was then linked to the ATLAS Run Control software, which is mandatory for the integration in ATLAS, as it controls the configuration, the start and the end of data taking of the whole experiment.

Each event contains the information of a bunch-crossing identification number (BCID), a number representing in which of the 25 ns slices of proton bunch revolution in the accelerator the collision was observed. The event information from all the ATLAS sub-detectors needs to contain a BCID which should coincide over all the sub-systems.

When the BCID in an event of one sub-detector doesn't match the global BCID, it is detected by the ATLAS TDAQ software, which proceeds to re-synchronize the sub-detector. For this, data taking is stopped for the de-synchronized sub-detector and started again with a starting BCID equalling the current value plus one. The re-synchronization process is implemented for each sub-detector in ATLAS, including the AFP detector. If the re-synchronization fails the sub-detector gets disabled (stop-less removal), meaning that global data taking continues but data from that detector is ignored.

During data taking, a sub-detector read-out system issues a busy signal whenever it is

not ready to accept further triggers to read-out a new event due to e.g. de-synchronization, configuration loss or read-out dead time, which can lead to a stop-less removal. In case of a sub-detector not being responsive, there are mechanisms for on-line recovering. This is the *TTC-restart* procedure (Timing Trigger and Control). In order to recover a permanently disabled sub-detector, the TTC-restart command can be sent, which temporarily pauses global data taking to completely stop the affected sub-system and start it again, following all the steps done in a fresh start of data taking. Finally, it gets re-synchronized and global data taking continues. This is usually a very drastic measure, as the ATLAS data taking is paused during all the process, which can suppose several minutes of data lost in big sub-systems. For this reason, another procedure as the *stop-less recovery* is usually implemented, which does not affect global data taking. However, the TTC-restart procedure in AFP takes only ∼5 seconds thanks to the small size of the detector and the high speed of RCE, so the impact is almost negligible, and therefore the implementation of a stop-less recovery in AFP is not needed.

For the verification of the AFP DAQ integration with ATLAS the detector needed to show negligible impact in data taking during high trigger rates (∼90-100 kHz), that is, not sending BUSY signals to the ATLAS DAQ system which would stop global data taking. Moreover, it needed to show the capability to be recovered in case of permanent disabling, i.e. that the TTC-restart procedure was functional. For this, the AFP system was included in global ATLAS data taking together with other sub-systems with random high rate triggers up to 100 kHz, showing that AFP was not generating busy signals. In order to test the TTC-restart capability, during the same run, a busy signal was manually generated, which led AFP to be stop-less removed after which the TTC-restart command was issued, which recovered AFP back into data taking.

Hence, the AFP system passed all the verifications: it is capable of taking data in the global ATLAS TDAQ system, it can withstand high read-out rates with no impact on data taking and it is possible to recover the detector in case it is disabled from data taking within a minimum amount of time and with a minimum impact on the global TDAQ system. This allowed the AFP system to participate in ATLAS runs in combination with the full ATLAS detector thereafter.

On-line Monitoring

In order to obtain real-time information about the performance of the AFP detector modules to react to read-out misbehaviour, on-line monitoring was implemented.

The software used for AFP on-line monitoring is GNAM [122], similarly to other ATLAS sub-systems, which is integrated into the ATLAS TDAQ system. GNAM takes a (user-defined) sub-sample of events during data taking, decodes the data from byte-stream to human-readable information and fills user-defined ROOT-based histograms. The implementation of the histogramming and decoding needs to be done on a case-by-case basis for each detector, as the encoding of each sub-system event information varies from one to another, as well as the parameters that need to be monitored.

Examples of on-line monitoring plots implemented for AFP are sensor hit-maps (Fig. 4.18), hit multiplicity distributions and plane-to-plane correlations (Fig. 4.19).

Trigger Integration

AFP trigger signals needed to arrive at the Central Trigger Processor in the ATLAS counting room inside the ATLAS L1 latency of 86 bunch crossings, i.e. 2.15 μs, in order to observe a trigger from the AFP detectors. Since AFP detectors are over 200 m away from ATLAS this becomes challenging: the diffractive proton needs to travel the 217 m of beam-pipe before reaching both stations, where the trigger signals are generated by the

Local Trigger Boards (see Sec. 2.3.5) and travel back via an air-core cable, with a $0.9c$ transmission speed, to the counting house where the ATLAS L1 system resides. Further delay are due to signal logic operations and signal formation.

By default, the logic used for the trigger formation for each station was the Majority Vote: two out of the three planes participating in the trigger signal formation were required to send a trigger signal to the hit-bus chip in the LTB. Other possibilities were the OR and AND of the three signals. However, the OR option is sensitive to noise, as a single noisy plane would generate a high background trigger rate, while the logical AND is sensitive to time-walk and specially sensitive to inefficiency. Therefore the Majority Vote logic was chosen as a compromise.

With the configuration in place after installation, it was observed that the trigger signals arrived ∼10 ns too late. Nevertheless, the delay from the signal formation can be minimized by means of increasing the bias voltage of the discriminator of the FE-I4 chip, which is controlled by the `DisVbn` register. In particular, it affects the speed of the discriminator and the time-walk contribution from the comparator. The downside of increasing this register is that the current consumption also increases. The effect of this register was studied in the laboratory: with a radioactive source pointing towards an FE-I4 module and a scintillator (for time reference) on the back, the signal of both FE-I4's HitOr and scintillator were observed in an oscilloscope on coincidence. The delay of the FE-I4 with respect to the scintillator was measured. The current was monitored all the time. Results of this test are shown in Fig. 4.12. As a compromise between current consumption and trigger signal formation, `DisVbn` was set to 100 (up to that point the default value was 26). As a result, AFP triggers from both Far and Near stations reached the ATLAS L1 system in the last available bunch-crossing at the expense of an average 60 mA chip current increase.

The integration of AFP signals into the ATLAS L1 system allowed the possibility to use AFP-based L1 triggers during ATLAS data taking, which was used in low pile-up conditions to obtain the data used for the analysis presented in this thesis (see Chapter 5).

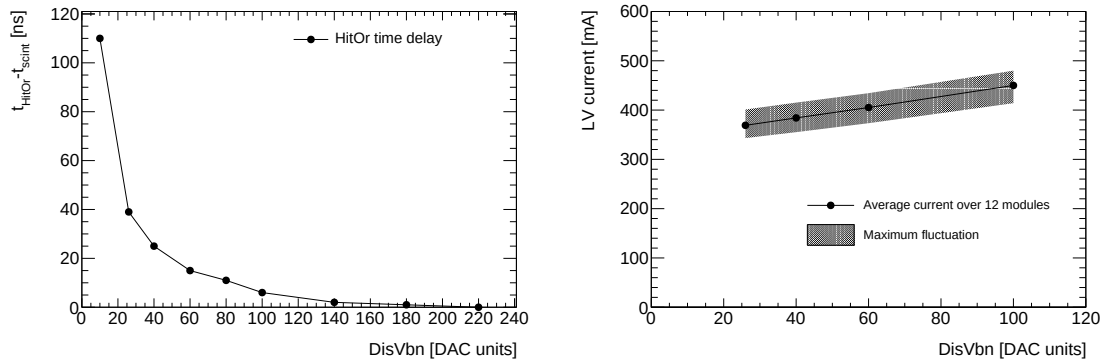

Figure 4.12.: HitOr signal time delay (left) with respect to a time reference scintillator and chip current consumption (right) as a function of the `DisVbn` chip register. The currents of 12 modules were measured for each register value: the points correspond to the average of all measurements while the band shows the measurement of the maximum deviation from the average.

4.3. Detector Commissioning and Operation

4.3.1. Detector Operation

The AFP detector was powered after its installation in the LHC tunnel. The current consumption of the FE-I4 chip as a function of time over the year is shown in Fig. 4.13 (top). After initial detector read-out tests the devices were left constantly powered on. Only in two occasions the modules were switched off: on April the sensors (chip voltage and bias voltage) were powered off for two days during scrubbing in the LHC machine to prevent possible side-effects in the sensors electronics and during one month (mid June–mid July) for hardware and software updates regarding network security, during which the readout systems were not allowed to run. The current consumption after the reduction of the trigger signal generation time (see Sec. 4.2.2), was constant throughout the year with 450–500 mA. Since the silicon tracker was not inserted during standard luminosity collisions, and hence radiation damage was negligible the chip current consumption was not affected. During operation in 2017, on the other hand, the AFP Roman Pots were allways inserted during standard pile-up runs, which caused the SiT to recieve a higher fluence. As a consequence, an increment of the LV current of the tracker modules was observed [123].

The modules were operated under a temperature of ∼-5 °C during most of the year with small fluctuations which correspond to a temperature increment due to beam presence in the beam pipe (see Fig. 4.13). In special occasions the temperature was varied up to 25 °C in order to determine a calibration between the air cooler output pressure and the resulting temperature in the detectors: during the first months of operation the temperatures in the far and near stations differed by ∼5 °C which required a new pressure-to-temperature calibration. Since power consumption of the chip is non-negligible (∼1 W), the operation of the chip affects the temperature in the detectors. Therefore, in some instances the temperature dropped from -5 °C to -15 °C just by switching off the chips.

The leakage current of all the modules over the year 2016, biased at the operational voltages listed in Tab. 4.8, are shown in Fig. 4.13. The current limit was set to 100 μA, which was only reached during high voltage tests. Due to the initial low quality of the modules in terms of IV behaviour the overall leakage current trend is not predictable, as currents other than bulk current may play an important role. This makes difficult to explain the differences in current trends of the different modules. One plane (far station plane 3) was operated at lower voltage (-4 V instead of -5 V) during a long period in between physics runs since the leakage current was observed to dangerously increase close to the compliance level, possibly because the operational voltage was set in the breakdown regime for this sensor. However, during physics runs it was operated at its operational voltage under expert supervision.

On the 1st of November the high voltage was powered off since no further physics runs were expected and the full AFP was completely powered off on the 5th of December.

4.3.2. Module Calibration

The AFP tracker modules operational parameters were a threshold of 2,000 electrons and a response of 10 Bunch Crossings (25 ns) to an injection of 20,000 electrons (also expressed as 10 ToT at 20 ke$^-$). This calibration was tested in the past in test-beams (see Sec. 3.6.3) in which a high hit efficiency was observed at 14° angle. It was not possible to obtain lower thresholds with a good calibration for some modules. Threshold results are shown in Fig. 4.14 at different times, including the measurement before installation (February 2016) for comparison. Only one module showed a 10% larger threshold than the target before installation, which may be related to a difference in the set-up, as the target threshold was

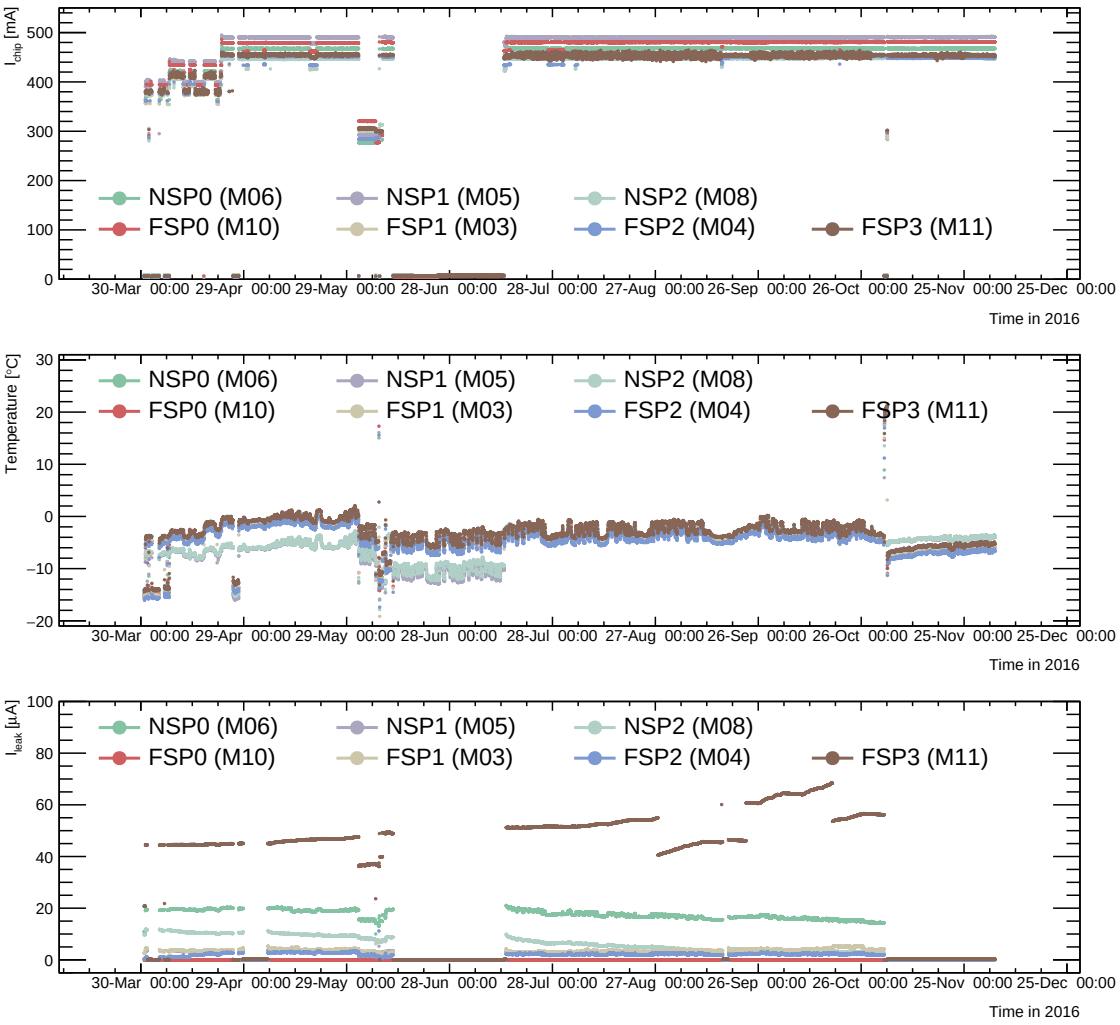

Figure 4.13.: Current from the FE-I4 low voltage line (top), temperatures as measured from the NTC in the pixel modules (middle) and sensor leakage current (bottom) during the 2016 operation of AFP.

always reached in the tunnel.

Once installed, the modules were calibrated using the final calibration parameters on April 2016 and checked afterwards before physics runs. It has been observed in the IBL detector that the calibration parameters (threshold and ToT) can shift with increasing radiation damage in FE-I4 devices [124]. However all measured threshold values are consistent with the target threshold during the year, since in 2016 operation the AFP tracker was not exposed to enough radiation to observe the effect. The noise was measured at the same time as the thresholds, the summary of the noise measurements is shown in Fig 4.15. All noise values before installation are consistently higher than the ones obtained after calibration in the tunnel, maybe due to the different conditions of temperatures and chip register parameters. Only Far station plane 0 (FSP0) shows higher noise after installation since the measurements performed in the tunnel, as opposed to the ones at SR1, were done with HV off. Even though the FSP0 was not biased, the noise increase with respect the other modules was marginal.

During calibration, hot pixels were masked, both in the readout and in the trigger signal generation. The distribution of the masked pixels over all the planes and the fraction

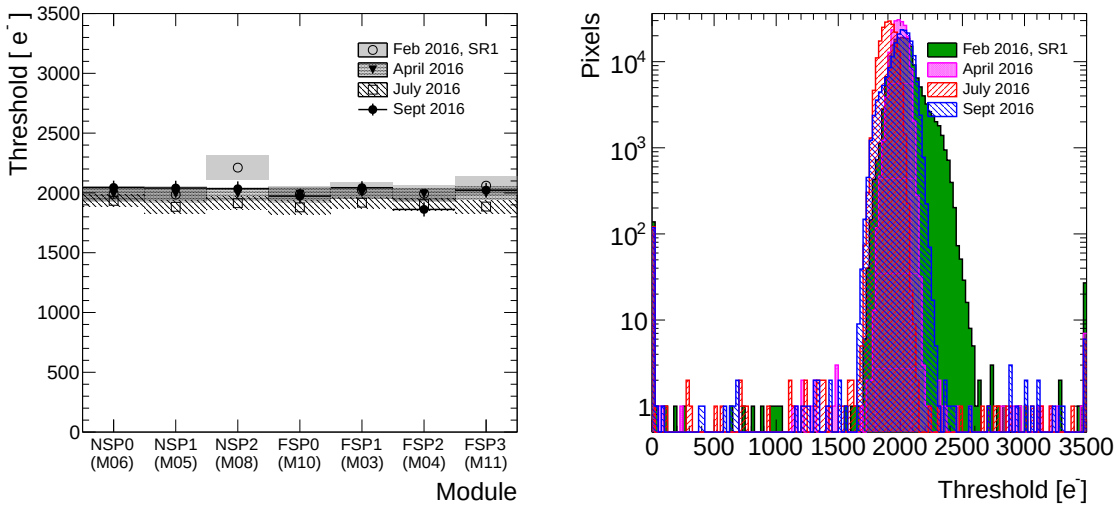

Figure 4.14.: Thresholds after calibration to a target threshold of 2,000 e^- in the installed AFP modules measured at different times. The left distribution shows the average threshold for each tuning, while the right distribution shows the threshold distribution for all the pixels.

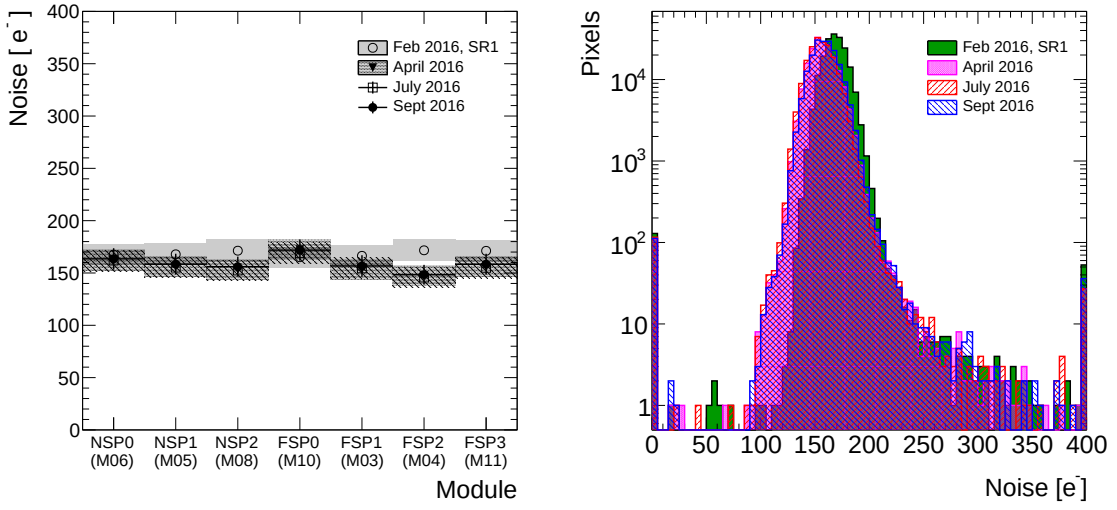

Figure 4.15.: Noise after calibration to a target threshold of 2,000 e^- in the installed AFP modules measured at different times. The left distribution shows the average noise for each tuning, while the right distribution shows the noise distribution for all the pixels.

of pixels masked per plane are shown in Fig. 4.16. Only one module had ∼4% of pixels masked, while for the rest of the planes the number of disabled pixels is below 1.5%.

4.3.3. Read-out Timing

For standard data taking with 25 ns bunch-to-bunch spacing, readout needs to be done in a single bunch crossing. The readout window can be reduced to one BC, that is, signals generated during one bunch crossing in the event are recorded. However a phase difference can exist between signal formation and clock. In such case, signals can be read-out over

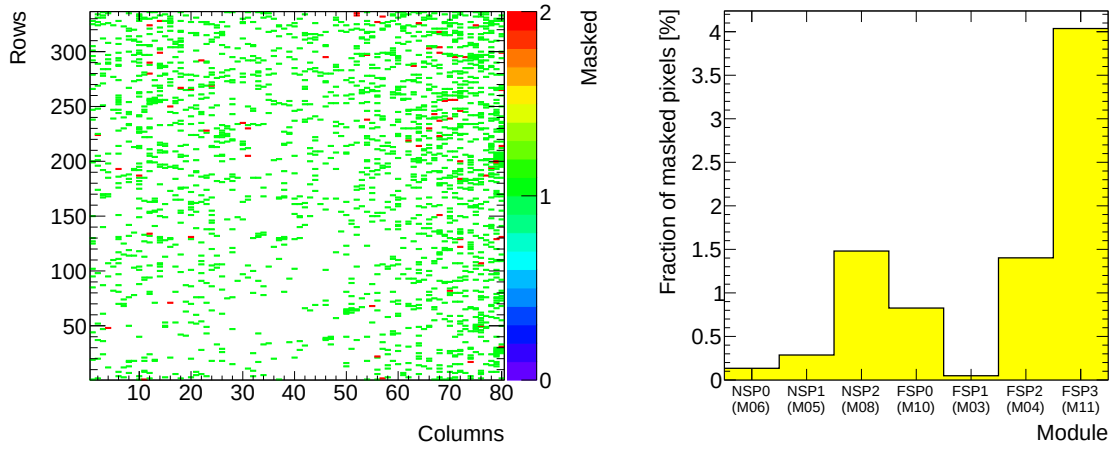

Figure 4.16.: Summary of all the masked pixels during AFP 2016 operation: pixels masked in all the modules (left) and the fraction of masked pixels for each module (right).

more than one bunch crossing as lower signals may arrive a bunch crossing late due to time-walk. If the detector is not corrected for such phase, it can lead to a large amount of events to be lost during a single-bunch-crossing readout data taking. In order to correct for that effect, the module read-out needs to be *timed-in* with the clock.

One feature of the AFP readout system is the ability to add an offset to the data output of each pixel module in units of 1/8 of a bunch crossing, which is exploited for the detector timing-in.

During a large bunch spacing fill with collisions[3], data was taken with different phase offsets or "phase parameters", with a time difference of 3.125 ns. This is called a *timing scan*. The timing scan is performed with a read-out window of 4 BC. Then, for each phase step the in-time efficiency is measured by calculating the fraction of hits recorded in a particular bunch-crossing over the total number of hits. This is determined for low (ToT$<$5) and high (ToT$\geq$5) signal hits to account for time-walk (see Fig.4.17, left). The phase for which the in-time efficiency for high signal hits is largest is taken as the operational value. The effect of the time-walk in the in-time efficiency can be seen in Fig.4.17 (right), where the in-time efficiency is plotted as a function of the ToT response for the operational phase values ($\pm$1): the efficiency greately drops for the lowest ToT, as they are read-out 1 BC later.

During the hit read-out, the FE-I4 chip uses a digital threshold to recognize low ToT hits which can cause time-walk. This threshold is defined by the HitDiscConfig register (see Sec. 3.3.1). Events with low ToT (i.e. with ToT$\leq$HitDiscConfig) hits are encoded as "small hits" or "late hit" in the same bunch crossing as the high ToT hits, correcting for time-walk. Fig. 4.9 shows the obtained in-time efficiency with two different settings of the HitDiscConfig chip register. By setting the threshold for small hits to ToT$\leq$2, the operational value for data taking, an in-time efficency of about 99% can be obtained for any hit.

It is interesting to observe the time behaviour of the module with no operational bias voltage (Fig.4.17, bottom). Without bias voltage, the silicon bulk is under-depleted and the charge collected is lower and, hence, it suffers from time-walk more often. This translates into a higher signal time spread and thus lower in-time efficiency, in addition to the already low hit reconstruction efficiency.

[3]In such conditions, the LHC accelerator is filled with bunches of protons with a distance of several bunch crossings from one another.

Table 4.9.: In-time efficiency measured for each of the AFP planes at their optimal phase parameters. The read-out chip can record low ToT hits (with ToT≤HitDiscConfig) as late hits to correct for time-walk. In bold it is shown the results for the final operational parameters.

	HitDiscConfig 0			**HitDiscConfig 2**		
	ToT<5	ToT≥5	All	ToT<5	ToT≥5	**All**
NSP0	53.0%	99.7%	90.0%	92.7%	99.5 %	**98.9%**
NSP1	54.9%	99.6%	89.0%	93.6%	99.4%	**98.8%**
NSP2	74.9%	99.7%	93.6%	99.0%	99.6%	**99.5%**
FSP0	1.9%	67.4%	55.3%	2.1%	69.0%	**61.9%**
FSP1	63.2%	99.5%	92.3%	94.0 %	99.2%	**98.7%**
FSP2	56.5%	99.3%	90.6%	84.9 %	99.1%	**97.7%**
FSP3	55.5%	99.7%	90.0%	90.0 %	99.6%	**98.6%**

4.3.4. AFP Insertions

Roman pot insertion is done from the CERN Control Center (CCC) by an automatic sequence, which moves the pots to the position determined during beam-based alignment (BBA, see below). A system of springs in the Roman Pots retract the pot in case the motor power is lost or switched off by emergency retraction. The position of the Pots are monitored at all times by the station's motor and a Linear Variable Differential Transformer (LVDT). Whenever the position is measured to be 250 μm closer to the beam than the nominal one the beam is dumped for safety, and as a consequence the Pots are retracted (a warning message is issued at a position 200 μm closer than the target position). These limits, as well as the nominal position, are set based on the BBA results.

The Roman Pots are inserted at a nominal position of 20σ (where σ refers to the beam width at the each station's position) from the beam centre, which corresponds to 2–4 mm (the beam is wider in the Near station). The only exception is during the beam-based alignment and loss maps procedures, described in the following section.

Table 4.10 shows all the instances in which the AFP detector was inserted into the LHC beam pipe.

Table 4.10.: Summary of AFP insertions in 2016

Date	Fills with AFP inserted	TDAQ Mode	
19-22 April	1st Alignment and Loss Maps	AFP only	Commissioning
23 April	3 bunches	AFP only	Commissioning
24-25 April	12 bunches	AFP only	Commissioning
7 May	49/86 bunches	with ATLAS	Commissioning
9 May	300 bunches	with ATLAS	Commissioning
13 May	600 bunches	with ATLAS	Commissioning
1 August	600 bunches	with ATLAS	Physics ($\langle\mu\rangle \sim 0.03$)
21 September	2nd Alignment and Loss Maps	with ATLAS	Commissioning
8 October	600 bunches	with ATLAS	Physics ($\langle\mu\rangle \sim 0.3$)
14 October	100 bunches	with ATLAS	Commissioning

Beam Based Alignment and Loss Maps

In order to determine the position of the Roman Pot floor with respect to the proton beam, and hence the nominal data taking position, the *beam-based alignment* procedure

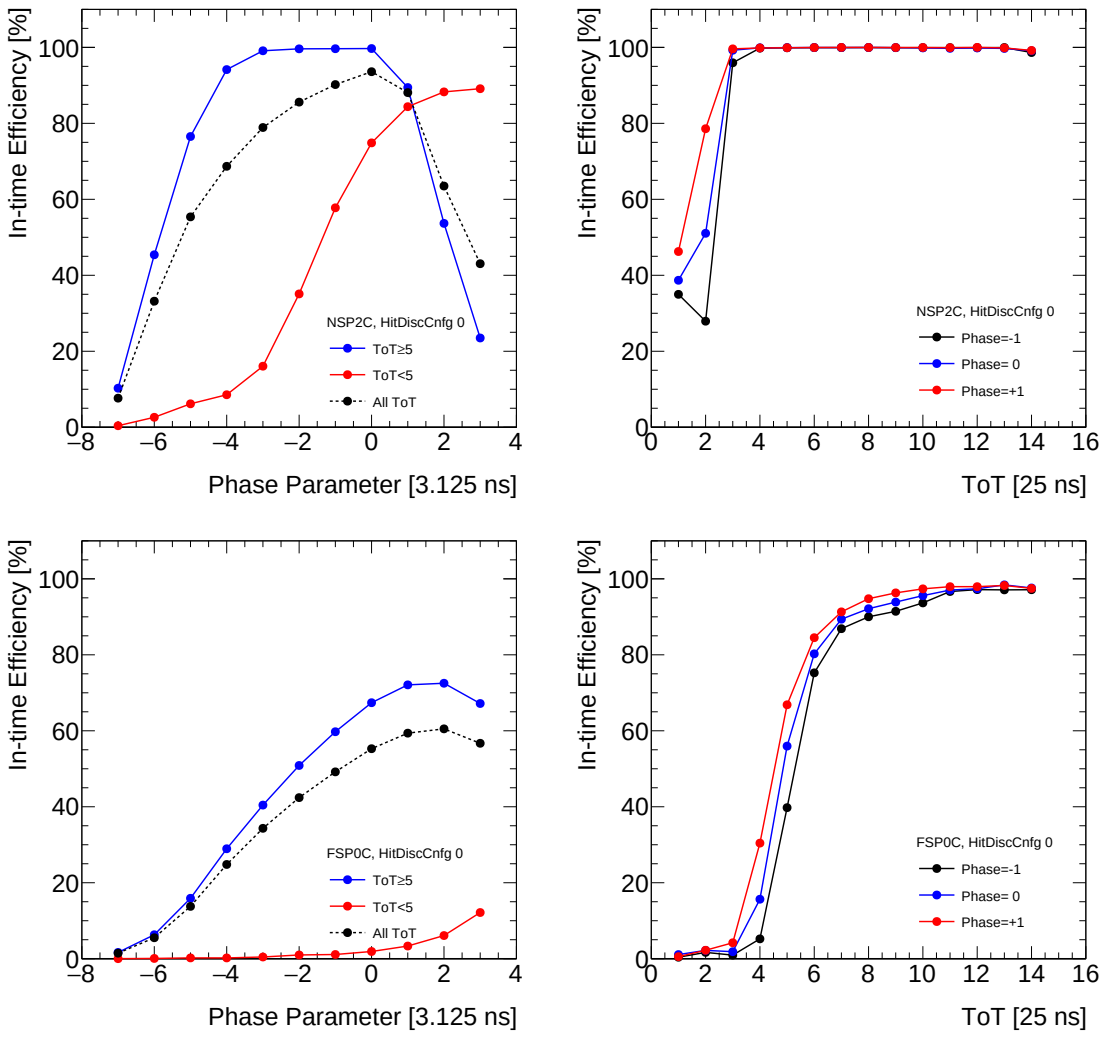

Figure 4.17.: Results from timing in two AFP detectors: the in-time efficiency, i.e. the fraction of hits read-out in a certain bunch-crossing since the L1 accept signal as a function of the time phase parameter in units of 3.125 ns (left) and the in-time efficiency as a function of ToT response for three phases around the optimal (right). Here, the phase parameter 0 is defined as the values used for data taking, using a HitDiscConfig value of 0 (see text). The top plots show the results for Near station Plane 2, with an operational bias voltage of 10 V, while the bottom results show the equivalent for Far station Plane 0, i.e. a module operated with no bias voltage.

is performed. To do so, the beam is trimmed by a collimator in the LHC to a known beam size. The actual size varies at each position in the accelerator, however, the width σ is constant along the ring. The Roman Pots are slowly inserted towards the beam-pipe centre while the beam is circulating. In parallel the activity in the Beam Loss Monitor (BLM) sensors placed nearby the position of the stations are monitored. When the Pot reaches the trimmed proton beam, the rate observed in the BLM steeply increases. As the beam size at each position along the accelerator is known from simulations, the position with respect to the beam centre can be calculated. Afterwards, the Pot gets retracted by 2σ and the same procedure is repeated with another station until the BBA is completed for all the stations.

The beam based alignment is followed by the *loss maps* procedure. The goal is to

determine how safe it is to position the Pots at nominal data taking distance from the beam. For this, the RPs are moved to the nominal position (20σ). Then, the beam orbit is distorted in position and transverse momenta: the beam should never touch the Roman Pots. Hence, no rate increment should be observed in the BLMs.

Both procedures are performed in dedicated fills and they are mandatory before taking data for the first time after installation,when the beam optics have changed and/or after any intervention in the RP in which the movement could have been potentially modified, as they define the physics position (BBA) and show whether it is safe to position the Pots close to the beam (Loss Maps). During the year 2016 two BBA were performed, the results of which were used in the AFP physics runs (see Sec. 4.3.4) and are contained in Table 4.11.

LHC Luminosity Ramp-up

After a technical stop period, LHC operation is re-started by increasing the luminosity from run to run until reaching nominal intensity. This process is called *luminosity ramp-up*. This is performed by increasing the number of proton bunches in the machine that circulate inside both LHC beam-pipes. Each proton bunch has a revolution frequency of ∼11 kHz, and the injection (or *fill*) has a structure in time (*bunch structure*), segmented in units of bunch crossings (25 ns). In addition, only paired bunches can produce collisions, i.e. the same bunch crossing contains a proton bunch in each of the LHC beams. During the luminosity ramp-up, the number of paired/colliding bunches per fill is increased in steps from one to ∼2000, usually every 3 fills[4]. Hence, this process can take several weeks in the case of periods after year-end technical stops (the number of steps are reduced after other technical stops and machine development periods).

In order to validate that the Roman Pots at beam position do not impose a danger to the normal LHC operation at high intensities, AFP is inserted in each of the luminosity steps, normally at the end of the second fill and at the beginning of stable beams of the third fill of each luminosity step.

During these fills the average pile-up was nominal, and therefore the data of such runs is not useful for physics analysis without the Time-of-Flight detector available. However, it served to study the behaviour of the detector.

Fig. 4.18 shows the hitmap of one of the planes in AFP taken during a run with 300 colliding bunches, which shows the expected behaviour of diffractive protons (see Fig. 3.14) with little contribution from the beam-halo. The hit multiplicity in the same plane for the same run is shown in Fig. 4.19. A peak at two hits per event is observed, which is expected due to the 14° tilt of the sensor planes. Moreover, the correlation between consecutive planes was observed during this run, which also indicates a good detector behaviour.

The trigger rate as a function of number of colliding bunches was monitored to study the trigger formation. It was observed a non-linear dependence between trigger rate and number of bunches, and hence with luminosity (see Fig. 4.20). It was concluded that this effect is a consequence of the length of the trigger signal leading to dead time. The trigger signal generated from the HitOr from the modules has a length equal to the ToT, which follows a Landau distribution, with a typical length of 5–10 bunch crossings. In cases where the bunch-to-bunch spacing is significantly greater than that, the length of the trigger signal will be short enough to allow a new trigger signal in the following filled bunch. However, as the bunch spacing decreases, it starts to be more probable for two trigger signals to overlap. In such scenarios only the first trigger signal is seen. Fig. 4.21 showcases this effect: in this example, two trigger signals of 5 bunch crossing lengths are generated. In the first scenario, the hits arrive with a difference of 7 clock cycles in time and therefore the two triggers are recorded separately. In the second scenario, however,

[4]Each injection can last few hours, and the fill can last longer than 12 hours with stable collisions before being dumped.

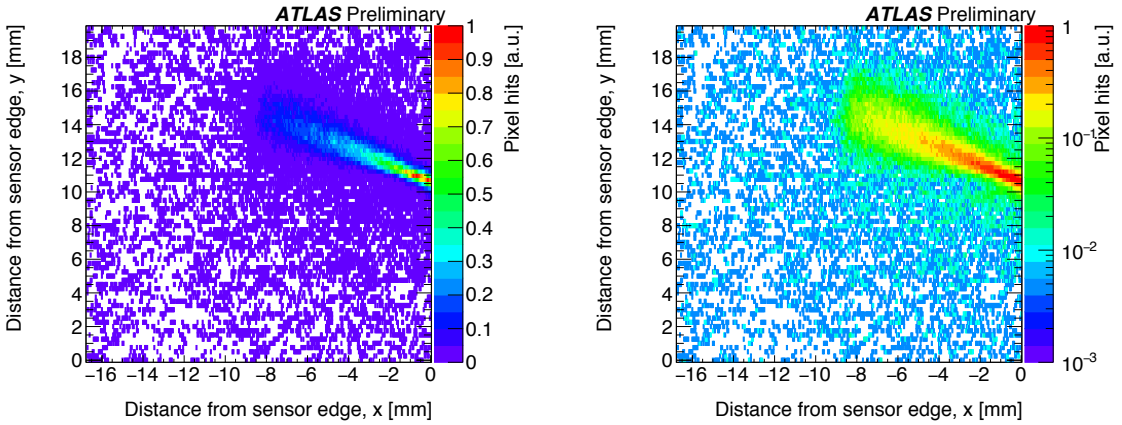

Figure 4.18.: Number of raw unclustered pixel hits in arbitrary units of a tracker plane in the Near Station side C (205 m from the ATLAS interaction point) in the AFP detector in linear (left) and logarithmic scale (right). Distances are in the local reference frame of the plane. The data was taken during the 300 bunches LHC luminosity ramp-up step (10th of May 2016) at nominal 20 sigma position from the beam. AFP was triggered by ATLAS triggers. The diagonal line corresponds to the detected diffractive protons.

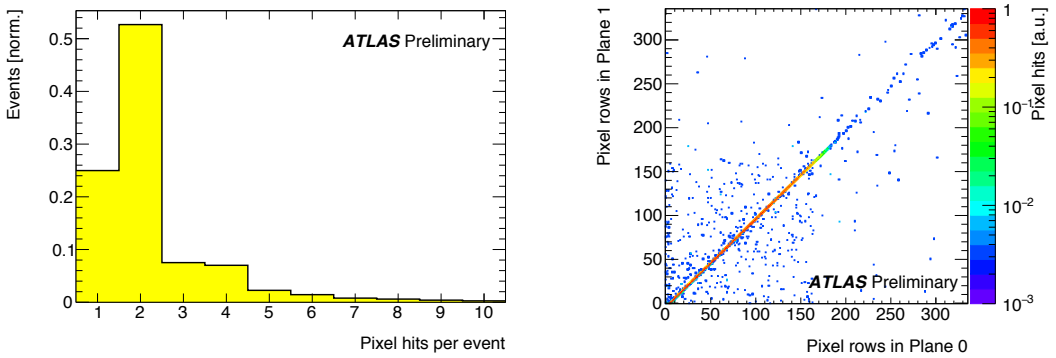

Figure 4.19.: Number of raw un-clustered pixel hits per event (left) of a tracker plane and the pixel row correlation between hits in two consecutive tracker planes in the Near Station side C in the AFP detector. The correlation is done with events with maximally two hits to avoid events with too many hits (multi-particle events and delta-electrons). The data was taken during the 300 bunches LHC luminosity ramp-up (10th of May 2016) at nominal 20 sigma position from the beam. AFP was triggered by ATLAS triggers. The tracker planes were installed at a tilt of 14° (in x-direction) so that each particle is expected to typically fire 2 pixels.

the trigger signals arrive in 2 BC distance, which result in a single trigger 7 BC long, reducing the rate over the first case. This effect has a higher impact at higher luminosities and with higher number of colliding bunches, which means that triggering from the silicon tracker is mostly useful for low luminosity runs. At higher luminosities (for physics) a lower dead-time trigger from AFP is needed (in 2017 a ToF trigger has been implemented).

AFP insertions were stopped at 600 bunches since it was observed that its presence in beam position increased the radiation in the ALFA detector (see Sec. 2.2.5) to levels that could make the ALFA detector unusable. In order to continue the program of the AFP

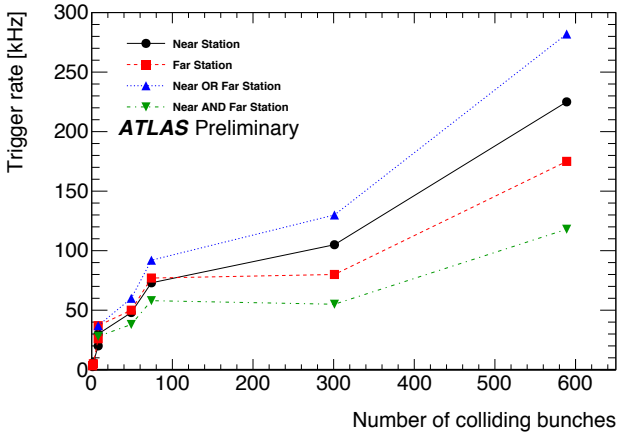

Figure 4.20.: Trigger rates sent from the AFP detector at nominal 20σ position from the beam as a function of number of colliding bunches during LHC luminosity ramp-up after YETS 2015-2016.

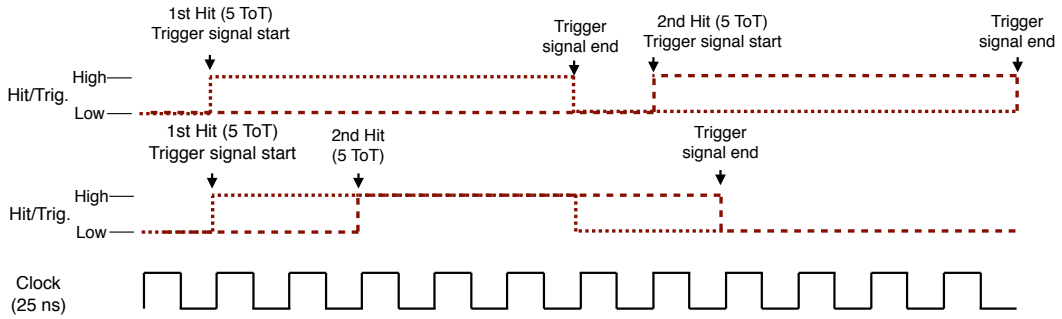

Figure 4.21.: Sketch showing the trigger rate effect of the bunch crossing spacing. Two hits are recorded in the same station, with an overall length of 5 bunch crossings each. In the top scenario, the two hits are separated by 6 clock cycles, so both triggers are recorded individually. In the bottom scenario, the two hits arrive with 2 clock cycle difference, hence the trigger signals resulting from the two hits are merged into one.

detector while securing the ALFA detector, a limit of 600 bunches and a total luminosity limit with the Roman Pots inserted was agreed.

AFP Physics Runs

In 2016 the one-arm AFP detector was installed without a Time-of-Flight system. The lack of Time-of-Flight detector implies that there is no possibility of pile-up removal, i.e. it is not possible to determine from which proton-proton interaction the diffractive proton measured in AFP comes in high pile-up conditions. This is the case for standard LHC runs in ATLAS where the average number of collisions is about 25 every (filled) bunch crossing (during 2016). For this reason, data useful for AFP physics analyses needs to be taken in low pile-up special runs.

In order to achieve low pile-up the luminosity needs to be lowered while maintaining the same bunch crossing frequency (Eq. 2.4). This can be achieved without modifying the beam optics either with lower intensity bunches or by beam separation. The beam

separation approach, used to reduce pile-up in special runs for AFP, consists in increasing the distance between the beams at the ATLAS interaction point by few beam widths (σ) so that only the protons from the tails of the beam distribution collide.

Two special AFP physics runs were taken during 2016:

- Run 305359 (fill 5151): A very low pile-up run ($\langle\mu\rangle \sim 0.03$).
- Run 310216 (fill 5386): A low pile-up run ($\langle\mu\rangle \sim 0.3$), on which the analysis presented in the next chapter is based.

In all the runs, the AFP tracker was sending triggers to the ATLAS Level-1 system, which allowed the use of AFP-based triggers. In particular the logical AND of trigger signals between the Near and Far station was used for the implementation of the trigger items. Data taking parameters during these special runs are summarized in Table 4.11.

Table 4.11.: Data taking and beam parameters during runs 305359 (fill 5151) and 310216 (fill 5386). All positions are expressed with respect to the nominal beam position. The station positions are the distance from the Roman Pot wall to the nominal beam 1 position, the position of the edge of the detector to the wall of the Roman Pot is still unknown.

Parameter	Run 305359	Run 310216
LHC fill number	5151	5386
Colliding bunches at IP1	578 bunches	589 bunches
Betatron at IP1 (β^*)	0.4 m	0.4 m
Mean pile-up ($\langle\mu\rangle$)	0.017–0.034	0.24–0.30
Beam separation at IP1	$5.0\sigma_{hor}$, 1.0–$2.5\sigma_{vert}$ [a]	5.0–$5.2\sigma_{hor}$
Beam centre at Near station	1.495 mm	1.612 mm
Beam width at Near station (σ_{NS})	0.202 mm	0.202 mm
Near station position (20σ)	5.535 mm	5.652 mm
Beam centre at Far station	0.362 mm	0.419 mm
Beam width at Far station (σ_{FS})	0.108 mm	0.108 mm
Far station position (20σ)	2.522 mm	2.579 mm
TCL4 collimator position	8.57 / -10.00 mm (15.1σ)	8.77 / -9.82 mm (15.1σ)
TCL5 collimator position	10.96 / -12.51 mm (35.2σ)	11.26 / -12.22 mm (35.3σ)

[a] Since the pile-up decayed over time, the vertical beam separation was re-adjusted from 2.5 to 1.0σ in in order to recover the ∼0.03 mean pile-up, see Fig. 4.22. In the second low-μrun CMS was running with reduced luminosity as well by beam separation, reducing the usual luminosity decay over time which caused the decrease in pile-up in the first run.

In an AFP physics run, the LHC normally fills the machine with the agreed fill structure to reach stable beams at nominal luminosity and pile-up. At stable beam conditions all collimators are in their standard position. Then, the collimator TCL5, placed before AFP at 190 m from the IP, opens up to 35 times the width of the beam at that position (i.e. $35\sigma_{beam,TCL5}$) and briefly after the AFP Roman Pots are moved into data taking position. In order to reduce pile-up, the proton beams are separated at the interaction point until the desired (and agreed) μ is achieved. During all this procedure, both ATLAS and AFP are taking data. Fig. 4.22 shows the average pile-up during the two low-μ runs as a function of *luminosity block*, which is a period of time (∼1 min) during which the data taking conditions are considered constant.

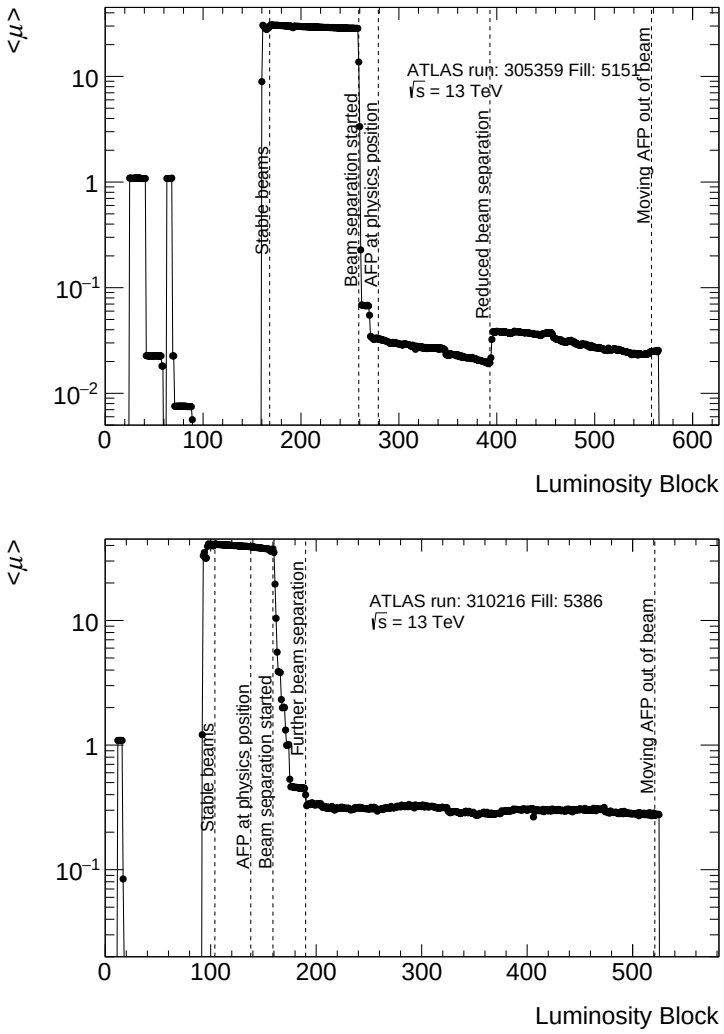

Figure 4.22.: Average pile-up as a function of luminosity block (∼1 min) during run 305359 (fill 5151, top) and run 310216 (fill 5386, bottom). The times in which AFP was inserted/removed from the proton beam, and the times where beam separation was performed are indicated in the plot with dashed lines.

5. Performance of AFP: Selection of Single Diffractive Events

Proton–proton collision data was successfully taken in 2016 a few months after the installation and commissioning of the AFP detector. As described in the previous chapter, the detector consisted only in silicon trackers at one side of ATLAS during that year. The aim of the early measurements was to gain experience in the operation of the detector.

This chapter describes a first study on the performance of the AFP detector in triggering diffractive-like events, using the data obtained in a special low pile-up run during the year 2016. The goal was to observe a correlation between the protons observed by the AFP silicon tracker and the diffractive signatures as measured in the ATLAS calorimeter.

5.1. Introduction

Diffraction is a phenomenon taking place in hadron collisions, when no quantum numbers are exchanged. While in proton–proton collisions diffractive interactions are usually soft processes that significantly contribute to the total cross section, the possibility of probing the partonic structure of diffraction by measurements of high-p_{T} jets produced in diffractive events was first proposed by Ingelman and Schlein [125]. Such events were then observed in $p\bar{p}$ interaction at the CERN SPS collider by the UA8 experiment [13], which measured produced jets and a diffractively scattered intact anti-proton.

The discovery of diffractive jets opened a new topic of research in hadron physics – hard diffraction. It has been extensively studied at HERA and Tevatron as well as on the theory side, but today the diffraction mechanism is not yet fully understood.

Diffractive production of jets has already been studied at the LHC by the ATLAS [24] and CMS [25] experiments. In both measurements, the diffractive events were distinguished from the non-diffractive ones by a different pattern of energy deposits measured in the calorimeters. With a forward detector like AFP, diffractive events can be selected by requiring a forward proton signature (see Sec. 1.2.1). Moreover, its use can extend such studies to high pile-up scenarios via a Time-of-Flight detector to determine the interaction vertex of the protons in the central ATLAS detector.

In this study, events triggered by the one-armed AFP detector with jets in the final state are selected from collisions obtained in dedicated low-μ runs, with the goal to prove that this event sample is enriched in diffractive events. The objective of the one-armed AFP configuration was to be able to reconstruct the kinematic parameters of the proton, using the position measurement in the two stations. However, by the time the analysis was performed, the kinematic reconstruction of the proton was still under development. Hence, to prove that proton tagged events (i.e. events triggered by forward proton detection at AFP) are diffractive rich, the silicon tracker position information from the AFP detector is correlated with the energy deposition in the ATLAS calorimeter.

5.2. Signal and background processes

The signal processes in this analysis are diffractive events of the form $pp \to pX$, where X is any combination of objects with at least one jet. In such events one of the protons emit

a Pomeron, which undergoes a hard scattering with the second proton, while the former leading proton leaves the interaction intact and escapes the ATLAS detector acceptance at very small scattering angles that can be detected in the AFP detector.

Due to the lack of a Time-of-Flight detector at the time of data taking the primary vertex from which the proton measured at AFP comes from is unknown. Even though the data used for this analysis was taken at low pile-up, background is dominated by pile-up events with one non-diffractive collision overlapped by a diffractive collision with a leading proton arriving at the AFP detector.

5.3. Observables

This section describes the observables used in the analysis: AFP tracker clusters, calorimeter clusters, jets, primary vertices, proton relative energy loss and rapidity gaps. Their reconstruction is presented as well.

5.3.1. AFP Silicon Tracker Clusters

The AFP silicon tracker measures the proton position in each of the tracker planes. The tracker planes are segmented into 336×80 pixels of 50×250 μm^2 pitch. However, due to charge sharing a single proton can produce a signal (hit) in more than one pixel in each plane, creating a *cluster* of hits. In fact, due to the 14° angle geometry, it is expected that each proton yields two hits in most of the events.

Clusters are reconstructed by grouping neighbouring pixel hits in the same event for each silicon tracker plane. Each cluster produces a measurement of the proton position: in this case, the centre-of-gravity algorithm is used, by calculating the average position weighted by the charge collection information (ToT), in the same way that was studied in previous test-beams (see Sec. 3.6.6).

For this analysis, one plane (Near station plane 0) was used as reference to measure the protons position since, when this analysis was performed, the AFP track reconstruction was in an early stage of development. Nevertheless, as seen in Chapter 3, the single-plane resolution in the short pixel direction is nearly 6 μm (in a 14° tilt configuration and with a ToT-weighting algorithm for centre-of-mass determination) and thus, this approach does not suffer from low position resolution.

In addition, the total charge deposited by the particle causing the cluster of hits can be estimated by the sum of the ToT of all the pixels included in the cluster, i.e. the *cluster ToT*. The silicon tracker modules were calibrated to a 2000 e$^-$ threshold and a response of 10 ToT units for a charge collection of 20000 e$^-$ (see Sec. 4.3.2).

5.3.2. Calorimeter Clusters and Jets

The ATLAS Calorimeter measures the energy deposition and their location of charged and neutral particles that penetrate the system. During reconstruction, the signals of all the calorimeter hits are corrected for local calorimeter channel defects, to form the *calorimeter cell*. The cells are clusterized as follows (*topological clustering*): the cluster seeds are found from cells with a signal $> 4\sigma_{noise}$. This threshold is later lowered to $2\sigma_{noise}$, and neighbouring cells to the seed ones are grouped together, and finally this process is repeated with all calorimeter cell signals. This process results in a collection of *calorimeter topological clusters* [126].

Jets are reconstructed from calorimeter topological clusters. In ATLAS, the default reconstruction algorithm is the anti-k_{T} algorithm [127], with a radius parameter $R = 0.4$. To reconstruct the jets in an event, the measured transverse momenta k_{T}^i are grouped according to the distance between them: the distances between all the objects are calculated, and

the nearest objects are clustered together. This procedure is repeated until all the objects are clustered in jets.

The reconstructed jets undergo a jet calibration procedure that accounts for pile-up effects and detector features [128]. First, the jet p_{T} is corrected for possible contributions from additional pile-up activity, and thus removes the pile-up and number of primary vertices dependence of the jet p_{T} measurement. Then, the jet energy is corrected for the detector jet energy response as a function of pseudo-rapidity. Finally, jets are corrected for differences in the jet response between data and MC simulations.

In this study, a jet is required to have a minimum transverse momentum of $p_{\mathrm{T}} \geq$20 GeV (or $p_{\mathrm{T}} \geq$30 GeV) after the jet energy calibration is applied.

5.3.3. Primary Vertices

A primary vertex is reconstructed from at least two tracks in the ATLAS Inner Detector [129]. Three algorithms are combined for track reconstruction [130]. The first one, the *inside-out algorithm*, starts from 3-point seeds in the silicon detectors (pixel detector or SCT) and adds hits compatible with the previous ones moving away from the interaction point using a Kalman filter, and extends the tracks into the TRT. The result is the track reconstruction of primary particles. In the *outside-in algorithm*, used to identify tracks from the decay of the primary particles, track searching is started from reconstructed TRT segments and are extended inwards by adding silicon hits not considered in the previous algorithm. Finally, the *TRT-standalone algorithm* reconstructs the remaining tracks not associated with any silicon track segment. Afterwards, tracks are associated to primary vertices, which, as mentioned before, must contain at least two tracks and its position needs to be consistent with the beam spot (the beam collision region). If a vertex fails the second condition, it is regarded as a secondary vertex, i.e. a vertex originating from the decay of a primary particle.

The primary vertices in the data sample used in this study were reconstructed so that each reconstructed track used for vertexing has a minimum transverse momentum of $p_{\mathrm{T}} >$100 MeV and a maximum pseudo-rapidity of $|\eta| < 2.5$.

5.3.4. Proton Relative Energy Loss

One of the signatures of a diffractive event is a proton that leaves intact the interaction point and loses a small amount of momentum in the collision. As a consequence, one can expect a low proton relative energy loss (ξ), which is defined as

$$\xi = \frac{E_0^p - E_f^p}{E_0^p}, \tag{5.1}$$

where E_0^p (E_f^p) is the proton energy before (after) the collision. In principle, the proton energy loss can be reconstructed from the AFP detector information. From the proton position measurement of each of the two stations, the proton trajectory along the beam pipe can be reconstructed. From that trajectory and the knowledge of the LHC beam optics, the kinematics of the proton (i.e. ξ and p_{T}) can be inferred. However, the reconstruction of the proton energy loss is only possible if the precise beam optics and the position of the detector with respect to the beam position are known, which was not the case at the time of performing this analysis. As an alternative, the ATLAS calorimeter information is used to reconstruct ξ (ξ_{cal}) [131]:

$$\xi_{\mathrm{cal}} = \frac{1}{\sqrt{s}} \sum_i p_T^i e^{-\eta_i}, \tag{5.2}$$

where the sum is over all calorimeter topo-clusters in the detector with p_T>200 MeV (to reduce the effect of the calorimeter noise). The same approach was used in other ATLAS diffraction studies without forward proton detection [24] where it was shown that ξ_{cal} is a good estimator of the proton relative energy loss. The sign in the exponent depends on the direction of the diffractive proton, however the AFP detector – and therefore the triggering proton – is at 210 m in the C-side of ATLAS (i.e. at negative pseudo-rapidities), thus only one sign needs to be taken into account, similarly to studies performed by CDF with Roman Pots [18].

It is worth noting that ξ_{cal} is a measurement of all activity in the calorimeter, while ξ depends on the leading proton energy alone. It is of course possible to have a measurement of ξ_{cal} even in non-diffractive collisions with no protons leaving the IP. Moreover, ξ_{cal} is sensitive to pile-up events. Since AFP requires a proton to trigger an event, pile-up events usually consist of a diffractive and a non-diffractive collision in the same event, which constitute the main background in the analysis.

However, the behaviour of ξ_{cal} in non-diffractive and diffractive events does differ:

- In a purely *non-diffractive* data set, the ξ_{cal} distribution is expected to be peaked at 1, i.e. all the beam energy is enclosed in the calorimeter, in the case of a 4π detector coverage. However, since some energy is lost due to detector efficiency and acceptance such peak is observed at lower values. In addition, there is a contribution from so-called proton-dissociation processes for which the proton remnants' transverse size is limited and would not give a signal in the forward region of the calorimeter, which translates into an exponential fall-off in the non-diffractive ξ_{cal} distribution. The shape of the fall-off depends thus on the acceptance of the ATLAS calorimeter.

- On the other hand, *single diffractive* events are expected to be softer than non-diffractive collisions with no signal of proton remnant in the direction of the diffractive proton. Therefore, diffractive events will accumulate at moderate ξ_{cal} (lower than 0.1). Moreover, a proton tag implies that the ξ_{cal} distribution is convoluted within the ξ acceptance of the proton tagger detector. Simulations have shown that the acceptance in ξ is $0.03 \lesssim \xi \lesssim 0.1$ for the optics nominal values in which low-μ data was taken in 2016 (see Fig. 5.1).

This variable will be used to determine the presence of diffractive events in the data set.

5.3.5. Forward Rapidity Gap

Large rapidity gaps are another diffractive event signature. The presence of rapidity gaps in diffractive events is due to the exchange of uncoloured objects like the Pomeron in the usual diffractive model. However, in diffractive proton-proton collisions, due to interactions of gluons and the presence of coloured proton remnants, it is difficult to preserve a region of phase space without coloured connections (gap survival probability).

The forward rapidity gap ($\Delta\eta^F$) is defined as the pseudo-rapidity range from the end of the calorimeter acceptance ($|\eta| = 4.9$) until the first instance of a calorimeter cluster of $p_T \geq 200$ MeV or track of $p_T \geq 200$ MeV (in $|\eta| < 2.5$). Bad quality tracks are rejected from the measurement (see Table 5.1). Due to the configuration of the AFP detector in the context of this analysis (only tracker detectors in the C-side, $\eta < 0$), it is possible to differentiate between the rapidity gap measured from the negative ($\Delta\eta^F_{z<0}$) and positive ($\Delta\eta^F_{z>0}$) edge of the calorimeter. In this way, e.g. $\Delta\eta^F_{z<0} = 3.2$ ($\Delta\eta^F_{z>0} = 3.2$) corresponds to an event with no calorimeter or tracker activity in $-4.9 < \eta < -1.7$ ($1.7 < \eta < 4.9$). Here, larger rapidity gaps are expected in the $z < 0$ edge of the calorimeter, which corresponds to the side of ATLAS in which AFP was installed.

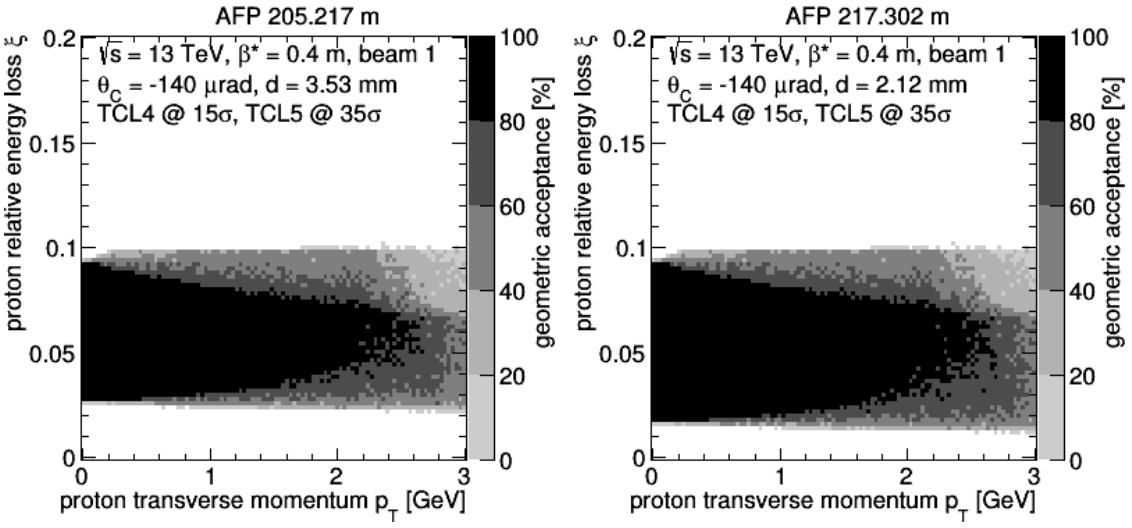

Figure 5.1.: Simulation of the AFP acceptance in ξ and p_{T} in the Near (left) and Far (right) stations with the nominal optics parameters in the AFP physics runs and inserted at 20σ from the LHC proton beam. Taken from [29].

Cut	Value
Minimum p_{T}	200 MeV
Maximum η	2.5
Maximum pixel holes	1
Minimum silicon (pixel + SCT) hits	7
Maximum silicon holes	2
No more than one shared module:	
– maximum shared pixel hits, or	1
– shared SCT hits	2
Minimum Si hits if the track has shared hits:	10

Table 5.1.: Track quality cuts used for the determination of the forward rapidity gap in the $|\eta| < 2.5$ region. A "hole" is defined as the absence of a hit in the track's trajectory.

5.4. Event selection

The data used for this study was taken during one of the two low pile-up physics run dedicated for AFP, run 310216, with an average pile-up of about 0.3, as described in Sec. 4.3.4. Although a lower pile-up would reduce the background events, as events with more than one primary vertex are less probable, problems in event reconstruction of the lower pile-up data set (run 305259) prevented its use for this study.

Run 310216 has a total of 86,062,100 recorded events, including data triggered by any of the active trigger signals. In the following sections, the event selection of the considered data set is presented.

5.4.1. Event Trigger

Events that satisfy the following two triggers are used in this analysis, and two sets of events are differentiated accordingly:

- "MBTS trigger" (`HLT_j10_L1MBTS_2`), where there has been two signals in the Minimum Bias Trigger Scintillator (MBTS) distributed in any side (i.e. two in side A

and none in side C, one in each side or two in side C and none in side A) at Level 1, and 10 GeV jets in the calorimeter has been reconstructed at High Level Trigger. Events that pass the triggers are treated as reference as they are dominated by non-diffractive events. During data taking, this trigger was heavily pre-scaled, by a factor 1999.9, i.e. only 0.05% of the total events that satisfy this trigger condition are recorded.

- "AFP trigger" (`HLT_j10_L1AFP_C_AND`), where both C-Near and C-Far stations have sent a trigger signal at Level 1, and a 10 GeV jet in the calorimeter has been reconstructed at the High Level Trigger. As opposed to the MBTS trigger, the pre-scale factor was set to 1.5–2.0 during data taking, i.e. 66.7%–50.0% (respectively) of the events fulfilling this trigger condition are recorded.

The same cuts are applied to the events in both categories when applicable. The goal of the analysis is to show that the AFP-triggered selection contains an excess of diffractive-like events compared to the minimum bias trigger.

The AFP L1 trigger signal generated from each station consists of a majority vote trigger logic, in which two out of three planes registered a hit. Therefore, at least four planes (two in each station) should send a trigger signal to produce a L1 AFP trigger. Only 0.28% of the events triggered by this signal have <4 AFP planes with hits, which could be caused by triggers arriving one bunch crossing late to the ATLAS trigger system (AFP triggers arrive in the last possible bunch crossing for each event). In addition, a cut on events with >4 SiT planes for the AFP-triggered selection is performed in order to ensure that both stations have registered a signal.

5.4.2. Good Luminosity Blocks

As mentioned in Sec. 4.3.4, data taking starts before AFP is moved into the beam. Therefore, only the events in luminosity blocks (groups of events taken during almost 1 minute of data taking during which similar detector conditions are assumed) where AFP was inserted in beam position are selected. Fig. 5.2 shows the number of events as a function of luminosity block after the full event selection (see Sec. 5.4.6), during which AFP was in physics position and ready to take data. The event rate is weighted by pre-scales to account for trigger configuration differences along the run. After corrections, the number of events per luminosity block is consistent with the average pile-up evolution (see Fig. 4.22).

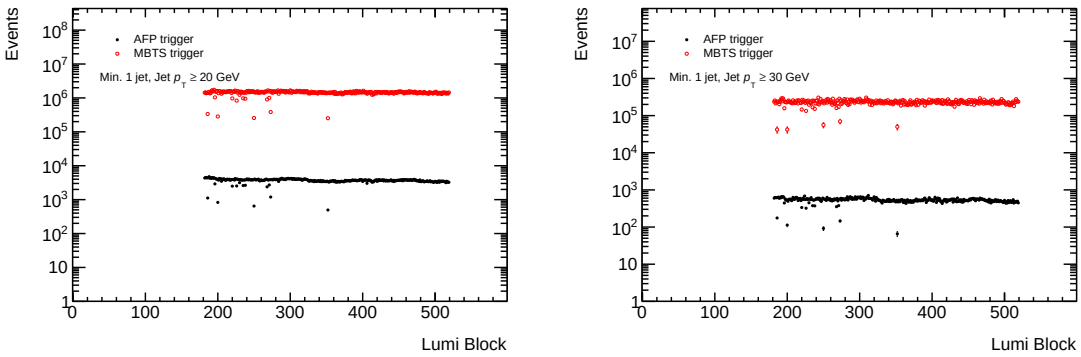

Figure 5.2.: Number of events vs Luminosity Block for Minimum Bias (red) and AFP (black) triggered data after full event selection (see Sec. 5.4.6), with $p_T \geq 20$ GeV (left) and $p_T \geq 30$ GeV. Events are weighted by pre-scale (AFP: 1.5 or 2.0; MBTS: 1999.9063) to correct for trigger configuration differences along the run.

The injection of proton bunches, i.e. groups of protons in pockets of 25 ns distance, into the LHC beam pipe is done following a bunch structure. The fill bunch structure in the data taken used for this analysis consisted in one isolated paired bunch, a train of 12 consecutive bunches, and 12 trains of 48 consecutive bunches. It was observed that events from the first isolated bunch and the train of 12 bunches showed a higher average number of primary vertices, indicating that the pile-up on such events was higher (see Fig. 5.3). Therefore, for the sake of uniformity, events from those bunches are discarded. Fig. 5.3 shows that $\langle N_{\text{vtx}} \rangle$ is systematically higher in AFP-triggered events, as will be discussed in Sec. 5.4.4.

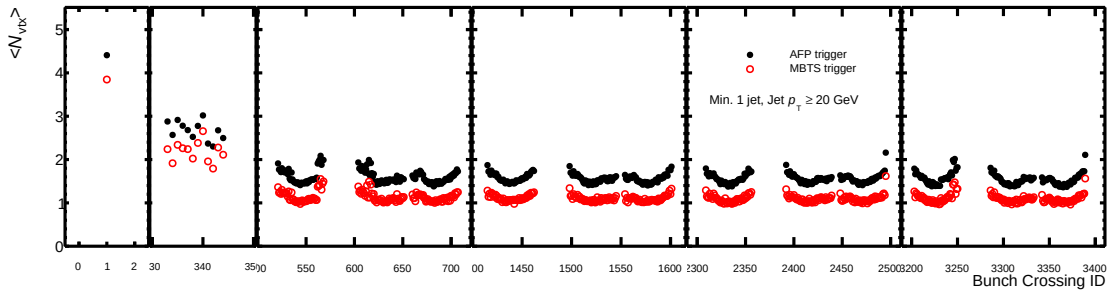

Figure 5.3.: Average number of reconstructed vertices as a function of the bunch crossing ID for Minimum Bias (red) and AFP (black) triggered data with $p_{\text{T}} \geq$20 GeV. The first isolated bunch and the 12 bunches train show a significantly higher $\langle N_{\text{vtx}} \rangle$.

5.4.3. Roman Pot Splashes

There is a non-negligible probability of protons interacting with the Roman Pot walls and the sensors themselves. In such cases the number of clusters in each plane is larger than one, which complicates the identification of the diffractive proton and therefore complicates the determination of its kinematic properties. Fig. 5.4 shows the number of clusters per event distribution for each of the stations. It can be observed how the distribution tail becomes larger at the farthest plane of each station. This could be caused by secondary interactions of the protons in the Roman Pots.

The events with more than one cluster per AFP plane are cut out to prevent such splashes, which removes 29% of the AFP-triggered events. A more sophisticated selection cut based on the track reconstruction could potentially recover a fraction of these events.

5.4.4. Primary Vertices

In Fig. 5.5 the number of primary vertices in AFP and MBTS data are shown. It is clear that the number of primary vertices is larger in AFP-triggered events than in MBTS-triggered events. Such difference can be explained as follows: both MBTS and AFP triggers select events with jets with p_{T}>10 GeV. However, AFP accepts events with a forward proton, which is more likely in events with larger number of interactions (or primary vertices), while the MBTS trigger does not favour any process. Therefore, events with more than one interaction are more likely to be triggered by AFP with respect to MBTS.

Even though the pile-up in the AFP special runs is small, events with more than one interaction are still possible. Then, non-diffractive events can be overlapped to single diffractive events, which can then trigger AFP. Events with more than one (or no) primary vertex are rejected. Moreover, it is possible that an overlap between single diffractive and

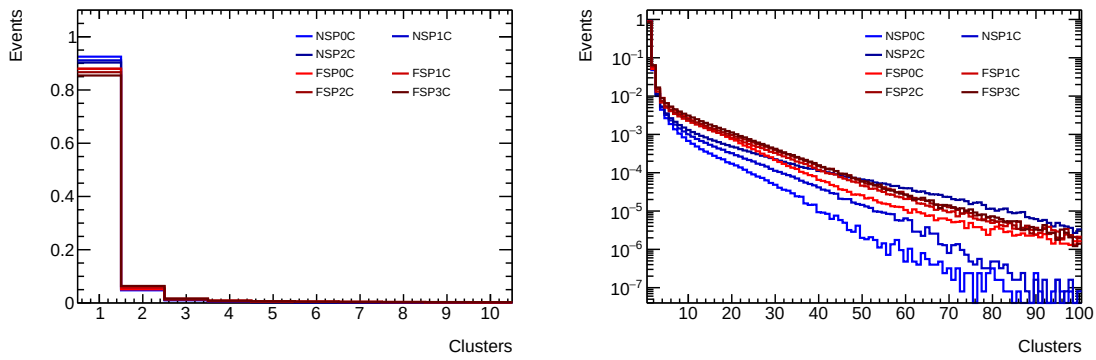

Figure 5.4.: Cluster number distribution for each of the planes from near (blue) and far (red) stations in linear (left) and logarithmic (right) scale. Darker shades indicate increasing plane number (hence larger distance from the interaction point).

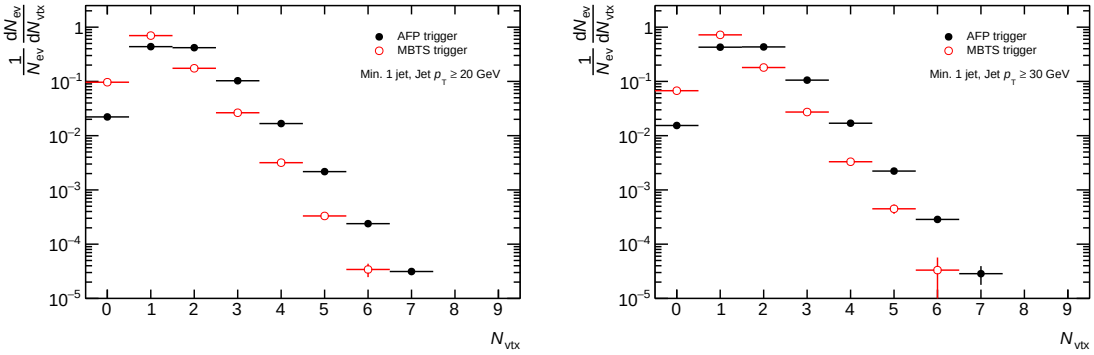

Figure 5.5.: Distribution of number of vertices before primary vertex selection for AFP triggered data (black) and Minimum Bias triggered data (red), with p_{T} ≥20 GeV (left) and p_{T} ≥30 GeV.

non-diffractive event happens in a two-interaction event but due to the tracking inefficiency of ATLAS only one primary vertex is reconstructed.

5.4.5. Number of Jets

Events with at least one reconstructed jet are selected. This jet needs to have a minimum transverse momentum of 20 GeV and a pseudo-rapidity of $|\eta| \leq 3.0$. The p_{T}^{jet} ≥30 GeV condition was also studied.

In order to remove the contribution of pile-up jets in the ξ_{cal} calculations, events which are likely to include pile-up jets are discarded. To this end, all jets in an event are required to pass the Jet-Vertex-Tagger (JVT) selection cut [132]. JVT is an estimator of the likelihood of a jet associated to tracks from a primary vertex originating from either a hard scatter event or a pile-up event. The JVT parameter distribution of all the jets in the working range of the Jet-Vertex-Tagger is shown in Fig. 5.6: the parameter ranges from 0 to 1, where 1 is the most likelihood that the jet originated from a hard scatter vertex, while jets with no associated tracks are assigned a JVT=-0.1. As this study is restricted to events with exactly one primary vertex, jets with no associated tracks originate from non-reconstructed pile-up vertices and, therefore are discarded. The abrupt drop in the JVT distribution is also a consequence of the one vertex event selection, which constrains

the possible values of the JVT likelihood.

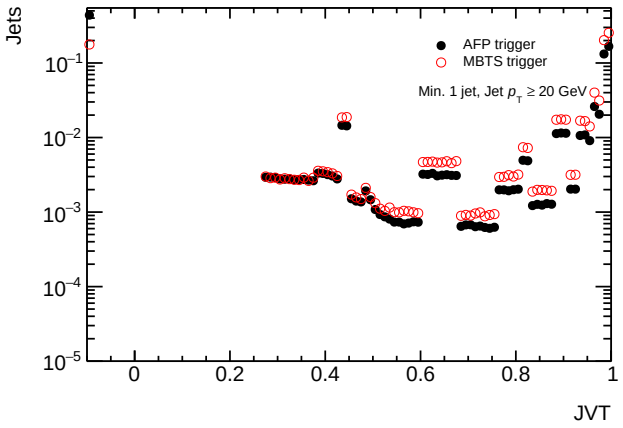

Figure 5.6.: Jet-Vertex-Tagger distribution for AFP triggered data (black) and Minimum Bias triggered data (red), with p_{T} ≥20 GeV in events with exactly one primary vertex. The value JVT=-0.1 is assigned to jets with no associated tracks.

5.4.6. Event Selection Cut Flow

A summary of the number of the surviving events after each consecutive cut described in previous sections is shown in Table 5.2. Pre-scales are not accounted, hence these numbers refer to raw number of events. After all the cuts are applied, the AFP data set contains 626,103 (90,644) events while in the minimum bias reference data set 242,878 (38,752) events are remaining when a jet p_{T} threshold of 20 GeV (30 GeV) is used.

	p_{T}^{jet} ≥20 GeV		$p_{\mathrm{T}}^{\mathrm{jet}}$ ≥30 GeV	
Cut	AFP	MinBias	AFP	MinBias
Trigger	12746376	1102281	12746376	1102281
Good Lumi Block	12687442	1084659	12687442	1084659
BCID Cut	7131166	965130	7131166	965130
Max 1 Cluster/AFPplane	5058433	–	5058433	–
Min 5 AFPplanes hit	5009137	–	5009137	–
All jets pass JVT	3874761	674817	3874761	674817
Min 1 jet with p_{T} ≥20/30 GeV, $\lvert\eta\rvert$ ≤3.0	1410055	333852	208833	50780
Exactly 1 Primary Vertex	626103	242878	90644	38752

Table 5.2.: Cut flow in Minimum Bias and AFP-triggered data with two different jet transverse momentum thresholds. Note that event numbers are not corrected for trigger prescales (AFP: 1.5 and 2.0; MBTS: 1999.9063).

5.5. Results

The characteristics of the events remaining after the event selection described in Sec. 5.4 are shown in this section. Non-diffractive events are dominant in MBTS-triggered events and hence MBTS is used as a reference to such events. AFP-triggered data is compared to that of the MBTS-triggered data sample to determine that the AFP proton tag is able to trigger on diffractive-rich events.

No full detector simulation was available at the time of performing this study which made the correction of the results for detector effects (like AFP detector acceptance) impossible to study and hence, most of the results shown in the following are regarded as "detector-level" measurements.

5.5.1. AFP Tracker

The position of the particle hit clusters in one AFP tracking plane (see Sec. 5.3.1) is shown in Fig. 5.7. The hit pattern is a consequence of the LHC beam optics. The distribution is compatible with previous simulation studies [29], which is an indication that the AFP detector was identifying diffractive protons during data taking as expected. It can be observed an accumulation of clusters below the diffractive proton band which could originate from beam background. However, this effect is negligible for the purpose of this analysis and orders of magnitude lower than the signal events.

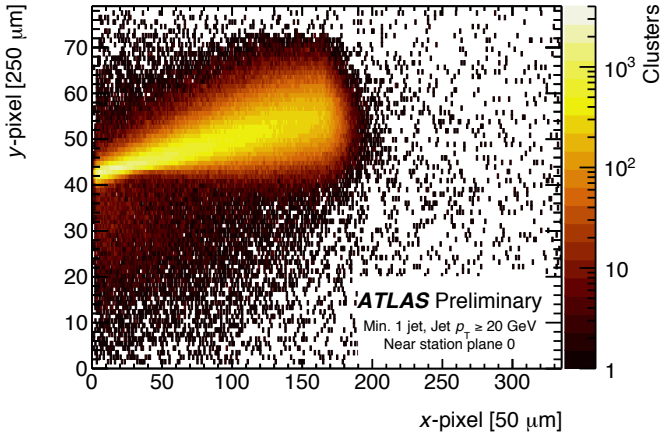

Figure 5.7.: The (x, y)-distribution of AFP clusters in a plane of the Near station ($z = -205$ m) for events with a jet satisfying $p_{\mathrm{T}} > 20$ GeV and $|\eta| < 3.0$ in the final state. The positions of the clusters are in pixel units (i.e. 50×250 $\mu\mathrm{m}^2$).

Fig. 5.8 shows the cluster ToT distribution averaged over six planes (with non-zero bias voltage). As expected, this distribution follows a Landau⊗Gaus distribution, and shows a most probable value (MPV) of 7.8 ToT, which translates to ∼15,600 e^- charge collection, compatible to the expected MPV for a minimum ionizing particle in 230 μm of silicon at 14° (about 16,500 e^-). The cluster ToT distribution of Far station plane 0 shows a peak in lower values (blue histogram in Fig. 5.8) since it was operated without bias voltage and hence below the full charge collection regime (see Table 4.8).

5.5.2. Jets in Event Selection

The jet multiplicity after the event selection is shown in Fig. 5.9 (top). It can be observed how the number of events with high jet multiplicities is slightly lower in the AFP-triggered sample, which could be related to the fact that the proton triggering the forward detector contains a large fraction of the collision energy. However, the p_{T} distribution of the leading (highest p_{T}) and second-leading (second highest p_{T}) jets shown in Fig. 5.9 (middle and bottom, respectively), shows a similar distribution for either trigger selection.

Since AFP has acceptance in detecting forward protons (with $\gtrsim$90% of the original beam energy) along the $z < 0$ side of ATLAS, it is expected an asymmetry in the η distribution of jets. This is observed in the η distribution of leading and second-leading

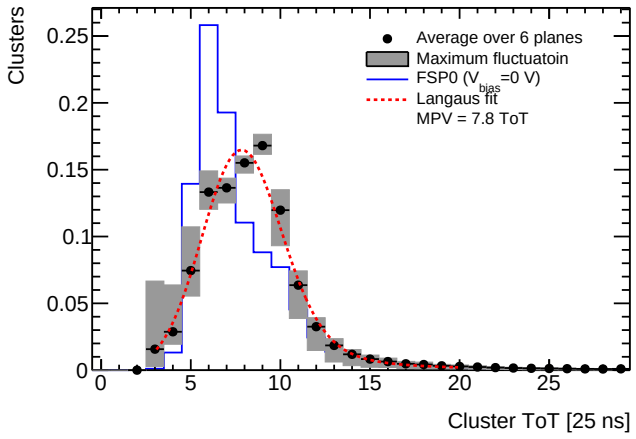

Figure 5.8.: Average cluster ToT distribution of all planes, except Far station plane 0 (with $V_{bias} = 0$ V). The bands indicate the fluctuation along the planes.

jet in Fig. 5.10: while jets are mostly symmetric around $\eta = 0$ in the MBTS data sample, the AFP-triggered events show a jet distribution more populated in the $\eta > 0$ region. This is a first indication that the events measured in the AFP detector and the central ATLAS detector are correlated.

5.5.3. Diffractive Signatures

The measured ξ_{cal} distributions at detector level obtained with either AFP or MBTS triggers are presented in Fig. 5.11. The most notable feature is the double peak structure in the AFP-triggered data. The lower peak corresponds to events where AFP detected a proton with energy in the central detector system significantly lower than in the MBTS sample, a strong indication of a diffractive process. This basically demonstrates that the main objective of the AFP as a detector system has been achieved. The higher peak in the ξ_{cal} distribution of the AFP-triggered data, which is similar to the MBTS based distributions, is understood in terms of pile-up effects in which a non-diffractive process overlaps with a diffractive one or beam-halo particles that generates a signal in the AFP detector.

The MBTS-triggered distribution is normalized so that the distribution peak bin (-0.70$<\xi_{\text{cal}}<$-0.65) matches the AFP data at the observed peak at large ξ_{cal}, which allows for a shape comparison and an approximate estimation of the size of the background contribution under the diffractive peak at low ξ_{cal}. The normalized MB-triggered distribution provides a good description of the large ξ_{cal} region.

Figure 5.12 shows the correlation between the x-position of the clusters in the first plane of the Near station and the measured ξ_{cal} of the event from the AFP-triggered data. Two different populations can be distinguished. For low ξ_{cal} values, a clear $x - \xi_{\text{cal}}$ correlation is observed, indicating the presence of diffractive events. This correlation is a consequence of the effect of the LHC machine dipoles and quadrupoles modifying the position of the leading protons according to their energy (and therefore, as a function of ξ_{cal}). On the contrary, for the population at larger ξ_{cal} values, there is no such correlation, confirming that the events in this region are due to pile-up effects.

Another signature of diffractive processes is the presence of large rapidity gaps in the detector. Figure 5.13 shows the uncorrected normalized forward rapidity gap $\Delta\eta^F_{z<0}$ and $\Delta\eta^F_{z>0}$ distributions at the detector level for the AFP and MBTS trigger data sets. The integral of both distributions were normalized to the unity. The $\Delta\eta^F_{z<0}$ distribution for the

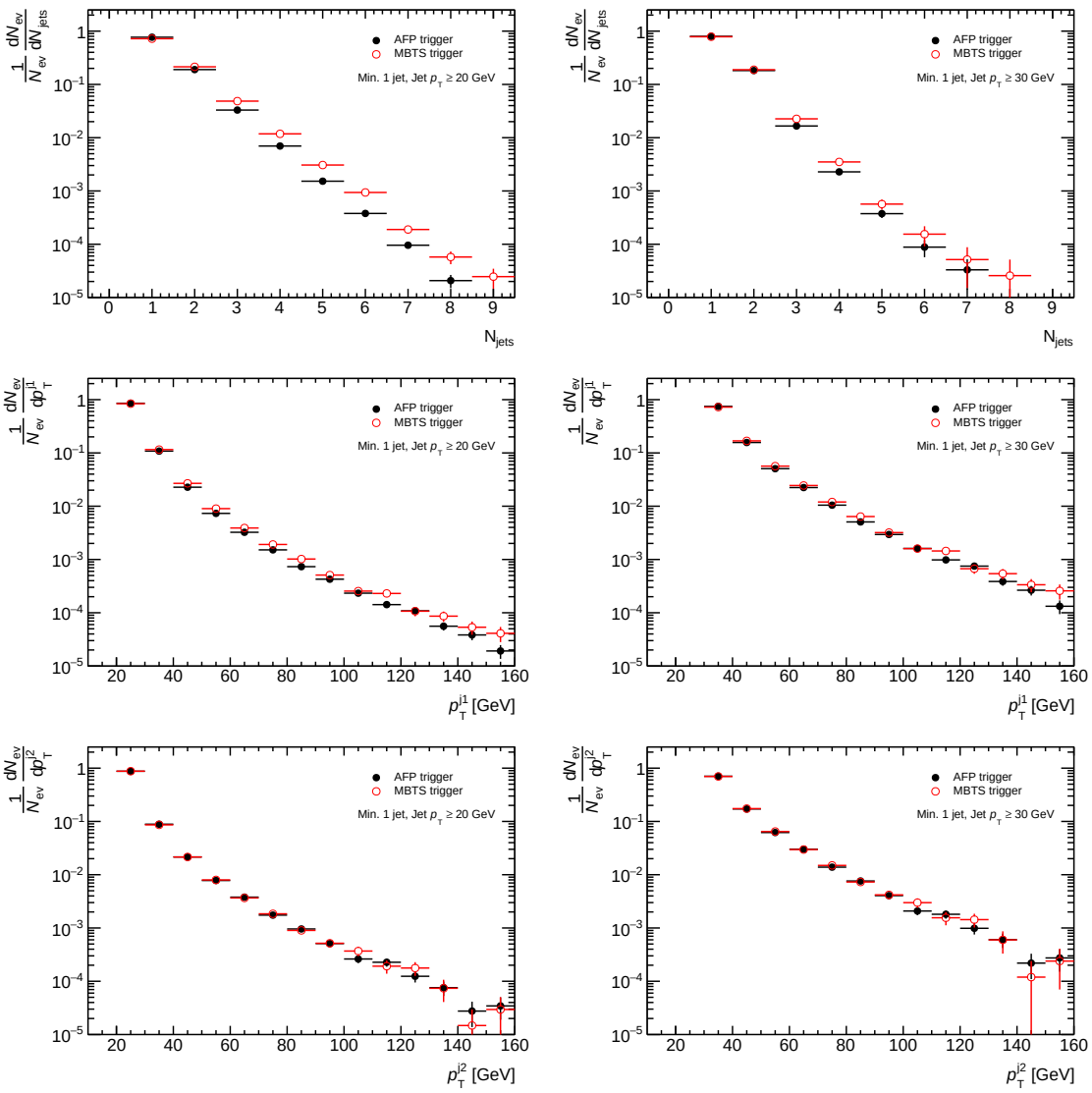

Figure 5.9.: Top: jet multiplicity per event in the AFP and MB selected data samples for events with at least one jet with $p_T > 20$ GeV (left) and $p_T > 30$ GeV (right) and $|\eta| < 3.0$. Middle: measured transverse momentum distribution of the leading jets (highest p_T (left)), for the same event selection. Bottom: measured transverse momentum distribution of second-leading jets (second highest p_T) for the same event selection. The area under all distributions are normalized to the unity.

AFP-triggered data shows a more prominent tail towards large values compared that of the MBTS data, indicating that the AFP-triggered sample is enriched in diffractive processes compared with the MBTS sample. It can be observed how the rapidity gap distribution on the AFP-triggered data approaches that of the MBTS-triggered data in the $z > 0$ direction, as the proton tagging is performed in the $z < 0$ direction.

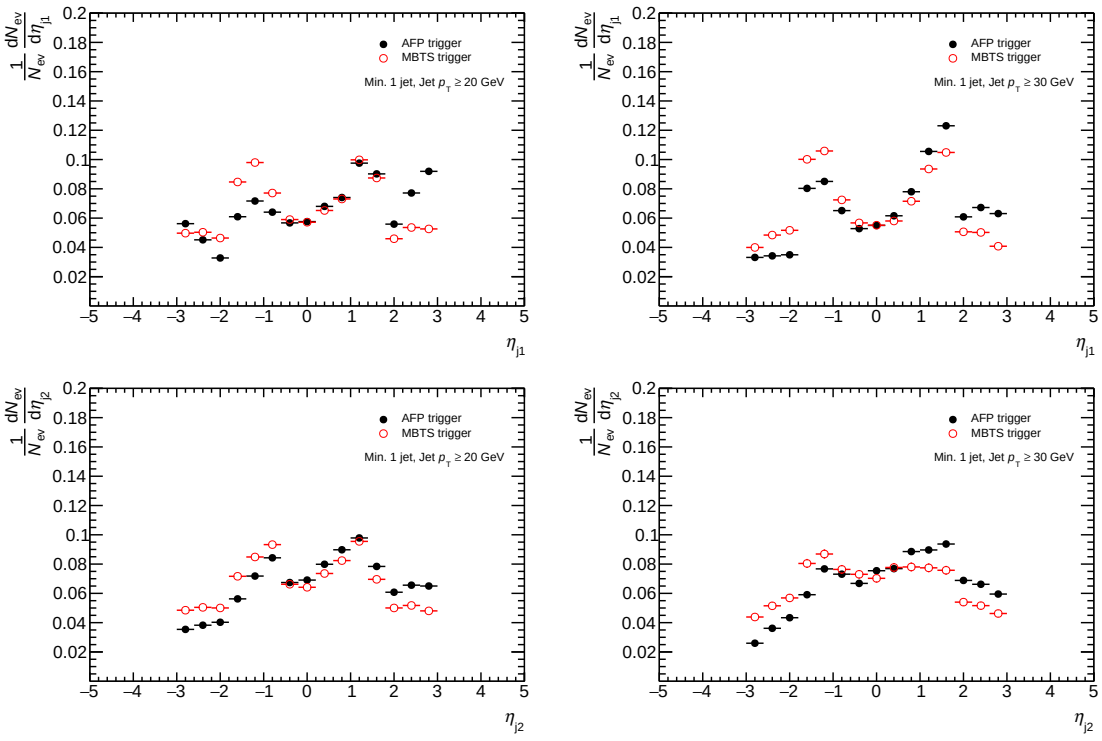

Figure 5.10.: Top: measured transverse momentum distribution of the leading jets (highest p_{T} (left)), for the AFP and MB selected data samples for events with at least one jet with $p_{\mathrm{T}} > 20$ GeV (left) and $p_{\mathrm{T}} > 30$ GeV (right) and $|\eta| < 3.0$. Bottom: measured transverse momentum distribution of the second-leading jets (second highest p_{T}) for the same event selection. The area under all distributions are normalized to the unity.

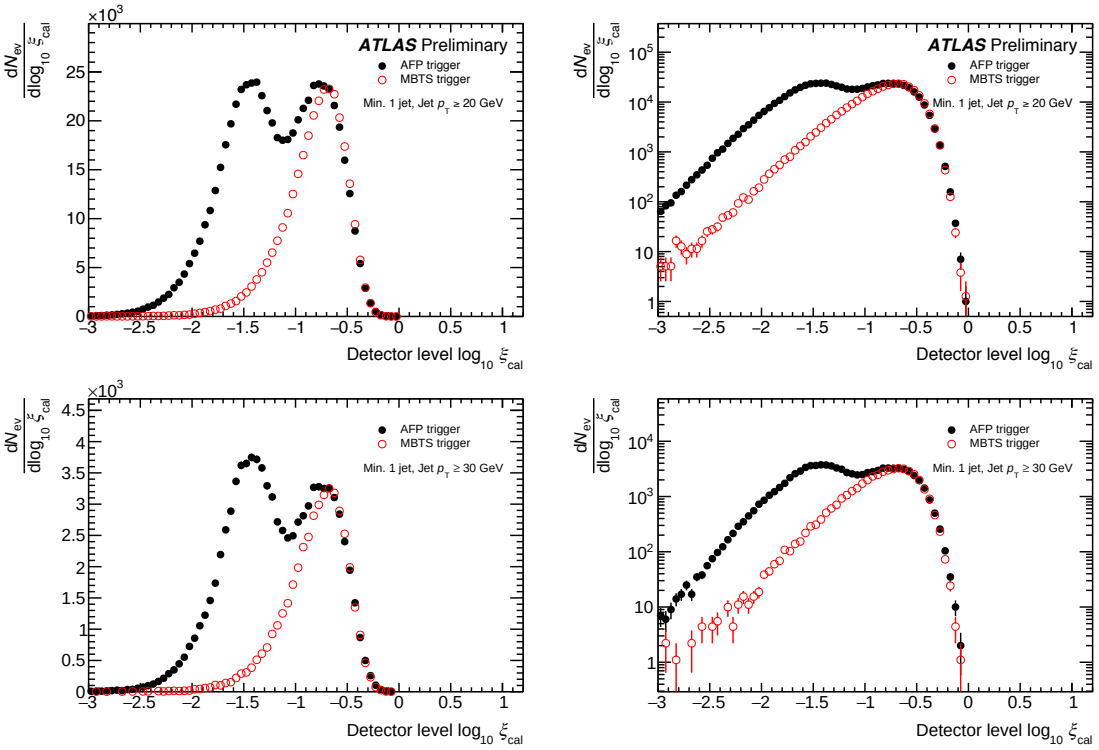

Figure 5.11.: Measured ξ_{cal} distribution in AFP and MB selected data samples on linear (left) and logarithmic (right) scale, for events with at least one jet with $p_{\text{T}} > 20$ GeV (top) and $p_{\text{T}} > 30$ GeV (bottom) with $|\eta| < 3.0$. The MB data is normalized to the AFP data in the largest ξ_{cal} bin.

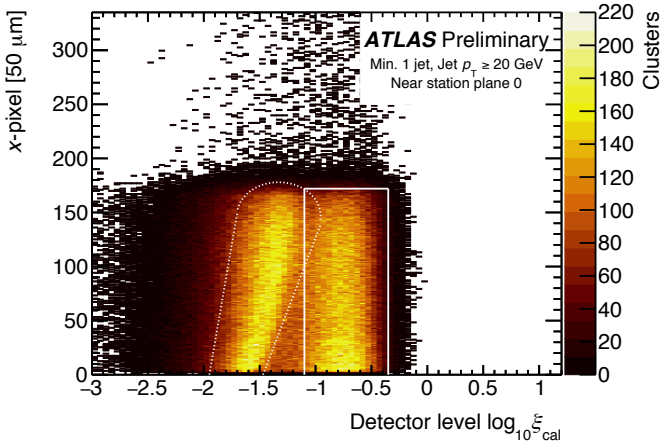

Figure 5.12.: 2D distribution of the x-position of AFP clusters in the Near station plane 0 ($z = -205$ m) as a function of the measured ξ_{cal} in the ATLAS calorimeter for events with AFP clusters and a jet with $p_{\text{T}} > 20$ GeV and $|\eta| < 3.0$ in the final state, from the AFP-triggered data.

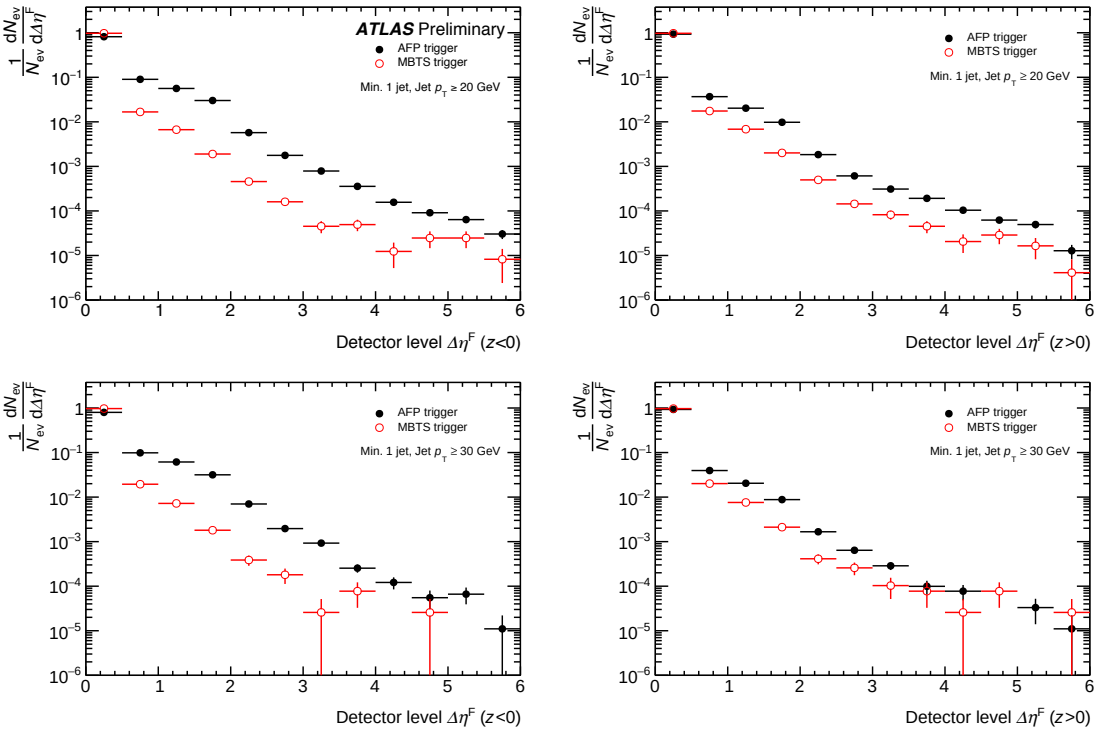

Figure 5.13.: Measured rapidity gap distribution from the AFP side ($\Delta\eta^F_{z<0}$ (left)) and opposite ($\Delta\eta^F_{z>0}$ (right)) in the AFP and MB selected data samples for events with at least one jet with $p_T > 20$ GeV (top) and $p_T > 30$ GeV (bottom) and $|\eta| < 3.0$. The area under all distributions are normalized to the unity.

6. Summary and Outlook

This thesis described the characterization and qualification of the 3D pixel sensor technology, the production and installation of the ATLAS Forward Proton (AFP) tracker modules and the operation of the detector in 2016, during which only the silicon tracker was installed in one side of ATLAS.

The AFP detector is a forward detector installed at about 210 m at either side from the ATLAS interaction point and few millimetres close to the LHC proton beam in order to detect and reconstruct the kinematics of protons emerging intact from collisions at very shallow angles. Events with such signatures allow the study of so-called diffractive events, in which no quantum number is exchanged by at least one of the protons. It also allows the study of Central Exclusive Production (CEP) events, which have the advantage that, using forward detectors such as AFP in combination with the ATLAS central sub-systems, it is possible to detect all the products of the event in a clean environment. CEP events can yield any possible resonance, allowing the search for new particles. In order to allow such measurements, the AFP design consists of a silicon tracker and a Time-of-Flight detector.

To ensure a good performance of the detector, the silicon tracker needs to fulfil the following requirements: radiation hardness with non-uniform fluences due to the very focused expected beam profile, small inactive edges of $<$200 μm in order to move the active region of the tracker planes as close as possible to the proton beam and a good position resolution (about 10$\times$30 μm^2) to ensure a good kinematic reconstruction resolution.

The 3D pixel silicon sensor technology is the choice for the AFP tracker to cope with its performance requirements. It consists of silicon devices in which the electrodes are column-like penetrating the bulk. This type of sensors, coupled with the FE-I4 read-out chip, has been characterized in the past for its usage in the inner-most layer of the ATLAS Inner Detector, the IBL. The sensors, fabricated both at CNM and FBK and originally designed for IBL, contain a 1.5 mm non-instrumented edge which needs to be removed (slim-edged) to fulfil AFP needs. Due to the differences in requirements between IBL and AFP, several test-beam campaigns were performed to qualify these detectors also for AFP. It was demonstrated that FE-I4 3D pixel detectors fulfil all the requirements for the AFP tracker. 3D detectors were irradiated up to AFP fluence, about 3×10^{15} n_{eq}/cm^2, either with a 12$\times$12 mm^2 23 GeV proton beam or through an aluminum mask with a hole using 23 MeV protons to reach a non-uniform fluence distribution in the sensor. In both cases, a hit efficiency of at least 97% (under optimal conditions of bias voltage and chip parameters) at perpendicular beam incidence was found for the highest measured voltages in the irradiated region, showing that these devices are radiation hard enough for AFP. The effect of dicing to distances of 87–215 μm from the last instrumented pixel was studied in test-beams for the two (CNM and FBK) sensor designs. It was found that the guard-ring structure present in the CNM design prevents the charge collection from beyond the last pixel, while for FBK sensors with no guard-ring the sensitive region can extend by about 100 μm beyond the last pixel with high enough voltages. In both cases $<$200 μm inactive edge was achieved. A single plane position resolution along the short pixel direction of 6 μm was obtained at a 14° angle with respect to the normal incidence. For the long pixel direction, the single-plane resolution is consistent with the digital resolution (72 μm), but by staggering the four planes in an AFP tracker it is theoretically possible to achieve a pointing resolution of down to 18 μm along that direction. Both sensor designs fulfil all the requirements for AFP. Finally, CNM devices were produced for AFP installation because

the FBK production line was being upgraded.

In addition, the read-out of the silicon tracker and the Time-of-Flight prototype detector with the same system was exercised in an integration test-beam, which allowed for the study of the ToF system with the full electronics using track information. The timing detector prototype showed a hit efficiency of about 99% for the highest measured voltage, with the downside of a high crosstalk (66–92%). Finally, a time resolution with two bars per train (i.e. half the final ToF system) was measured to be 35 to 37±6 ps for the maximum voltage, which is compatible with the low-luminosity requirement of 30 ps resolution. With a four bars per train configuration and the optimization of operation parameters it is expected to reach the 10-20 ps resolution needed for high-luminosity data taking conditions.

After the positive test-beam results and a favourable decision to install AFP, the silicon tracker module production started. A low yield in the sensor fabrication was observed in the first CNM fabrication run which required a high module production yield. In total, 17 modules were produced from the low-yield sensor production, out of which 14 were found acceptable. A total of 7 of these modules were installed in two Roman Pot stations in the C-side of ATLAS in February 2016.

The AFP detector was successfully commissioned and integrated with the ATLAS trigger and read-out system. This allowed AFP to take the first low pile-up physics data during 2016 in combination with the rest of the ATLAS sub-detectors.

To verify the performance of the detector and its integration into ATLAS, AFP-triggered events in one of the low pile-up data sets was studied: the relative proton energy loss distribution was calculated as measured from the ATLAS calorimeter (ξ_{cal})[1] from AFP-triggered events and compared to the one obtained from events triggered by the Minimum Bias Trigger Scintillator (MBTS). The AFP-triggered data distribution showed a bump with respect to its MBTS-triggered counterpart around the expected ξ from AFP, demonstrating that the events triggered by AFP are rich in diffractive protons.

The AFP detector was completed during the 2016-2017 LHC winter shutdown with the installation of two Roman Pots on the A-side of ATLAS, a Time-of-Flight system in the far station of each side and a 4-plane silicon tracker in every Roman Pot (AFP now contains a total of 16 3D pixel modules). During 2017, with the addition of the ToF detector, AFP took data at low and standard pile-up conditions. This data is being analyzed. First studies show a ToF performance lower than expected in terms of efficiency, which is still under investigation. An upgrade of the ToF detector is on-going. The use of silicon-based detectors as a possible future alternative for the AFP ToF system has been recently proposed, the so-called Low Gain Avalanche Detector (LGAD) [133], which consists of a silicon diode with a built-in multiplication layer.

The operation of the AFP detector is foreseen until the end of Run 3, before the luminosity upgrade of the LHC, the HL-LHC. The proposal for a forward detector in the HL-LHC era is being studied.

[1] The kinematic reconstruction of the proton from AFP information was not available at the time of performing the study.

A. ATLAS coordinate system

The origin of the ATLAS coordinate system (see Fig. A.1) is taken at centre of the detector and of the beam-pipe, i.e. the nominal interaction point (IP). The Z-axis is chosen to be along the beam direction, positive (negative) on the A-side (C-side) of ATLAS, the X-axis is taken pointing the centre of the LHC ring and Y-axis points upwards. The particles momentum measured in the XY plane is referred as transverse momentum p_{T}. Nevertheless, it is more common to use a spherical coordinate system: the radius R, the azimutal angle θ and the polar angle ϕ. The angle ϕ ranges from $-\pi$ to π with respect to the X axis, while θ is measured from the positive Z-axis and ranges from 0 to π. While differences in azimuthal angles are Lorentz boost invariant, differences in polar angles are not. For this reason an invariant coordinate variable, the rapidity y, is introduced:

$$y = \frac{1}{2} \ln \left(\frac{E + p_z}{E - p_z} \right). \tag{A.1}$$

Rapidity's shortcoming is the need of measuring energy and momentum along the beam axis. However, for highly relativistic particles (as is mostly the case in ATLAS events), it is equal to the pseudorapidity η:

$$\eta = -\ln \left(\tan \frac{\theta}{2} \right) \tag{A.2}$$

which is purely geometrical dependent and $\Delta\eta$ is boost invariant. The absolute value of the pseudorapidity ranges from 0 (vertical) to ∞ (along the beam axis). For instance, the full coverage of the ATLAS detector is $|\eta| < 4.9$, which corresponds to $0.94\ ^\circ < |\theta| \leqslant 90\ ^\circ$.

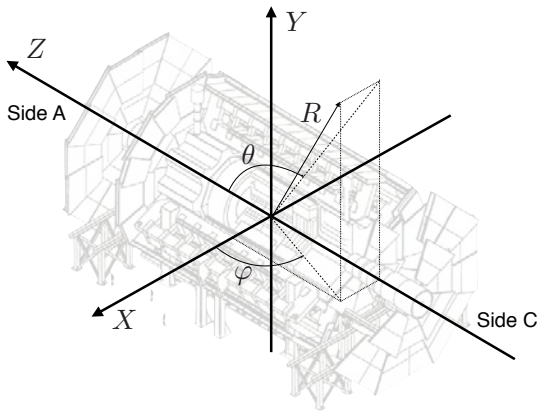

Figure A.1.: The ATLAS reference system. Background ATLAS image taken from [134].

List of Figures

List of Tables

Bibliography

[1] C. Patrignani et al. "Review of Particle Physics". In: *Chin. Phys.* C40.10 (2016), p. 100001. DOI: 10.1088/1674-1137/40/10/100001.

[2] Lyndon Evans and Philip Bryant. "LHC Machine". In: *Journal of Instrumentation* 3.08 (2008), S08001.

[3] V. N. Gribov and L. N. Lipatov. "Deep inelastic e p scattering in perturbation theory". In: *Sov. J. Nucl. Phys.* 15 (1972). [Yad. Fiz.15,781(1972)], pp. 438–450; L. N. Lipatov. "The parton model and perturbation theory". In: *Sov. J. Nucl. Phys.* 20 (1975). [Yad. Fiz.20,181(1974)], pp. 94–102; Guido Altarelli and G. Parisi. "Asymptotic Freedom in Parton Language". In: *Nucl. Phys.* B126 (1977), pp. 298–318. DOI: 10.1016/0550-3213(77)90384-4; Yuri L. Dokshitzer. "Calculation of the Structure Functions for Deep Inelastic Scattering and e+ e- Annihilation by Perturbation Theory in Quantum Chromodynamics." In: *Sov. Phys. JETP* 46 (1977). [Zh. Eksp. Teor. Fiz.73,1216(1977)], pp. 641–653.

[4] Richard D. Ball et al. "Parton distributions from high-precision collider data". In: *Eur. Phys. J.* C77.10 (2017), p. 663. DOI: 10.1140/epjc/s10052-017-5199-5. arXiv: 1706.00428 [hep-ph].

[5] The ATLAS Collaboration. *Summary plots from the ATLAS Standard Model physics group*. URL: https://atlas.web.cern.ch/Atlas/GROUPS/PHYSICS/CombinedSummaryPlots/SM/.

[6] The CMS Collaboration. *Summaries of CMS cross section measurements*. URL: https://twiki.cern.ch/twiki/bin/view/CMSPublic/PhysicsResultsCombined.

[7] A. Donnachie and P. V. Landshoff. "Total cross-sections". In: *Phys. Lett.* B296 (1992), pp. 227–232. DOI: 10.1016/0370-2693(92)90832-O. arXiv: hep-ph/9209205 [hep-ph].

[8] S. Donnachie et al. "Pomeron physics and QCD". In: *Camb. Monogr. Part. Phys. Nucl. Phys. Cosmol.* 19 (2002), pp. 1–347.

[9] Morad Aaboud et al. "Measurement of the total cross section from elastic scattering in pp collisions at $\sqrt{s} = 8$ TeV with the ATLAS detector". In: *Phys. Lett.* B761 (2016), pp. 158–178. DOI: 10.1016/j.physletb.2016.08.020. arXiv: 1607.06605 [hep-ex].

[10] A. Aktas et al. "Dijet Cross Sections and Parton Densities in Diffractive DIS at HERA". In: *JHEP* 10 (2007), p. 042. DOI: 10.1088/1126-6708/2007/10/042. arXiv: 0708.3217 [hep-ex].

[11] A. Aktas et al. "Measurement and QCD analysis of the diffractive deep-inelastic scattering cross-section at HERA". In: *Eur. Phys. J.* C48 (2006), pp. 715–748. DOI: 10.1140/epjc/s10052-006-0035-3. arXiv: hep-ex/0606004 [hep-ex].

[12] T. Affolder et al. "Diffractive dijets with a leading antiproton in $\bar{p}p$ collisions at $\sqrt{s} = 1800$ GeV". In: *Phys. Rev. Lett.* 84 (2000), pp. 5043–5048. DOI: 10.1103/PhysRevLett.84.5043.

[13] R. Bonino et al. "Evidence for Transverse Jets in High Mass Diffraction". In: *Phys. Lett.* B211 (1988), p. 239. DOI: 10.1016/0370-2693(88)90840-4.

[14] J. G. Zweizig et al. "Test of a Data Driven Trigger Processor for Experiment UA8". In: *Nucl. Instrum. Meth.* A263 (1988), pp. 188–195. DOI: 10.1016/0168-9002(88)91033-9.

[15] P. Van Esch et al. "The H1 forward proton spectrometer at HERA". In: *Nucl. Instrum. Meth.* A446 (2000), pp. 409–425. DOI: 10.1016/S0168-9002(99)01276-0. arXiv: hep-ex/0001046 [hep-ex].

[16] "The ZEUS detector: Status report 1993". In: (1993). DOI: 10.3204/PUBDB-2017-12635.

[17] F. D. Aaron et al. "Combined inclusive diffractive cross sections measured with forward proton spectrometers in deep inelastic *ep* scattering at HERA". In: *Eur. Phys. J.* C72 (2012), p. 2175. DOI: 10.1140/epjc/s10052-012-2175-y. arXiv: 1207.4864 [hep-ex].

[18] T. Aaltonen et al. "Diffractive dijet production in $\bar{p}p$ collisions at $\sqrt{s}$=1.96 TeV". In: *Phys. Rev. D* 86 (3 Aug. 2012), p. 032009. DOI: 10.1103/PhysRevD.86.032009.

[19] Konstantin A. Goulianos. "Hadronic diffraction: Where do we stand?" In: *Results and perspectives in particle physics. Proceedings, 18th Rencontres de Physique de la Vallee d'Aoste, La Thuile, Italy, February 29-March 6, 2004*. 2004, pp. 251–274. arXiv: hep-ph/0407035 [hep-ph].

[20] T. Aaltonen et al. "Diffractive W and Z Production at the Fermilab Tevatron". In: *Phys. Rev.* D82 (2010), p. 112004. DOI: 10.1103/PhysRevD.82.112004. arXiv: 1007.5048 [hep-ex].

[21] T. Aaltonen et al. "Observation of Exclusive Dijet Production at the Fermilab Tevatron $p^{-}\bar{p}$ Collider". In: *Phys. Rev.* D77 (2008), p. 052004. DOI: 10.1103/PhysRevD.77.052004. arXiv: 0712.0604 [hep-ex].

[22] Victor Mukhamedovich Abazov et al. "High mass exclusive diffractive dijet production in $\mathbf{p\bar{p}}$ collisions at $\sqrt{\mathbf{s}}$ = 1.96 TeV". In: *Phys. Lett.* B705 (2011), pp. 193–199. DOI: 10.1016/j.physletb.2011.10.013. arXiv: 1009.2444 [hep-ex].

[23] A. Abulencia et al. "Observation of Exclusive Electron-Positron Production in Hadron-Hadron Collisions". In: *Phys. Rev. Lett.* 98 (2007), p. 112001. DOI: 10.1103/PhysRevLett.98.112001. arXiv: hep-ex/0611040 [hep-ex].

[24] ATLAS Collaboration. "Dijet production in $\sqrt{s}$ = 7 TeV *pp* collisions with large rapidity gaps at the ATLAS experiment". In: *Phys. Lett.* B754 (2016), pp. 214–234. DOI: 10.1016/j.physletb.2016.01.028. arXiv: 1511.00502 [hep-ex].

[25] CMS Collaboration. "Observation of a diffractive contribution to dijet production in proton-proton collisions at $\sqrt{s} = 7$ TeV". In: *Phys. Rev.* D87.1 (2013), p. 012006. DOI: 10.1103/PhysRevD.87.012006. arXiv: 1209.1805 [hep-ex].

[26] Georges Aad et al. "Rapidity gap cross sections measured with the ATLAS detector in *pp* collisions at $\sqrt{s}$ = 7 TeV". In: *Eur. Phys. J.* C72 (2012), p. 1926. DOI: 10.1140/epjc/s10052-012-1926-0. arXiv: 1201.2808 [hep-ex].

[27] Georges Aad et al. "Measurement of exclusive $\gamma\gamma \to \ell^{+}\ell^{-}$ production in proton-proton collisions at $\sqrt{s}$ = 7 TeV with the ATLAS detector". In: *Phys. Lett.* B749 (2015), pp. 242–261. DOI: 10.1016/j.physletb.2015.07.069. arXiv: 1506.07098 [hep-ex].

[28] Morad Aaboud et al. "Measurement of exclusive $\gamma\gamma \to W^{+}W^{-}$ production and search for exclusive Higgs boson production in *pp* collisions at $\sqrt{s} = 8$ TeV using the ATLAS detector". In: *Phys. Rev.* D94.3 (2016), p. 032011. DOI: 10.1103/PhysRevD.94.032011. arXiv: 1607.03745 [hep-ex].

[29] L Adamczyk et al. *Technical Design Report for the ATLAS Forward Proton Detector*. Tech. rep. CERN-LHCC-2015-009. ATLAS-TDR-024. May 2015.

[30] C. Marquet et al. "Probing the Pomeron structure using dijets and γ+jet events at the LHC". In: *Phys. Rev.* D88.7 (2013), p. 074029. DOI: 10.1103/PhysRevD.88.074029. arXiv: 1306.4901 [hep-ph].

[31] The ATLAS Collaboration. "Observation of a new particle in the search for the Standard Model Higgs boson with the ATLAS detector at the LHC". In: *Phys. Lett.* B716 (2012), pp. 1–29. DOI: 10.1016/j.physletb.2012.08.020. arXiv: 1207.7214 [hep-ex].

[32] The CMS Collaboration. "Observation of a new boson at a mass of 125 GeV with the CMS experiment at the LHC". In: *Phys. Lett.* B716 (2012), pp. 30–61. DOI: 10.1016/j.physletb.2012.08.021. arXiv: 1207.7235 [hep-ex].

[33] S. Fichet et al. "Probing new physics in diphoton production with proton tagging at the Large Hadron Collider". In: *Phys. Rev.* D89 (2014), p. 114004. DOI: 10.1103/PhysRevD.89.114004. arXiv: 1312.5153 [hep-ph].

[34] Cinzia De Melis. "The CERN accelerator complex. Complexe des accélérateurs du CERN". In: (July 2016). General Photo.

[35] The ATLAS Collaboration. "The ATLAS Experiment at the CERN Large Hadron Collider". In: *Journal of Instrumentation* 3.08 (2008), S08003.

[36] The CMS Collaboration. "The CMS experiment at the CERN LHC". In: *Journal of Instrumentation* 3.08 (2008), S08004.

[37] The ALICE Collaboration. "The ALICE experiment at the CERN LHC". In: *Journal of Instrumentation* 3.08 (2008), S08002.

[38] The LHCb Collaboration. "The LHCb Detector at the LHC". In: *Journal of Instrumentation* 3.08 (2008), S08005.

[39] The ATLAS Collaboration. *ATLAS Luminosity Public Results from Run 2*. URL: https://twiki.cern.ch/twiki/bin/view/AtlasPublic/LuminosityPublicResultsRun2.

[40] Joao Pequenao. "Computer generated image of the whole ATLAS detector". Mar. 2008.

[41] Norbert Wermes and G Hallewel. *ATLAS pixel detector: Technical Design Report*. Technical Design Report ATLAS. Geneva: CERN, 1998.

[42] M Capeans et al. *ATLAS Insertable B-Layer Technical Design Report*. Tech. rep. CERN-LHCC-2010-013. ATLAS-TDR-19. Sept. 2010.

[43] Y Unno. "ATLAS silicon microstrip semiconductor tracker (SCT)". In: *Nucl. Instrum. Methods Phys. Res., A* 453.1-2 (2000), pp. 109–20.

[44] Michal Turala. "The ATLAS semiconductor tracker". In: *Nucl. Instrum. Methods Phys. Res., A* 466.2 (2001), pp. 243–54.

[45] The ATLAS TRT Collaboration. "The ATLAS Transition Radiation Tracker (TRT) proportional drift tube: Design and performance". In: *JINST* 3 (2008), P02013. DOI: 10.1088/1748-0221/3/02/P02013.

[46] Adrian Vogel. "ATLAS Transition Radiation Tracker (TRT): Straw tube gaseous detectors at high rates". In: *Nucl. Instrum. Meth.* A732 (2013), pp. 277–280. DOI: 10.1016/j.nima.2013.07.020.

[47] Joao Pequenao. "Computer generated image of the ATLAS inner detector". Mar. 2008.

[48] The ATLAS Collaboration. *Radiation Simulation Public Results*. URL: https://twiki.cern.ch/twiki/bin/view/AtlasPublic/RadiationSimulationPublicResults.

[49] Joao Pequenao. "Computer Generated image of the ATLAS calorimeter". Mar. 2008.

[50] *ATLAS liquid-argon calorimeter: Technical Design Report*. Technical Design Report ATLAS. Geneva: CERN, 1996.

[51] *ATLAS tile calorimeter: Technical Design Report*. Technical Design Report ATLAS. Geneva: CERN, 1996.

[52] "ATLAS muon spectrometer: Technical design report". In: (1997).

[53] Y. Arai et al. "ATLAS muon drift tube electronics". In: *JINST* 3 (2008), P09001. DOI: 10.1088/1748-0221/3/09/P09001.

[54] Konstantinos Nikolopoulos et al. "Cathode strip chambers in ATLAS : Installation, commissioning and in situ performance". In: *Proceedings, 2008 IEEE Nuclear Science Symposium, Medical Imaging Conference and 16th International Workshop on Room-Temperature Semiconductor X-Ray and Gamma-Ray Detectors (NSS/MIC 2008 / RTSD 2008): Dresden, Germany, October 19-25, 2008*. 2008, pp. 2819–2824. DOI: 10.1109/NSSMIC.2008.4774958.

[55] Joao Pequenao. "Computer generated image of the ATLAS Muons subsystem". Mar. 2008.

[56] C. Ferretti and H. Kroha. "Upgrades of the ATLAS Muon Spectrometer with sMDT Chambers". In: *Nucl. Instrum. Meth.* A824 (2016), pp. 538–540. DOI: 10.1016/j.nima.2015.11.043. arXiv: 1603.09544 [physics.ins-det].

[57] G. Aielli, Marcello Bindi, and Alessandro Polini. "Performance, operation and detector studies with the ATLAS Resistive Plate Chambers". In: *JINST* 8 (2013), P02020. DOI: 10.1088/1748-0221/8/02/P02020.

[58] "ATLAS magnet system: Technical design report". In: (1997).

[59] M Bruschi. "The ATLAS luminosity monitor". In: *Nucl. Instrum. Methods Phys. Res., A* 623.ATL-LUM-PROC-2009-001. ATL-COM-LUM-2009-006 (Apr. 2009). Deadline: April 20th 2009, 371–373. 3 p.

[60] Peter Jenni, Marzio Nessi, and Markus Nordberg. *Zero Degree Calorimeters for ATLAS*. Tech. rep. LHCC-I-016. CERN-LHCC-2007-001. Geneva: CERN, Jan. 2007.

[61] S. Abdel Khalek et al. "The ALFA Roman Pot Detectors of ATLAS". In: *JINST* 11.11 (2016), P11013. DOI: 10.1088/1748-0221/11/11/P11013. arXiv: 1609.00249 [physics.ins-det].

[62] Georges Aad et al. "Measurement of the total cross section from elastic scattering in pp collisions at $\sqrt{s} = 7$ TeV with the ATLAS detector". In: *Nucl. Phys.* B889 (2014), pp. 486–548. DOI: 10.1016/j.nuclphysb.2014.10.019. arXiv: 1408.5778 [hep-ex].

[63] A. Sidoti. "Minimum Bias Trigger Scintillators in ATLAS Run II". In: *JINST* 9.10 (2014), p. C10020. DOI: 10.1088/1748-0221/9/10/C10020.

[64] ATLAS TDAQ. *ATLAS TDAQ Approved Plots*. URL: https://twiki.cern.ch/twiki/bin/view/AtlasPublic/ApprovedPlotsDAQ.

[65] Berardi, V and Catanesi, et al. *Total cross-section, elastic scattering and diffraction dissociation at the Large Hadron Collider at CERN: TOTEM Technical Design Report*. Technical Design Report TOTEM. Geneva: CERN, 2004.

[66] F. Anghinolfi et al. "High-Resolution Time Interpolator Based on a Delay Locked Loop and an RC delay line". In: *IEEE J. Solid-State Circ.* 34.10 (1999), pp. 1360–1366.

[67] L. Nozka et al. "Design of Cherenkov bars for the optical part of the time-of-flight detector in Geant4". In: *Optics Express* 22.23 (Nov. 2014), p. 28984. DOI: 10.1364/oe.22.028984.

[68] *AFP LTB Documentation*. URL: https://edms5.cern.ch/nav/EDA-03330-V1-0.

[69] D. S. Smith et al. "Development of the hitbus chip platform for the ATLAS DBM detector at CERN". In: *2013 IEEE 56th International Midwest Symposium on Circuits and Systems (MWSCAS)*. Aug. 2013, pp. 1204–1207. DOI: 10.1109/MWSCAS.2013.6674870.

[70] S. Ask et al. "The ATLAS central level-1 trigger logic and TTC system". In: *JINST* 3 (2008), P08002. DOI: 10.1088/1748-0221/3/08/P08002.

[71] ATLAS TDAQ. *Timing, Trigger and Control (TTC) Systems for the LHC*. URL: http://ttc.web.cern.ch/TTC/.

[72] Richard Kass et al. "The new radiation-hard optical links for the ATLAS pixel detector". In: *Meeting of the APS Division of Particles and Fields (DPF 2013) Santa Cruz, California, USA, August 13-17, 2013*. 2013. arXiv: 1310.1062 [physics.ins-det].

[73] David Bertsche. "Opto-box: Optical modules and mini-crate for ATLAS pixel and IBL detectors". In: *EPJ Web Conf.* 126 (2016), p. 05002. DOI: 10.1051/epjconf/201612605002.

[74] K. Korcyl et al. "Readout and Trigger for the AFP Detector at the ATLAS Experiment at LHC". In: *J. Phys. Conf. Ser.* 898.3 (2017), p. 032025. DOI: 10.1088/1742-6596/898/3/032025.

[75] M. Kocian. "Readout and trigger for the AFP detector at ATLAS experiment". In: *JINST* 12.01 (2017), p. C01077. DOI: 10.1088/1748-0221/12/01/C01077.

[76] E. Banaś et al. "Detector Control System for the AFP detector in ATLAS experiment at CERN". In: *J. Phys. Conf. Ser.* 898.3 (2017), p. 032022. DOI: 10.1088/1742-6596/898/3/032022.

[77] R. M. Sternheimer, M. J. Berger, and S. M. Seltzer. "Density Effect for the Ionization Loss of Charged Particles in Various Substances". In: *Atom. Data Nucl. Data Tabl.* 30 (1984), pp. 261–271. DOI: 10.1016/0092-640X(84)90002-0.

[78] L. Rossi et al. *Pixel Detectors*. Particle Acceleration and Detection. Berlin: Springer-Verlag, 2006. ISBN: 9783540283324, 9783540283331. DOI: 10.1007/3-540-28333-1.

[79] H. Bichsel. "Straggling in Thin Silicon Detectors". In: *Rev. Mod. Phys.* 60 (1988), pp. 663–699. DOI: 10.1103/RevModPhys.60.663.

[80] William R. Leo. *Techniques for Nuclear and Particle Physics Experiments*. Springer Berlin Heidelberg, 1994. DOI: 10.1007/978-3-642-57920-2.

[81] M.J. Berger et al. *XCOM: Photon Cross Sections Database*. URL: https://www.nist.gov/pml/xcom-photon-cross-sections-database.

[82] W. Shockley. "Currents to Conductors Induced by a Moving Point Charge". In: *Journal of Applied Physics* 9.10 (Oct. 1938), pp. 635–636. DOI: 10.1063/1.1710367.

[83] Simon Ramo. "Currents induced by electron motion". In: *Proc. Ire.* 27 (1939), pp. 584–585. DOI: 10.1109/JRPROC.1939.228757.

[84] Jörn Lange. "Differential Top-Quark-Pair Cross Sections in pp Collisions at $\sqrt{s} = 7$ TeV with CMS and Charge Multiplication in Highly-Irradiated Silicon Sensors". PhD thesis. Hamburg U., 2013.

[85] A. Vasilescu (INPE Bucharest) and G. Lindstroem (University of Hamburg). *Displacement damage in silicon, on-line compilation*. URL: https://rd50.web.cern.ch/rd50/NIEL/.

[86] Michael Moll. "Radiation damage in silicon particle detectors: Microscopic defects and macroscopic properties". PhD thesis. Hamburg U., 1999.

[87] Sherwood I. Parker, Christopher J. Kenney, and Julie Segal. "3-D: A New architecture for solid state radiation detectors". In: *Nucl. Instrum. Meth.* A395 (1997), pp. 328–343. DOI: 10.1016/S0168-9002(97)00694-3.

[88] C. Kenney et al. "Silicon detectors with 3-D electrode arrays: fabrication and initial test results". In: *IEEE Transactions on Nuclear Science* 46.4 (1999), pp. 1224–1236. DOI: 10.1109/23.785737.

[89] Banqiu Wu, Ajay Kumar, and Sharma Pamarthy. "High aspect ratio silicon etch: A review". In: *Journal of Applied Physics* 108.5 (Sept. 2010), p. 051101. DOI: 10.1063/1.3474652.

[90] M. Backhaus. "The upgraded Pixel Detector of the ATLAS Experiment for Run 2 at the Large Hadron Collider". In: *Nucl. Instrum. Meth.* A831 (2016), pp. 65–70. DOI: 10.1016/j.nima.2016.05.018.

[91] S. Grinstein et al. "Module production of the one-arm AFP 3D pixel tracker". In: *JINST* 12.01 (2017), p. C01086. DOI: 10.1088/1748-0221/12/01/C01086. arXiv: 1611.01005 [physics.ins-det].

[92] M Albrow et al. *CMS-TOTEM Precision Proton Spectrometer*. Tech. rep. CERN-LHCC-2014-021. TOTEM-TDR-003. CMS-TDR-13. Sept. 2014.

[93] Fabio Ravera. "The CT-PPS tracking system with 3D pixel detectors". In: *JINST* 11.11 (2016), p. C11027. DOI: 10.1088/1748-0221/11/11/C11027.

[94] Philippe Grenier et al. *Technical Design Report for the ATLAS ITk Pixel Detector: Pixel TDR*. Tech. rep. ATL-COM-UPGRADE-2017-020. Geneva: CERN, Nov. 2017.

[95] CMS Collaboration. *The Phase-2 Upgrade of the CMS Tracker*. Tech. rep. CERN-LHCC-2017-009. CMS-TDR-014. Geneva: CERN, June 2017.

[96] J Albert et al. "Prototype ATLAS IBL Modules using the FE-I4A Front-End Readout Chip". In: *JINST* 7 (2012), P11010. DOI: 10.1088/1748-0221/7/11/P11010. arXiv: 1209.1906 [physics.ins-det].

[97] H. C. Kästli. "Frontend electronics development for the CMS pixel detector upgrade". In: *Nucl. Instrum. Meth.* A731 (2013), pp. 88–91. DOI: 10.1016/j.nima.2013.05.056.

[98] Mauricio Garcia-Sciveres. *RD53A Integrated Circuit Specifications*. Tech. rep. CERN-RD53-PUB-15-001. Geneva: CERN, Dec. 2015.

[99] J. Lange et al. "3D silicon pixel detectors for the High-Luminosity LHC". In: *JINST* 11.11 (2016), p. C11024. DOI: 10.1088/1748-0221/11/11/C11024. arXiv: 1610.07480 [physics.ins-det].

[100] D. Vázquez Furelos et al. "3D sensors for the HL-LHC". In: *JINST* 12.01 (2017), p. C01026. DOI: 10.1088/1748-0221/12/01/C01026. arXiv: 1610.08889 [physics.ins-det].

[101] J. Lange et al. "Radiation hardness of small-pitch 3D pixel sensors up to HL-LHC fluences". In: 2017. arXiv: 1707.01045 [physics.ins-det].

[102] M. Povoli et al. "Design and testing of an innovative slim-edge termination for silicon radiation detectors". In: *JINST* 8 (2013), p. C11022. DOI: 10.1088/1748-0221/8/11/C11022.

[103] M. Garcia-Sciveres et al. "The FE-I4 pixel readout integrated circuit". In: *Nucl. Instrum. Meth.* A636 (2011), S155–S159. DOI: 10.1016/j.nima.2010.04.101.

[104] Miroslav Havránek et al. "Measurement of pixel sensor capacitances with sub-femtofarad precision". In: *Nucl. Instrum. Meth.* A714 (2013), pp. 83–89. DOI: 10.1016/j.nima.2013.02.038.

[105] J. Grosse-Knetter et al. *USB based readout system for ATLAS FE-I3 and FE-I4*. URL: http://icwiki.physik.uni-bonn.de/twiki/bin/view/Systems/UsbPix.

[106] R. Herbst et al. "Design of the SLAC RCE Platform: A general purpose ATCA based data acquisition system". In: *Proceedings, 21st Symposium on Room-Temperature Semiconductor X-ray and Gamma-ray Detectors (RTSD 2014): Seattle, WA, USA, November 8-15, 2014*. 2016, p. 7431254. DOI: 10.1109/NSSMIC.2014.7431254.

[107] Ryan Herbst Dong Su Mathew Graham. *RCE Application Development Workshop*. URL: https://indico.cern.ch/event/546846/.

[108] Hendrik Jansen et al. "Performance of the EUDET-type beam telescopes". In: *EPJ Techniques and Instrumentation* 3.1 (Oct. 4, 2016), p. 7. ISSN: 2195-7045. DOI: 10.1140/epjti/s40485-016-0033-2.

[109] C Hu-Guo et al. "A ten thousand frames per second readout MAPS for the EUDET beam telescope". In: (2009).

[110] EUDAQ Software Developers. *EUDAQ Website*. URL: http://eudaq.github.io.

[111] EUTelescope Software Developers. *EUTelescope: A Generic Pixel Telescope Data Analysis Framework*. URL: http://eutelescope.web.cern.ch.

[112] ROOT Software Developers. *ROOT Data Analysis Framework*. URL: https://root.cern.ch/.

[113] Garrin McGoldrick, Matevž Červ, and Andrej Gorišek. "Synchronized analysis of testbeam data with the Judith software". In: *Nucl. Instrum. Meth.* A765 (2014), pp. 140–145. DOI: 10.1016/j.nima.2014.05.033.

[114] V. Blobel. "Software alignment for tracking detectors". In: *Nucl. Instrum. Meth.* A566 (2006), pp. 5–13. DOI: 10.1016/j.nima.2006.05.157.

[115] R. E. Kalman. "A New Approach to Linear Filtering and Prediction Problems". In: *Journal of Basic Engineering* 82.1 (1960), p. 35. DOI: 10.1115/1.3662552.

[116] K.N. Sjøbæk. *Full simulation of a testbeam experiment including modeling of the Bonn Atlas Telescope and Atlas 3D pixel silicon sensors*. 2010.

[117] J. Lange et al. "Beam tests of an integrated prototype of the ATLAS Forward Proton detector". In: *Journal of Instrumentation* 11.09 (2016), P09005.

[118] S. Kulis and D. Danheim. *Telescope Resolution Calculator*. URL: https://skulis.web.cern.ch/skulis/telescope.

[119] L. Nozka et al. "Construction of the optical part of a time-of-flight detector prototype for the AFP detector". In: *Optics Express* 24.24 (Nov. 2016), p. 27951. DOI: 10.1364/oe.24.027951.

[120] I. Lopez Paz. "Experience with CNM 3D sensors for the ATLAS IBL". Talk at the 9th "Trento" Workshop on Advanced Silicon Radiation Detectors (3D and p-type Technologies). 2014.

[121] J. Lange et al. "3D silicon pixel detectors for the ATLAS Forward Physics experiment". In: *Journal of Instrumentation* 10.03 (2015), p. C03031.

[122] P Adragna et al. *GNAM and OHP: Monitoring Tools for ATLAS experiment at LHC.* Tech. rep. ATL-DAQ-CONF-2007-023. ATL-COM-DAQ-2007-013. Geneva: CERN, May 2007.

[123] F. Förster. "3D Silicon Tracker for AFP - From Qualification to Operation". Talk at the 26th International Workshop on Vertex Detectors. 2017.

[124] Karola Dette. "Total Ionising Dose effects in the FE-I4 front-end chip of the ATLAS Pixel IBL detector". In: *JINST* 11.11 (2016), p. C11028. DOI: 10.1088/1748-0221/11/11/C11028.

[125] G. Ingelman and P. E. Schlein. "Jet Structure in High Mass Diffractive Scattering". In: *Phys. Lett.* B152 (1985), pp. 256–260. DOI: 10.1016/0370-2693(85)91181-5.

[126] W Lampl et al. *Calorimeter Clustering Algorithms: Description and Performance.* Tech. rep. ATL-LARG-PUB-2008-002. ATL-COM-LARG-2008-003. Geneva: CERN, Apr. 2008.

[127] Matteo Cacciari, Gavin P. Salam, and Gregory Soyez. "The Anti-k(t) jet clustering algorithm". In: *JHEP* 04 (2008), p. 063. DOI: 10.1088/1126-6708/2008/04/063. arXiv: 0802.1189 [hep-ph].

[128] ATLAS Collaboration. "Jet energy scale measurements and their systematic uncertainties in proton-proton collisions at $\sqrt{s} = 13$ TeV with the ATLAS detector". In: CERN-EP-2017-038 (Mar. 2017).

[129] G. Piacquadio, Kirill Prokofiev, and A. Wildauer. "Primary vertex reconstruction in the ATLAS experiment at LHC". In: *J. Phys. Conf. Ser.* 119 (2008), p. 032033. DOI: 10.1088/1742-6596/119/3/032033.

[130] T Cornelissen et al. *Concepts, Design and Implementation of the ATLAS New Tracking (NEWT).* Tech. rep. ATL-SOFT-PUB-2007-007. ATL-COM-SOFT-2007-002. Geneva: CERN, Mar. 2007.

[131] John C. Collins. "Light cone variables, rapidity and all that". In: (1997). arXiv: hep-ph/9705393 [hep-ph].

[132] ATLAS Collaboration. Tagging and suppression of pileup jets with the ATLAS detector. Tech. rep. ATLAS-CONF-2014-018. Geneva: CERN, May 2014.

[133] J. Lange et al. "Gain and time resolution of 45 μm thin Low Gain Avalanche Detectors before and after irradiation up to a fluence of 10^{15} n_{eq}/cm^2". In: *JINST* 12.05 (2017), P05003. DOI: 10.1088/1748-0221/12/05/P05003. arXiv: 1703.09004 [physics.ins-det].

[134] CERN Courier. *ATLAS: A titan fit for the LHC (archive).* URL: http://cerncourier.com/cws/article/cern/35874.